LA-14182-T
Thesis

Ultrasonic Concentration in a Line-Driven Cylindrical Tube

This thesis was accepted by the Electrical and Computer Engineering Department, Portland State University, Portland, Oregon, in partial fulfillment of the requirements for the degree of Doctor of Philosophy. The text and illustrations are the independent work of the author and only the front matter has been edited by the IM-1 Writing and Editing Staff to conform with Department of Energy and Los Alamos National Laboratory publication policies.

Los Alamos National Laboratory, an affirmative action/equal opportunity employer, is operated by the University of California for the United States Department of Energy under contract W-7405-ENG-36.

LA-14182-T
Thesis
Issued: December 2004

Ultrasonic Concentration in a Line-Driven Cylindrical Tube

Gregory Russ Goddard

Los Alamos
NATIONAL LABORATORY
EST.1943

The World's Greatest Science Protecting America

DISSERTATION APPROVAL

The abstract and dissertation of Gregory Russ Goddard for the Doctor of Philosophy in Electrical and Computer Engineering were presented October 15, 2004, and accepted by the dissertation committee and the doctoral program.

COMMITTEE APPROVALS:

Branimir Pejcinovic, Chair

Pui Tak Leung

Gregory Kaduchak

Dipen Sinha

Gerald Recktenwald
Representative of the Office of
Graduate Studies

DOCTORAL PROGRAM APPROVAL:

Malgorzata Chrzanowska-Jeske,
Director
Electrical and Computer Engineering
Ph.D. Program

ULTRASONIC CONCENTRATION IN A LINE DRIVEN CYLINDRICAL TUBE

by

GREGORY RUSS GODDARD

A dissertation submitted in partial fulfillment
of the requirements for the degree of

DOCTOR OF PHILOSOPHY
in
ELECTRICAL AND COMPUTER
ENGINEERING

Portland State University

ACKNOWLEDGEMENTS

I want to thank my parents, whose love and support made this endeavor possible. They gave me encouragement and reassurance in every step of the process. I can not thank them enough.

Few students are lucky enough to have one good mentor. I was fortunate enough to have two great mentors, Dr. Dipen Sinha, and Dr. Gregory Kaduchak. I owe an enormous debt of gratitude to both of them for their invaluable guidance in this endeavor, and for their patient instruction even when it required many repetitions. They adeptly kept me moving in the right direction, while imparting their enthusiasm, insight and advice regarding not only my research, but other issues as well. They exemplify the standards of personal and professional excellence that I will continue to strive towards.

I would also like to thank John Martin and Dr. Steven Graves from the National Flow Cytometry Resource for their work towards the preliminary demonstration of acoustic focusing in a flow cytometer. They assistance was invaluable. Thanks to Dave Lizon and Roger Lujan for help with the mechanical design, and Dr. Christopher Kwiatkowski and Dave Lizon for many helpful discussions along the way.

I would also like to express my appreciation for the people who caused me to learn by the virtue of our numerous lively discussions and arguments. They are: Scott MacIntosh, Oana Marina, Dr. Mahlon Wilson, Dr. Ian Campbell, Judith Valerio, and a former fellow basement dweller, Dr. Jon

Warner.

I am also extremely grateful to the Electronic and Electrochemical Materials and Devices Group at Los Alamos National Laboratory for giving me the opportunity to work along side so many wonderful researchers while pursuing my doctorate. They made the work that much more enjoyable.

Finally, I am grateful for the financial support from the Laboratory-Directed Research & Development program, which provided the funding for my research.

TABLE OF CONTENTS

LIST OF TABLES

LIST OF FIGURES

ABSTRACT

An abstract of the dissertation of Gregory Russ Goddard for the Doctor of Philosophy in Electrical and Computer Engineering presented October 15, 2004

Title: Ultrasonic Concentration in a Line Driven Cylindrical Tube

The fractionation of particles from their suspending fluid or noninvasive micromanipulation of particles in suspension has many applications ranging from the recovery of valuable reagents from process flows to the fabrication of microelectromechanical devices. Techniques based on size, density, solubility, or electromagnetic properties exist for fulfilling these needs, but many particles have traits that preclude their use such as small size, neutral buoyancy, or uniform electromagnetic characteristics. While separation by those techniques may not be possible, often compressibility differences exist between the particle and fluid that would allow fractionation by acoustic forces. The potential of acoustic separation is known, but due to inherent difficulties in achieving and maintaining accurate alignment of the transduction system, it is rarely utilized.

The objective of this project is to investigate the use of structural excitation as a potentially efficient concentration/fractionation method for

particles in suspension. It is demonstrated that structural excitation of a cylindrically symmetric cavity, such as a tube, allows non-invasive, fast, and low power concentration of particles suspended in a fluid. The inherent symmetry of the system eliminates the need for careful alignment inherent in current acoustic concentration devices. Structural excitation distributes the acoustic field throughout the volume of the cavity, which also significantly reduces temperature gradients and acoustic streaming in the fluid; cavitation is no longer an issue.

The lowest-order coupled modes of a long cylindrical glass tube and fluid-filled cavity, driven by a line contact, are tuned, via material properties and aspect ratio, to achieve a coupled dipolar vibration of the system, shown to generate efficient concentration of particles to the central axis of the tube. A two dimensional elastodynamic model of the system was developed and subsequently utilized to optimize particle concentration within the system. The effects of tubing, fluid, and particle material properties, tube geometry, fluid flow, and tube length on the structural excitation and consequently power requirements and concentration quality within the tube were investigated theoretically and experimentally. Limitations of the method are discussed, as well as ways to minimize or compensate for deleterious effects. Finally a preliminary demonstration of the efficacy of acoustic concentration is presented.

1-INTRODUCTION

A variety of industries including material processing, polymer recycling, and the biosciences have a need for a method to concentrate, fractionate or separate dispersions of particles from their suspending fluid, or noninvasively manipulate particles in suspension. Over the last decade micro- and nanotechnology have become increasingly important for engineering. Several problems inherent in mechanical handling of small parts, such as fragility of the parts or adhesion to the positioning instruments, make non-contact manipulation methods highly attractive. With the ability to manipulate and orient particles, fabrication of periodic structures, or materials with anisotropic material properties such as conductivity, susceptibility, or mechanical strength becomes possible, thus opening a new field of material science. The ability to discriminate and quantify distinct populations of cells/cell organelles has become increasingly important with the growing trend to focus biological studies on various cell types.

Techniques based on size, density, solubility, or electromagnetic properties are commonly utilized within these fields, but many particles have traits that preclude the use of those techniques, such as small size, neutral buoyancy, or uniform electromagnetic characteristics. However, compressibility differences often exist between the particles and the suspending fluid that would allow fractionation by acoustic forces when other

fractionation methods are not feasible. The potential of acoustic separation is known, but due to inherent difficulties in achieving and maintaining accurate alignment of the transduction system, it is rarely utilized.

The research detailed in the following chapters involves the introduction and investigation of a new method of acoustically concentrating particles contained in fluid suspension. Through the mechanical excitation of a cylindrically symmetric cavity, such as a tube, this method eliminates the need for accurate alignment inherent in other acoustic methods. Additionally, the deleterious effects, which plague other acoustic fractionation methods, are nearly eliminated with the method investigated in this research.

In the following sections, several applications for particle concentration, fractionation, or manipulation will be discussed followed by descriptions of acoustic and non-acoustic methods that have been applied to fulfill those needs. The strengths and weaknesses of each of those methods will then be broached. It will be demonstrated that mechanical excitation of a cylindrically symmetric cavity, such as a tube, allows non-invasive, fast, and low power concentration of particles suspended in a fluid contained within the cavity.

1.1-Motivation

From the recovery of valuable reagents from process flows to the selective separation and recovery of polymer particles in production reactors, a need exists for an efficient method of fractionating particles from their suspending fluid. A variety of separation or fractionation methods are available for particle suspensions. Filters, sieves, and screens are inexpensive, relatively fast, and are therefore commonly used in a variety of industries with efficiencies as high as 100%. Gravitation and centrifugation methods, based on size or density differences, are often used for higher concentrations of particles, when ultrafiltration or filter clogging become concerns. Electric and magnetic fields have also been applied towards this end with 80-95% separation efficiencies and processing times far shorter than the previous two methods. While all of these methods have proven highly effective, and are therefore prevalent in a large range of industries, very few separation or purification methods for particles in solution discriminate the solids based on compressibility. Particles with traits such as small size, neutral buoyancy, or uniform electromagnetic characteristics pose difficulties for the aforementioned methods, requiring excessive time, prohibitive pressure drops, or extremely high electromagnetic fields.

While these traits may prohibit separation by other means, often

compressibility differences still exist between the particles and the fluid. Particles within a cavity, subjected to an acoustic field experience a drift force that transports them to local pressure or velocity potential minima depending on the acoustic density-compressibility contrast ratio between the particles and the surrounding fluid.

1.2-Existing Acoustic Techniques

The use of acoustic standing waves to concentrate initially homogeneously suspended particles at acoustic pressure nodal or antinodal planes in a fluid was first described by Kundt and Lehmann[1]. The effect was initially used only in the visualization of ultrasonic waves. However, the acoustic force can be used to, concentrate[1-5] fractionate[6-15] position[16-24], orient or align particles non-invasively [25,26].

Polymer recycling provides an example of a system where standard separation methods fail. The polymers to be sorted typically have a very narrow density distribution, but vary considerably in modulus. Gupta et al. developed a continuous acoustic fractionation method specifically for this application. Their system consisted of a parallel planar transducer/reflector pair and a flow splitter in a columnar configuration. They demonstrated separation of high and low density polyethylene microparticles of overlapping

size distributions using a periodic swept frequency drive signal. Mandralis et al. [27,28] utilized a narrow gap rectangular half-wavelength channel with a collection tube positioned along the midplane at one end of the cavity. They claimed that driving the cavity across the thin dimension of the long channel with alternating frequencies accelerated the concentration process and allowed for efficient collection. Mandralis et al. used bidirectional laminar flows and swept excitation frequency in an end-driven cylindrical geometry to further enhance concentration. Tolt and Feke[7,8,29] also used a cylindrical geometry and periodic swept frequency driven system similar to Gupta et al., but in contrast the resonance of the cavity was tuned to coincide with the axial resonances of the cylindrical tube. This coincidental resonance is shown to allow for more efficient separation of particles from the fluid. Semyonov and Maslow[30] also investigated a similar cylindrical system.

Over the last decade micro- and nanotechnology have become increasingly important for engineering. Mechanical handling of the parts yields several problems; fragility of the parts leads to breaking, humidity leads to adhesion of particles to positioning instruments, and individual handling is extremely time consuming. These problems can be avoided through the use of a non-contact manipulation method such as provided by acoustical forces.

Coakley et al. [31,32] investigated an end-driven cylindrical cavity with a traveling wave used to concentrate and subsequently position particles in a suspension. The traveling wave was induced either by two opposing transducers driven at slightly different frequencies or a transducer-reflector system with swept excitation frequency in their research. This superposition of traveling waves created a pseudo-standing wave with nodal planes moving slowly in space. They relied on a combination of Rayleigh streaming and inhomogeneity of the beam field to provide radial forces in the cylinder and thus concentrate to the axis. Haake and Dual[33] utilized an alternative approach in which the frequency input to opposing transducers was constant. By attaching different electrical impedances to the piezoceramic transducers, they achieved tunability of the reflection coefficient and could thereby control the nodal positions of the standing wave.

Another common type of traveling wave particle positioning device utilizes two ultrasonic transducers with intersecting beams driven out of phase relative to one another. Such a system was researched by Yamakoshi et al.[19, 34] and independently by Kozuka et al[35]. The two traveling waves generate an acoustic black line in front of the two transducers and thereby a spatially modulated acoustic force and acoustic radiation force perpendicular to the wave propagation direction. While Yamakoshi et al. investigated the

two-transducer one-dimensional case, Kozuka et al. used four transducers in a tetrahedral arrangement to achieve three dimensional particle micromanipulation. Frequency differences between one or more of the excitation transducers allowed translation of particles trapped at the intersection point.

Another common technique for acoustically positioning particles does not use a traveling wave, but rather a focused standing wave. One such system was studied by Hertz et al. [36-38]. Their system consisted of a confocal transducer/reflector pair with particle trapping occurring at the focus. They investigated applications for enhancing existing optical sensor sensitivities through size-selective trapping of particles in the active optical probe region. Yamakoshi et al. researched a similar focused acoustic trap for microbubbles as it could be applied for drug delivery. Another novel approach that utilizes leaky wave transducers was researched by Takeuchi et al[2]. They immersed two nonparallel surface acoustic wave (SAW) transducers in a suspension of glass spheres in water. Particle positioning was possible by alternating excitation of the transducers.

With the ability to manipulate and orient particles, fabrication of periodic structures, or materials with anisotropic material properties such as conductivity, susceptibility, or mechanical strength becomes possible. Saito

also used a rectangular cavity. They drove the transducer with a swept frequency signal. However, unlike Benes et al, the particle collection tube was near the wall rather than at the center. Similar h-shaped acoustic particle filters to Hill et al. were also studied by, Böhm et al[46], Hawkes et al[47], Harris et al[48], and Kozuka[49]. Böhm et al. investigated the ideal angle of operation under reduced and increased gravity conditions. Harris et al developed a method for micro-manufacturing such concentration chambers using lithography.

Other applications of biological interest include primary separation of cells and suspending phase, cross linking of micro particles coated with immunological molecules[50], and investigation of cell-cell interactions. A pre-concentration stage can increase sensitivity of existing detection technologies or serve as an acoustic particle trap.

The ability to discriminate and quantify distinct populations of cells/cell organelles has become increasingly important with the growing trend to focus biological studies on various cell types. Flow based cytometry and cell sorting are unique techniques that permit the identification, analysis and purification of cells based on their expression of specific markers[51]. Flow cytometry is used for a variety of analyses including: cell cycle analysis, viability, ion influx, and cell sorting. It works by passing cells in a single-file

through a laser beam by continuous flow of a fine stream of the suspension while photon detectors measure scattered light and fluorescence at several different wavelengths. The benefit of utilizing acoustic particle focusing rather than hydrodynamic focusing has not yet been fully realized. It is towards this last application, in analytical biology, that the applications of this research are directed.

1.3-Research Summary

Present research investigates a novel acoustic particle-positioning device where the acoustic excitation is generated by the entire structure, as opposed to a localized transducer, differing from all of the works referenced in section 1.2. The inherent symmetry of the system eliminates the need for careful alignment inherent in current acoustic concentration devices. By vibrating the entire structure as an extended source, there is appreciable acoustic energy transfer into the fluid. This results in particle concentration over the entire length of the flow chamber, translating into longer residence times of the particles within the acoustic positioning field and, consequently, lower pressure levels to drive the acoustic focusing field. Furthermore, the distribution of the acoustic field throughout the volume of the cavity significantly reduces temperature gradients and acoustic streaming in the

fluid. This new approach could lead to a simpler, more efficient technique for particle manipulation with applications stretching from process flow separation to micromanipulative nanotechnology to flow cytometry, one of the driving factors for this research.

The lowest-order structural modes of a long cylindrical glass tube driven by a piezo-ceramic with a line contact are tuned, via material properties and aspect ratio, to match resonant modes of the fluid-filled cavity. The cylindrical geometry eliminates the need for accurate alignment of a transducer/reflector system, in contrast to the cases of planar, confocal, or traveling wave fields.

Optimization of concentration efficiency requires an accurate model of the system. Such a model would allow for a methodical search for optimal experimental parameters for efficient structurally driven acoustic concentration as well as elucidate the dynamics of particle concentration. For the purposes of this investigation, a two dimensional elastodynamic global matrix approach was utilized. In chapter 2, this two-dimensional elastodynamic global matrix approach is derived and compared to other standard vibration modeling techniques. As validation of model accuracy, the exterior surface vibration amplitudes of six types of glass tube was measured and compared to predicted surface vibration amplitude. These exterior

vibration patterns are correlated to dynamics within the fluid, including a modal analysis of concentration at different frequencies. A characteristically dipolar vibration was predicted, and observed to be the only mode that efficiently induced concentration within the tube. Finally, exploratory predictions are made for various tube materials to determine other potential tube materials for efficient structurally excited acoustic concentration.

Chapter 3 provides a description of forces exerted on particles in an acoustic field, and calculations revealed rotational asymmetry in the force distribution within the cavity, leading to differences in concentration quality relative to the drive transducer excitation direction.

Chapter 4 focuses on the quality evaluation and imaging of particle concentration via an experimental parametric evaluation of effects on concentration quality, speed, and relative stability. The primary technique for investigation was microscopic imaging of the concentration pattern. Several parameters are investigated including input power, flow rate, particle size, tube aspect ratio, tube materials, fluid selection, and optimization of multiple transducer excitations. Experiments showed that the lower energy density in the cavity, brought about through excitation of the whole cylinder, resulted in reduced cavitation, convection, and thermal gradients.

Chapter 5 describes the limitations on particle and fluid selection,

excitation frequency and power input, tube aspect ratio, and the perturbations from particles in the cavity or temperature changes of the system These inherent limitations on the method are discussed in order of magnitude: acoustic contrast ratio, the basis for particle and fluid selection, power input, tube aspect ratio and corresponding excitation frequency, thermal perturbation of resonance and finally particle perturbation of resonance Methods for extending the usable range of the structurally driven concentration method are also discussed.

Since the objective of this research project was to investigate the use of structural excitation as a potentially efficient concentration/fractionation method for particles in suspension, practical application of the method was necessary to evaluate efficacy. Chapter 6 describes a preliminary demonstration of acoustic concentration applicability to the replacement of sheath flow in flow cytometry. The elimination of sheath fluid would reduce power and consumable requirements, resulting in increased portability of the instrument. Two experiments to validate the applicability of this method to the application are described.

Structural excitation as a method of acoustic concentration proved to be an effective and efficient method for manipulating particles in suspension. The applications are varied including separation/fractionation of suspended

particles, micro-manipulative nanotechnology, novel material fabrication, and improvement of analytical techniques in biology. Chapter 7 summarizes the results and proposes future directions of research.

2-CYLINDRICAL VIBRATION MODEL

2.1-Introduction

Particles within a cavity experience a time-averaged drift force that transports them to local potential minima. In a planar standing wave, this corresponds to nodal or anti-nodal positions depending on the acoustic contrast ratio between the particles and the surrounding fluid.

The present research investigates the system diagrammed in Fig. 2-1. It is argued that vibration of the entire structure as an extended source allows appreciable acoustic energy transfer into the fluid. It is further claimed that the inherent symmetry of the system eliminates the need for careful alignment inherent in the acoustic concentration devices. The results of the experimental investigation of these assertions as they apply to particle concentration, the intended application of this research, are described in chapter 4. A typical concentration pattern for one of the tubes, namely soft glass, is shown in figure 2-2. However, efficient optimization of the experimental parameters requires an accurate model of the line-driven structure for both parameter evaluation and elucidation of the particle concentration mechanism. It is therefore the purview of this chapter to develop, and subsequently verify a model of the line-driven cylindrical

system. For the purposes of this investigation, axial waves are ignored, allowing reduction of the problem to two dimensions and significant reduction in computation time, as shown in Fig. 2-3. A two dimensional elastodynamic global matrix approach is utilized.

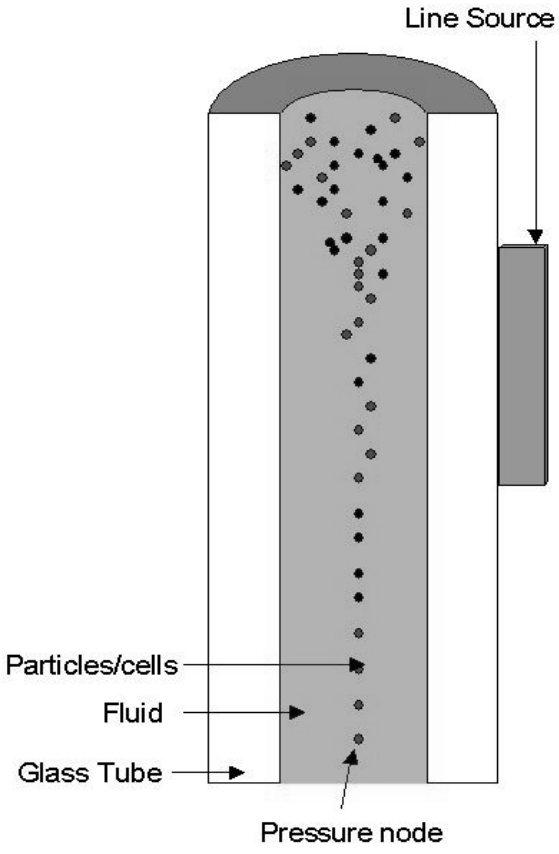

Figure 2-1. Diagram of experimental concentration tube with piezoceramic line source indicated.

et al. [39-41] -studied the use of acoustic standing waves to generate polymer composites with two-dimensional artificial lattice structure. They solidified glass particles into a polysiloxane resin and verified periodicity via optical diffraction off the lattice. Forces that exert torque on particles are also present in a sound field, inducing spin or alignment. Yamahira et al derived expressions for the torque on fibers in an ensonified liquid and experimentally verified their predictions with polystyrene fibers in sugar solution.

Microfluidic devices based on this principle have the potential to trap and filter particles from samples prior to analysis or separate and position particles within the flow channels. Acoustic concentration of biological cells could be incorporated in a fully automated analysis system providing contamination-free high-speed, real-time measurements. Sparey-Taylor et al[42] investigated such an application for automation of lab-on-a-chip systems.

Benes et al[43] developed a continuous-flow ultrasonic production filter for in-line bio-cell filtering. Their cell consisted of a rectangular cavity and a transducer/reflector pair. They are able to demonstrate thousands of hours of continuous operation at volumes up to 250 L per day with minimal effect on cell viability. The collection tube resided coincident to the central axis.

In another continuous-flow ultrasonic filter investigation, Hill et al. [44,45],

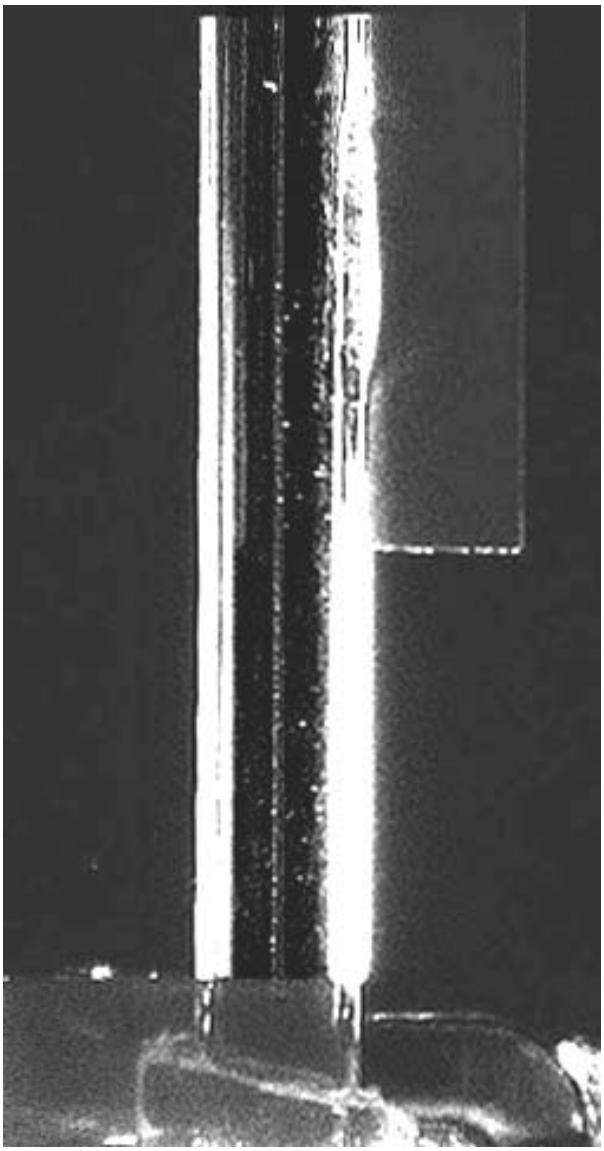

Figure 2-2. Concentrated 10-micron polystyrene beads in water-filled soft glass at 417 kHz.

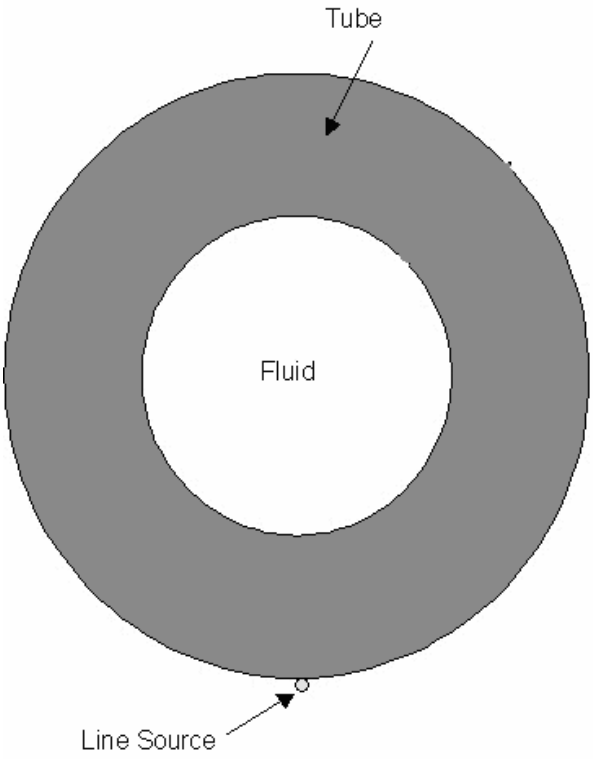

Figure 2-3. Diagram of system reduced to two-dimensions.

The vibrational modes of cylindrical elastic shells were first described by Rayleigh[52] in his analysis of extensional vibrations of infinitely long shells. Baron and Bleich[53, 54] later extended his membrane model, to include bending effects. Love[55] developed a shell theory that included bending moments and shear forces. Other thin shell theories were developed by Flugge[56], Vlasov[57], Donnell[58, 59] and Sanders[60], but by the very definition of a thin shell theory, did not include any shear deformation or rotary inertia

terms. Leissa[61] wrote a monograph including a fairly comprehensive listing of thin elastic circular cylindrical shell vibration models. The inclusion of shear terms led to the development of several thick shell models with validity for higher thickness to diameter ratios, such as Mirsky and Hermann[62, 63].

The methods for modeling the vibration of cylindrically layered systems fall into three major categories. The first of these, utilizes finite element or finite difference methods. Another technique uses propagator matrices. The third category of modeling techniques for cylindrical cavities uses the 2-D equations of elastodynamics written in the form of a global matrix describing the system.

2.2-Finite Element Approach

Finite element models subdivide systems under analysis into interconnected elements that represent sections of the material. As stresses are applied to a system, the sections in the material react in such a way that they influence the reaction of their adjacent sections. The finite element model simulates this behavior by solving differential equations for each of the elements that represents a section in the material. Finite element methods can easily adapt to irregular and unstructured computational meshes and inhomogeneous and anisotropic material properties. They require a

discretized set of points, which fill up the domain (or volume) of interest. The points are connected into elements by an automated mesh generation program. There are two main types of meshes: structured and unstructured. The simplest structured mesh is like the regular set of squares on a sheet of graph paper. Unstructured grids do not have any predefined element size or shape and in two dimensions can include triangles or other shapes as well as the quadrilaterals used by structured grids.

Several finite-element modeling techniques have been applied to cylindrically layered systems. One such technique put forth by Von Flotow[64] for the analysis of vibrations of structural networks and later applied to cylindrical shells by Borgiotti and Rosen[65, 66], uses a state vector approach. Under this method, the elastodynamic field is decomposed into azimuthal harmonics, and the shell is simplified as a set of first-order ordinary differential equations from Newton's and Hooke's laws, which govern the dependence upon longitudinal coordinate of a "state vector" and completely identify the elastodynamic state at each cylinder location.

The solution to the homogeneous problem, without external excitations, provides a set of characteristic waveguide modes and the dyadic Green's function, which describes the forced point excitation, is constructed as a linear combination of the waveguide modes with the boundary

conditions establishing the values of the coefficients. The components of the state vector are force and moment resultants per unit circumferential length and linear and angular velocities. The vector satisfies a linear first-order vector/matrix differential equation defined by the 2-D stress/strain relationships integrated over cylindrical shell thickness and Newton's law for translation and rotation with linear variation through the shell thickness. This approach allows for direct calculation of mechanical power flow through the system while maintaining versatile applicability to arbitrary structures. Another finite element or finite difference technique was used by Skelton and James[67] in their analysis of anisotropic layered cylinders. They wrote effective stiffness matrices for each fluid and solid element in the system. While finite element techniques allow for modeling of point excitations, they become computationally inefficient for high frequencies where significant increase in spatial sampling is required. Additionally exponential decay of interference between longitudinal and shear waves is not modeled elegantly in this approach.

2.3-Transfer Matrix Approach

Another method for modeling a layered cylindrical system is through the use of transfer matrices, also referred to as propagator matrices[68, 69]. In

geophysics it is known as the Thomson-Haskell approach. It has been used to model axisymmetric[70, 71] and non-axisymmetric cylindrical shells and boreholes[72]. Transfer matrix methods are capable of modeling scattered signal amplitudes under a variety of incident wave-shapes at arbitrary incident angles. The reflection and transmission coefficients are calculated for each layer by expressing the displacements and stresses in terms of the scalar and vector potential functions and formulating the characteristic equations in terms of their amplitudes in individual layers by satisfying the interfacial and boundary conditions as a function of incidence angle. A matrix consisting of layer thickness, mass density, effective elastic constants and attenuation represents each layer. The coefficients are then iteratively evaluated through consecutive layers. This technique is fairly computationally efficient for arbitrary number of layers, but suffers from instability for thin layers and high frequencies. Wang and Rokhlin[73] proposed a modification of the transfer matrix method with increased stability. Rather than recursively calculating transmission and reflection coefficients, they used a matrix of density, sound speed and attenuation for each layer to generate an effective stiffness matrix for all layers. While their method does increase the stability, evanescence across layers still requires careful formulation to maintain the numerical stability.

2.4-Global Matrix Approach

The third method uses a global matrix approach[74-81]. Wang and Rokhlin proved that all of three of the methods were equivalent although they differed in computational efficiency and stability. Although global matrix methods are less computationally efficient than transfer matrix methods for large number of layers, global matrix methods provide the greatest numerical stability when properly formulated. Jensen et al. present a more thorough comparison of global matrix methods to propagator matrices in their book. The 2-D equations of elastodynamics in the form of global matrix methods have previously been used to model infinitely long cylindrical shells excited by acoustic plane waves at normal[78-86]oblique[87] incidences. These papers do not suggest a way to address the issue of structural complexity or generalize to arbitrary excitation sources.

2.5-Direct Global Matrix Approach

The direct global matrix approach described by Ricks and Schmidt was chosen for the purposes of this research based on their treatment of regions of numerical instability. In their model, the cylindrical coordinate system is chosen with the z-axis coincident with the axis of the cylindrical layers, the layers are numbered n=1 to N where layer 1 includes r=0 and

layer N extends to infinity. The variable R_n corresponds to the boundary between layer n and n+1. All layers are assumed to be isotropic and homogeneous viscoelastic with Lame' constants λ_n and μ_n and density ρ_n. Fig. 2-4 diagrams a cross-section of the fluid-filled cylindrical system with inner and outer radii labeled.

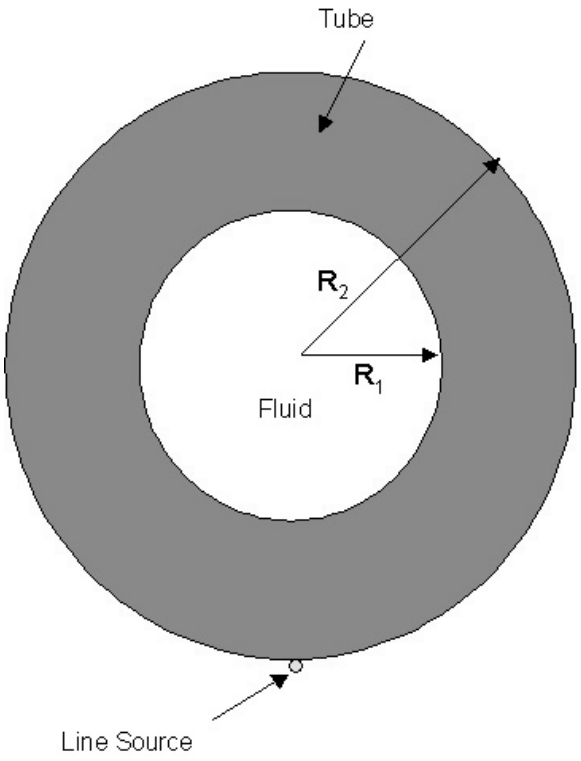

Figure 2-4. Diagram of angle scan apparatus used to measure surface vibration of the glass tube.

The subscript refers to the layer number described by the constants. If the layer is a solid then the displacement field u_n is governed by the 2-D

equations of elastodynamics written in Eq. 2.1.

$$(\lambda_n + 2 \cdot \mu_n)\nabla\nabla \cdot \vec{u}_n - \mu_n \nabla \times \nabla \times \vec{u}_n + \vec{f_n} = \rho_n \ddot{\vec{u}}_n \quad (2.1)$$

The variable f_n refers to the applied force per unit volume in layer n. The longitudinal and shear wave speeds are related to the Lame' coefficients as described in Eqs. 2.2 and 2.3. Optionally, viscoelastic attenuation can be modeled by allowing the Lame' coefficients to be complex.

$$c_l = \sqrt{(\lambda_n + 2\mu_n)/\rho_n} \quad (2.2)$$

$$c_s = \sqrt{\mu_n / \rho_n} \quad (2.3)$$

The corresponding wave numbers are expressed as

$$h_n = \omega / c_l \quad (2.4)$$

$$k_n = \omega / c_s \quad .(2.5)$$

Any terms involving c_{sn} and k_n are ignored and μ_n=0 for fluid layers, since It is assumed no transverse stress transfers from the solid to the fluid, and no shear waves in the fluid. A time dependent ring force of $e^{-i\omega t}$, is assumed without loss of generality, since the time dependence of other forcing functions, including point or line excitation, can be synthesized from time-harmonic forces by using a Fourier integral over frequency. Similarly an angular dependence of $e^{iv\tau}$ is assumed, where v is the order, without loss of generality. Fourier series summation over integer orders yields modes, while

summation over complex orders synthesizes traveling waves. The displacement field can be expressed as the linear superposition of homogeneous and particular solutions shown in Eq. 2.6.

$$\vec{u}_n = \vec{u}_n^{\,H} + \vec{u}_n^{\,P} \tag{2.6}$$

The homogeneous solutions are source-free solutions to the Helmholtz equations. The particular solutions are waves that would emanate from the ring forces in layer n if the layer extended over all space. The sum of the homogeneous solutions and the particular solutions, so-called “free space” waves, satisfy the boundary conditions. Therefore the homogeneous field is governed by

$$(\lambda_n + 2\cdot\mu_n)\nabla\nabla\cdot\vec{u}_n^{\,H} - \mu_n\nabla\times\nabla\times\vec{u}_n^{\,H} + \rho_n\omega^2\vec{u}_n^{\,H} = 0 \tag{2.7}$$

Using the Helmholtz vector decomposition, the field can be expressed in terms of scalar displacement potentials as

$$\vec{u}_n^{\,H} = \nabla\Phi_n + \nabla\times(a_z\Psi_n) + \frac{1}{k_n}\nabla\times\nabla\times(a_z X_n) \tag{2.8}$$

The potentials satisfy the Helmholtz equations,

$$(\nabla^2 + h_n)\Phi_n = 0 \tag{2.9}$$

$$(\nabla^2 + k_n)\Psi_n = 0 \tag{2.10}$$

$$(\nabla^2 + k_n)X_n = 0 \tag{2.11}$$

Since only the radial and azithmul directions are of interest, the

differential equations may be expressed as

$$\frac{d^2\Phi_n}{dr^2}+\frac{1}{r}\frac{d\Phi_n}{dr}+(h_{rn}^2-\frac{v^2}{r^2})\Phi_n=0 \qquad (2\text{-}12)$$

$$\frac{d^2\Psi_n}{dr^2}+\frac{1}{r}\frac{d\Psi_n}{dr}+(k_{rn}^2-\frac{v^2}{r^2})\Psi_n=0 \qquad .(2.13)$$

Similarly the particular solutions can be expressed as[76]

$$\vec{u}_I^P=\nabla\Phi_I+\nabla\times(a_z\Psi_I)+\frac{1}{k}\nabla\times\nabla\times(a_zX_I),(R_2-\varepsilon)\le r\le R_2 \qquad (2.14)$$

$$\vec{u}_E^P=\nabla\Phi_E+\nabla\times(a_z\Psi_E)+\frac{1}{k}\nabla\times\nabla\times(a_zX_E),R_2\le r\le(R_2+\varepsilon) \qquad .(2.15)$$

The subscripts E and I refer to the interior and exterior regions and ε refers to an infinitesimal interval. Continuity of stress and displacement are assumed at $r=R_2$. Then integrate each of the vector components over a vanishingly small interval of r. Although any pair of the Bessel and Hankel functions J, Y, $H^{(1)}$, or $H^{(2)}$ would satisfy the differential equations, desire for numerical stability dictates that the homogeneous and particular solutions are represented as

$$\Phi^P = \sum_{\upsilon=0}^{\infty} \left(\frac{iR_2 F_r}{4\rho_2 \omega^2} \left[\frac{dH_\upsilon^{(1)}(h_2 r)}{dr} \right]_{r=R_2} J_\upsilon(h_2 r) \right) e^{j(\upsilon\theta - \omega t)} \tag{2.16}$$

$$\Psi^P = \sum_{\upsilon=0}^{\infty} \left(\frac{\upsilon R_2 F_r}{4\rho_2 \omega^2} H_\upsilon^{(1)}(k_2 R_2) J_\upsilon(k_2 r) \right) e^{j(\upsilon\theta - \omega t)} \tag{2.17}$$

$$\Phi_n^H = \sum_{\upsilon=0}^{\infty} \left(A_{n\upsilon} H_\upsilon^{(1)}(h_n r) / H_\upsilon^{(1)}(h_n R_{n-1}) + B_{n\upsilon} J_\upsilon(h_n r) H_\upsilon^{(1)}(h_n R_n) \right) e^{j(\upsilon\theta - \omega t)} \tag{2.18}$$

$$\Psi_n^H = \sum_{\upsilon=0}^{\infty} \left(C_{n\upsilon} H_\upsilon^{(1)}(k_n r) / H_\upsilon^{(1)}(k_n R_{n-1}) + D_{n\upsilon} J_\upsilon(k_n r) H_\upsilon^{(1)}(k_n R_{n-1}) \right) e^{j(\upsilon\theta - \omega t)} \tag{2.19}$$

This formulation affords numerical stability over a wide range of frequencies and circumferential orders. This is achieved in three requirements on the global matrix definition. The first is a requirement that evanescence across layers should decouple the global system into separate subsystems, so solution values caused by sources on one side of the layer should have vanishing influence on sources on the opposite side of the evanescent layer. A properly structured global matrix forces this automatically when the system is solved by Gaussian elimination with partial pivoting. Effectively, the global matrix partitions itself, and the vanishing coefficients suppress the propagation of numerical round off errors during back-substitution.

The second requirement on the global matrix is the choice of the pair

of cylindrical Bessel and Hankel functions used in the expression of the solutions. In order to maintain stability for orders much greater than the product of the wave number and the radial coordinate, and still maintain numerical stability for evanescence, only the $H^{(1)}$ and J pairing avoids the pitfalls of computation with finite precision.

The third requirement is for the selection of normalization terms that cancel overflow and underflow conditions. Normalization terms consisting of Hankel functions of the first kind evaluated at inner or outer radii of each layer are alternately multiplied and divided by each of the terms. These terms elegantly cancel the over flow of the Hankel functions of r and the underflow of the Bessel functions of r for orders much larger than the product of the wave number and coordinate r. For evanescence across layers, they implement the decoupling described above. Since the Hankel functions are already evaluated, there is no computational expense to assure this numerical stability. The coefficients $A_{n\nu}$, $B_{n\nu}$, $C_{n\nu}$, and $D_{n\nu}$ will be determined from the boundary conditions for each layer. F_r is the amplitude of the radial forcing function. Since the boundary conditions are expressed in terms of the displacement and stresses at each surface, the displacements in layer n are expressed as

$$\vec{u}_{rn} = \frac{d\Phi_n}{dr} + \frac{iv}{r}\Psi_n \quad (2.20)$$

$$\vec{u}_{\theta n} = \frac{iv}{r}\Phi_n - \frac{d\Psi_n}{dr} \quad .(2.-21)$$

Hooke's Law in cylindrical coordinates for layer n yields the pair of equations:

$$\vec{\sigma}_{rrn} = -\lambda_n h_n^2 \Phi_n + 2\mu_n\left(\frac{d^2\Phi_n}{dr^2} + \frac{iv}{r^2}\Psi_n + \frac{iv}{r}\frac{d\Psi_n}{dr}\right) \quad (2.22)$$

$$\vec{\sigma}_{r\theta n} = \mu_n\left(\frac{2iv}{r}\left(-\frac{\Phi_n}{r} + \frac{d\Phi_n}{dr}\right) - \frac{v^2}{r^2}\Psi_n + \frac{1}{r}\frac{d\Psi_n}{dr} - \frac{d^2\Psi_n}{dr^2}\right) \quad (2.23)$$

The global matrix is constructed using the unknown displacements and stresses associated with the homogeneous waves, written in terms of an amplitude vector and set equal to the displacements and stresses due to the particular solutions arising from the forcing excitation. Solutions for the coefficients are determined by applying Cramer's rule[88]. Equivalently, the equation shown in Eq. 2.12 can be solved using Gaussian elimination with partial pivoting. Both techniques work reliably if the equations are scaled to make all of the matrix coefficients dimensionless. To do so, divide the displacement equations by the compression wave number of the fluid layer, h_1 and divide all stress equations by $\lambda_1 h_1^2$. The choice of the reference layer is not critical, but the fluid layer was chosen since the Lame' coefficient for a fluid only contains longitudinal sound speed, and therefore simplified the

equation. The boundary conditions, which generate the global matrix, are

$$\vec{u}_{r1}^{H}(R_1) = \vec{u}_{r2}^{H}(R_1) \quad (2.24)$$

$$\vec{\sigma}_{r1}^{H}(R_1) = \vec{\sigma}_{r2}^{H}(R_1) \quad (2.25)$$

$$\vec{\sigma}_{r\theta 2}^{H}(R_1) = 0 \quad (2.26)$$

$$\vec{\sigma}_{rr2}^{H}(R_2) = \vec{\sigma}_{rr}^{P}(R_2) \quad (2.27)$$

$$\vec{\sigma}_{r\theta 2}^{H}(R_2) = \vec{\sigma}_{r\theta}^{P}(R_2) \quad .(2.28)$$

The variables R_1 and R_2 are the internal and external tube radii respectively. The boundary conditions require continuity of displacement at the inner boundary R_1. The radial stress is continuous at R_1. Since the cylinder is fluid filled, no shear stress is assumed present at the fluid-solid interface at R_1. Since the system is being driven at the outer surface, radial and angular stresses are continuous and equal to the particular solutions at the outer boundary R_2. Since the Hankel function of the first form is not defined at r=0, the coefficients A_1 and C_1 go to zero. If the cylindrical system was not assumed bounded at the outer radius, R_2, by a pressure relief fluid such as air, then due to a similar divergence of the Bessel function at r equals infinity demands the coefficients B_3 and D_3 go to zero. The finite width of the element is accounted for in the calculations by applying a Gaussian weighting function about the point $\theta = {}^{3\pi}/_{2}$ radians to the forcing function of the

particular solutions. A 32-bit Fortran program was written to perform the computation. To maintain generality the scalar potentials are defined as complex. This allowed for both viscoelastic attenuation and traveling waves, although neither was used for the purposes of this research. The results are stored in text files and later analyzed and plotted using Matlab code.

2.6-Theory Results

The model is applied to the soft glass tube shown in figure 2-2. The material properties of soft glass were determined by matching the measured index of refraction, density, longitudinal sound speed, and coefficient of thermal expansion to soda lime glass. A longitudinal sound speed of 5900 m/s, shear sound speed of 3300 m/s, and density of 2.43 g/cm^3 are used for the soft glass[89]. The tube has an inner diameter of 2 mm and an outer diameter of 4 mm. The water in the cavity is assumed to have a density of 1 g/cm^3 and a sound speed of 1487 m/s. The density and sound speed of the 10-micron polystyrene beads are 1.06 g/cm^3 and 2350 m/s respectively. They were assumed to be of low enough concentration to minimally perturb the effective material properties of the fluid in the cavity.

The graphs shown in Fig. 2-6 as well as all of the subsequent graphs of pressure and velocity of the wave were individually normalized against

their maximum value. The gray scale used is shown in figure 2-5. The minimum to maximum scale values of 0 and 1, are shown left to right. Figure 2-5C shows potential experienced by the particles, and is therefore plotted such that the large negative value is black, with increasing values towards zero at the right end, in white.

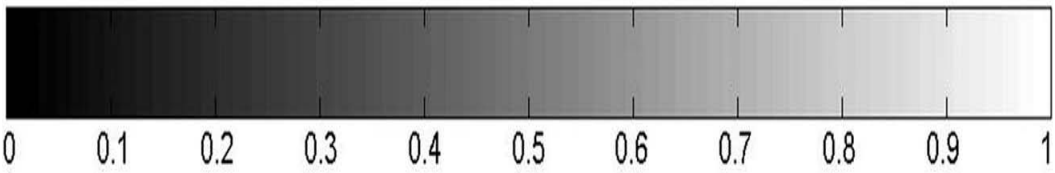

Figure 2-5 Normalized gray scale used for graphs.

The pressure and velocity of the wave were calculated for a 417 kHz excitation frequency, and are shown in figure 2-6A and 2-6B. As can be seen in the figure, the mode at 417kHz exhibits a dipolar structure. Figure 2-6C shows the potential experienced by the polystyrene beads in the cavity. The acoustic force on the particles is the gradient of the potential. Figure 2-6D shows the magnitude of the acoustic force on the polystyrene beads in the cavity. It can be seen that the particles experience a force driving them to the center of the cavity. This corresponds well to the observed experimental concentration of the particles to the central axis of the soft glass tube at 417 kHz.

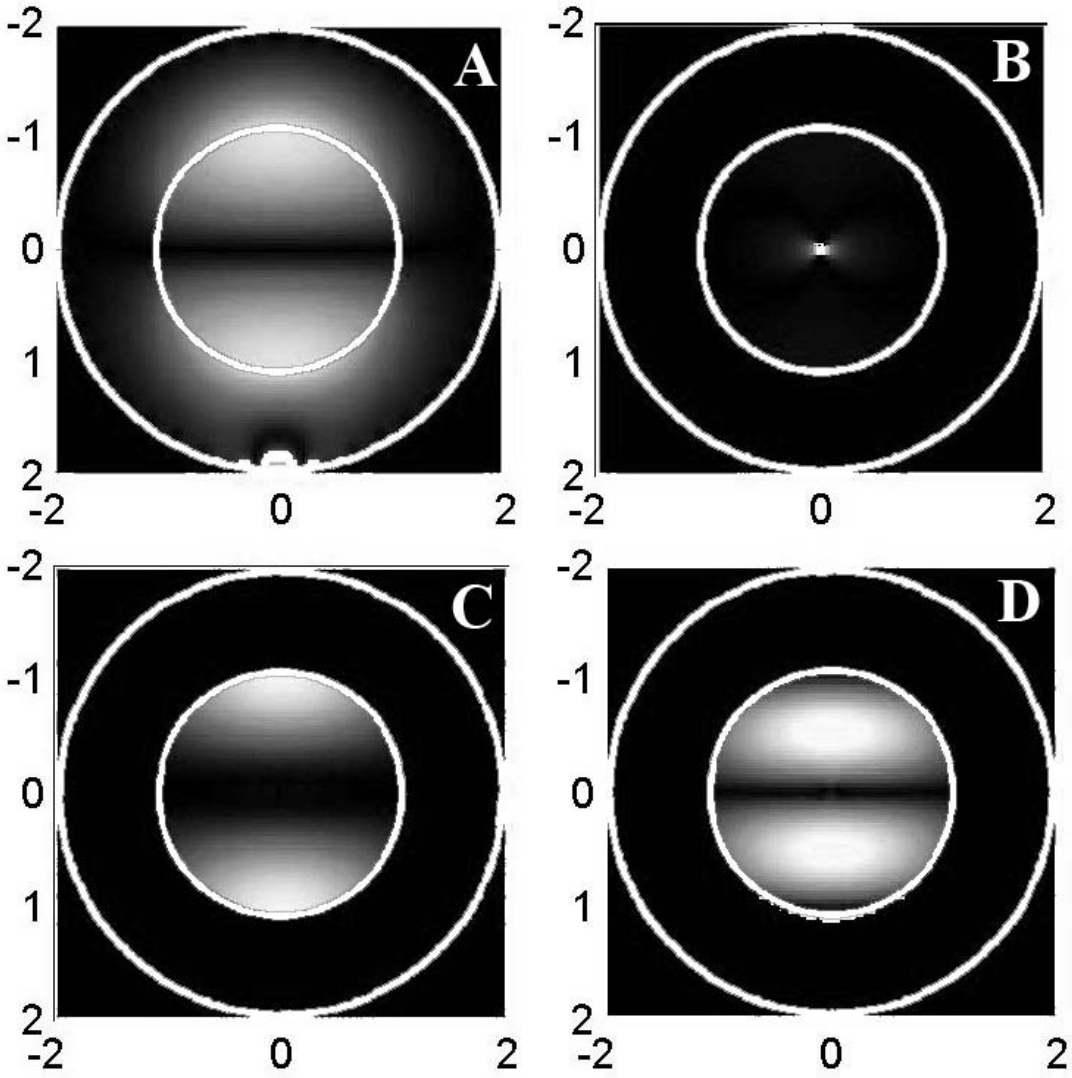

Figure 2-6 Predicted for water filled soft glass tube at 417 kHz(A) Pressure inside cavity and radial stress in the glass (B) Velocity (C) Potential experienced by 10-micron polystyrene beads (D) Acoustic force experienced by 10-micron polystyrene beads. (All) Inner and outer tube radii indicated in white

To experimentally verify the validity of the model, beyond the

predictions of particle concentration position, it is necessary to specifically verify the mode structure predicted by theory. The following section details the steps taken towards this evaluation of validity.

2.7-Apparatus

Due to the inherent difficulty in directly measuring the sound pressure inside the tube, and thus directly verifying the vibration model discussed previously, external surface displacement of the tube was calculated for comparison to experimental results and consequent elucidation of the forces within the cavity. Three types of glass, soft, borosilicate and quartz, and four aspect ratios of tube are experimentally characterized under excitation frequencies ranging from 300 kHz to 700 kHz in 0.5 kHz increments. For the purpose of time efficiency, the model was calculated over the same range at 1 kHz intervals. The vibration model was evaluated for each type of tube for air and water filled states. Additionally, as a method of further confirmation, the predicted spectral positions of resonances are verified experimentally. The primary reason for restriction of the frequency range arose from the bandwidth limitations of the excitation transducer. For aesthetic purposes, the excitation source was located at the 270-degree mark for the calculated and experimental data presentation. The demarcations around the polar axis

are given in degrees, while the radial axis in both figures indicated the absolute value of displacement. The values of sound speed and density of air used in the calculations are 340 m/s and 10^{-6} g/cm^3. Water was assumed to have sound speed of 1487 m/s and density of 1 g/cm^3. The driving transducer was affixed along the long axis of the tube using cyano-acrylate glue as diagrammed in figure 2-1. For the angular vibration measurements, the tube was mounted to a computer controlled angular stepper motor stage and probed with a pinducer shown from above Fig. 2-7 and a side view Fig. 2-8. A pinducer is a transducer with much greater length than diameter. The Vexta PX245M-02 angular stage was connected to a VP9000 stepper motor controller. A photo of the stepper motor controller is shown in Fig.2-9.

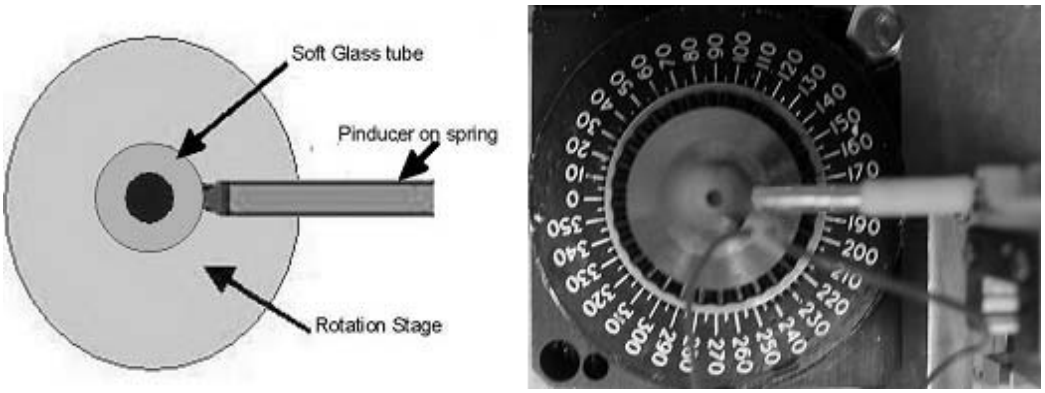

Figure 2-7. Diagram of angle scan apparatus used to measure surface vibration of the glass tube.

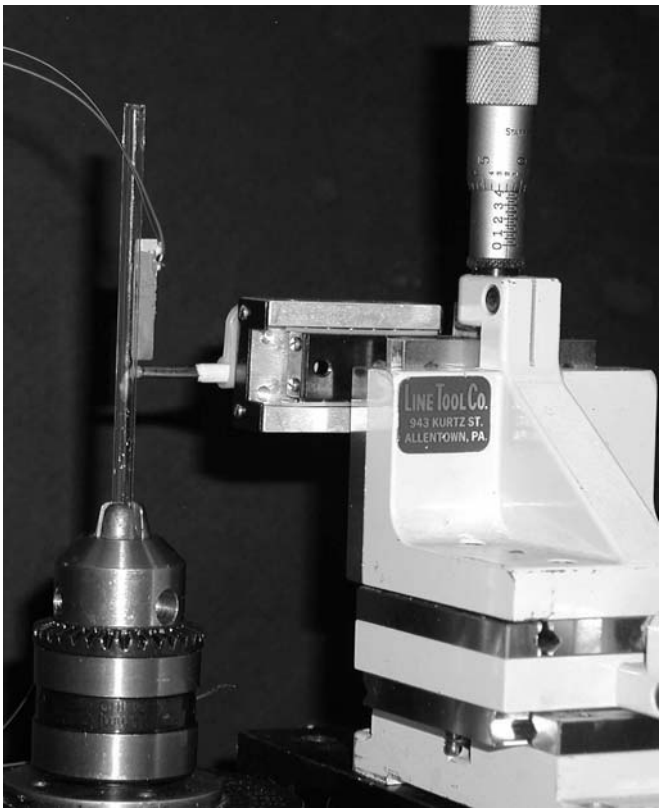

Figure 2-8. Side view of angle-scan apparatus used to measure surface vibration of the glass tube.

Figure 2-9. Picture of Velmex VP9000 stepper motor controller.

The pinducer was contacted to the tube immediately below the drive transducer to allow for full 360^{o} measurement of vibration. Differences between the measurements when adjacent to the transducer versus below it are negligible except when both the pinducer and drive transducer are within 1cm of the mounting chuck. Software was written to control the angular scanning stage and capture the data. The angular resolution of the stepper motor and angular stage was approximately 100 steps per degree. A half hemisphere of solder was affixed to the end of the pinducer to assure point contact with the tube, and thus minimize angular integration of the signal. To maintain constant contact with the tube, the pinducer was mounted on a

spring-loaded linear slide. The pinducer/spring assembly was attached to a three-axis stage to allow accurate positioning of the probe. Each type of tube was characterized both air-filled and water-filled several times to assure reproducibility. Spectral data of the vibrations of the system are performed using an Agilent 8712ES network analyzer capable of scanning from 300-1300GHz. The network analyzer is displayed in Fig. 2-10

Figure 2-10. Agilent network analyzer used for spectral characterization.

The length dimension of the tube varied over the same range as the soft glass. The inner and outer diameters of the tube are shown in table 2-1.

Glass Type	Inner Diameter	Outer Diameter
SG-Soft glass(soda-lime)	2.01mm	3.97mm
RG-Regular glass (borosilicate)	1.57mm	3.84mm
TQ-Thin quartz	1.24mm	3.86mm
QQ-Thick quartz	1.40mm	7.52mm
AQ-Quartz	1.23mm	5.78mm
BQ-Quartz	3.72mm	8.94mm
CQ-Quartz	5.24mm	7.75mm
DQ-Quartz	4.14mm	6.54mm
EQ-Quartz	7.15mm	9.65mm
CT-Capillary Tube (borosilicate)	1.03mm	1.77mm

Table 2-1 Table of inner and outer tube diameters. Two letter designations of each type of tube are listed.

As stated above, several different glass tubes were used during the course of these experiments. They are identified by two letter designations of SG, RG, QQ(aka Q), TQ, AQ, BQ, CQ, DQ, and EQ. A side-by-side comparative picture of the tube dimensions is shown in Fig.2-11.

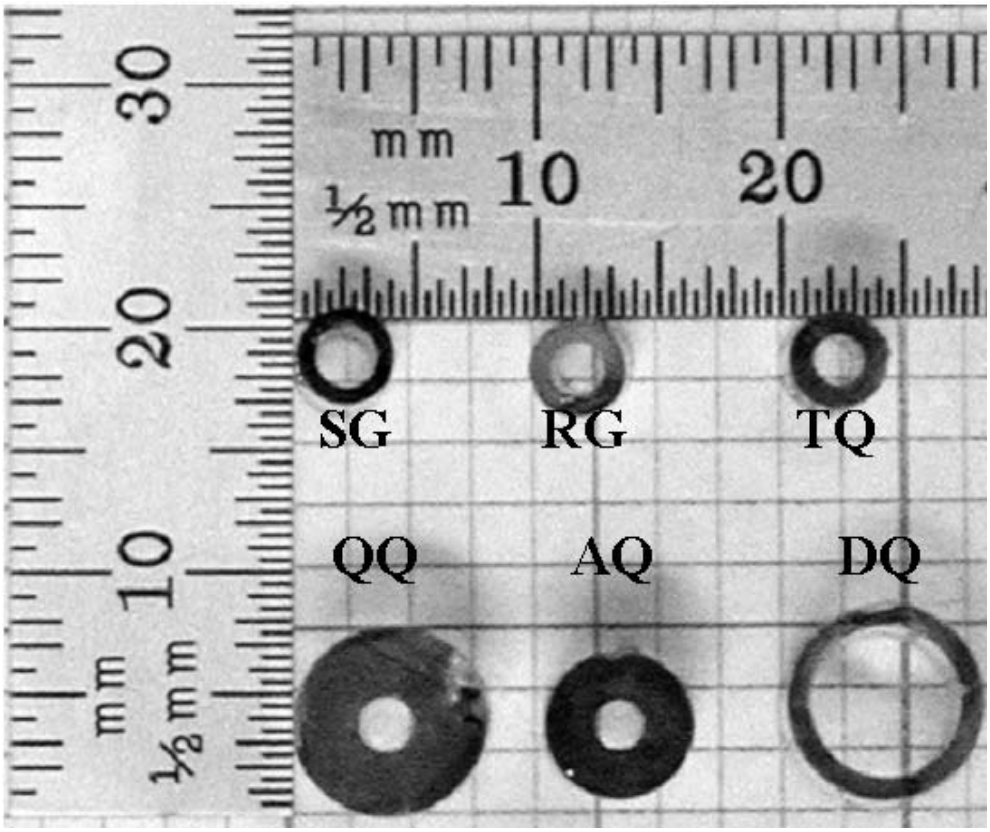

Figure 2-11 Dimensional comparative picture of tube used. Reference millimeter scale shown above and at left. Ink at ends used to increase contrast.

2.8-Data and Results

The external surface vibration of soft glass tube was compared against the results of the vibration model. . The material properties of soft glass were determined by matching the measured index of refraction, density, longitudinal sound speed, and coefficient of thermal expansion to

soda lime glass. A longitudinal sound speed of 5900 m/s, shear sound speed of 3300 m/s, and density of 2.43 g/cm^3 are used for the soft glass. The outer surface vibration of the soft glass tube at 417 kHz is displayed in Fig.2-12.

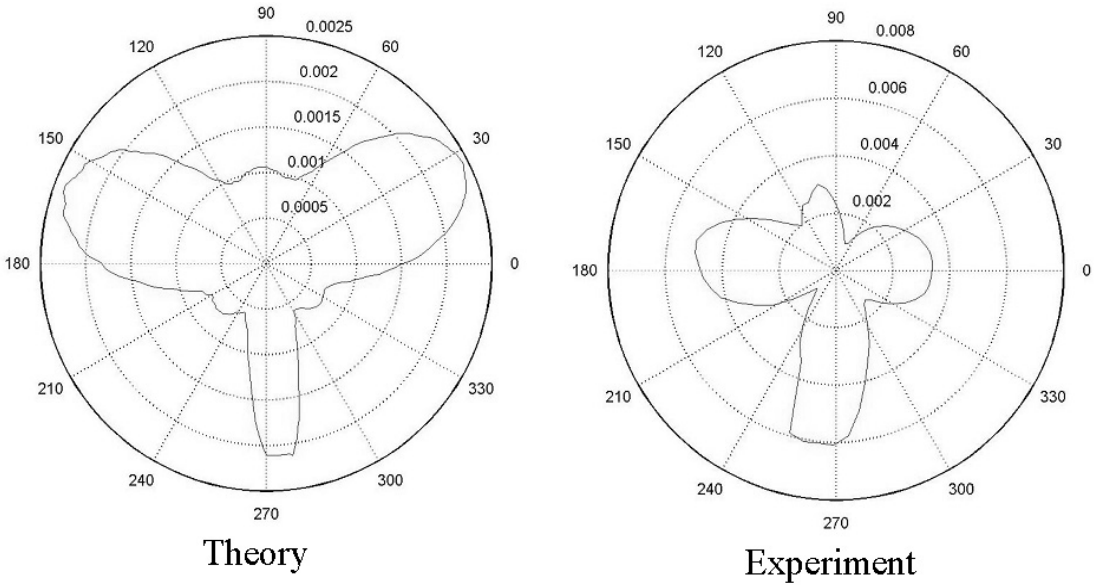

Figure 2-12. Results of surface vibration measurements at 417 kHz for air filled soft glass tube compared with prediction of 2-D elastodynamic equations.

Experimentally measured surface vibration of the tube matched up as a quadrupole for air filled, as predicted by the two dimensional elastodynamic equations as can be seen in Fig.2-12. Three primary lobes at approximately 120-degree relative angles and a directly opposite smaller lobe can be seen in calculated and measured results as evidenced in the figure. Differences in the width of the drive displacement are due to width of the physical drive

transducer coupling to the narrower Gaussian distribution used as a source for the calculations.

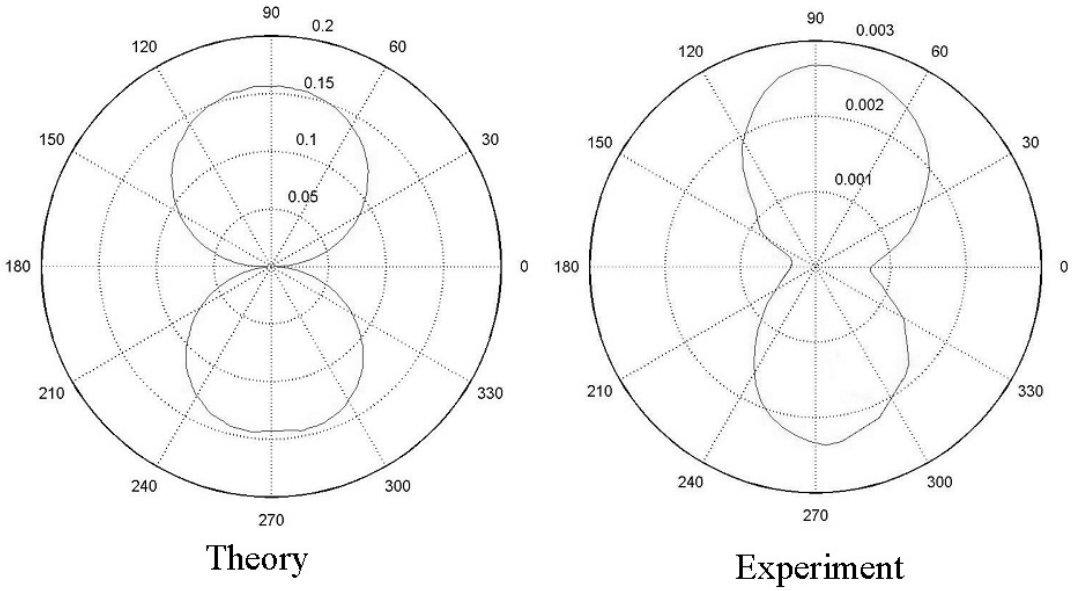

Figure 2-13 Results of surface vibration measurements at 417 kHz for water filled soft glass tube compared with prediction of 2-D elastodynamic equations.

When the tube is filled with water, the quadrupole collapses to a strong dipole as predicted by theory and shown in Fig.2-13. The coupling of energy into the cavity, absent in the air-filled case, but present in the water-filled case is the likely cause of the quadrupole to dipole mode collapse. Again, differences in the width of the drive displacement are likely due to width of the drive transducer coupling. Fig. 2-14A shows the predicted radial radiation pressure in the cavity and radial stress in the surrounding soft glass

tube. Fig. 2-14B shows a plot of calculated velocity. From the predictions of force experienced by the particles coupled with the dipole mode shown in figures 2-13, 2-6, and repeated in figure 2-14, for the water-filled soft glass, it is logical to argue that dipole vibration efficiently couples energy into the cavity.

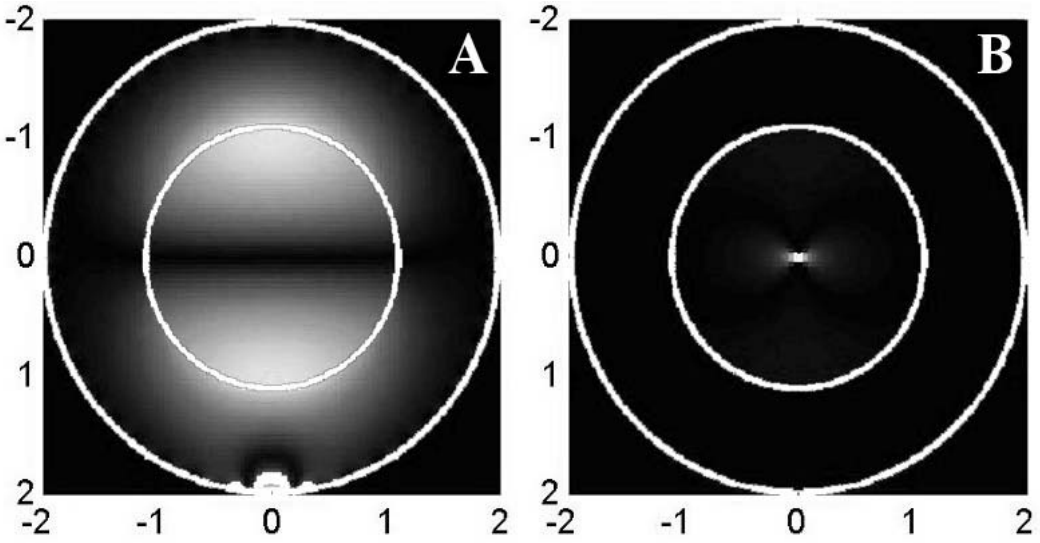

Figure 2-14 (A) Predicted pressure inside cavity and radial stress in the glass at 417 kHz for water filled soft glass tube.(B) Predicted velocity in the cavity (Both) Internal and external boundaries of the tube indicated in white.

The vibration model predicted another resonance at 485 kHz. This resonance was verified experimentally. The surface vibration for the air-filled case is shown in Fig.2-15.

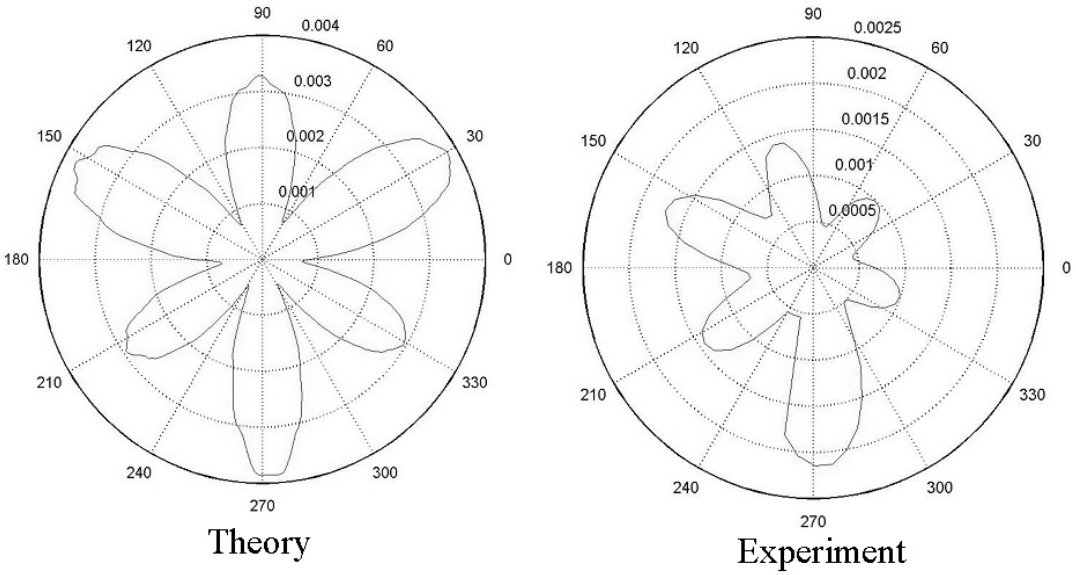

Figure 2-15. Results of surface vibration measurements at 485 kHz for air-filled soft glass tube compared with prediction of 2-D elastodynamic equations.

As can be seen in Fig.2-16, the vibration at 485 kHz is hexapolar with angular separations of 60 degrees. Slight imperfections in the coupling between the tube and pinducer, asymmetry in the drive transducer coupling, non-concentricity of the tube, or non-circularity of the tube are all possible causes of the asymmetry of the experimental data shown in both Fig.2-15 and Fig. 2-16. When the tube is filled with water, the hexapolar structure remained, as shown in Fig.2-16. This indicated that the resonance at 485 kHz is dominated by the glass tube and is unlikely to couple energy into the fluid in the cavity.

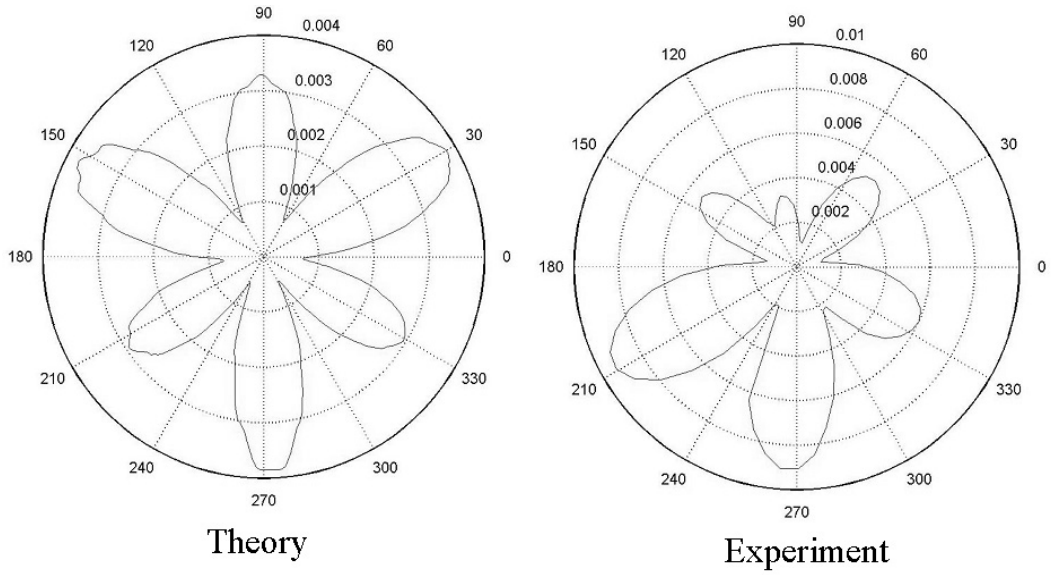

Figure 2-16. Results of surface vibration measurements at 485 kHz for water-filled soft glass tube compared with prediction of 2-D elastodynamic equations.

This assertion can be justified by looking at the predicted energy transfer from the glass into the cavity. Fig. 2-17 displays the pressure in the fluid and stress in the tube. As expected, minimal energy is coupled into the cavity and the mode is dominated by excitation of the glass. While this mode would not concentrate particles in the fluid filled cavity, it did provide two correctly predicted resonances as confirmation of the validity of the vibration model for the soft glass tube. Fig. 2-17B shows the velocity. Unlike the resonance at 417 kHz, there is a local minimum at the center of the cavity and small velocity gradient across the cavity. Since polystyrene beads should

be attracted to velocity anti-nodes, the central minimum and somewhat even distribution of velocity within the cavity would be expected to drive the particles out of the center, however, minimal energy is coupled into the cavity at this frequency, so this mode would not be expected to concentrate particles in suspension.

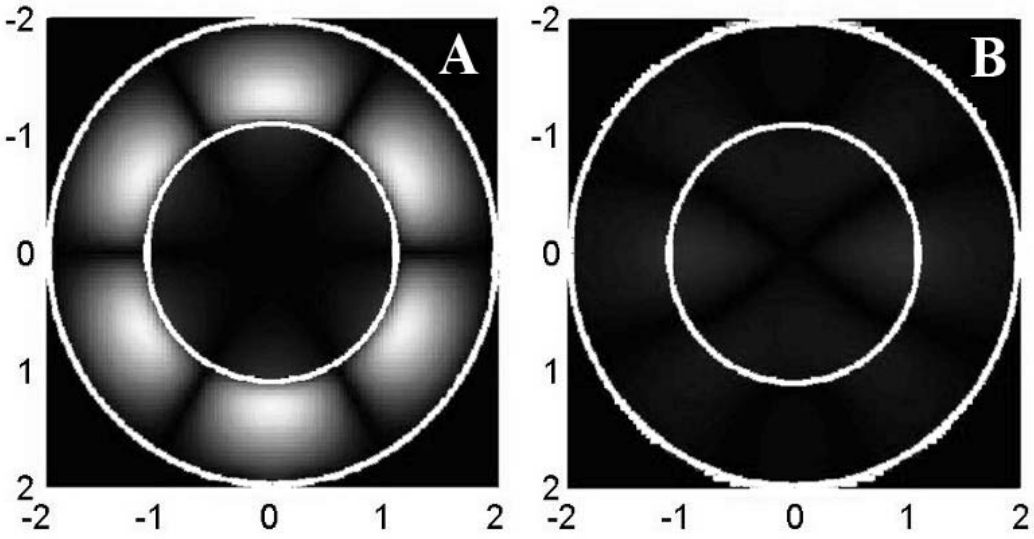

Figure 2-17 (A) Predicted pressure inside cavity and radial stress in the glass at 485 kHz for water filled soft glass tube.(B) Predicted velocity in the cavity (Both) Internal and external boundaries of the tube indicated in white.

In order to determine the importance of tube material properties on the ability of the structural excitation to concentrate, two tubes with similar dimensions as the soft glass but made of borosilicate and quartz glass were chosen for the next set of comparative evaluations.

The borosilicate tube, also denoted as RG or regular glass, has a density of 2.13 g/cm^3, a longitudinal sound speed of 5640 m/s, and shear sound speed of 2840 m/s according to tabulated values of acoustic properties. The vibration model predicted two resonances, at 380 kHz and 490 kHz. The vibration results when the tube is air-filled at 380 kHz are presented in Fig. 2-18. This mode formed a tripole structure. Again, the width of the drive transducer used in the experiments is greater than the forcing function width used in the model. This additional width increased the width of the measured forcing leg of the tripole. Both predicted and experimental data shows two lobes at approximately 150 degrees on either side of the drive lobe located at 270 degrees. As before, reflection asymmetry in the measured data across the y-axis is probably due to several physical asymmetries of the system.

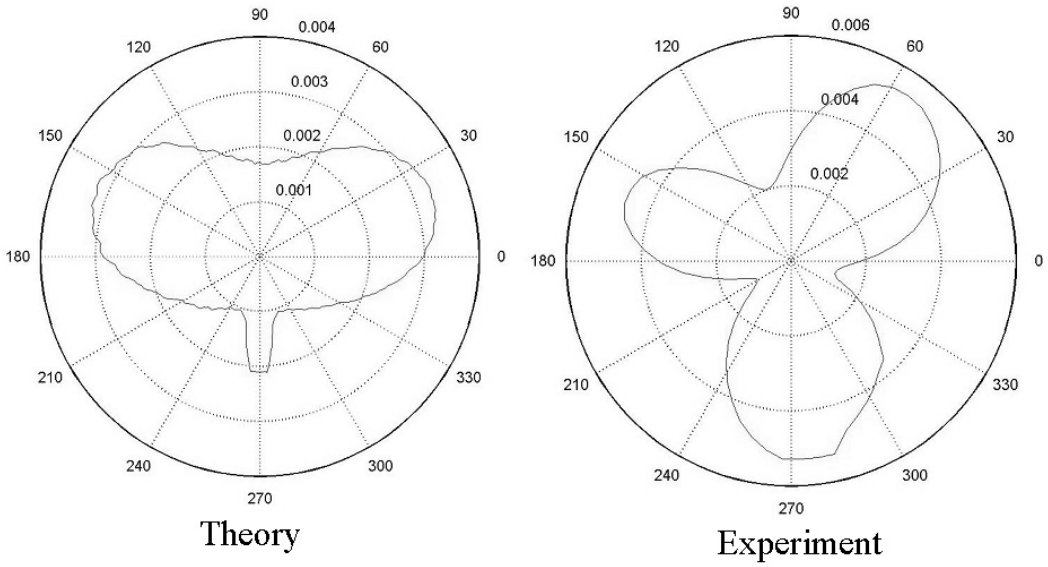

Figure 2-18. Results of surface vibration measurements at 380 kHz for air-filled regular glass tube compared with prediction of 2-D elastodynamic equations.

Fig. 2-19 shows the effect of adding water to the interior of the cavity. As can be seen, the tripole collapses to a dipolar vibration.

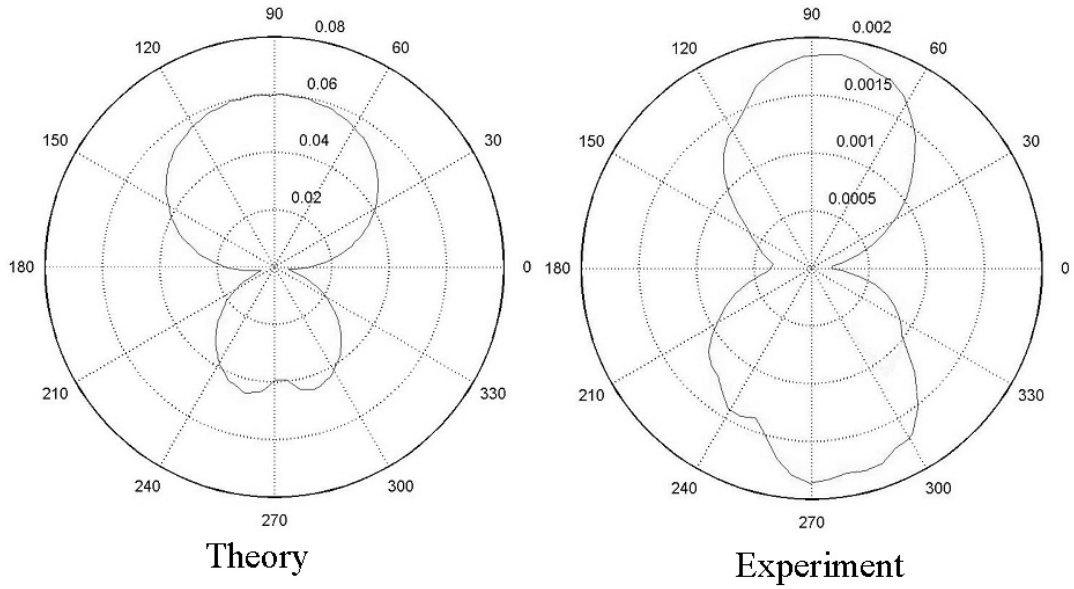

Figure 2-19. Results of surface vibration measurements at 380 kHz for water-filled regular glass tube compared with prediction of 2-D elastodynamic equations.

The change in mode structure due to the introduction of water indicated a coupled resonance of the tube with the internal cavity. In order to verify the coupling, the radial stress in the tube and pressure in the cavity are calculated for the water-filled case. The results of the calculation are shown in Fig.2-20A. As before, velocity is also calculated, with the results displayed in Fig.2-20B. Again, there is a velocity anti-node at the center of the cavity corresponding to a region of predicted particle concentration.

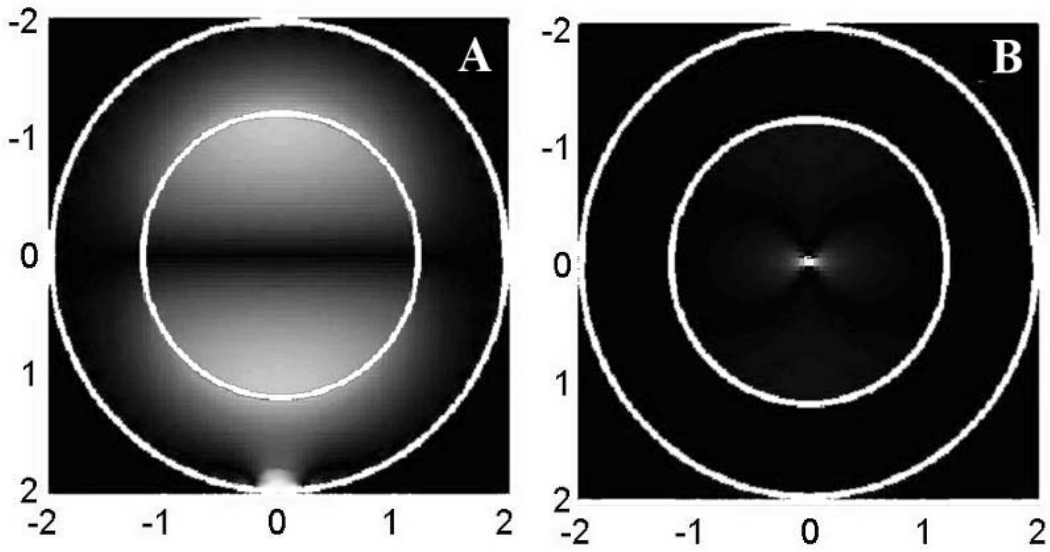

Figure 2-20. (A) Predicted pressure inside cavity and radial stress in the glass at 380 kHz for water filled regular glass tube.(B) Predicted velocity in the cavity (Both) Internal and external boundaries of the tube indicated in white.

As can be seen in Fig.2-20, the resonance at 380 kHz couples into the cavity well. Also worth noting is the dipole character of the coupling. Subsequent concentration measurements confirmed that particles do concentrate at 380 kHz in regular glass. The second resonance of the borosilicate glass tube is at 490 kHz. The model predictions and measurement results for the air-filled case are displayed in Fig.2-21. As can be seen in the figure, this mode has a hexapolar structure.

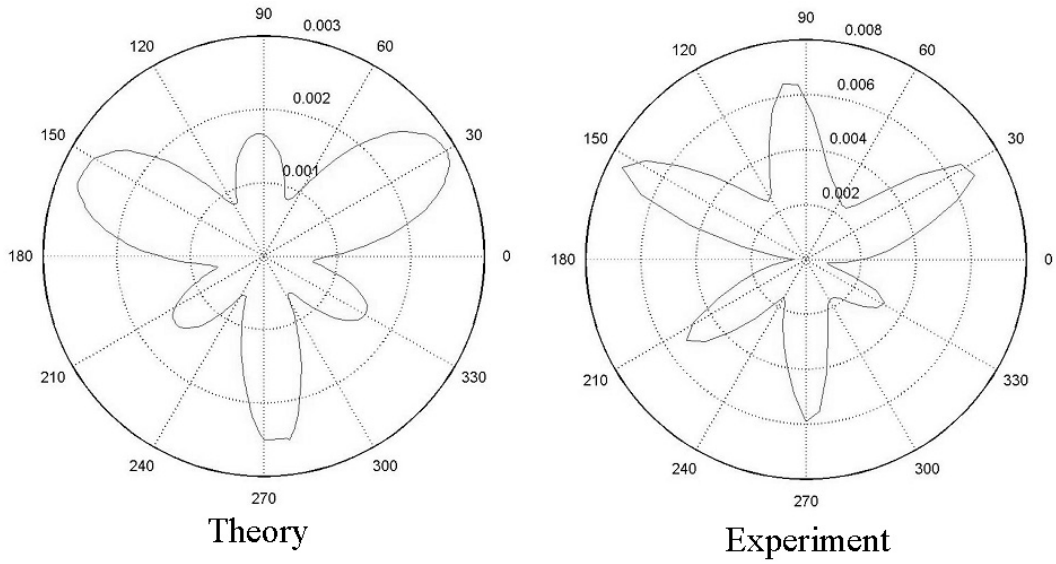

Figure 2-21. Results of surface vibration measurements at 490 kHz for air-filled regular glass tube compared with prediction of 2-D elastodynamic equations.

The addition of water to the cavity did not change the character of the vibration significantly as can be observed Fig. 2-22. As in the case of the 485 kHz resonance of soft glass, lack of response to the changes in the contents of the cavity is indicative of an absence of mode interaction with the cavity. The calculation results are displayed in Fig.2-23A.

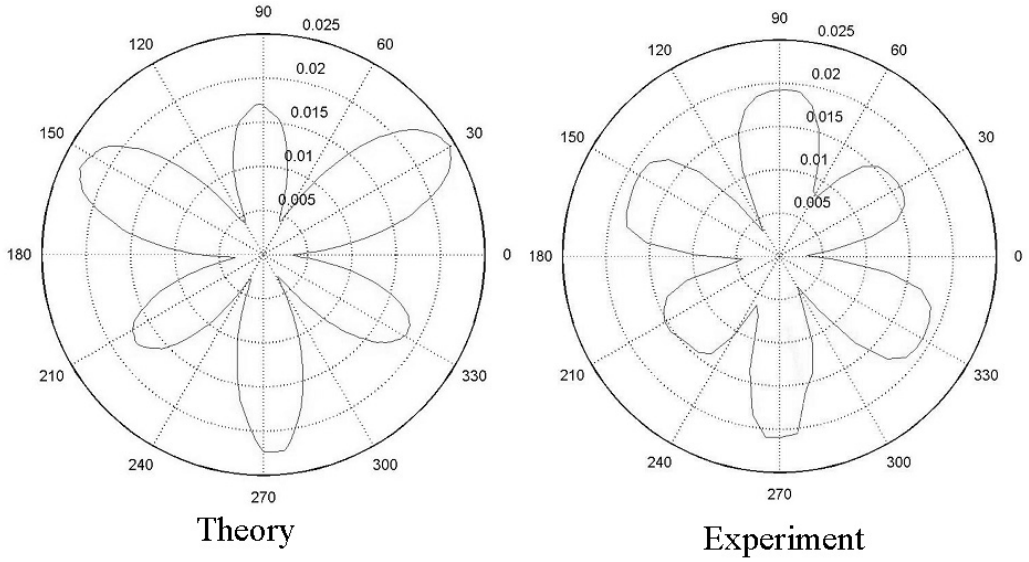

Figure 2-22. Results of surface vibration measurements at 490 kHz for water-filled regular glass tube compared with prediction of 2-D elastodynamic equations.

The hexapolar vibration of the tube can be seen in Fig.2-23. As expected, the majority of the energy is in the glass tube with minimal transfer to the fluid-filled cavity. Velocity calculations, presented in Fig.2-23B, further confirm the assertion of negligible coupling into the cavity and lack of observed particle concentration in experiments at 490 kHz. It should be noted that a similar mode is predicted and observed in soft glass tube.

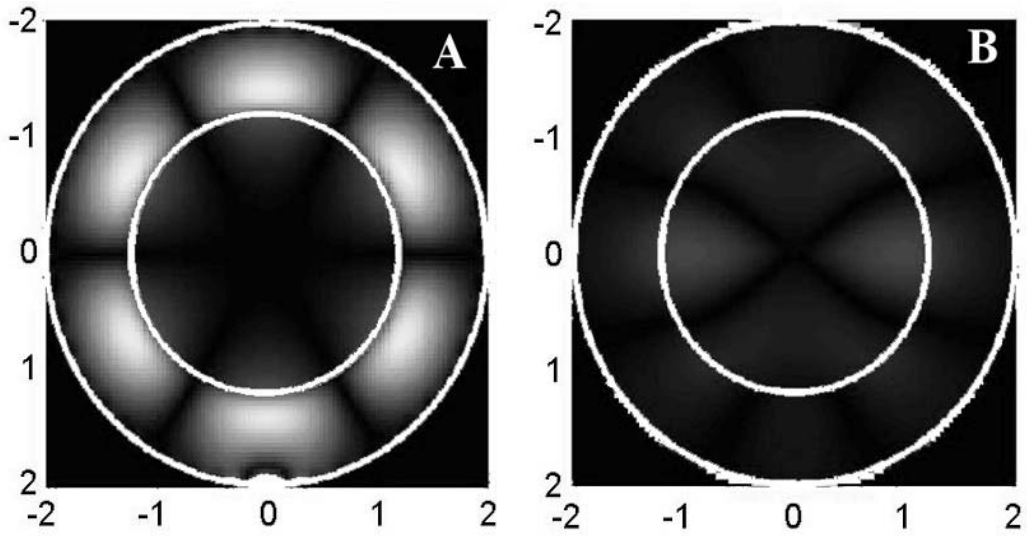

Figure 2-23. Predicted pressure inside cavity and radial stress in the glass at 490 kHz for water filled regular glass tube. .(B) Predicted velocity in the cavity (Both) Internal and external boundaries of the tube indicated in white.

Thin quartz glass tube, also denoted as TQ to distinguish from thicker-walled quartz used in subsequent experiments, is found to have a density of 2.65 g/cm^3, a longitudinal sound speed of 5700 m/s, and shear sound speed of 3920 m/s according to tabulated values of acoustic properties. The model predicted a resonance at 435 kHz. A comparison of predicted to measured vibration for the air-filled cavity is shown in Fig.2-24. The vibration of the quartz tube, both calculated and measured, shows a quadrupole structure with strong tripole tendencies similar to the pattern seen with soft glass. Following that comparison, it would be expected that this mode would

collapse to a coupled dipolar mode when the cavity is filled with fluid. When this measurement is undertaken, the results confirm the validity of that assertion. The results are displayed in Fig.2-25.

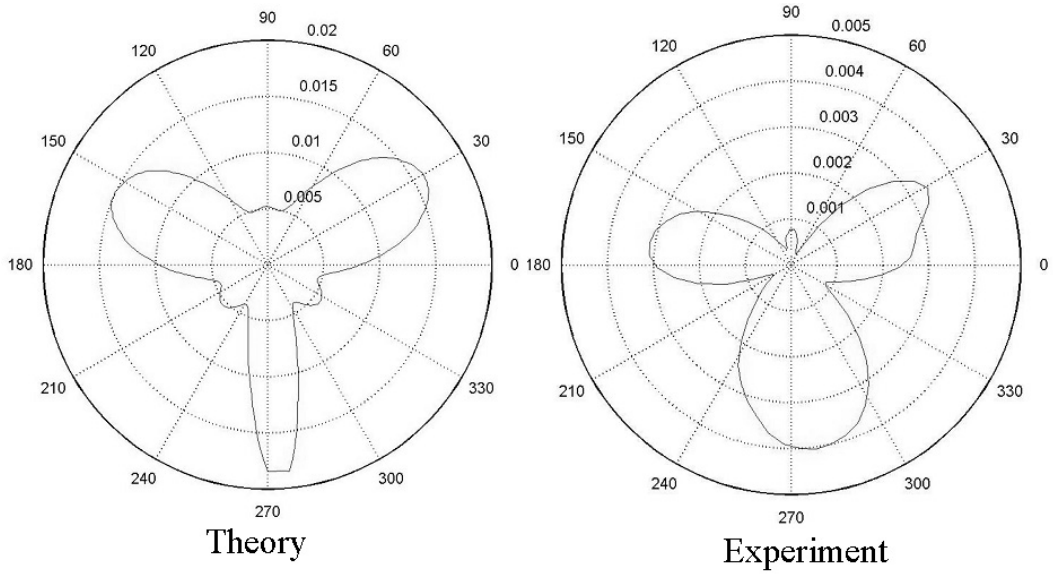

Figure 2-24. Results of surface vibration measurements at 435 kHz for air-filled quartz glass tube compared with prediction of 2-D elastodynamic equations.

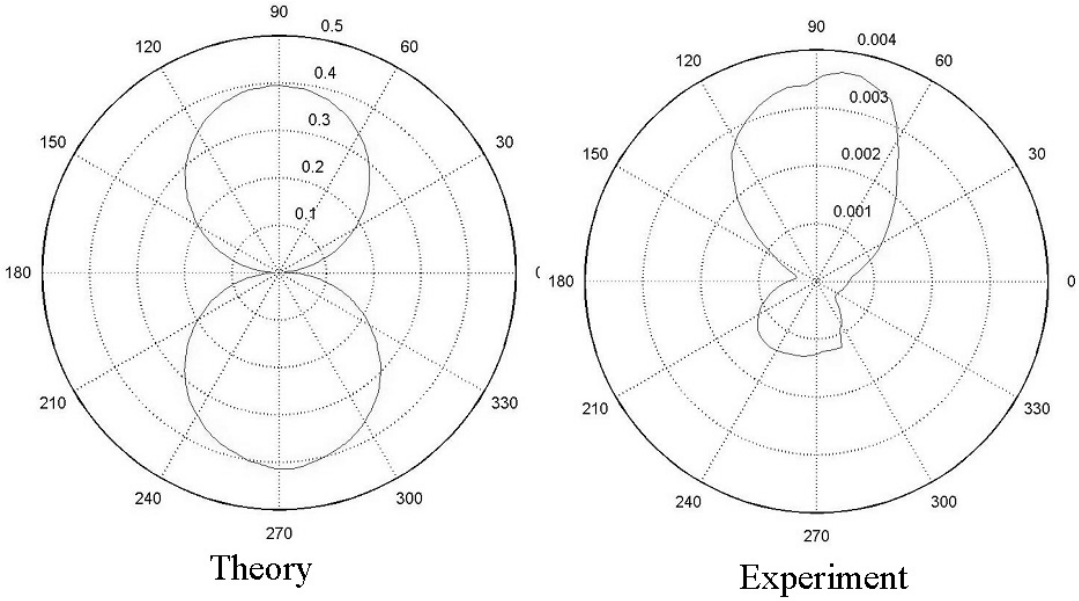

Figure 2-25. Results of surface vibration measurements at 435 kHz for water-filled quartz glass tube compared with prediction of 2-D elastodynamic equations.

To continue the analogy, it would be expected that the coupled dipolar mode coupled energy from the structure to the fluid-filled cavity efficiently. Stress calculations, shown in Fig.2-26, provided confirmatory proof of cavity excitation. Additionally, particles are experimentally observed to concentrate within the thin quartz tube at 435 kHz.

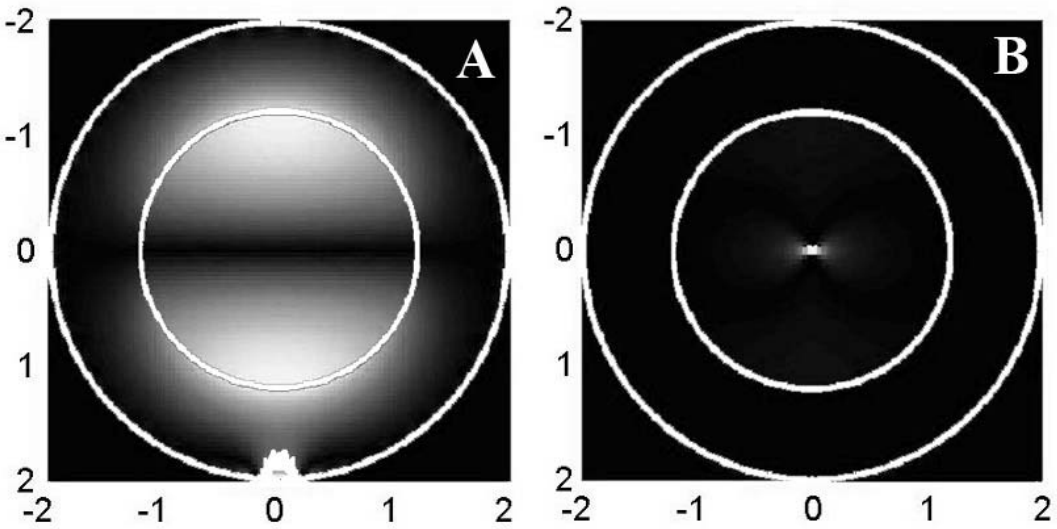

Figure 2-26. Predicted pressure inside cavity and radial stress in the glass at 435 kHz for water filled thin quartz glass tube. (B) Predicted velocity in the cavity (Both) Internal and external boundaries of the tube indicated in white.

The thin quartz tube had another resonance at 470 kHz. The surface vibration was calculated and subsequently measured for the air-filled case; the results are presented in Fig.2-27. As can be seen in the figure, the vibration is hexapole with three dominant lobes at approximately 120-degree separation. The tube is also modeled and measured when filled with water at 470 kHz. A comparison of the calculated and observed vibration pattern is shown in Fig.2-28. The dominant tripole structure present for the air filled case split into a more hexapolar structure when the tube is filled with water. The width of the side lobes in the measurements of the water filled thin

quartz tube is probably due to several asymmetries in the experiment, including, but not limited to imperfect coupling of the drive transducer or pinducer to the tube, noncircularity of the tube, or nonconcentricity of the tube.

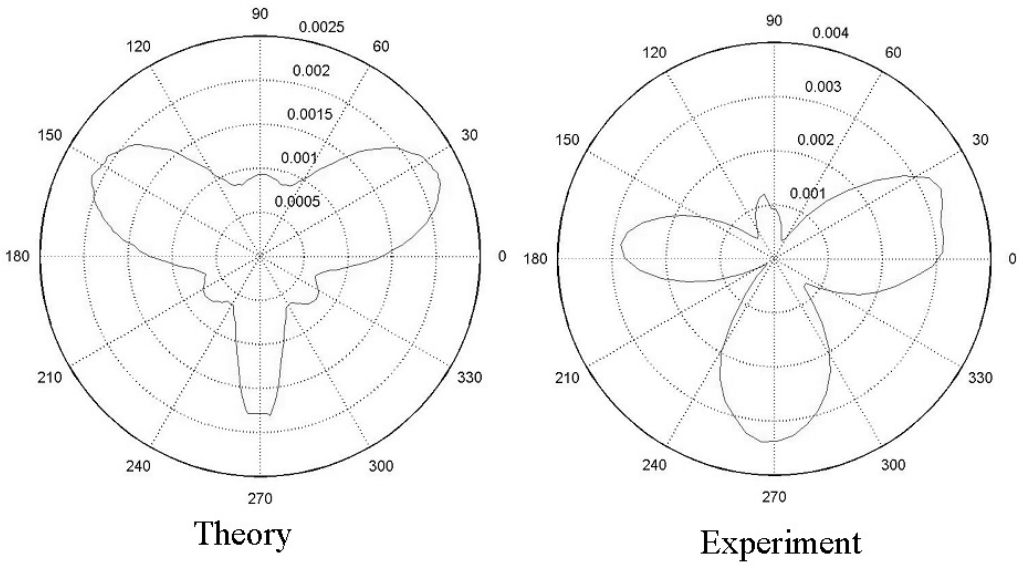

Figure 2-27. Results of surface vibration measurements at 470 kHz for air-filled quartz glass tube compared with prediction of 2-D elastodynamic equations.

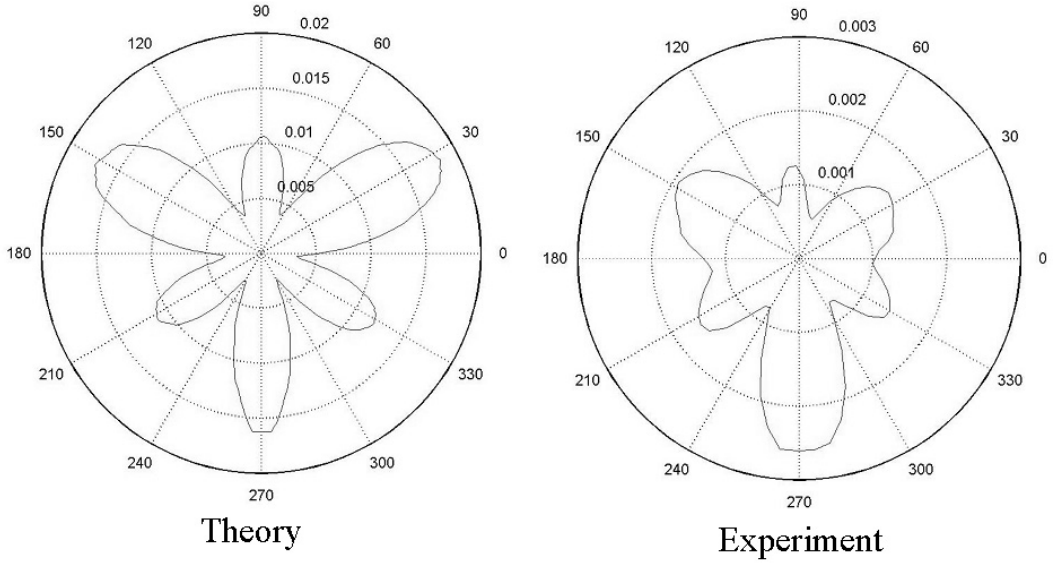

Figure 2-28. Results of surface vibration measurements at 470 kHz for water-filled quartz glass tube compared with prediction of 2-D elastodynamic equations.

If the pattern seen in the previous two types of tube continues, it would be expected that the hexapole would not couple energy into the cavity efficiently. Stress calculations, shown in Fig. 2-29, provided confirmatory proof. Additionally, the displacement vibration is also calculated and displayed in Fig. 2-29B. Again, it can be seen in Fig. 2-29B that a velocity minimum exists at the center, thus precluding particle concentration. This assertion is verified experimentally.

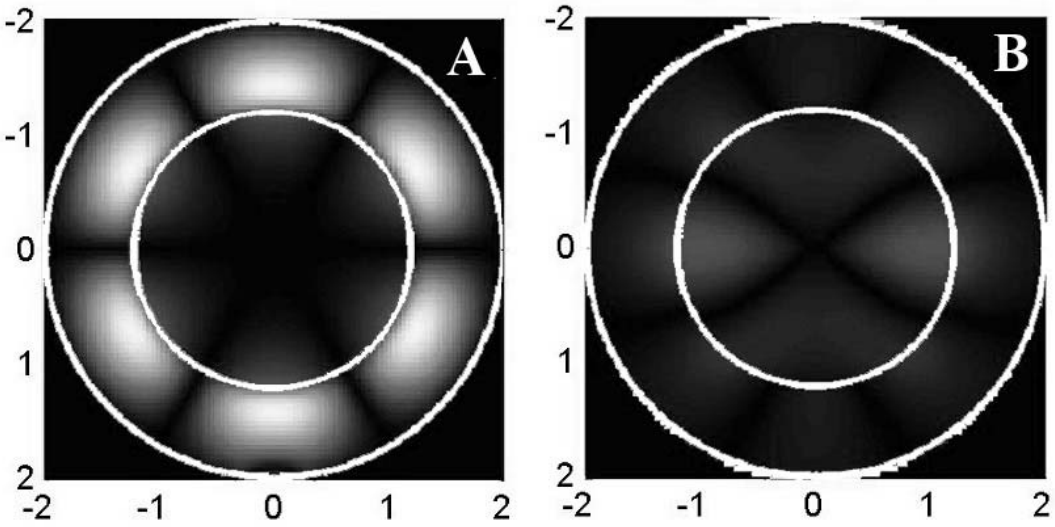

Figure 2-29. Predicted pressure inside cavity and radial stress in the glass at 470 kHz for water filled thin quartz glass tube. (B) Predicted velocity in the cavity (Both) Internal and external boundaries of the tube indicated in white.

It seemed that, although soft glass was the initial choice of material, other types of glass with similar dimensions worked equally well.

In order to determine the importance of outer diameter and hence wall thickness on the ability of the structural excitation to couple energy into the cavity, two tubes with similar inner dimension as the soft glass but larger outer diameters were chosen for the next set of comparative evaluation. tube availability dictated the use of quartz tube. Since thin quartz had shown comparable behavior to soft glass, it could be argued that this material replacement did not serve as another variable for the experiments. All quartz

tube is assumed to have the same density, and sound speeds in the longitudinal and shear directions.

Thick quartz tube, designated as QQ or Q, had a predicted and experimentally verified resonance at 435 kHz. The comparison of calculated and measured vibration is shown in Fig. 2-30. The pattern possessed two well-defined lobes at 90 and 270 degrees and two pairs of less sharply defined lobes centered at 0 and 180 degrees. When the tube is filled with water, the six-lobed pattern collapsed to a tube-cavity coupled dipolar vibration, as shown in Fig. 2-31. As can be observed, there is good correspondence of the experiments to the model predictions for both air-filled and water-filled cases.

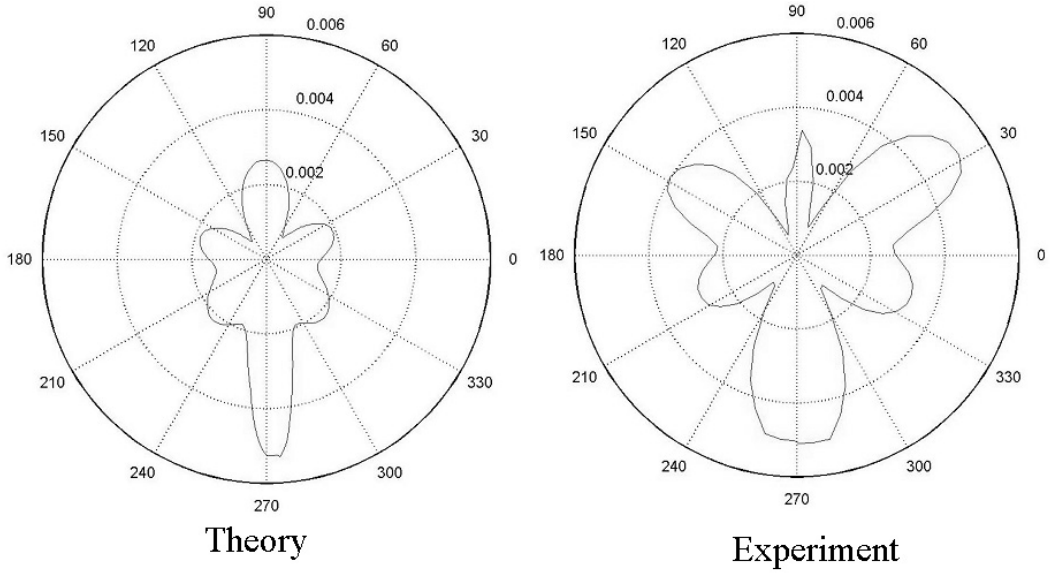

Figure 2-30. Results of surface vibration measurements at 435 kHz for air-filled quartz glass tube compared with prediction of 2-D elastodynamic equations.

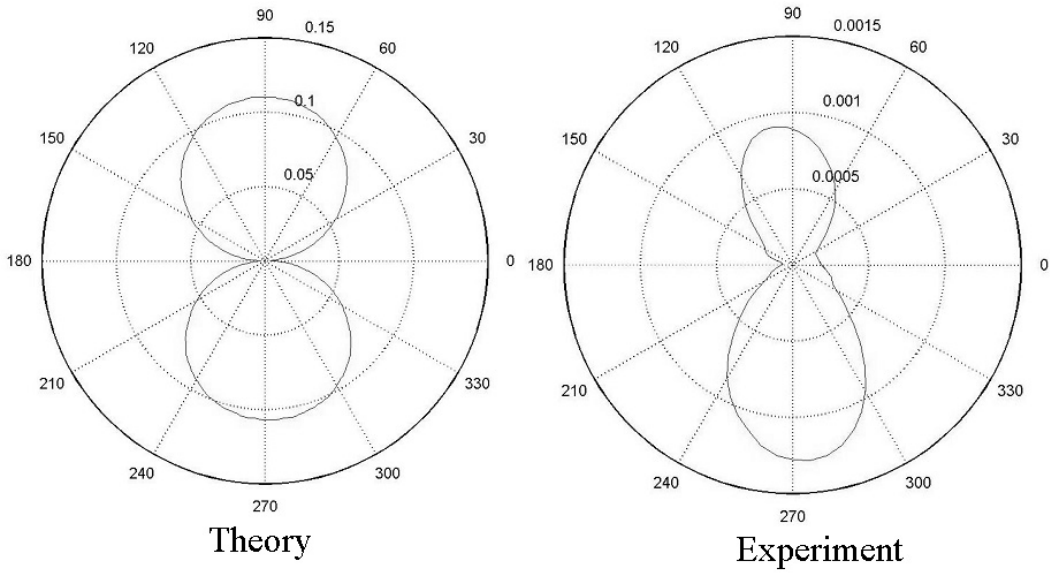

Figure 2-31. Results of surface vibration measurements at 435 kHz for water-filled quartz glass tube compared with prediction of 2-D elastodynamic equations.

It should be noted that the QQ tube had an elliptical cross-section. If any effect is observed due to the asymmetry, including any deviation from the circular approximation of the calculated predictions, it is minimal. The perturbation could be argued as small for the wavelengths used to excite the tube, therefore very little effect would be expected. It does suggest, however, that structural excitation for concentration is robust against transducer misalignment or structural asymmetry.

If the pattern of behavior in which the dipole motion indicates good coupling still holds, then it would be expected that particle concentration

should occur at 435 kHz. Good coupling does occur, as evidenced by the plot of pressure within the tube, shown in Fig. 2-32. Additionally, particle concentration does occur at 435 kHz.

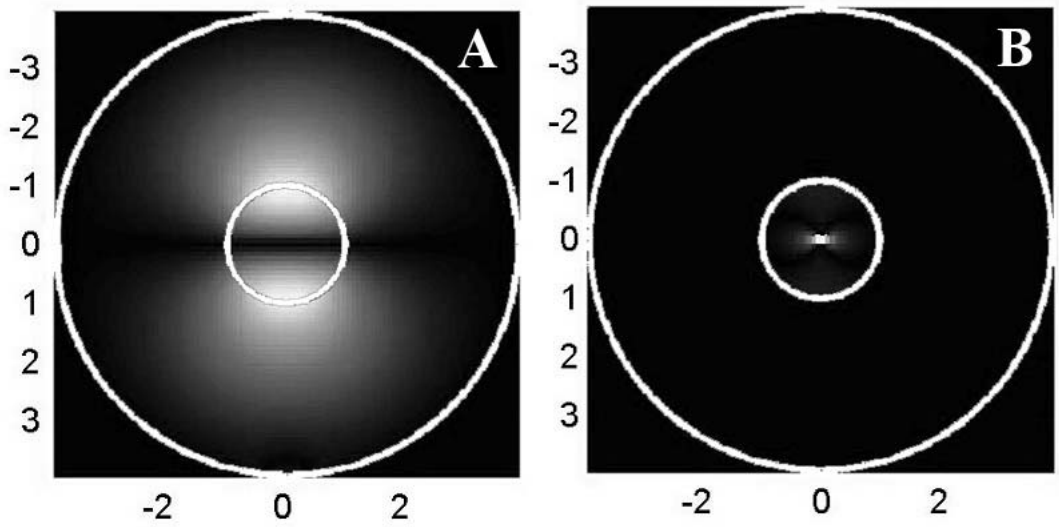

Figure 2-32. Predicted pressure inside cavity and radial stress in the glass at 435 kHz for water filled thick quartz glass tube. (B) Predicted velocity in the cavity (Both) Internal and external boundaries of the tube indicated in white.

To further investigate the effect of outer tube diameter/wall thickness, a quartz tube with a smaller outer diameter than QQ was used. The tube is designated by the two-letter identifier AQ. The tube possessed a resonance at 472 kHz. Vibration model calculations at that frequency for the air filled case yielded the pattern presented in Fig. 2-33. Although the pattern would most accurately characterized as hexapolar, there are only three clearly

defined poles with a small lobe opposite the drive transducer lobe. The two side nodes are wide and each poorly split into a pair of lobes. The measured data therefore, bore a gross resemblance to the model results. When the tube is filled with water, as shown in Fig. 2-34, the vibration pattern collapsed to a dipole.

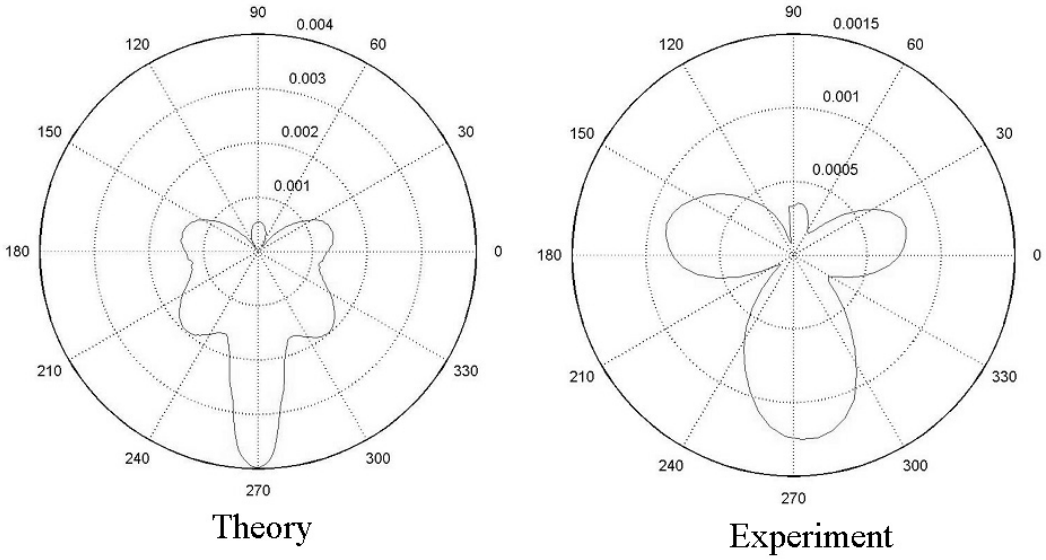

Figure 2-33. Results of surface vibration measurements at 472 kHz for air-filled quartz glass tube compared with prediction of 2-D elastodynamic equations.

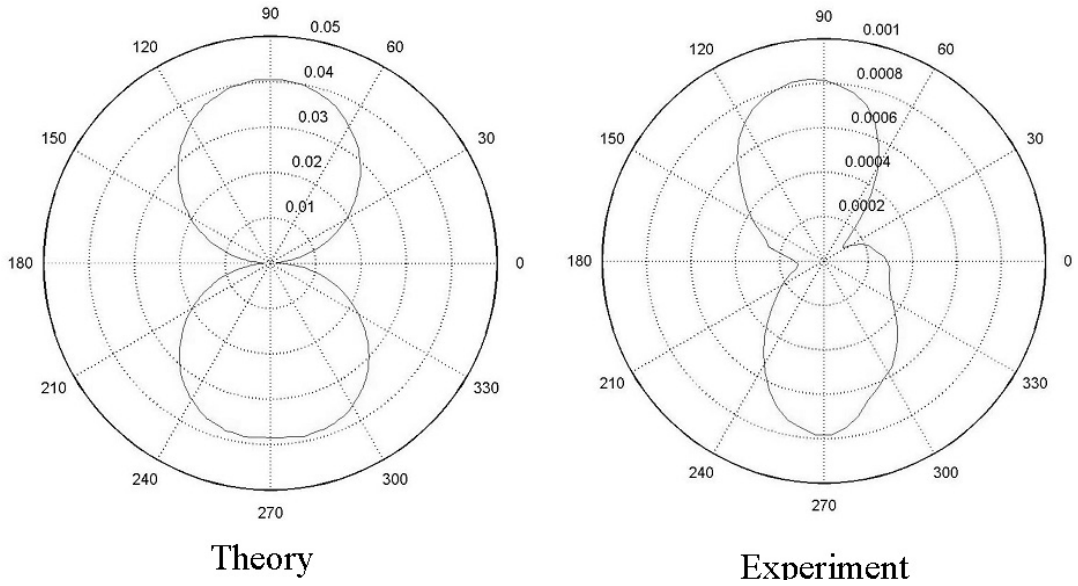

Figure 2-34. Results of surface vibration measurements at 472 kHz for water-filled quartz glass tube compared with prediction of 2-D elastodynamic equations.

From the results from the previous tube, it is deduced that this dipole motion would once again yield successful coupling into the cavity. As before, the validity of this claim is verified by calculating the stress in the glass. The results of the calculations are displayed in Fig. 2-35. Suspended particles are observed to concentrate in the AQ quartz tube at 472 kHz, providing further confirmation of the deduction.

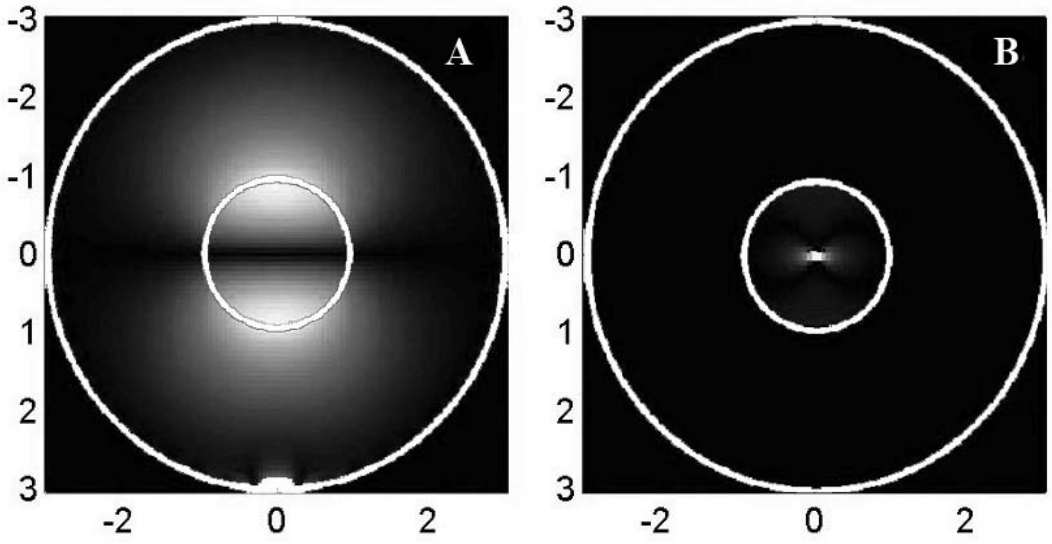

Figure 2-35. Predicted pressure inside cavity and radial stress in the glass at 472 kHz for water filled thick AQ quartz glass tube.(B) Predicted velocity in the cavity (Both) Internal and external boundaries of the tube indicated in white.

From the results of the experiments with quartz tubes QQ and AQ, it is reasoned that internal radius is the dominant factor in determining coupling into the cavity for glass tube. This is expected from comparison of the wavelengths of sound in the glass tube versus the water in the cavity. A small change in the cavity dimension equates to a large change in the phase of the acoustic wave in the water. A small change in the tube dimension only equates to a small change in phase of the wave within the tube. As further confirmation of that determination, a tube with comparable outer diameter to QQ, but larger inner diameter was used. The tube used is designated DQ.

Model predictions versus experimental measurements of the air-filled state are compared in Fig. 2-36 at 440 kHz. A similar comparison in the water-filled state is presented in Fig. 2-37 at the same frequency as in Fig. 2-36. As can be seen in the figures, the addition of water into the cavity causes a collapse of the octapole vibration to a hexapole. This suggests a coupled resonance between the tube and fluid-filled cavity. The experimental results show good correspondence to the predictions in both cases. The slight asymmetry of the experimental results arose from either inherent asymmetry of the tube or imperfect contact of the probe transducer as the tube rotated on the angular scanning stage.

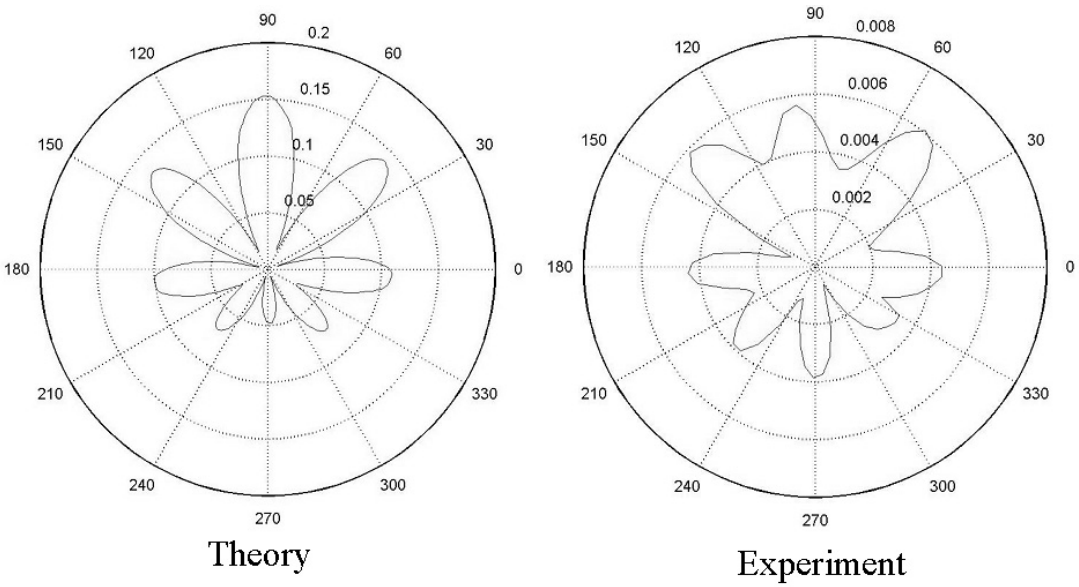

Figure 2-36. Results of surface vibration measurements at 440 kHz for air-filled quartz glass tube compared with prediction of 2-D elastodynamic equations.

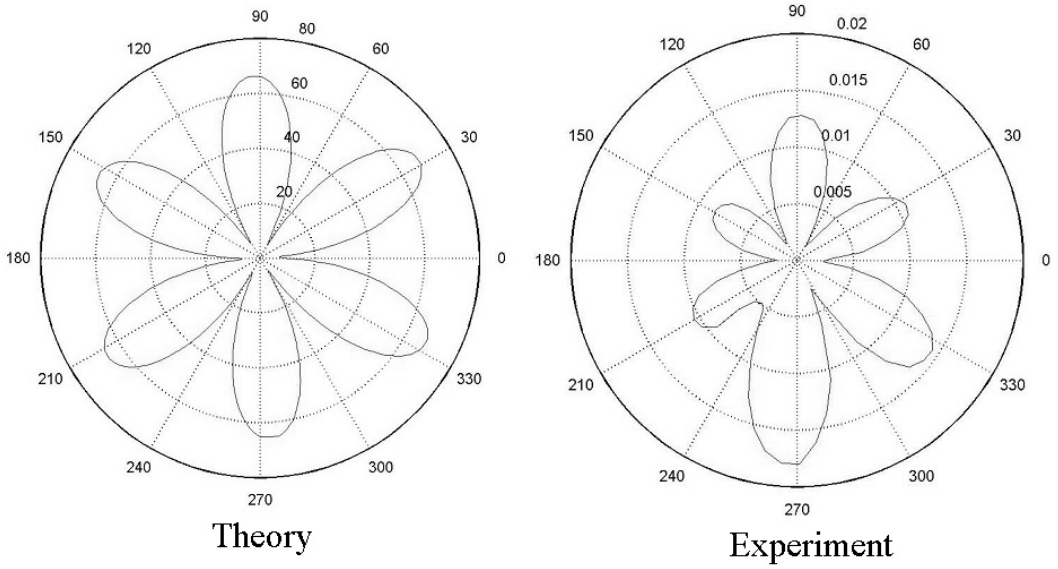

Figure 2-37. Results of surface vibration measurements at 440 kHz for water-filled quartz glass tube compared with prediction of 2-D elastodynamic equations.

The change in the vibration in response to the addition of water indicated that some degree of coupling of energy occurred from the quartz tube to the fluid-filled interior. Although energy is coupled into the cavity, no acoustic concentration of particles in suspension is observed during experimental trials at any power level. Fig. 2-38 displays the pressure in the cavity and radial stress in the tube.

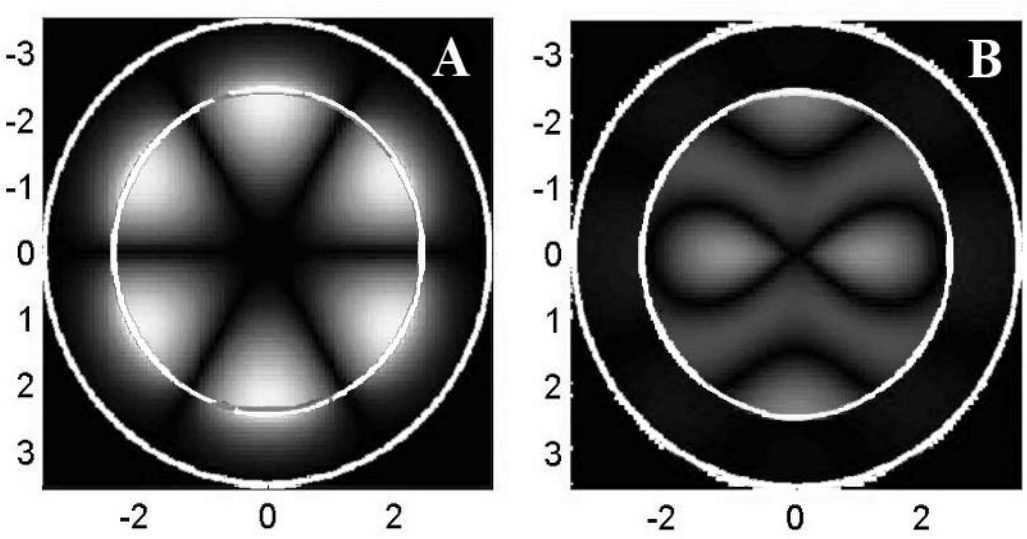

Figure 2-38. Predicted pressure inside cavity and radial stress in the glass at 440 kHz for water filled DQ quartz glass tube.(B) Predicted velocity in the cavity (Both). Internal and external boundaries of the tube indicated in white.

From the figure, it could be argued that coupling of energy into a low order mode such as a dipole would be more efficient at providing pressure on the particles. Higher order modes such as the quadrupole and hexapole modes predicted by theory were also predicted to couple less energy into the fluid-filled cavity. It is worth noting that there is good correspondence between predicted and measured results both in spectral position and character of vibration.

Based on the experiments and simulations summarized above, it could be argued that the lack of dependence on glass type, or outer diameter

exhibited by the coupled dipole mode arose from the glass serving as a nearly completely rigid boundary for the fluid filled cavity. Tube materials with sound speeds closer that that of water, such as plastic, would be expected to show greater dependence on aspect ratio of the tube.

2.9-Predictions For Alternate Tube Material

Glass tube was chosen for three primary reasons; optical transparency, chemical resistant and perhaps most importantly, availability in a variety of sizes and dimensions. The necessity for optical transparency arose to facilitate easier application to flow cytometry. Although plastic and metal tube is beyond the scope of our experimental measurements, several different types of plastic and metal tube were investigated theoretically to establish the viability of their use. The results of this investigation are summarized in the following section.

Two types of plastic tube were theoretically investigated. They were chosen at the extremes of density and stiffness to aid in extrapolating the general behavior of plastics under line excitation. The first type investigated is low-density polyethylene(LDPE). The dimensions are assumed to be the same as in the case of soft glass. The density is taken to be 0.9 g/cm^3 ; longitudinal and transverse sound speeds are assumed to be 1940 m/s and

540 m/s respectively. Since the purpose of this section is exploratory rather than explanatory, there is very little value in presenting surface vibration predictions. Instead, only stress and velocity data is displayed and expounded upon. The polyethylene tube had several resonances, the most dominant of these are at 328 kHz, 409 kHz, 450 kHz, 513 kHz and 529 kHz. The stress and velocity comparative plot for water-filled LDPE at 328 kHz, 409 kHz, 450 kHz, and 513 kHz is presented in Fig. 2-39. As can be seen in Fig. 2-39, the majority of the resonances are vibrations of the LDPE tube with negligible coupling into the fluid-filled cavity. The main difference between the velocity modes is in the number of lobes present in the tube.

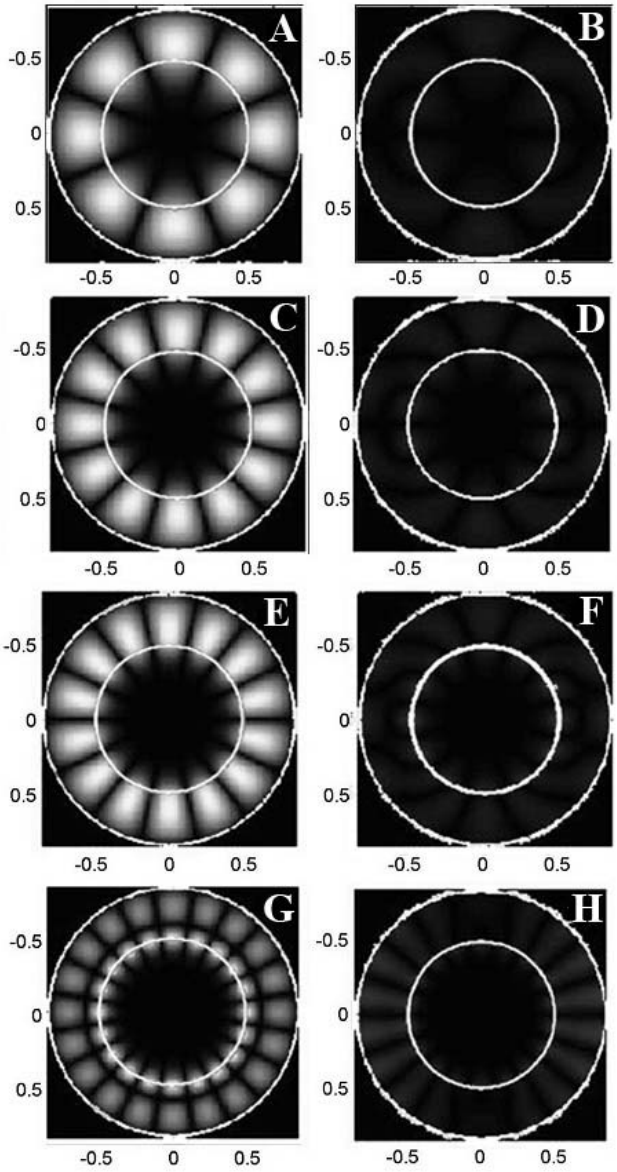

Figure 2-39. Predicted pressure at: (A)328 kHz (C)409 kHz (E)450 kHz (G)513 kHz Predicted velocity at: (B)328 kHz (D)409 kHz (F)450 kHz (H)513 kHz (Both). Internal and external boundaries of the tube indicated in white. Predictions for water-filled LDPE.

The stress and velocity comparative plot for the dipole vibration at 529 kHz is presented in Fig. 2-40 for clarity of visualization. As is visible in the figure, LDPE did support a dipole with good coupling into the cavity at 529 kHz. If the hypothesis put forth for glass tube held, then acoustic concentration should be possible at that frequency.

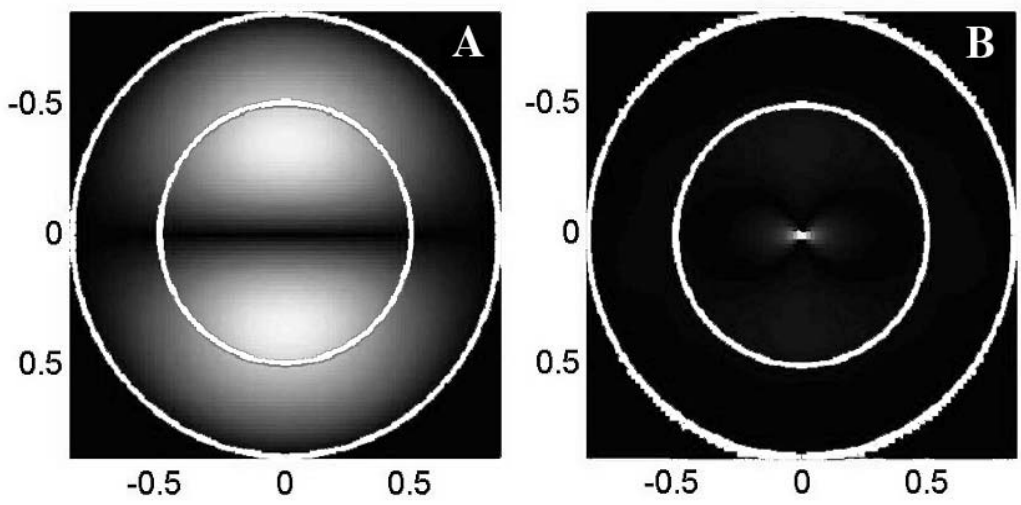

Figure 2-40. (A)Predicted pressure in fluid and stress in LDPE tube at 529 kHz (B)Predicted velocity in LDPE tube at 529 kHz (Both). Internal and external boundaries of the tube indicated in white.

Polystyrene(PS) tube was chosen for the other end of the plastic mechanical property spectrum. It is found to have compressional and shear sound speeds and density of 2350 m/s, 1120 m/s and 1.1 g/cm^3 respectively in a table of plastic acoustic properties. As with the theoretical analysis of low-density polyethylene, no surface vibration graphs were prepared, I opted

to instead simply calculate the stress and velocity. During analysis it is found that polystyrene tube of the same dimensions as the soft glass tube had resonances at several frequencies. The highest amplitude resonances are at 322 kHz, 455 kHz and 511 kHz.

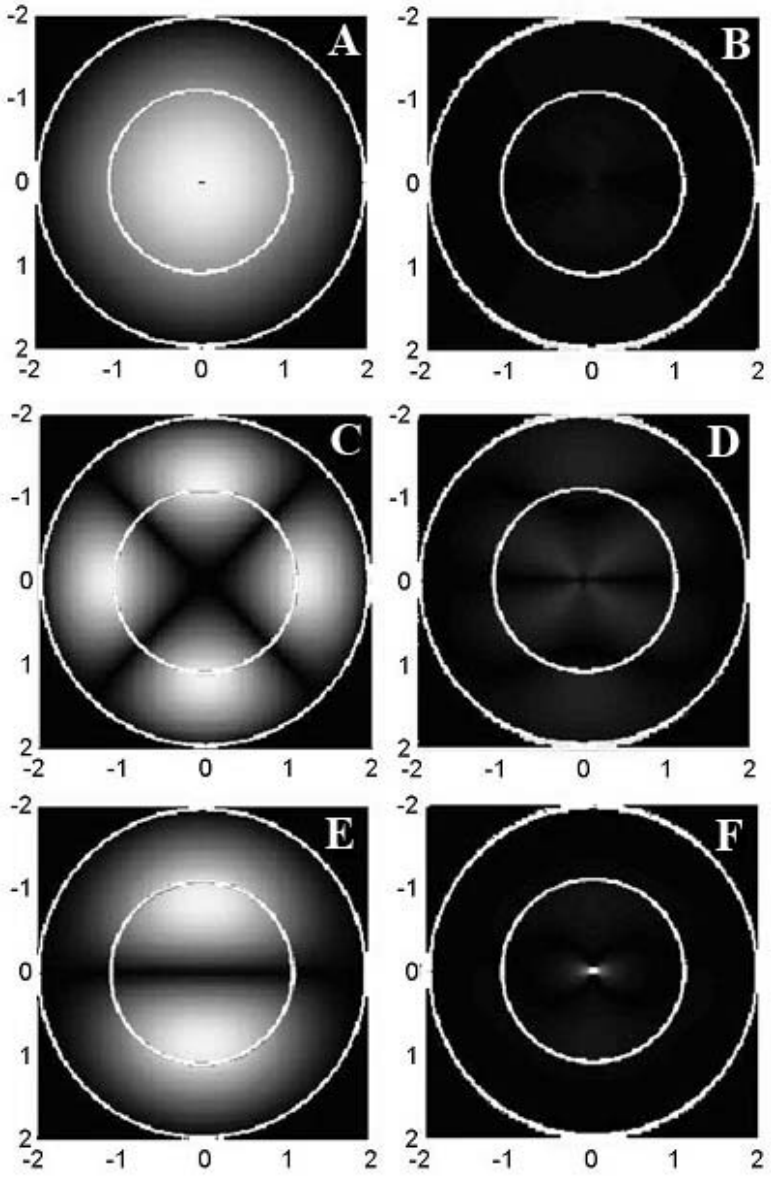

Figure 2-41. Predicted pressure at:(A)322 kHz(C)455 kHz(E)511 kHz Predicted velocity at:(B)322 kHz(D)455 kHz(F)511 kHz(Both). Internal and external boundaries of the tube indicated in white. Predictions for water-filled PS.

As can be seen in Fig. 2-41, the greater density and stiffness of the polystyrene as compared to the LDPE reduced the number of lobes and coupled more energy into the cavity. In addition, the spacing of the resonances increased dramatically. It is interesting to note, that of the three resonances shown in Fig. 2-41, only the mode at 511 kHz exhibiting dipole character possesses a central velocity anti-node. The quadrupole vibration does couple energy into the cavity, but due to the velocity node at the center, would not be expected to concentrate particles.

It seemed that, although glass was the choice of material for the purposes of this research, plastic tube with similar dimensions is also capable of dipolar motion, shown to be indicative of successful particle concentration in glass tube. It was previously stated that LDPE and PS were chosen as outliers of material properties and that the behavior of other plastics having intermediate density and stiffness could be extrapolated. The “softer” plastics, such as LDPE, are shown to decrease the spacing of the resonances. Unfortunately, stress calculations showed that only the coupled tube-fluid dipolar vibration coupled into the cavity efficiently. Replacement of glass tube with plastic tube is also predicted to shift the dipole resonance up in frequency. Following the equation for force on a particle in an acoustic field, it would be expected that the higher frequency would provide a greater

force on the particles, however higher frequencies are attenuated by plastic. The model used included the capability to account for frequency dependent attenuation by including an imaginary part of the wave number, but it is neglected in the interest of simplicity and computational efficiency. Ultimately selection of a particular type of plastic tube would be dependent on balancing the cost, chemical resistance, acoustic attenuation, and acoustic force on particles. The purpose of this theoretical investigation is to demonstrate the feasibility of using tube materials other than glass.

For the sake of completeness, three types of metal tube were theoretically investigated. Aluminum, brass, and stainless steel were chosen as the three metals to be evaluated so as to sample common low density, low stiffness, and low chemical reactivity metals respectively. As with the modeling of plastic tube, the dimensions of the metal tube was assumed to be the same as soft glass tube, for ease of comparison.

Aluminum tube is taken to have longitudinal sound speed of 6420 m/s, transverse sound speed of 3040 m/s, and density of 2.7 g/cm^3. The model predicted large resonances for the water-filled aluminum tube at: 416 kHz, 488 kHz, 845 kHz, and 854 kHz. The stress and velocity calculation results for 488 kHz and 854 kHz are plotted Fig. 2-42.

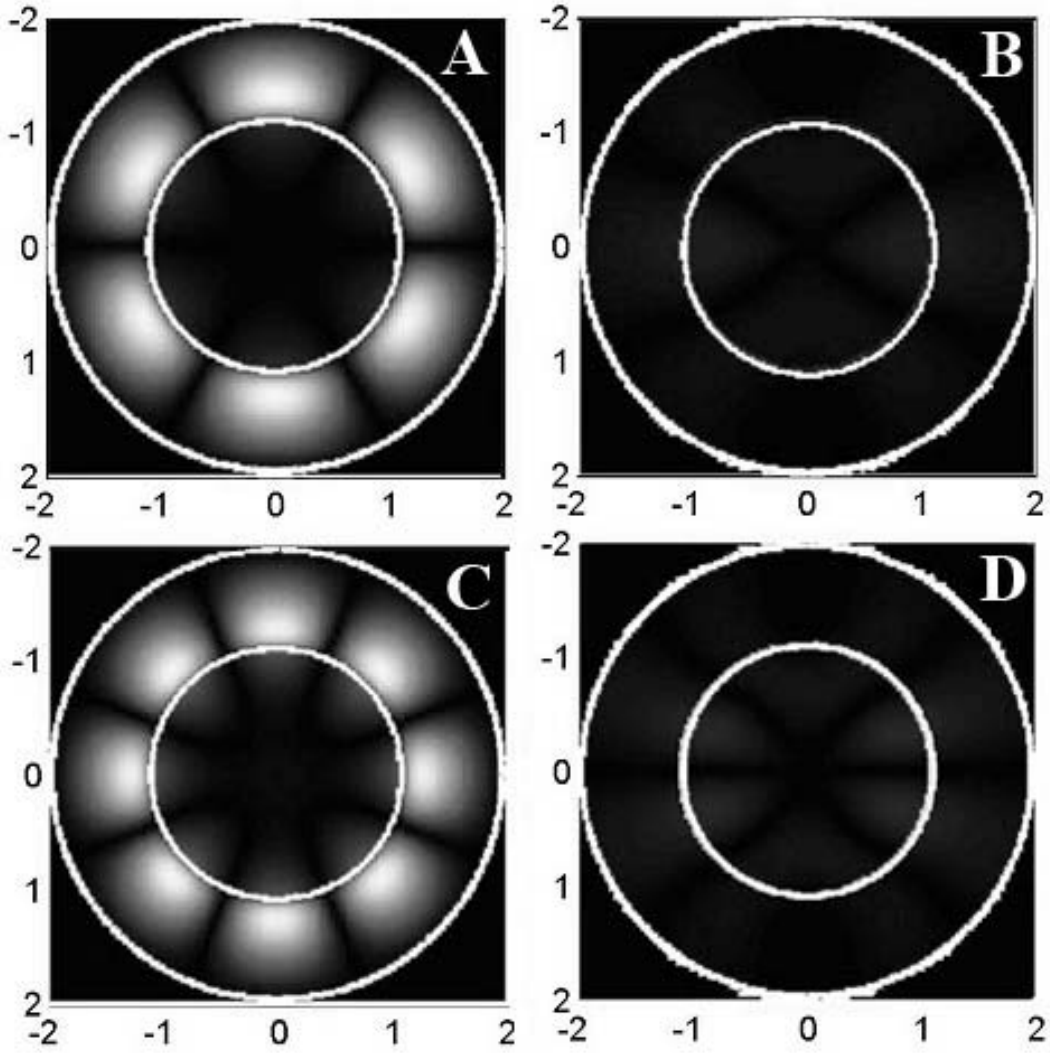

Figure 2-42. Predicted pressure at: (A) 488 kHz (C) 845 kHz. Predicted velocity at: (B) 488 kHz (D) 845 kHz. (Both) Internal and external boundaries of the water filled aluminum tube indicated in white.

As can be seen in Fig. 2-42, these two resonances are vibrations of the aluminum tube with negligible coupling into the fluid-filled cavity. These

are also the two most dominant of the four main resonances selected for presentation. Fig. 2-43 presents the stress and velocity data at 416 kHz and 854 kHz. Both resonances showed a central velocity maximum. The velocity at 854 kHz shows two sets of maxima in the cavity; one neighboring the wall and one at the center, compared to just the single peak at the center for 416 kHz. The tube stress at 416 kHz showed the familiar dipole vibration, while at 854 kHz, a two-ring mode is visible. It is probably unlikely that the higher frequency 854 kHz resonance could concentrate particles. From the results with soft glass, particles are attracted to pressure nodes, due to the relative compressibility of the particles as compared to the fluid. The 854 kHz resonance possessed a local pressure anti-node at the center of the cavity.

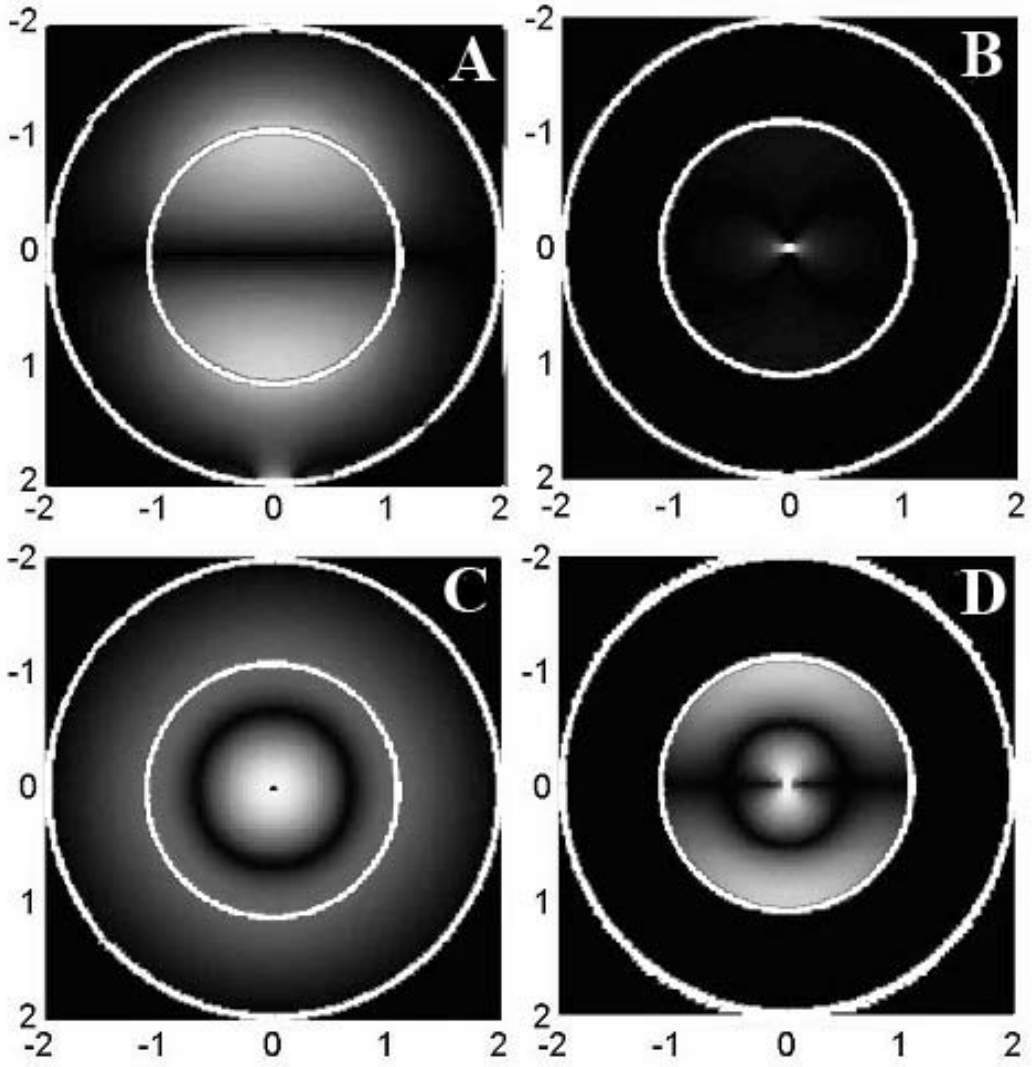

Figure 2-43. Predicted pressure at: (A) 416 kHz (C) 854 kHz. Predicted velocity at: (B) 416 kHz (D) 854 kHz. (Both) Internal and external boundaries of the water filled aluminum tube indicated in white.

For the evaluation of brass tube, the material properties were,

compressional sound speed of 4700 m/s, shear sound speed of 2110 m/s

and density of 8.6 g/cm^3 for 70/30 brass. Large resonances are predicted at: 355 kHz, 623 kHz, 693 kHz, and 878 kHz. As before, Fig. 2-44 displays the stress and velocity of the brass tube at 355, 623 and 878 kHz. Fig. 2-44 demonstrates that the modes at those frequencies are confined primarily to the tube, with minimal coupling into the water-filled cavity. It would be expected that no particle concentration would be observed at those frequencies.

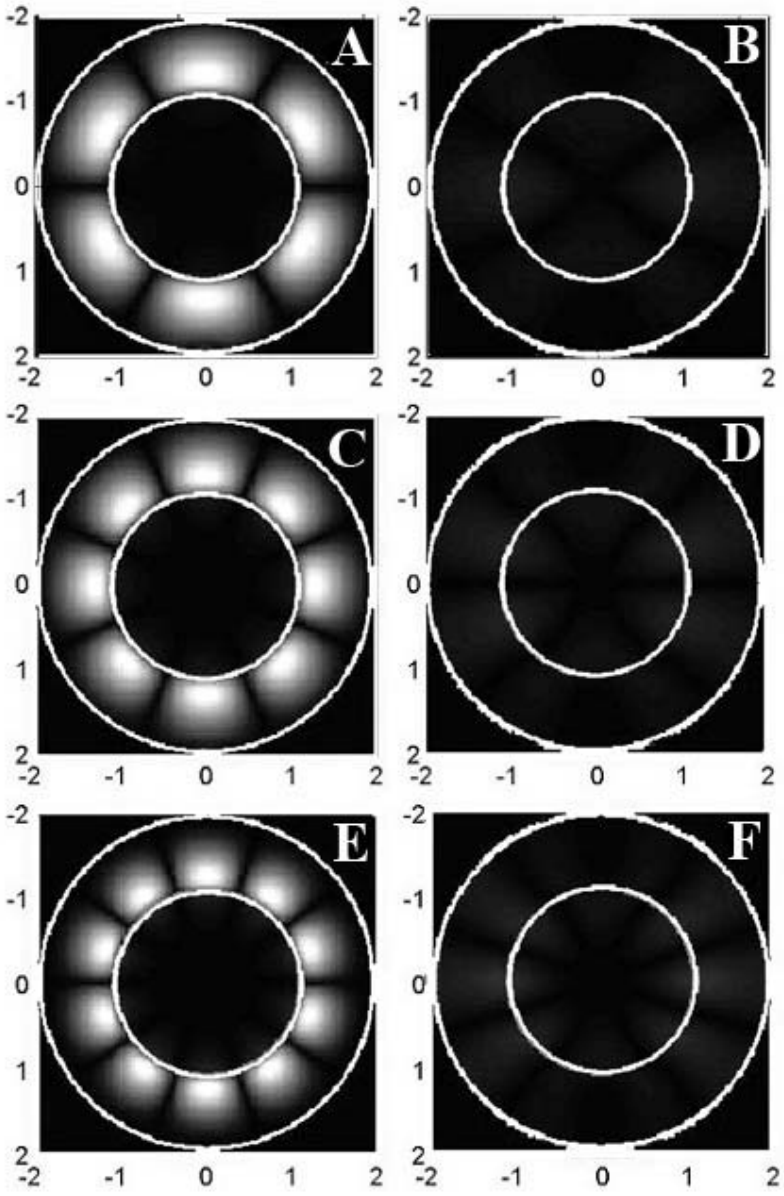

Figure 2-44. Predicted pressure at: (A) 355 kHz (C) 623 kHz. (E) 878 kHz. Predicted velocity at: (B) 355 kHz (D) 854 kHz (F) 878 kHz. (Both) Internal and external boundaries of the water filled brass tube indicated in white.

The predictions for the remaining resonant frequency at 693 kHz are presented in Fig. 2-45. Unlike previous tube, there is both a well-coupled central velocity maximum and central pressure node with a non-dipolar vibration. The mode could almost be described as a mode exhibiting both tube and cavity dipole vibrations. It would be likely, if the well-coupled pressure node hypothesis is true, that particles will concentrate at 693 kHz in brass tube of the dimensions used in the calculations.

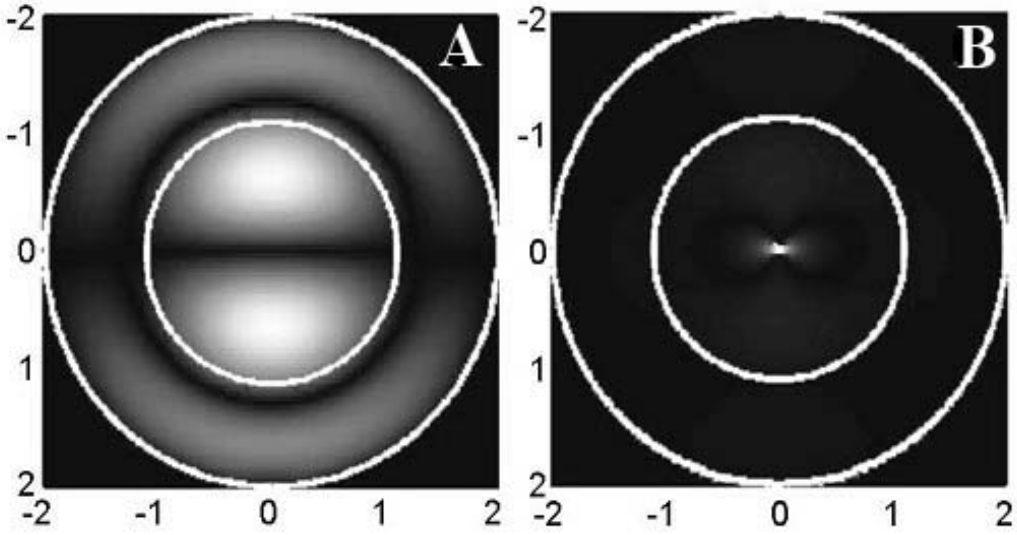

Figure 2-45. (A) Predicted pressure at: 693 kHz. (B) Predicted velocity at: 693 kHz. (Both) Internal and external boundaries of the water filled brass tube indicated in white.

Stainless steel tube used for the calculations is assumed to be type 347 and therefore have longitudinal sound speed, shear sound speed, and

density of 5790 m/s, 3100 m/s and 7.9 g/cm^3 respectively. Four large resonances are found for stainless steel tube at 403 kHz, 482 kHz, 856 kHz, and 993 kHz. The resonances are split into two categories, cavity-coupled, and cavity-uncoupled. The pressure/radial stress and velocity are displayed for each. The two cavity-uncoupled resonances at 482 kHz and 856 kHz are shown in Fig. 2-46, while the cavity-coupled modes at 403 kHz and 993 kHz are shown in Fig. 2-47. As can be seen in Fig. 2-46, the now familiar hexapole and octapole resonance pair are also predicted to be present in stainless steel tube.

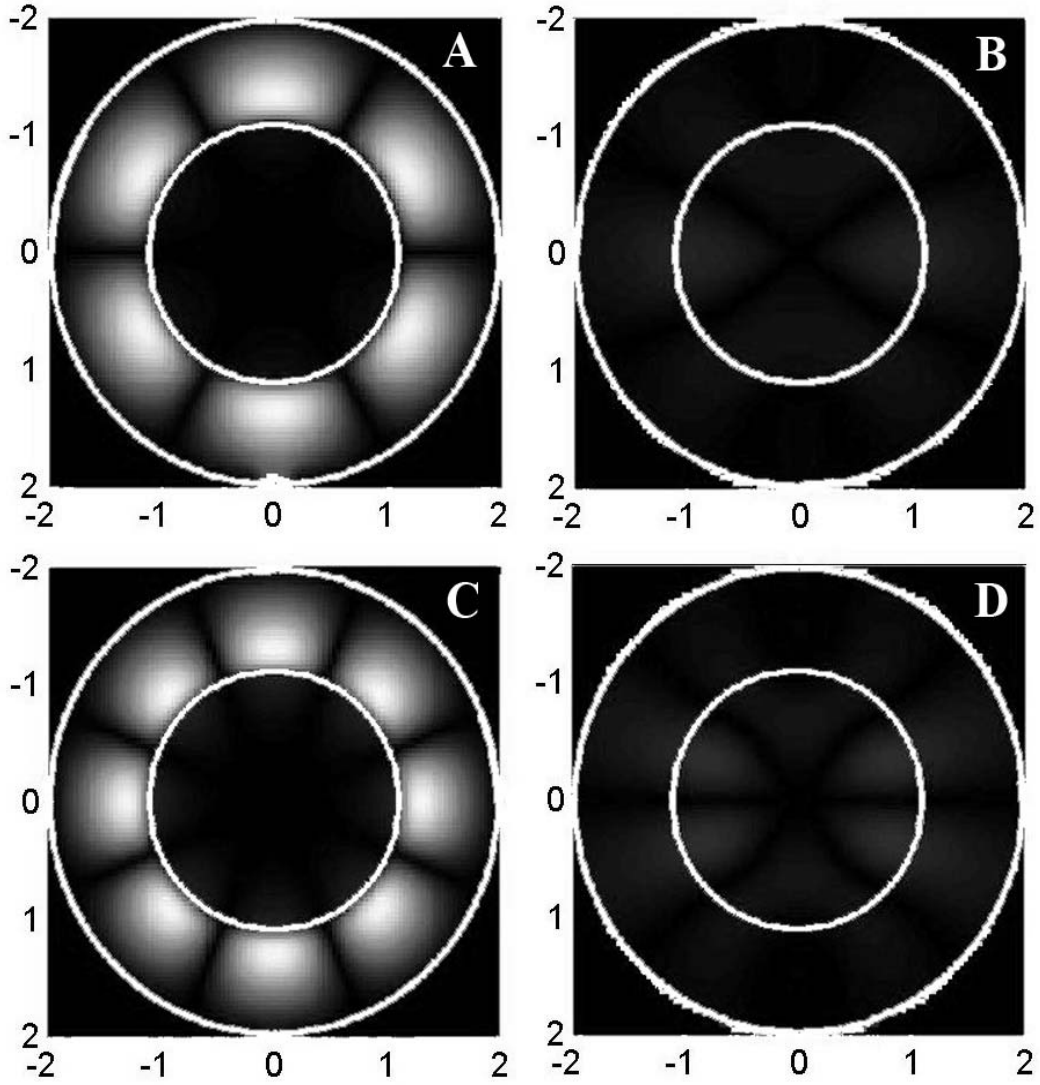

Figure 2-46. Predicted pressure at: (A) 482 kHz (C) 856 kHz. Predicted velocity at: (B) 482 kHz (D) 856 kHz. (Both) Internal and external boundaries of the water filled stainless steel tube indicated in white.

As can be seen in Fig. 2-46, these two resonances are vibrations of the stainless steel tube with negligible coupling into the fluid-filled cavity. Fig.

2-47A presents the stress and velocity data at 403 kHz and 993 kHz. Both resonances showed a central velocity maximum. The velocity at 993 kHz shows two sets of maxima in the cavity; one neighboring the wall and one at the center, compared to just the single peak at the center for 403 kHz. The tube stress at 403 kHz showed the familiar coupled dipolar vibration, while at 993 kHz, a twin-dipole mode is visible. Similar to brass tube, there is both a well-coupled central velocity maximum and central pressure node with a non-dipole vibration at 993 kHz. The mode could almost be described as a second order dipole with both tube and cavity dipole vibrations. It would be likely, if the well-coupled pressure node hypothesis is true, that particles would concentrate at 993 kHz in stainless steel tube of the dimensions used in the calculations. From the results with soft glass, particles are attracted to pressure nodes, due to the relative compressibility of the particles as compared to the fluid.

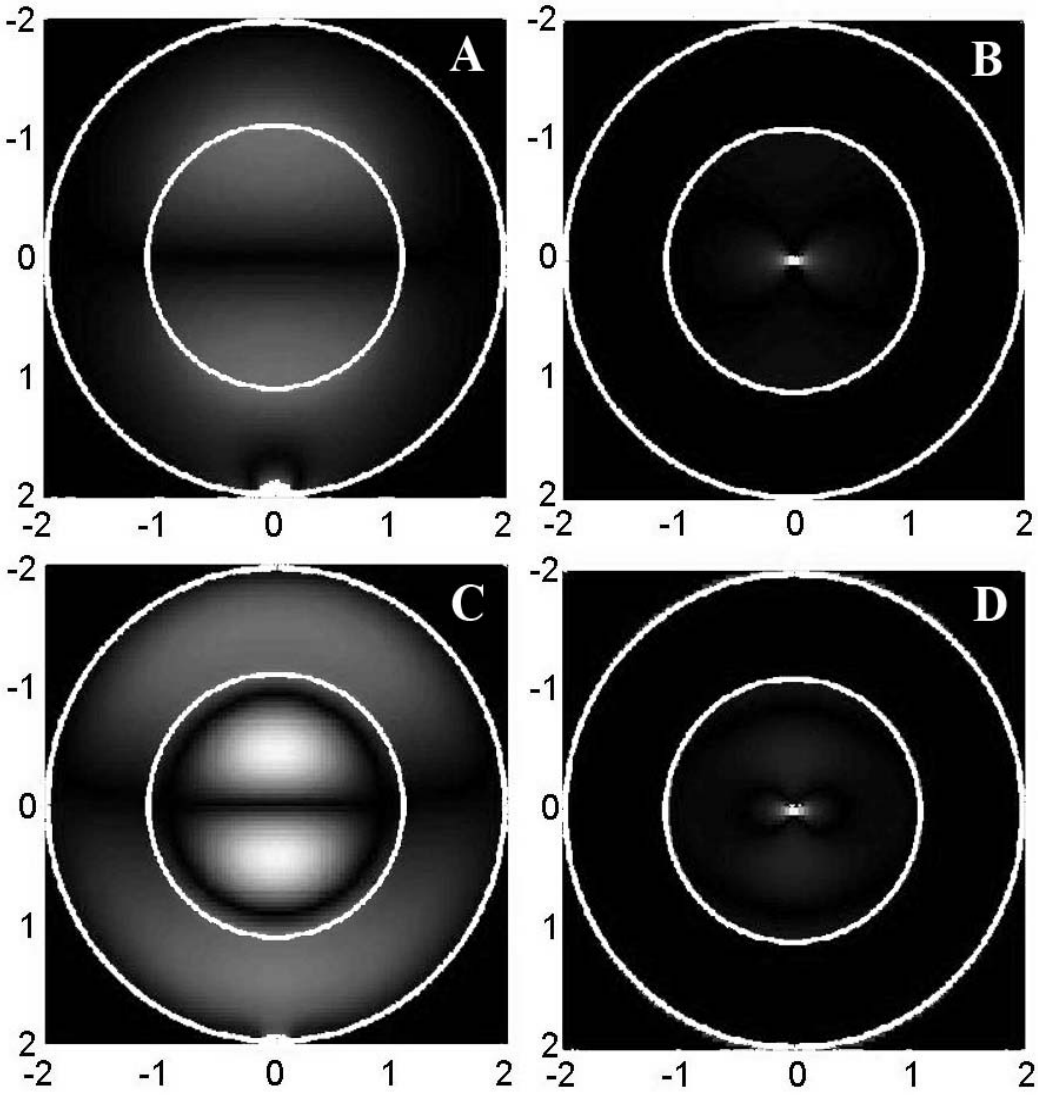

Figure 2-47. Predicted pressure at: (A) 403 kHz (C) 993 kHz. Predicted velocity at: (B) 403 kHz (D) 993 kHz. (Both) Internal and external boundaries of the water filled stainless steel tube indicated in white.

From the results of the theoretical investigation of metal tube, it seems likely that structural excitation of metal tube with similar dimensions to soft

glass is also capable of dipolar motion, shown to be indicative of successful particle concentration in glass tube. It was previously stated that the metals were chosen based on their exhibition of low density, low stiffness, and low chemical reactivity. While these properties did not allow extrapolation as proposed for the plastic tube modeled in a previous section, some conclusions could be drawn from the results. Hexapolar and octapolar modes are not predicted to appreciably couple into the cavity. As with plastic, the softer metal had smaller inter-resonance spacing. Density differences had very little effect on the cavity-uncoupled modes, and angular “smearing” of the second dipole mode. Also worth noting is the large loss of vibration amplitude in metals as compared to either glass or plastic. The frequency of the coupled structure-fluid dipolar vibration is shifted downward by the replacement of glass with metal. Ultimately selection of a particular tube material would be dependent on balancing the cost, chemical resistance, acoustic attenuation, and acoustic force coupled into the cavity on particles in suspension. The purpose of this theoretical investigation is in the interest of completeness in a feasibility study of using tube made of materials other than glass.

Although the resonances shown in the figures are the maximum amplitude modes and are plotted as normalized against each of their

respective maxima, there is a great deal of variation between relative amplitudes of the resonances for different materials. Metals showed the least vibration and hence the least energy coupled into the cavity. Plastics showed the greatest vibration amplitude; glass had amplitudes somewhere in between metals and plastics. Glass is observed to possess the best vibration coupling, experimentally. These observations could be explained by noting that maximal coupling occurs when impedances are matched. There are two coupling interfaces; the transducer-tubing interface and the tube-fluid interface. The model, in assuming an infinite line source, did not include PZT-tubing coupling, so the model would be biased towards the tube-fluid energy transfer. Plastic has acoustic impedance near that of water, so would therefore be expected to exhibit the best resonance coupling. The acoustic impedance of PZT, as it is a ceramic, is similar to glass. In optimization of the technique, it would be ideal if a transducer was carefully frequency and impedance matched to the tube and fluid to allow both interfaces maximal coupling efficiency. The character of dipole vibration, and consequent steep pressure and velocity profiles within the cavity suggested that particles within the cavity should experience more acoustic force perpendicular to the transducer face than parallel to it. This phenomenon should exhibit itself in the form of tighter focusing of the particles along the normal to the

transducer.

2.10-Conclusion

A general two-dimensional model for a line driven cylindrical tube has been developed. The validity of the model was experimentally verified for several types of air and fluid filled glass tube. Dipole vibration of the exterior of the tube is predicted to indicate efficient coupling from the cylindrical structure into the fluid-filled cavity. Experimental observations of particle concentration within the cavity corroborated this hypothesis. Furthermore, the potential use of alternate tube materials was theoretically evaluated. It was argued that while all materials are capable of dipolar vibration, the greatest coupling of energy into the cavity occurred with plastic tube. Metals are predicted to be a poor choice to replace the glass tube used for these experiments. Predictions of rotational asymmetry of acoustic forces within the cavity are also made based on the theoretical predictions, as they are inherent in dipolar vibration.

3-Acoustic Forces on Particles

3.1-Introduction

A key aspect of this research is the ability to concentrate particles in aqueous suspensions. Evaluation of vibrational modes of the tube was covered in chapter 2. The focus of this chapter is the description of forces exerted on particles in an acoustic field. The parameter limitations prescribed by theory are discussed in chapter 5.

Particles in a standing sound field experience several acoustic forces. One of the most dominant of these is an acoustic force parallel to the direction of sound propagation. This force transports the particles in the field to the nodes or anti-nodes of the standing wave. The magnitude of this force depends on the acoustic contrast between the particle and the medium. Inhomogeneities in the acoustic field lead to another force which, in the case of the planar standing wave, is generated perpendicular to the direction of sound propagation. It is also proportional to the acoustic contrast between particles and fluid. At higher field strengths, the sound field can induce fluid flow in the direction of sound propagation; this effect is called acoustic streaming. The streaming flow contributes a drag force on the particles. Once the particles are close to one another, the scattered acoustic field

contributes to an attractive or repulsive inter-particle force called Konig[90] or Bjerknes[91] force.

3.2-Primary Forces

In the first quantitative analysis of the acoustic radiation force on a particle in a sound field, King[92] considered the radiation force only, assuming incompressible spheres, noting that the radiation force on particles with radii less than a wavelength is greater in a standing than a traveling wave field. King determined the radiation pressure on a sphere by integrating the total sound pressure field on a rigid sphere over the surface of the sphere in a planar standing wave, freely suspended in non-viscous fluid. He derived the expression for the primary acoustic force acting on a rigid sphere with radius r, particle density, ρ_p, in a fluid of density ρ_f and standing wave of acoustic energy density ε can be expressed as

$$F = 4\pi\varepsilon R_0^2 (\frac{\omega}{c_f} R_0)(\frac{\rho_p + \frac{2}{3}(\rho_p - \rho_f)}{2\rho_p + \rho_f}) e^{i\omega t} \cos^2(\frac{\omega}{c_f} x) \quad . (3.1)$$

Embleton[93,94,95] extended King's treatment to the case of propagating cylindrical and spherical wave fields. Yosioka and Kawasima. [96] and Gorkov[97] separately extended the analysis to include the influence of particle compressibility on the force moving the particles to nodal or anti-nodal

positions. A fluid subjected to an acoustic field exerts hydrodynamic forces, proportional to the local velocities of the fluid on particles suspended in it. Since the particle and fluid compressibilities can be expressed as shown in equations 3.2 and 3.3 respectively, I can rewrite the force acting on a small compressible spherical particle in terms of particle and fluid compressibilities, β_p and β_f respectively and sound speeds of the fluid and particle, c_f and c_p respectively, as shown in Eq. 3.4.

$$\beta_p = \frac{1}{\rho_p (c_l^2 - \frac{4}{3} c_s^2)} \tag{3.2}$$

$$\beta_f = \frac{1}{\rho_f c_f^{\,2}} \tag{3.3}$$

$$F = \pi R_0^2 \varepsilon \sin\left(\frac{2\omega x}{c_f}\right)\left[\left(\frac{\omega R_0}{c_f}\right)^3 \left(\frac{\rho_p + \frac{2}{3}(\rho_p - \rho_f)}{2\rho_p + \rho_f} - \frac{\beta_f - \beta_p}{\beta_f}\right)\right] \tag{3.4}$$

The variable R_0 is the particle radius and x is the distance of the particle from a pressure anti-node. Depending on the relationships between the density and acoustic velocity of the particle and fluid, the particle will tend to move either to a pressure anti-node or a pressure node. Seven conditions are assumed in the derivation of this force equation.

1) The sound is a sinusoidal wave of a single frequency

2) The stationary waves are composed of plane progressive waves with the same amplitude traveling in opposite directions.
3) The particle size is significantly smaller than the wavelength of the sound wave.
4) The suspension is so dilute that there is no impact on the motion of the other particles in the vicinity.
5) The fluid is inviscid.
6) The sound field is not disturbed by either ultrasonic cavitation or suspended particles and thus the energy density is uniform.
7) There is no change in temperature due to the irradiation of sound.

The first two assumptions as well as requirement of a cavity dimension of some multiple of a half wavelength are required to establish a standing wave in the cavity. Violation leads to non-stationary waves in the resonator. The third condition significantly simplifies the equation by allowing the assumption of no wave coupling into the modes of the sphere. Adherence to the fourth condition removes the secondary force contributions. The combination of the third and fourth conditions eliminates absorption of acoustic radiation by the particles. The absorption of radiation by the liquid is eliminated and acoustic streaming is reduced by condition 5. Conditions six

and seven are difficult to maintain as well as the most critical to obtain good concentration.

Nyborg[98] derived equations for the acoustic force by extending the approaches of King and Embleton, which are equivalent to Gorkov for rigid spheres and standing plane waves, but included an additive term that is only dominant for uniform energy densities as in the case of traveling waves. The additive term is defined as the second order variation of the pressure. Higashitani, Fukushima, and Matsuno[99] accounted for diffusion of small particles, which they defined as particles less than 0.1μm in diameter, using a Boltzmann thermal distribution of particles to account for Brownian motion.

Westervelt[100] investigated the influence of fluid viscosity on the acoustic radiation pressure. He found that fluid viscosity effect arises due to losses within the boundary layer of the particles and is particularly significant for small spheres and low frequency traveling waves. The radiation force exerted by progressive waves can be several orders of magnitude higher than predicted by King's theory for the non-viscous case. Danilov[101,102] developed an expression for the effect of viscosity on acoustic radiation pressure on small suspended particles, but did not account for acoustic streaming.

Doinikov[101-105] solved the Navier-Stokes equations with second order

approximation to obtain general solutions for the radiation force in standing and traveling waves without restriction on particle size. He additionally differentiated between the viscosities of the medium and the particle. Doinikov determined that for a standing wave in a low viscosity fluid, and a dilute suspension in an arbitrary field, Gorkov's theory for non-interacting particles still provides a good description of the equilibrium particle distribution, but the effect of viscosity becomes significant for traveling waves, higher viscosity liquids, high particle concentrations or cases where Brownian motion is dominant. The viscosity compensation term decreases rapidly with increasing frequency and particle size. The ideal fluid approximation generates a good estimate of the radiation force any time the particle radius is much smaller than the wavelength and much greater than the viscous boundary layer thickness.

Under most conditions of practical interest, the radiation force in a traveling wave will be much smaller than in a standing wave of comparable energy density. The existing theories of acoustic radiation pressure on particles in a fluid neglect both dissipative effects, viscous and thermal. Doinikov obtained a general expression for radiation force including both viscous and thermal dissipative mechanisms for arbitrary dimension particles in an arbitrary field. For the case of a particle much smaller than a

wavelength and much bigger than the viscous and thermal wavelengths in the fluid in a planar standing wave, the equation can be simplified into the form in Eq. 3.5. The variables CF, Z_v and Z_t are defined in 3.6, 3.7, and 3.8 respectively. The viscous “wavelengths” in the fluid and particle, respectively, are defined as written in equations 3.9 and 3.10 respectively by Doinikov.

$$F = \pi R_0^2 \varepsilon \sin\left(\frac{2\omega x}{c_f}\right)\left[\left(\frac{\omega R_0}{c_f}\right)^3 CF\right] - \pi\varepsilon\left(\frac{\omega R_0}{c_f}\right)^3 \frac{2\eta_f}{\omega R_0^2} \tag{3.5}$$

$$CF = \left(\frac{5\rho_p - 2\rho_f}{3(2\rho_p + \rho_f)} - \frac{c_f^2 \rho_f}{3c_p^2 \rho_p} + \mathrm{Re}(Z_v)\frac{\sqrt{\frac{2\eta_f}{\rho_f \omega}}}{R_0} - \mathrm{Re}(Z_t)\frac{\sqrt{\frac{2\kappa_f}{\rho_f C_f \omega}}}{R_0} \right) \tag{3.6}$$

$$Z_v = 3\left(\frac{1-\frac{\rho_f}{\rho_p}}{2+\frac{\rho_f}{\rho_p}}\right)^2 \frac{(1+i)\left[1+\frac{\rho_f \delta_f}{\rho_p \delta_p}+\frac{2\rho_f}{R_0 \rho_p}\delta_{vp}+2\left(\frac{\rho_f}{\rho_p}\delta_p\right)^2\right]+\frac{2i\rho_f}{R_0 \rho_p}\frac{\eta_f}{\eta_p}\delta_f}{\left(1+\frac{\rho_f \delta_f}{\rho_p \delta_p}+\frac{\rho_f}{R_0 \rho_p}\delta_{vp}\right)^2+\left(\frac{\rho_f}{\rho_p}\delta_p\right)^2} \tag{3.7}$$

$$Z_t = \frac{3(1+i)((\gamma_f - 1)\rho_p c_p^2 - \frac{\alpha_f}{\alpha_p}(\gamma_p - 1)\rho_f c_f^2)(\frac{\alpha_f}{\alpha_p}\frac{2\kappa_f}{\rho_p C_f \omega} - \frac{\kappa_f}{\kappa_p}\frac{2\kappa_p}{\rho_p C_p \omega})}{2\rho_p c_p^2 \frac{\alpha_f}{\alpha_p}\sqrt{\frac{2\kappa_f}{\rho_p C_f \omega}}\left(\sqrt{\frac{2\kappa_f}{\rho_f C_f \omega}} + \frac{\kappa_f}{\kappa_p}\sqrt{\frac{2\kappa_p}{\rho_p C_p \omega}}\right)} \tag{3.8}$$

$$\delta_p = \sqrt{\frac{2\eta_p}{\rho_p \omega}} \tag{3.9}$$

$$\delta_f = \sqrt{\frac{2\eta_f}{\rho_f \omega}} \tag{3.10}$$

where ω is angular frequency, η refers to shear viscosity, c refers to sound speed, κ refers to thermal conductivity, R_0 is particle radius, C is heat capacity, γ is the ratio of specific heats, the subscripts p and f indicate particle and fluid properties respectively, and ε is energy density of the field.

The additional force in attenuating fluids induces acoustic streaming and consequently additional drag forces on the particles leading to increased scattered field amplitude. Viscous effects can be treated as a change in phase and amplitude relations between primary and scattered fields. The four terms in the definition of the contrast factor, CF, correspond to four sources of the acoustic forces on particles in the field; density contrast, compressibility contrast, fluid viscosity, and thermal conductivity respectively. Barmatz and Collas[108] derived an expression for the force on a fluid-suspended particle in a cylindrical or spherical acoustic wavefield. They assumed a rigid boundary between the fluid and solid. Utilizing the expressions for pressure and velocity of the wave from Ricks and Schmidt, an expression for the force on a particle in a cylindrical tube with an elastic boundary condition can be obtained. The expression is

$$F = -\nabla\left\{2\pi\varepsilon R^3 \sum_{n=0}^{\infty} A_n \left\{-\frac{Z_0}{3}\alpha - \frac{Z_1\rho_f}{2}\left[\beta - \varsigma\right]^2\right\} e^{in\theta}\right\} - \pi\varepsilon\left(\frac{\omega R_0}{c_f}\right)^3 \frac{2\eta_f}{\omega R_0^2} \quad (3.11)$$

$$\alpha = J_n^2(k_{rf}r)\cos^2(k_{zf}z) \quad (3.12)$$

$$\beta = \left(\frac{k_r}{\sqrt{k_r^2 + k_z^2}} J_{n+1}(k_{rf}r) + \frac{2n}{r\sqrt{k_r^2 + k_z^2}} J_n(k_{rf}r)\right)\cos(k_{zf}z) \quad (3.13)$$

$$\varsigma = \frac{k_z}{\sqrt{k_r^2 + k_z^2}} J_n(k_{rf}r)\sin(k_{zf}z) \quad (3.14)$$

$$Z_0 = \frac{2}{9}\left(\frac{\omega R_0}{c_0}\right)^3 \left(\frac{\rho_f c_f^2}{\rho_p c_p^2} - \frac{3}{2 + \frac{\rho_f}{\rho_p}} - \frac{\delta_v}{R_0} Z_v^* + \frac{\delta_t}{R_0} Z_t\right) \quad (3.15)$$

$$Z_1 = \frac{2}{9}\left(\frac{\omega R_0}{c_0}\right)^3 \left(\frac{1 - \frac{\rho_f}{\rho_p}}{2 + \frac{\rho_f}{\rho_p}} + \frac{\delta_v}{R_0} Z_v\right) \quad (3.16)$$

where ω is angular frequency, η refers to shear viscosity, γ refers to the ratio of specific heats, c is sound speed, κ is thermal conductivity, C refers to heat capacity, α refers to coefficient of volumetric thermal expansion, k_r is radial wavenumber, k_z is axial wavenumber, R_0 is particle radius, ε is energy density of the field in the fluid, and Z_v and Z_t are given in Eq. 3.7 and Eq. 3.8. The subscripts p and f refer to particle and fluid properties respectively.

Figure 3-1 shows the calculated trajectories of particles in the cavity of soft glass tube during excitation at the coupled dipole resonance frequency. The trajectories are found by numerically integrating the force equation given above for the coupled dipole mode described in the previous chapter. The vertical axis is distance from the center of the cavity. A horizontal line is visible on both plots at radius equal to zero. This is due to the numerical breakdown of the trajectory solutions at that point. Figure 3-1A showed the trajectories of particles along the axis normal to the drive transducer. Figure 3-1B presented the trajectories of particles along the axis parallel to the drive transducer. Gravity is assumed to act along the axis of the tube such as would be the case for a vertical tube. As can be seen in Fig. 3-1, the particles move to the central axis quicker along the normal to the transducer. Experimentally, this would yield a tighter concentration pattern normal to the transducers and faster particle movement to the pressure node along the normal axis.

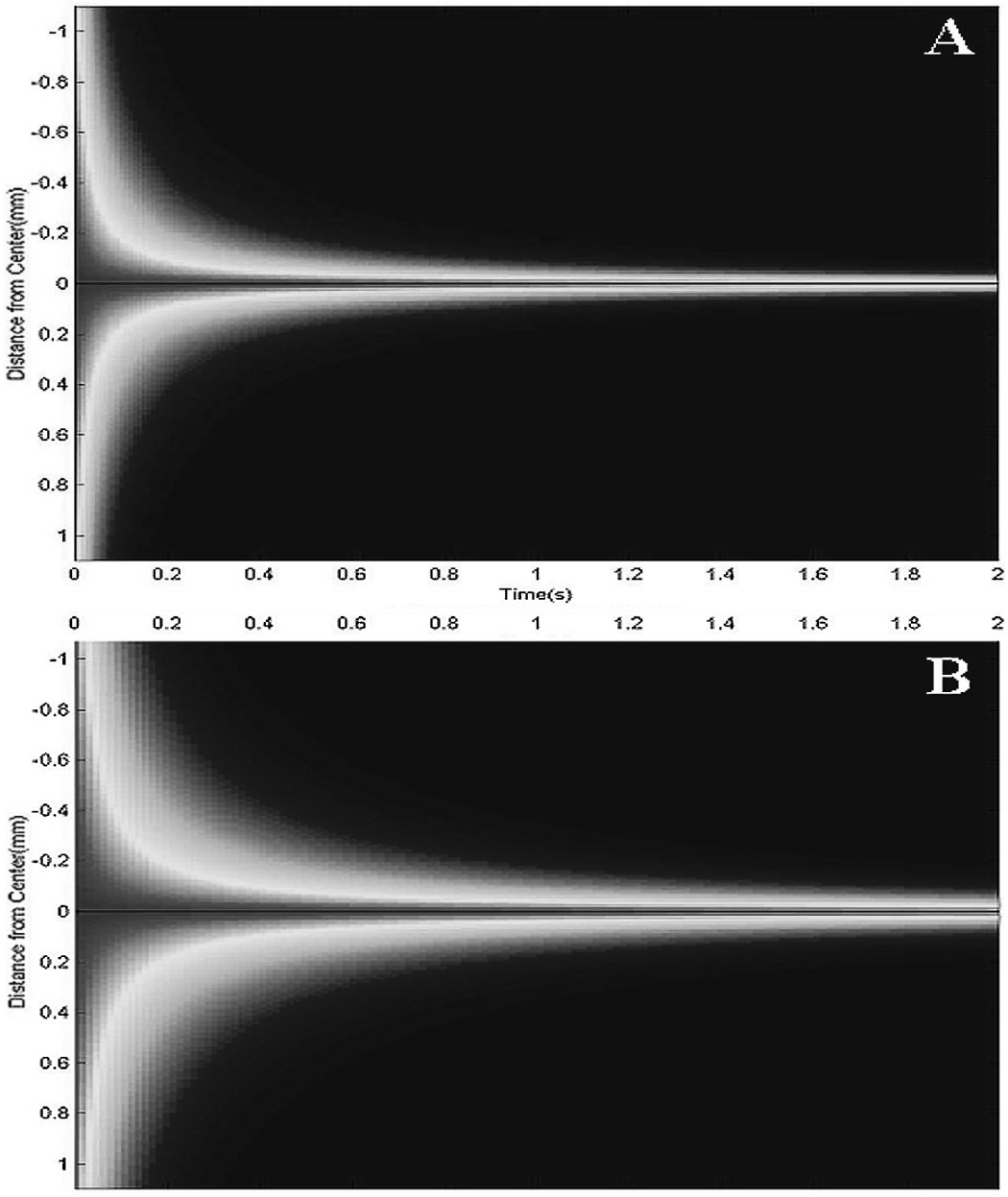

Figure 3-1. Calculated trajectories of particles in the cavity of soft glass tube during dipole excitation. The vertical axis is distance from the center of the cavity.in the specified direction. (A) Orthogonal (B)

Parallel.

Higashitani determined the number density of particles subjected to a one dimensional plane standing wave can be expressed in terms of particle and fluid compressibility as

$$\frac{\partial}{\partial t} n_p = \frac{K_B T}{6\pi\mu r} \frac{\partial^2}{\partial x^2} n_p - \frac{2\omega r^2 \varepsilon (1 - \frac{\beta_p}{\beta_f})}{c_f (3\xi_f - 2\eta_f)} \frac{\partial}{\partial x} n_p (\sin(2\frac{\omega}{c_f} x)) \quad (3.17)$$

The variable T is temperature, n_p is the number particle density, ξ is the bulk viscosity of the fluid, η is the shear viscosity of the fluid, μ is the net viscosity of the fluid, x is the distance from the face of the drive transducer, and K_B is the Boltzmann constant. In the case of a standing wave, the time dependence disappears and Eq. 3.17 can be rewritten as shown in Eq. 3.18. Equation 3.18 defines the variable q as a measure of the potential well experienced by the particles. The variable n_0 is the initial distribution density in particles per unit area normal to the standing wave axis; I_0 is the modified Bessel function of zero order, to account for particle number conservation under changing values of q.

$$n_p = \frac{kn_0}{\pi I_0(q)} e^{(q\cos(2kx))} \quad (3.18)$$

$$q = \frac{2\pi r^3}{K_B T} \varepsilon(1 - \frac{\beta_p}{\beta_f}) \quad (3.19)$$

In any real sound field there are non-uniformities in the field distribution, giving rise to components to the acoustic force perpendicular to the acoustic transmission direction or standing wave direction. This force is called the primary transverse force. It is due to inhomogeneous radiation from the transducer, divergence and interference effects within the cavity and viscosity of the fluid. It is only present at velocity antinodes, and thus only acts on particles that concentrate at those points. It has been shown by Hager and Benes[109], Gaida et al. [110] and Doblhoff-Dier et al. [111] to further concentrate particles into clusters adjacent to the local velocity maxima. Whitworth[112], and Whitworth et al. [113] investigated the relative amplitude of acoustic forces in a concentration tube. In order to do so, they rotated an ultrasonic concentration tube, driven parallel to and rotated about the central axis of the tube while observing particle trajectories.

3.3-Nonlinear and Second Order Forces

Nonlinear effects can give rise to time-independent flow, also called

acoustic streaming, in the fluid. Viscous drag forces exerted on the particles are due to two factors; acoustically induced flow velocity due to streaming and fluid velocity present in the absence of the sound field. The force exerted is proportional to the cross section of the particles and particle velocity, including fluid drag arising from fluid flow. Gould and Coakley[114] further expanded the analysis to include buoyancy, and acoustic streaming. Acoustic streaming is a generic term to describe time-averaged streaming induced in any fluid flow that is dominated by the fluctuating components. Doinikov[101-105] extended the analysis of acoustic radiation pressure to spherical particles of arbitrary radius and elasticity that takes fluid viscous and thermal dissipative mechanisms into account. He showed that the magnitudes of viscous and thermal dissipative effects in an axisymmetric traveling wave, such as a progressive plane wave, are of comparable magnitudes, but both dissipative effects can be several orders of magnitude smaller in a standing wave. The total radiation force can be expressed as the sum of the acoustic radiation pressure and the drag force caused by the stationary fluid flow induced by the sound field in the absence of particles. Doinikov found that for standing wave fields in low viscosity liquids, the second order terms could be neglected. Hilpert and Miller[115] argued for the inclusion of viscous dissipation and contact angle compensation for

determining resonance frequencies of systems where surface effects are of comparable magnitude to volume effects, such as for axially driven liquid columns in capillary tubes when the reflecting surface is a meniscus even in the case of inviscid liquids.

So far, only the interaction between the primary sound field and a single particle has been considered. As noted previously, in the case of two particles, the total sound field includes the primary field and a secondary scattered field from the other particle. This interaction was first investigated by Konig, who used hydrodynamic principles to develop an expression for the force between two spheres in an acoustic field including the primary field. Bjerknes later calculated the forces between oscillating spheres without the primary sound field. Thus the force between particles in an acoustic field is alternately known as Bjerknes force or Konig force. In a separate analysis Embleton[116] also evaluated the interaction force between two particles in a planar sound field. Expressions for the secondary radiation force between two particles in an ideal fluid and a uniform acoustic field are also derived for incompressible spheres by Weiser et al. [117] and compressible spheres by Crum[118]. Doinikov[119, 120] later compensated for viscous fluid. Most researchers studying the interaction of particles in a sound field have restricted the investigation to a wavelength much greater than the radii or

spacing of the particles in an inviscid fluid. Zheng and Apfel[121] however, calculated the interaction force without this restriction. The interaction force for two identical compressible spheres with radii r can be expressed as

$$F_{\text{int}} = \frac{4\pi R_0^6(\rho_p - \rho_f)^2(3\cos^2\theta - 1)}{6\rho_f d^4} v^2(x) - \frac{\omega^2 \rho_p (\beta_p - \beta_f)^2}{9d^2} p^2(x) \quad (3.20)$$

where F_{int} is the interaction force, θ is the angle between the centerline of the particles and the propagation direction of the incident sound wave, v(x) and p(x) are the velocity and pressure respectively of the unperturbed incident field at the position of the particles and d is the inter-particle distance. The first term is a repulsive force term unless the particles are lined up in the direction of sound propagation. The second term represents an attractive force term and is independent of particle orientation. The first term vanishes at pressure antinodes; the second term vanishes at pressure nodes. For particles attracted to the pressure nodes in a standing wave aligned parallel to the nodal planes the secondary radiation force is attractive and can be re-expressed as

$$F_{\text{int}} = -\frac{16\pi R_0^4 \varepsilon}{9d^2}\left(\frac{3\left(\frac{\rho_p}{\rho_f}-1\right)^2 \sin^2\left(\frac{\omega}{c_f}x\right)}{2d^2} + k^2\left(1-\frac{\beta_p}{\beta_f}\right)^2 \cos^2\left(\frac{\omega}{c_f}x\right)\right) \quad .(3.21)$$

In general the interaction force becomes significant only when the particles are in very close proximity, defined as within 2 to 3 particle radii. It typically causes the particles to form clusters within the nodal or anti-nodal planes of the acoustic field. Since the secondary radiation force between particles is dependent on incident field strength, it is affected by viscosity in qualitatively the same way as the primary force.

Hasegawa[122] investigated the change in radiation force caused by ultrasonic absorption by elastic spheres in a standing wave. In his analysis he only considered the frequency independent hysteresis type of absorption. The absorption is accounted for in the imaginary part of the wave number. Hasegawa found that the sound absorption by the particles could be neglected if the dimensions of the particles are small as compared to 1/k, also called the acoustic wavelength, and the volume fraction of particles is small.

The particles up to this point have been assumed as compressible, potentially absorptive elastic spheres. The angular alignment of particles was referred to briefly in the description of inter-particle forces due to scattering of

the primary sound field. However, in a sound field, there are also primary acoustic forces that exert torque on particles, inducing spin or alignment. Awatani[123, 124] first derived an expression for the radiation pressure on a cylinder. Wu et al[125] and Woodside et al. [126,127,] separately derived an expression for acoustic force on an infinite cylinder with diameter much less than a wavelength in a standing wave. The expression is limited to the case of an infinitely long immovable cylinder with the axis perpendicular to the direction of wave propagation. Yamahira et al later derived expressions for the motion of finite cylindrical fibers in an ensonified liquid. The translational and rotational acoustic forces on a neutrally buoyant cylindrical fiber in a fluid are

$$F_{trans} = -4\varepsilon R_0^2 \sin(2kx)(2G_r \frac{|\sin\theta|}{\cos\theta}\sin(\alpha) + 2\pi k R_0 G_a \cos\theta\cos(\alpha)) \quad (3.22)$$

$$F_{rot} = \frac{8R_0^3\pi\varepsilon l k^2}{k}\left(\frac{G_a|\cos\theta|\cos(2kx)}{\csc\theta\csc(\alpha)} + 2G_r\frac{-\alpha\cos(\alpha)+\sin(\alpha)}{\cot^2\theta}\right) \quad (3.23)$$

$$\alpha = kl\cos\theta \quad (3.24)$$

$$G_r = \frac{\frac{\rho_{pr}}{\rho_f} + \frac{2}{3}(\frac{\rho_{pr}}{\rho_f} - 1)}{(2\frac{\rho_{pr}}{\rho_f} + 1)} - \frac{\beta_{pr}}{\beta_f} \quad (3.25)$$

$$G_a = \frac{\frac{\rho_{pa}}{\rho_f} + \frac{2}{3}(\frac{\rho_{pa}}{\rho_f} - 1)}{(2\frac{\rho_{pa}}{\rho_f} + 1)} - \frac{\beta_{pa}}{\beta_f} \quad (3.26)$$

The variables G_r and G_a are density-compressibility coefficients. The subscripts “r” and “a” indicate the material properties in the radial and axial directions respectively. The subscripts “trans” and “rot” refer to the translational and rotational or torsional motions of the cylindrical particles respectively. The variable α is used to enhance readability of the equations. The variables R_0, l and θ refer to the radius of the particle, length of the particle and angle from parallel to the wave propagation direction

respectively.

The primary acoustic force typically has the greatest magnitude of the acoustically induced forces present in a standing wave. For 10-micron polystyrene beads in water, the acoustic force due to inhomogeneities in the acoustic field and secondary acoustic force, also known as the Konig or Bjerknes force, are approximately two orders of magnitude and six orders of magnitude smaller than the primary acoustic radiation force respectively. In a dilute suspension, where inter-particle distances are much larger than the particle radii and interactions are negligible, the secondary force is virtually nonexistent. Haar and Wyard[128] also studied the response of suspended particles with radii on the order of a few microns to a combination of acoustic, hydrodynamic, gravitational and diffusion forces.

3.4- Conclusion

The central focus of this research is the ability to concentrate particles in aqueous suspensions. The acoustic forces experienced by the particles were detailed. Viscous and thermal dissipative mechanisms were accounted for. Expressions for the primary acoustic force on a particle in a planar and cylindrical wave field are presented. Differences in acoustic force exerted on particles in the direction normal to the transducer face versus parallel to the

transducer face were predicted. Rotational forces on nonspherical particles due to the acoustic field were also described.

4-EXPERIMENTAL

The previous chapter dealt with the acoustic forces exerted on particles in a standing wave. The focus of this chapter rests on the quality evaluation and imaging of particle concentration. An experimental parametric evaluation of effects on concentration quality, speed, and relative stability is described.

Several experimental methods are used to investigate the concentration within the tube. The primary technique and the subject of this chapter utilize microscopic imaging. Power evaluations are performed to determine input power thresholds for the exhibition of various behaviors. I also investigated the effect of spatial and phase relationships for multiple transducer excitation of the tube on concentration quality and speed. Several aspect ratios and tube types are evaluated. Qualitative particle size effects are also determined. Two methods are used in the visualization process. In the first method, tube is affixed to a microscope slide near the edges of the slide. The slide is placed horizontally on a standard transmission stereomicroscope stage.

4.1-Method 1

Although the concentration pattern in the tube could be seen by eye,

observation of individual 10-micron particles required magnification. Two techniques were used for imaging the concentration pattern during the course of the research. The first technique utilized an Olympus BX41 bottom-illuminated microscope and 1280 x 1024 12-bit Cooke 235X50553 digital camera, set up as diagrammed in Fig. 4-1. The liquid flowed through the tube parallel to the table. The tube is glued at its ends to a microscope slide, for ease of mounting. A diagram of the microscope setup is displayed in Fig. 4-1A. A picture of the microscope and tube is visible Fig. 4-1B.

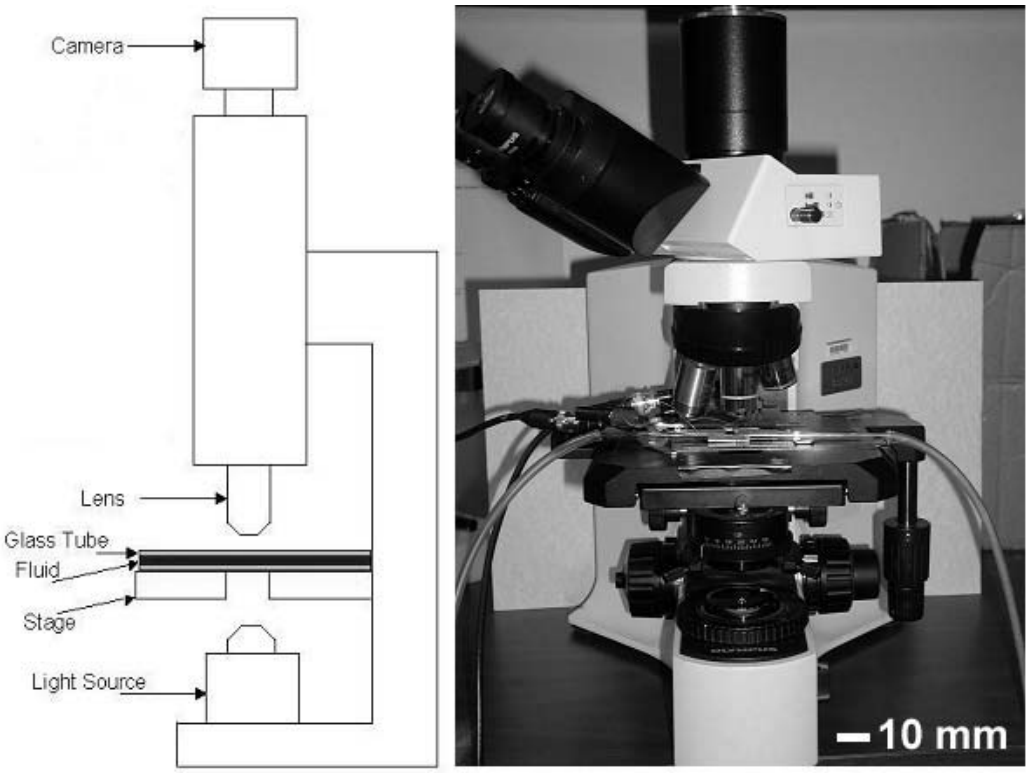

Figure 4-1(A)Diagram of bottom-illuminated microscope used to image the concentration pattern in tube.(B) Frontal picture of bottom illuminated stereo microscope

A section of 12 cm long soft glass tube is affixed to the microscope slide. Tygon tube is press-fit over approximately 1cm on each end of the tube for inflow and outflow of the particle suspension. Experiments were performed with both stationary and constant flow of the particle suspension. Typical flow rates were between 10-15 centimeters per second. The tube was driven at 0.8-0.9W of electrical power and 417 kHz to concentrate over a

10cm length with a single drive transducer. The concentration pattern, exemplified Fig. 4-2b, took approximately 5 seconds to form from an initially homogeneous suspension similar to that shown in Fig. 4-2a. Larger particles visible in the micrograph are agglomerations of particles.

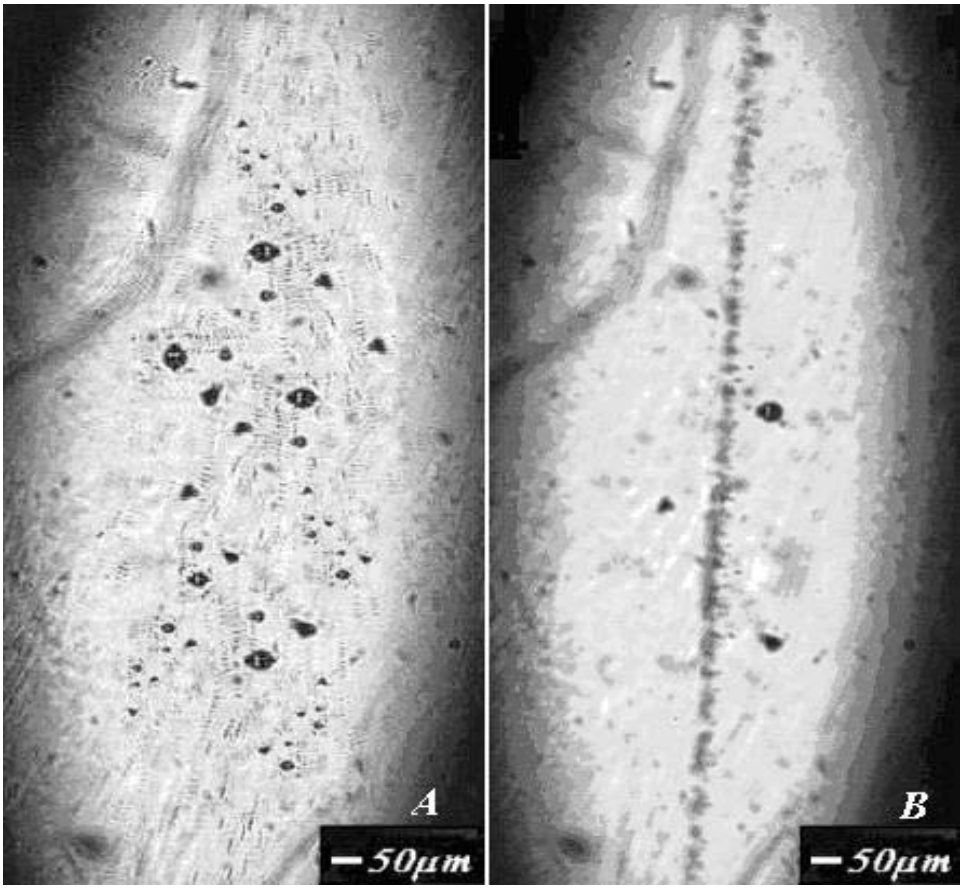

Figure 4-2 (A) Micrograph of un-concentrated 10-micron particles in soft glass tube. (B) Micrograph of concentrated 10-micron particles in soft glass tube.

As can be seen in Fig. 4-2b, the concentrating line is only a few

particle diameters across. The particles are ten microns in diameter. Various concentrations of beads ranging from 0.02% to 0.2% by weight were investigated. No significant differences are observed in concentration times, but higher concentrations of particles also showed increased agglomeration. The agglomerations are driven to the center faster than individual particles due to the larger acoustic force. This effect could potentially be useful for accelerating the concentration process. The agglomerations did not disassociate to individual particles at power levels less than 1W, well above the threshold of particle concentration. If this technique is used, the concentrated agglomerations can be quickly separated from the suspending fluid, then subjected to higher field strengths to recover individual particles. Alternately, a small amount of surfactant would significantly reduce aggregation of particles.

A section of thick-walled quartz tube, designated QQ was obtained for comparison with the soft glass tube. As with soft glass, particles are fed through the quartz tube and the concentration pattern at the predicted coupled dipolar resonance of 435 kHz was imaged using the bottom-illuminated microscope. A micrograph of the concentration pattern is shown in Fig. 4-3. As can be seen in the micrograph, the dipole does indicate a frequency at which concentration takes place and furthermore, the

concentrated particles did form a narrower line in the quartz as compared to the soft glass tube for the same power input of approximately 0.1W. The differences could be explained by either better transducer/tube coupling in quartz due to the larger radius of curvature, or mass loading effect on soft glass. Replacement of the drive transducers on both types of glass tube with narrower, and thereby less massive transducers did not affect the tightness of concentration. Furthermore, minimization of air bubbles in glue used for transducer attachment led to better concentration within the tube, thus confirming the importance of coupling. Coaxial alignment was found to be less important than the bond quality. The relative lower importance could attributed to the small variation in quality of cyanoacrylate glue joints inherent to surface-moisture curing glues. Small deviations in transducer angle with tube surface, up to approximately 25 degrees showed negligible effect on concentration quality. Angular vibration amplitudes supported this assertion, further emphasizing the importance of energy coupling into the tube.

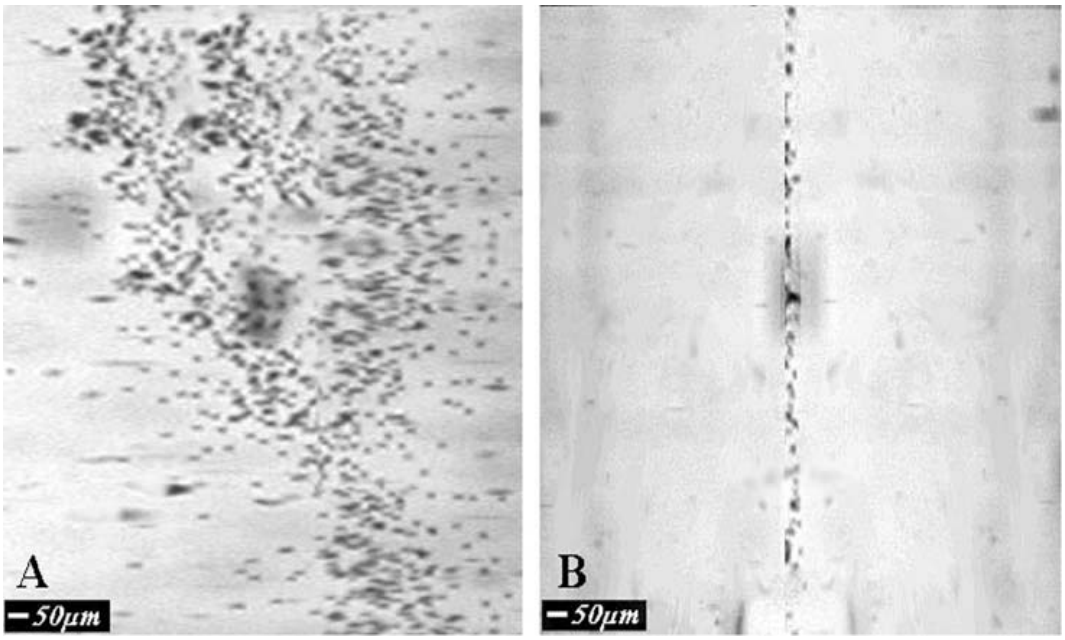

Figure 4-3 (A) Micrograph of un-concentrated 10-micron particles in QQ quartz tube. (B) Micrograph of concentrated 10-micron particles in QQ quartz tube.

4.2-Method 2

The narrow depth of field and limited range of motion available with the stereomicroscope made it necessary to find an alternative means of imaging the particles in the tube. The second imaging process used three finger clamps with foam inserts to assure non-rigid clamping. To replace the stereomicroscope, a Model KC Infinity Optics long distance microscope objective lens is attached to the Cooke camera, which is then mounted to an XY positioner on a Velmax MB2515WIJ54E linear slide for positioning. In

these experiments, the camera is positioned using Superior Electronics M062-LS09 stepper motors shown in Fig. 4-4, attached to a Velmax VP9000 controller, shown in Fig. 4-5.

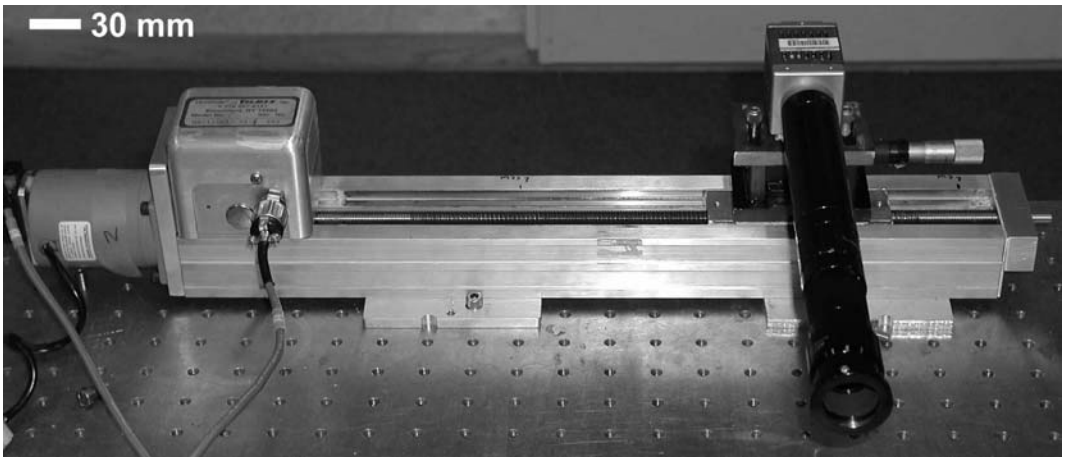

Figure 4-4. Picture of linear scanning stepper motor with long distance lens on CCD camera.

Figure 4-5. Picture of Velmex VP9000 stepper motor controller.

Fine adjustments to the position and focus were made using the XY stage. The tube is mounted using three finger clamps or foam-lined optics

mounts. The linear slide stepper motor is scanned manually using the hand control visible in the upper left portion of Figure 4-5. Commercial software accompanying the Cooke camera is used to capture single frame pictures and multi-frame movies. As with the stereomicroscope experiments, still and constant flow cases are investigated. Single images are taken without flow to allow resolution of individual particles for aesthetic rather than technical reasons. Two types and two aspect ratios of glass were imaged using the distance microscope. The additional freedom of motion conferred by the range of the linear slide removed the tube length limitations on imaging.

Vertical and horizontal drive orientations were tried with approximately equal success. The main differences arose due to greater acoustic force exerted perpendicular to the face of the transducer. Suspension of particles against gravitational settling required less power when the horizontally aligned tube is driven perpendicular to the table.

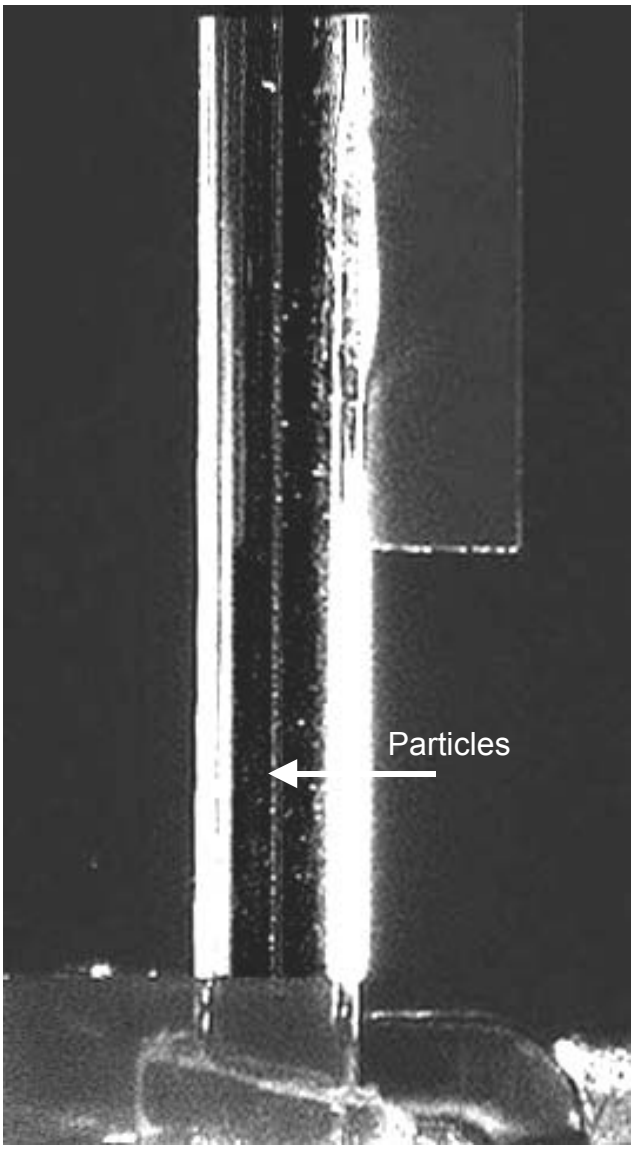

Figure 4-6. Concentrated particles in soft glass at 417 kHz with distance microscope.

Figure 4-6 shows a typical concentration pattern in a soft glass tube taken using the distance microscope. The single driving transducer can be

seen on the upper right side of the image. The transducer is approximately 3mm in thickness; the tube has an outer diameter of 4mm. The line down the center of the tube is approximately 25 microns in diameter, consisting of acoustically concentrated 10-micron polystyrene beads. The three finger clamp is visible at the bottom of the image. A standard desk lamp is used for illumination. As before, the transducer is driven at the soft glass resonance of 417 kHz. The soft glass tube is approximately 12 cm long.

4.3-Orientation

Longer sections of tube were characterized in a horizontal orientation. The tube is mounted on vertical mirror mounts using foam lined optical angle brackets. A typical setup is shown Figure 4-7. The optical mounting rods on either end of the tube incorporated a gear rack for rack and pinion vertical adjustment. The rods are mounted to XY stages to allow three-axis fine adjustment. Tubes ranged in length from 30 to 42cm based on availability. Particles, 3.5% by volume in deionized water are passed through the tube from right to left. At the dipole resonance of the coupled system consisting of the structure and cavity, the particles are observed to concentrate on the central axis along the entire length of the tube.

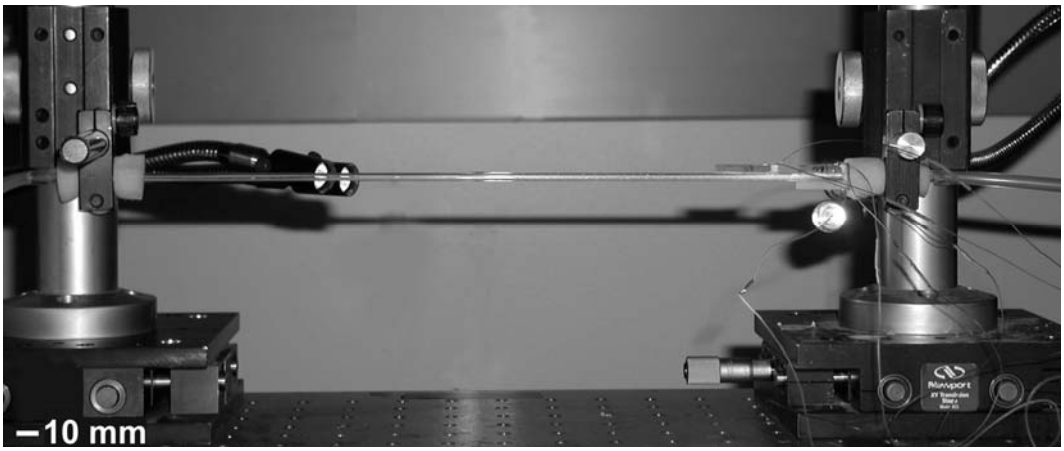

Figure 4-7. Foam lined optical mounting method for distance microscopy.

Figure 4-7 specifically shows a 40cm section of soft glass. Three transducers are visible on the right side of the tube. Another transducer is attached orthogonal to the other three, but is hidden in the photograph by the tube. Initially only one transducer was driven. A typical concentration pattern in soft glass is displayed in Fig. 4-8. The pattern took approximately five seconds to form at 0.25 watts and 417 kHz. The imaging point is 15 cm down axis from the drive transducer. The particles concentrated with approximately equal radial deviation for the entire visible length of the tube. No perturbation is seen to occur due to the foam inserts used for clamping of the tube. Acoustic concentration is only nominally faster in the region adjacent to the transducers, with almost simultaneous concentration throughout the tube. The progression to tighter concentration appeared logarithmic in time.

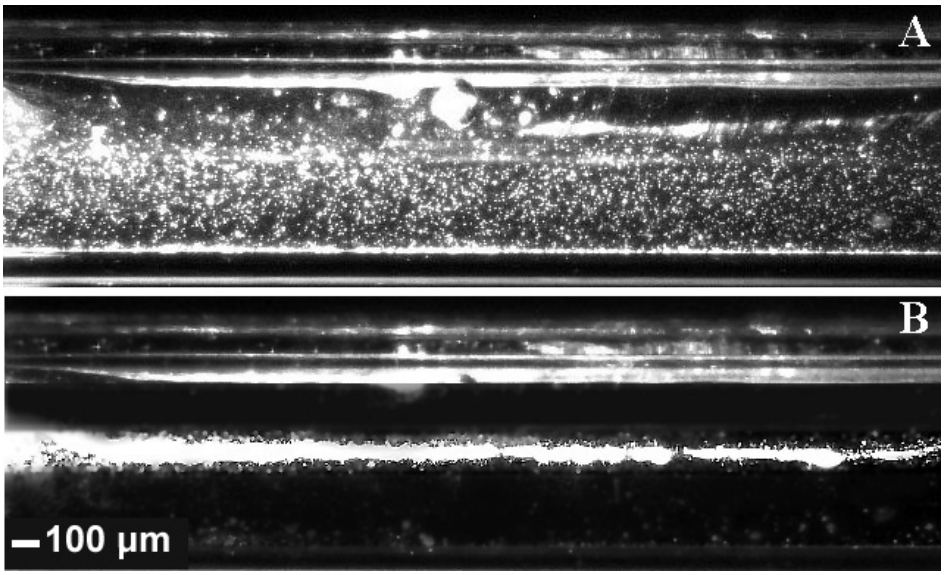

Figure 4-8. (A) Micrograph of un-concentrated 10-micron particles in soft glass tube. (B) Micrograph of concentrated 10-micron particles in soft glass tube

The tube was also imaged when the particles suspended in the fluid were passed through the cavity at approximately 25m m/second. A typical pattern is presented in Fig. 4-9.

It was predicted, in chapter 3, the coupled dipole mode would yield a tighter concentration pattern normal to the transducers and faster particle movement to the pressure node along the normal axis, than along the axis parallel to the transducer face. The horizontal geometry provided a method for verification of that assertion through determining the required input power for concentration and prevention of sedimentation. Balancing acoustic force

opposite gravity such that once a concentration pattern formed, it remained stable against gravitational settling provided a quantitative method of correlating electrical input power to acoustic radiation pressure on the particles suspended in the fluid-filled cavity. Diagrams of the two alignment directions of the excitation transducer are displayed in figure 4-9A and 4-9B. Orientation of the drive transducer parallel to the table required 0.12W of electrical power to prevent sedimentation and yield the concentration pattern shown in Fig. 4-10. When the transducer is aligned perpendicular to the table such that the transducer normal is parallel to the gravitational force, 0.086W of electrical power is required to concentrate and maintain suspension. A micrograph is presented in Fig. 4-11. As can be seen in the micrographs, the particle spread is greater when the transducer is aligned and driven parallel to the tabletop than when it is driven perpendicular to the table.

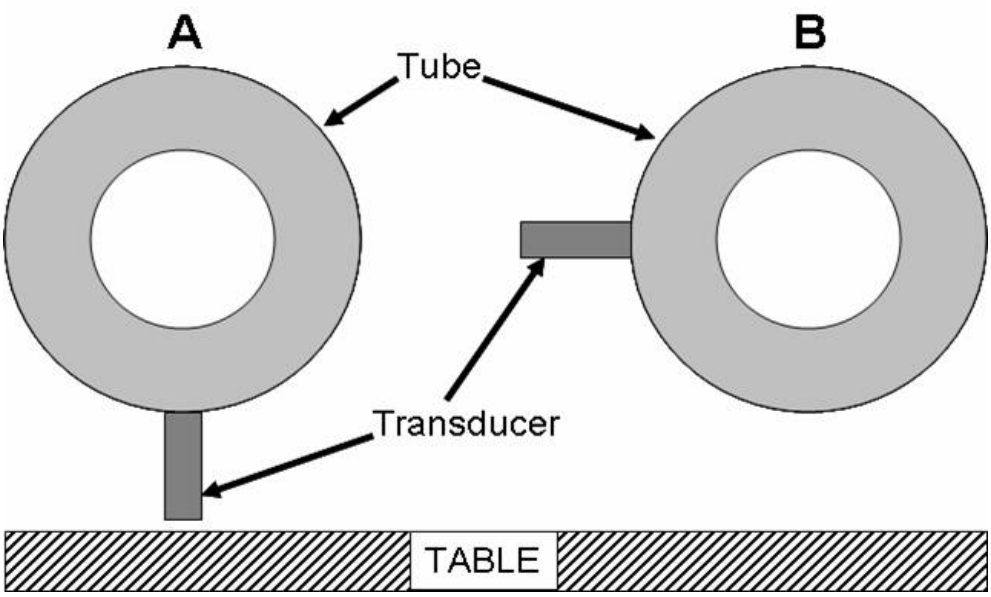

Figure 4-9. Diagram of alignment directions (A) Perpendicular to table . (B) Parallel to table.

No difference is observed between driving downward versus upward. Additionally, power consumption is approximately 27% lower when the drive transducer is perpendicular to the table. It could therefore be argued that the model prediction is supported by the experimental results.

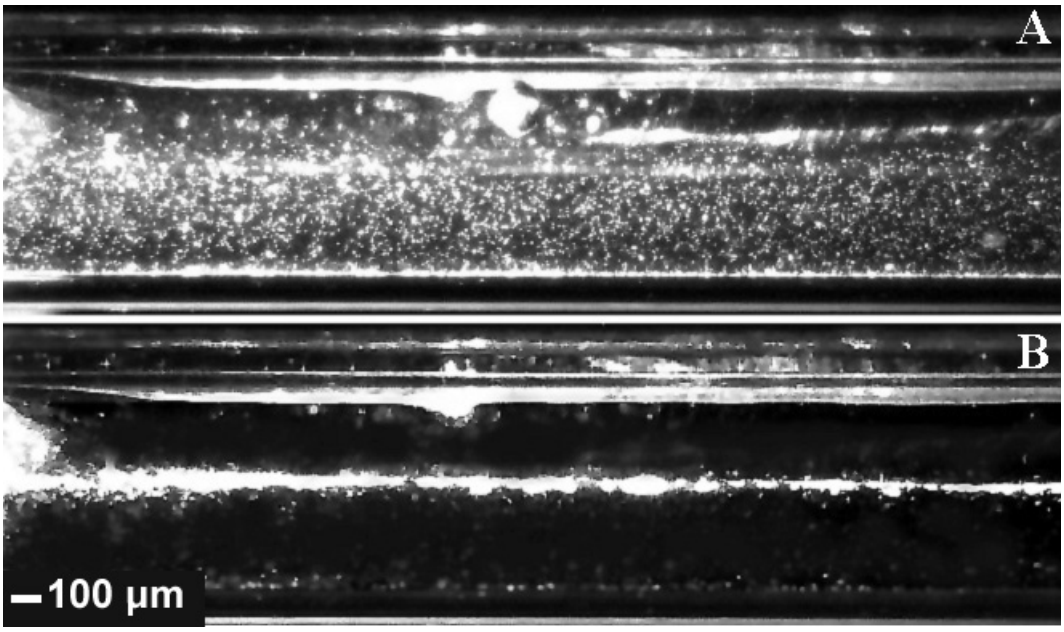

Figure 4-10. (A) Micrograph of un-concentrated 10-micron particles in soft glass tube. (B) Micrograph of concentrated 10-micron particles in soft glass tube. (Both) After five seconds 15cm from drive transducer parallel to the table.

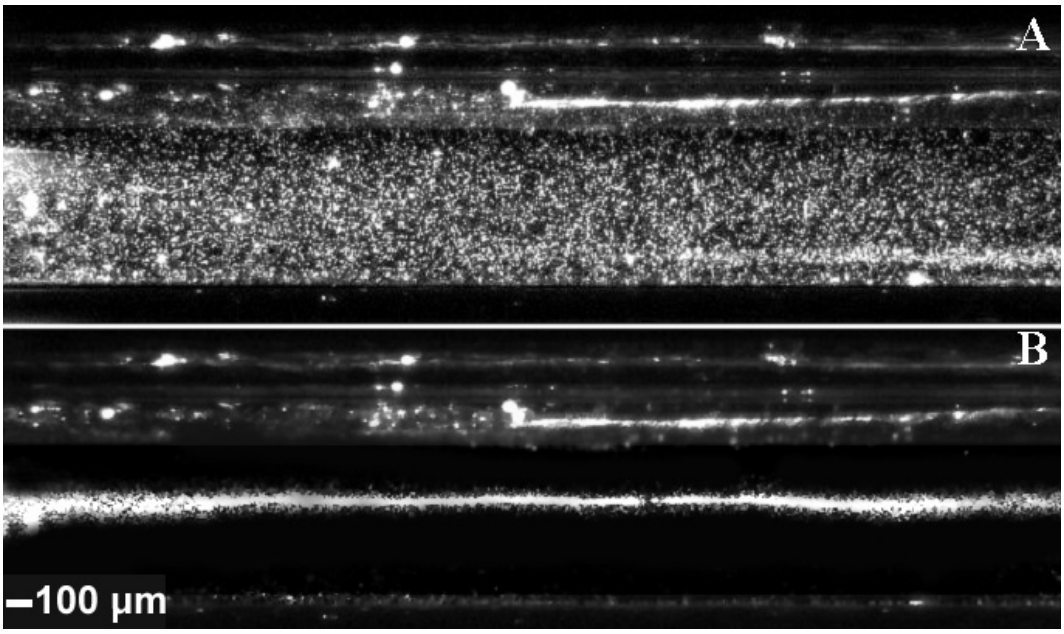

Figure 4-11. (A) Micrograph of un-concentrated 10-micron particles in soft glass tube. (B) Micrograph of concentrated 10-micron particles in soft glass tube. (Both) After five seconds 15cm from drive transducer perpendicular to the table.

4.4-Axial Standing Wave

When the tube is driven for longer periods of time, or at higher powers, another concentration pattern is observed. The line broke into discrete nodes along the central axis of the tube. The most likely cause of the nodal character is a weakly coupled standing wave along the cylinder central axis. This would cause some energy to be pumped into the mode but unless power or experiment duration is increased, the particles did not separate into nodes during the course of the experiment. Figure 4-12a showed a typical

nodal pattern. Excitation frequency, naturally, is observed to affect the nodal spacing. tube length and end clamping conditions are also observed to change the nodal spacing. An o-ring is placed at a nodal and an anti-nodal position on the tube in hopes of determining the perturbative effect of changing the outer boundary conditions. Figure 4-12b and Figure 4-12c present the micrograph results of that investigation.

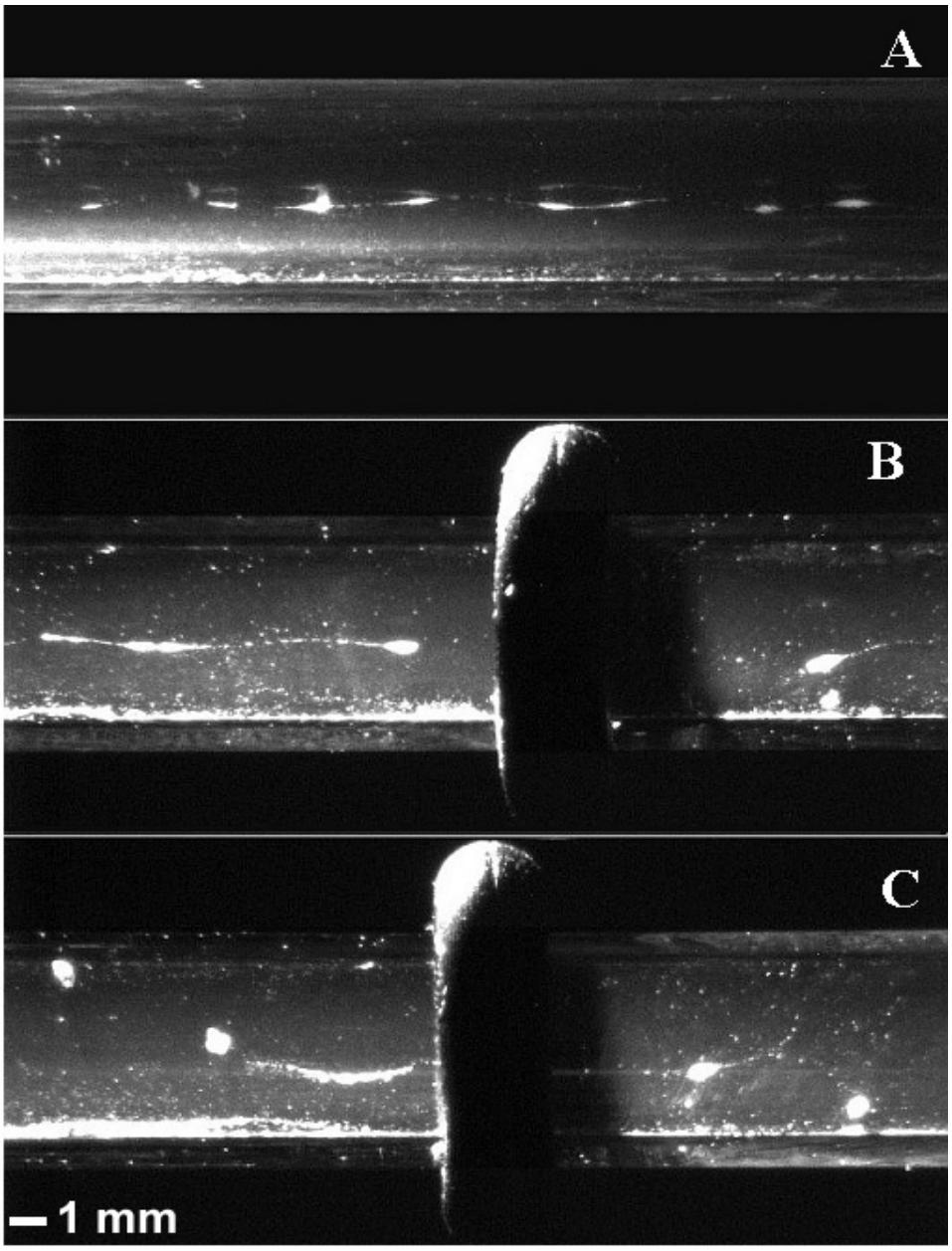

Figure 4-12. (A) Micrograph of nodal concentrated 10-micron particles in soft glass tube. (B) Micrograph of nodal perturbation by an o-ring on soft glass tube. (C) Micrograph of anti-nodal perturbation of an o-ring

on soft glass tube.

When the o-ring is placed at a nodal position, several of the neighboring nodes are partially converted back into the central linear pattern with some remnants of the unperturbed nodal spacing. Conversely, when the o-ring is placed at an anti-nodal position, the particles remained concentrated in nodes, but are distributed to central and wall positions. While the concentration to nodes at 0.12W of electrical power took approximately 30 seconds, the effect of the perturbation is seen almost immediately. As expected, with the exception of directly in front of the drive transducer, the o-ring affected concentration throughout the whole tube.

4.5-Vortex Formation

Stable concentration is observed until approximately 1.17W to 2W. If the electrical power is increased suddenly, the lower limit is applicable; slower ramping of input power allowed up to 2W before degrading to a series of vortices. A typical vortex pattern is shown in Fig. 4-13.

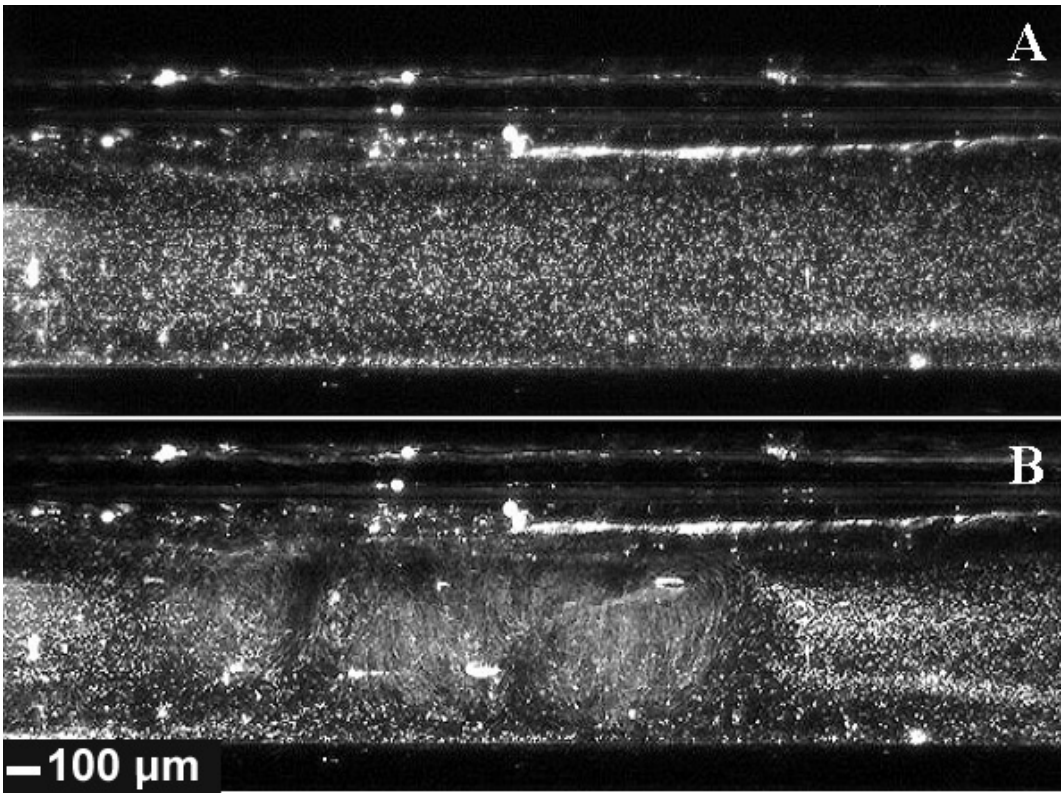

Figure 4-13. (A) Micrograph of un-concentrated 10-micron particles in soft glass tube. (B) Micrograph of vortices in soft glass tube.

Higher power input continued forming vortices until sufficient heating of the transducer occurred, inducing thermal convective currents and eventual boiling of the fluid or melting of the glue used to attach the transducer to the tube. Power limits for heating are dependent on effectiveness of cooling mechanisms. Figure 4-14 presents the creation and propagation of vortices in soft glass. The time delay between the sequential frames is about 2ms. Unlike the vortices in Fig. 4-13, the concentration

pattern had already partially formed when the threshold power is exceeded, thus providing slightly better contrast of the vortices.

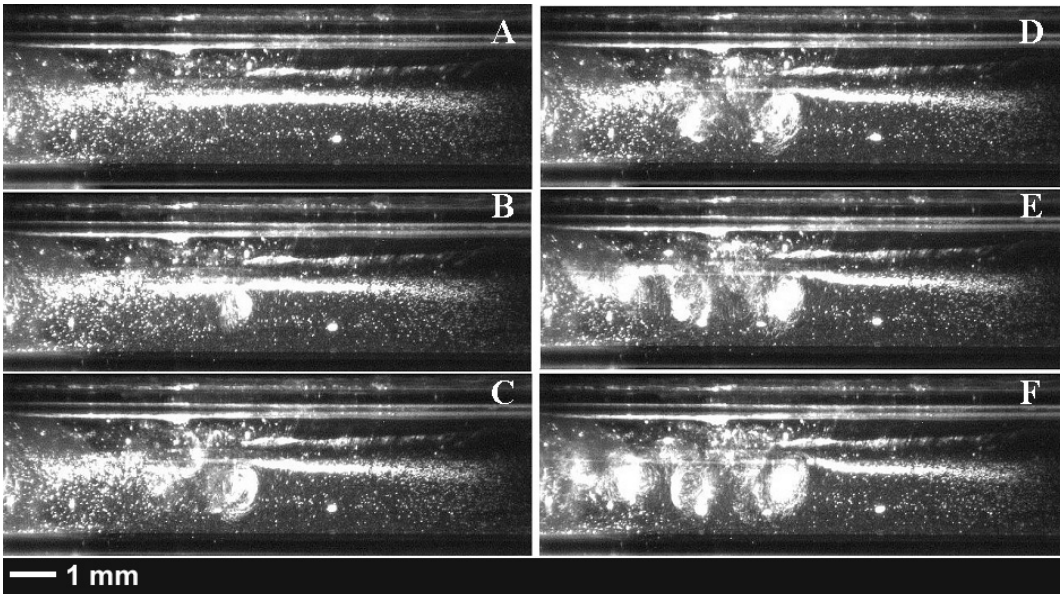

Figure 4-14. (A-F) Steps in creation and spreading of vortices of 10-micron particles in soft glass tube. Approximately 2 milliseconds between frames.

4.6-Material Dependence

Two other types of glass with similar radial dimensions were characterized for comparison with the soft glass. The first of these is a 43cm section of borosilicate glass also known as regular glass, designated RG. It possessed a coupled structure-cavity dipole resonance at 380 kHz as predicted by theory and experimentally verified. A similar arrangement of four

transducers as used for the soft glass case is utilized. Figure 4-15A presents a typical initial homogeneous distribution of particles within the tube, as imaged with the distance microscope. Figure 4-15B displays a typical concentration pattern as photographed approximately 20 seconds after application of the ultrasonic field.

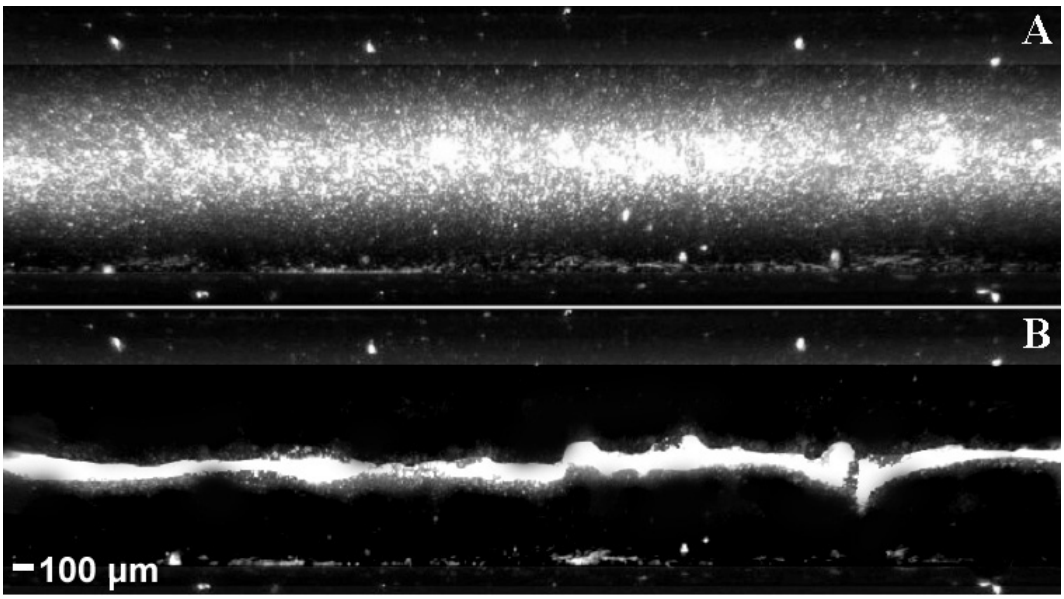

Figure 4-15. (A) Micrograph of un-concentrated 10-micron particles in borosilicate glass tube. (B) Micrograph of concentrated 10-micron particles in borosilicate glass tube.

As can be seen in the micrographs, the concentration pattern exhibited a semi-nodal character. This is caused by larger agglomerations of particles. Some axial forces are present, causing a “wavy” appearance to the pattern, but unlike later investigations, there did not appear to be any

appreciable axial standing wave. As in the soft glass case, the power limits for initial particle concentration to first vortex appearance are measured. Regular glass required 450mW of electrical power to initiate concentration within the tube. Relatively uniform concentration is observed until the input power approached about 1.2W, at which point vortices became visible within the cavity. As with the soft glass case, the vortices propagated throughout the tube, destroying the concentration pattern. When the electrical power is ramped up quickly, a lower threshold of approximately 900mW-1W is capable of inducing vortices. The higher electrical power thresholds are probably due to the mismatch between the resonance of the system and the resonance of the driving transducers.

4.7-Aspect Ratio

The tubes characterized thus far are of comparable radial dimensions. For comparison, a 42cm long section of thicker walled quartz was investigated. It had a similar inner radius to the other tubes, but had double the wall thickness. The coupled dipole resonance is located at 435 kHz, identical to the thin quartz tube, which indicated the greater importance of inner radius on the frequency of concentration. A similar arrangement of four transducers as in the soft glass case is attached to one end of the tube. As

before, the electrical power dependence of the concentration pattern from minimum formation electrical power to maximum electrical power before dissociation was investigated. Figure 4-16 displays a comparative plot at three electrical power levels. Figure 4-16A was taken as a reference at 0W input electrical power. When the electrical power is increased to approximately 102mW, the linear pattern shown in Fig. 4-16B began to form. Approximately 30 seconds elapsed between initial application of the field to a homogeneous suspension such as shown in Fig. 4-16A to the concentration shown in Fig. 4-16B at 102mW of electrical power. Figure 4-16C presents a distance micrograph of the pattern induced by electrical power levels greater than approximately 0.32W. The particles concentrated into distinct nodal positions. It could be argued that nodal concentration is also evidenced Fig. 4-16B, however, the particles did not form distinct nodes before settling occurred. The only reliable demarcation of linear versus nodal concentration occurred at 0.32W.

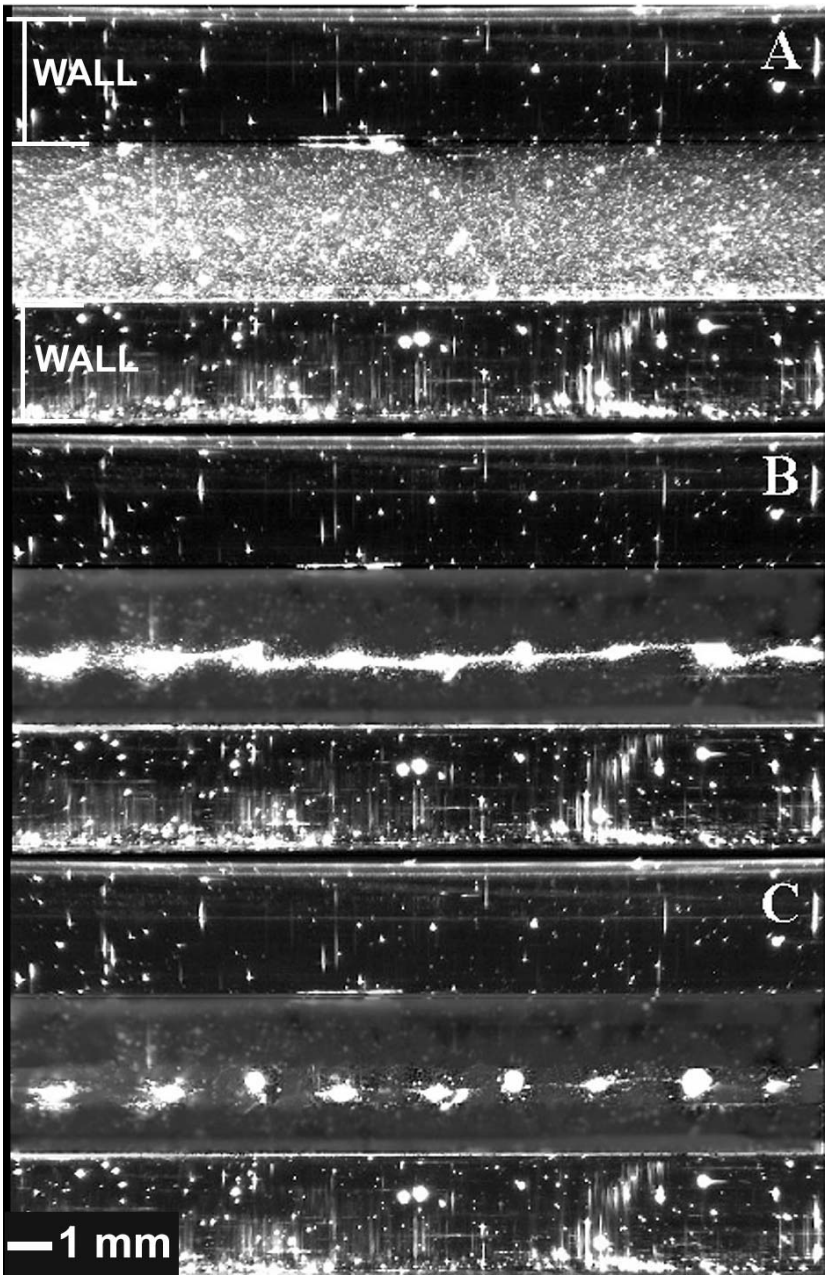

Figure 4-16. Distance micrographs of tube at three electrical power levels. (A)No power input (B) 102mW (C) 320mW.

The horizontal geometry again provided a method for verification of the assertion through determination of the required input electrical power for concentration and prevention of sedimentation. Sedimentation is prevented with 516mW of input electrical power to the drive transducer when the drive transducer is parallel to the table. Orientation of the transducer perpendicular to the table required 168mW of input electrical power to prevent sedimentation. The larger electrical power requirements for the thick quartz tube as compared to the soft glass tube could have been explained by several factors. Since the quartz is thicker, any attenuation of the signal within the glass would be magnified. The larger mass probably also required greater energy to excite the structural modes of the tube.

It was observed that the thick quartz had a very prominent elliptical cross-section and large number of bubble occlusions in the quartz walls of the tube. To investigate the importance of coupling versus system symmetry, one side of the tube was flattened to approximately one-half of the wall thickness as shown in Fig. 4-17 to determine the magnitude of dipole perturbation by asymmetries. The transducer, visible at the bottom of the picture is affixed to the rounded side of the tube directly across from the flattened portion to maintain left-right symmetry of the system. Neither minimum electrical power input for concentration nor resonance frequency

changed significantly when the quartz was flattened until the wall thickness at the flat face of the tube became less than about 75% of the inner tube diameter. No difference is observed from flattening the entire length of tube versus tapering from round to flat along the length of the tube. Although not shown in Fig. 4-17, a drive transducer is also placed on the flat face of the tube for determination of coupling effects. Required minimum input electrical power for concentration dropped to approximately 90mW when the flat portion of the tube is equal-to or greater-than the width of the driving transducer. This would be expected based on the previously observed sensitivity of concentration speed and quality to transducer-tubing coupling efficiency.

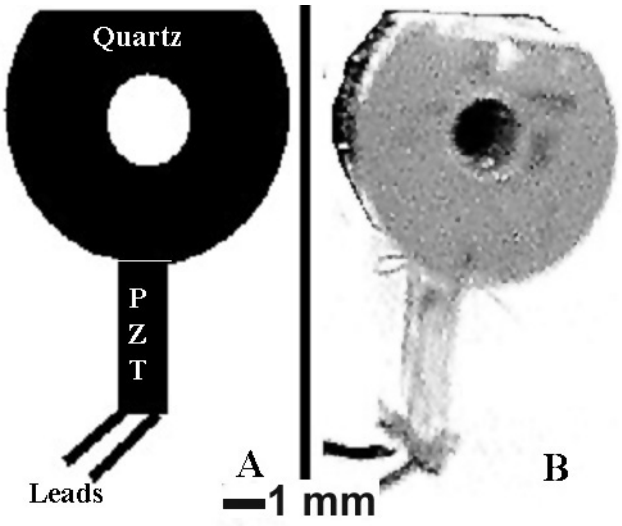

Figure 4-17. (A) Diagram of flattened thick quartz (QQ) tube. (B) Micrograph of flattened thick quartz (QQ) tube.

The benefits of the observed relative weak dependence on perturbations to the symmetry of the tube are threefold. First, the circularity and tolerances on the tube could be loosened with no deleterious effects. Next, the tube could be modified to allow for reproducible and more efficient coupling of drive transducers to the system. Third, while optical probing through the internal cylindrical fluid-tubing boundary still remains, the cylindrical lens effect of the outer boundary of the tube could apparently be eliminated through preparing optically flat external tube walls while still maintaining the coupled system dipole resonance conditions, as long as drive symmetry is maintained.

4.8-Particle Size Dependence

A 50cm section of thin walled quartz tube, designated TQ was characterized for further comparison. The coupled system dipole resonance of the TQ tube is at 435 kHz, again theoretically predicted and experimentally verified. A similar arrangement of four transducers as in the soft glass and regular glass cases was attached to one end of the tube. As before, the power dependence of the concentration pattern from minimum formation electrical power to maximum electrical power before dissociation was investigated. Two sizes of particles were investigated: 10 micron and 3.5 micron. Both types of particles concentrated and formed vortices at the same electrical power levels. Two main differences are observed between the two sizes of particles. The first of these is increase of the concentration time when 4-micron particles are substituted for 10-micron particles. Second, the concentration line for the 4-micron particles is wider than the 10-micron particles. Both of these effects could be explained by noting the proportionality of the acoustic force on the particles to their volume. Approximate time of concentration is about 3 seconds for 10-micron particles and 80 seconds for 4-micron particles. The spatial spread of the line of particles is about 3 to 4 particle diameters for 10-micron particles and about 15 particle diameters for 4-micron particles. The relative closeness of the two

spatial deviations is probably due to particle agglomeration and consequent greater force on the particles. Figure 4-18 displays a comparative plot of typical homogeneous distribution before application of the ultrasonic field and typical concentration pattern. Figure 4-18A is taken at 0W input power. When the electrical power is increased to approximately 88mW, the linear pattern shown in Fig. 4-18B begins to form. Approximately 30 seconds elapsed between initial application of the field to a homogeneous suspension such as shown in Fig. 4-18A to the concentration shown in Fig. 4-18B at 88mW of electrical power.

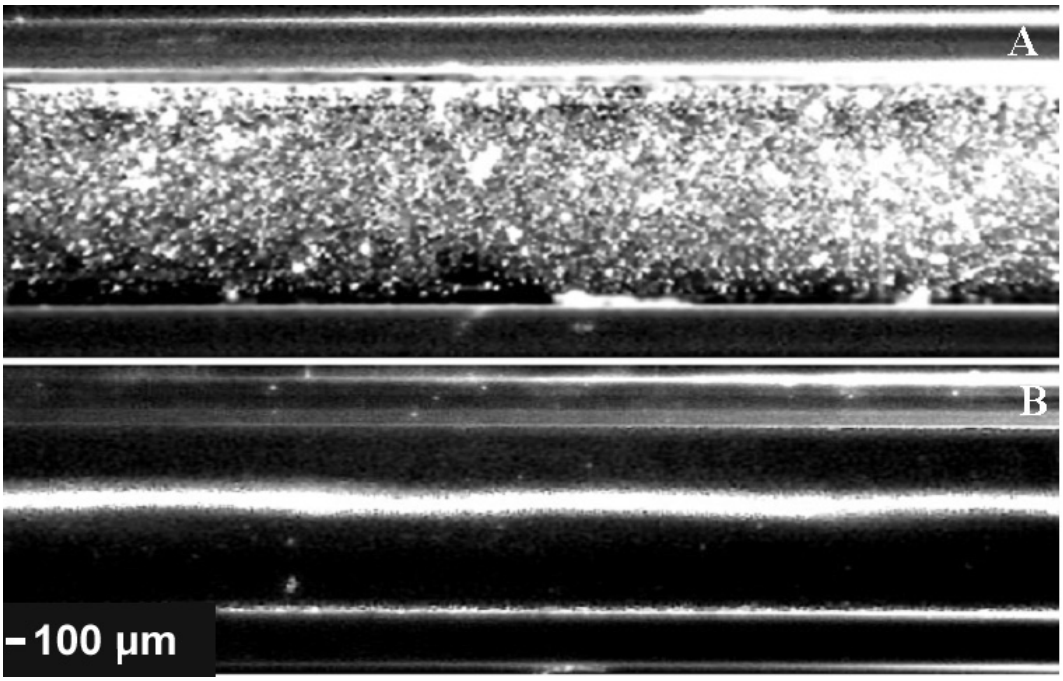

Figure 4-18. (A) Micrograph of un-concentrated 4-micron particles in thin quartz tube. (B) Micrograph of concentrated 4-micron particles in thin quartz tube.

No vortices are observed at higher electrical power levels, the concentration simply dissociated above approximately 500mW. As before, I determined the required input electrical power for concentration and prevention of sedimentation. Orientation of the drive transducer parallel to the table required 110mW of electrical power to prevent sedimentation. When the tube is aligned perpendicular to the table such that the transducer normal is parallel to the gravitational force, 74mW of electrical power is required to concentrate and maintain suspension. No difference is observed

between driving downward versus upward.

For the four types of tube characterized so far, all of the inner diameters are approximately the same. Each has coupled dipole resonances between 380 kHz and 435 kHz. The particular resonance of each tube is highly dependent on the inner diameter of the tube. A section of glass capillary tube 100mm long was selected for comparison. The inner and outer diameters are 1mm and 1.1mm respectively. Following the previous assertion, it would be expected that with a halving of the inner diameter would induce a requisite doubling of the resonance frequency.

Experimentally, the resonance is found at 841 kHz. The thickness resonance of the transducer was tuned to around 860 kHz. Using the method of Kwiatkowski and Marston[129], the predicted shift in frequency due to concentration of particles from a homogeneous suspension is 3.8 kHz for 10-micron particles, but only 0.022 kHz for 1-micron particles. Experimentally observed frequency shifts are 3 kHz for 10-micron particles and 0.02 kHz for 1-micron particles. Figure 4-19A presented the initial homogeneous distribution of 1-micron particles. A typical linear concentration pattern is shown in Fig. 4-19B. Due to the tighter curvature of the tube, and small size of the particles, only agglomerations of several 1-micron particles are optically resolved in the micrograph. Unlike previous tube, only two

transducers are attached to the tube; they are placed opposite one another. One of the drive transducers attached to the capillary tube was cut at an angle such that the thickness varied slightly over the length of the transducer. The angular transducer exhibited a much wider bandwidth and lower Q than it's rectangular mate on the opposite side of the capillary tube. When the angular transducer is driven, the concentration pattern yielded possessed an axial component, as shown in Fig. 4-19C. Each pattern took approximately 4-5 seconds to form from an initially homogeneous suspension.

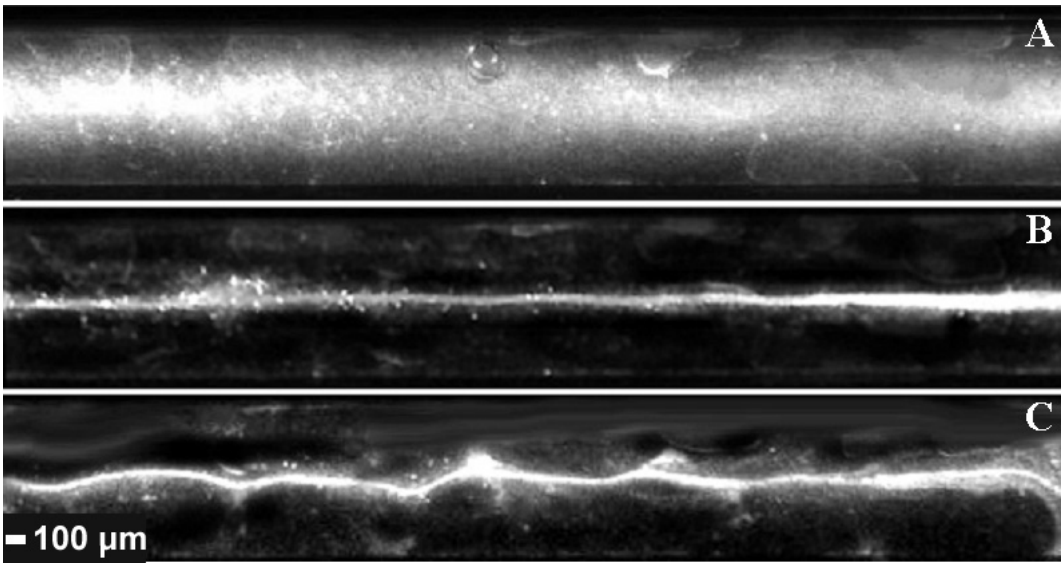

Figure 4-19. (A) Micrograph of un-concentrated 10-micron particles in glass capillary tube. (B) Power level 1 in glass capillary tube (C) Power level 2 in glass capillary tube.

The particle distributions of 1-micron particles observed in the glass

capillary tube are comparable to the 10-micron particle concentration patterns seen in the soft glass and thick quartz tube, and much sharper than the 4-micron particle distribution seen in thin quartz tube. This is expected due to the higher frequency structure-cavity coupled dipole resonance of the capillary tube. Slightly smaller inner diameter tube would be expected to exhibit even tighter concentration of 1-micron particles due to the cubic frequency dependence of acoustic radiation pressure. The tube would exhibit a fundamental lower scaling limit. If the particle size is kept constant while the tube diameter is decreased, a point would be reached when the particles would significantly perturb the cavity and the long wavelength limit could not be assumed. Conversely, if the particle size is decreased below a micron, Brownian motion would begin to dominate over acoustic radiation pressure, as mass decreased and the acoustic force exerted on the particle would drop in proportion to the particle volume.

4.9-Fluid Selection

Water was the medium of choice for these experiments for its ease-of-handling, abundance and ease of application to flow cytometry. However, it should be noted that the fluid used in our acoustic concentration apparatus is not limited to water. As proof of the applicability of the method to other

suspending fluids, reagent grade 4-propanol was used to suspend 0.25% by volume 10-micron polystyrene beads. As is expected, the replacement of water with 4-propanol caused a change in the coupled dipole resonance frequency in TQ quartz from 435 kHz to 446 kHz. A typical initial homogeneous suspension and concentration pattern are displayed in Fig. 4-20.

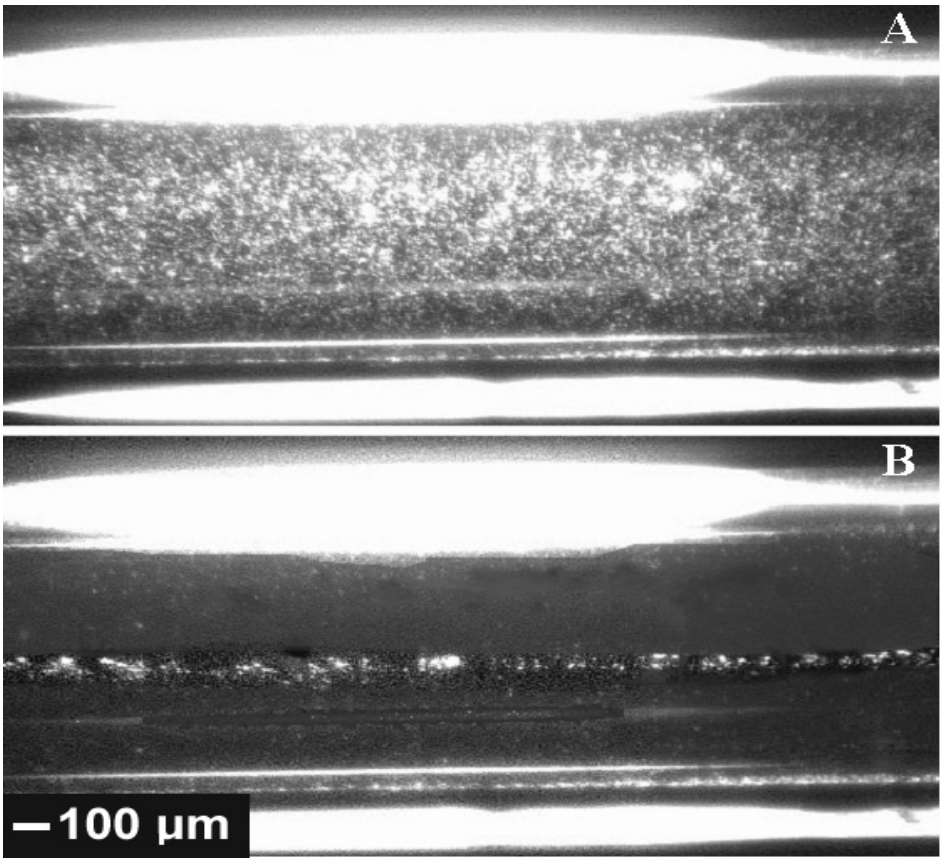

Figure 4-20. (A) Micrograph of un-concentrated alcohol-suspended 10-micron particles in thin quartz tube. (B) Micrograph of concentrated alcohol-suspended 10-micron particles in thin quartz tube.

The pattern shown in Fig. 4-20B took approximately 10 seconds to form from an initially homogenous distribution similar to that shown in Fig. 4-20A. Minimum input electrical power to achieve particle concentration is 10mW. No upper limit to applied power was observed, in that no vortex formation occurred up to the 35W power limit of the RF amplifier. A

reasonable explanation for this behavior is the greater acoustic impedance mismatch of both particles with fluid and fluid with walls. The fluid/particle acoustic contrast ratio is 880% larger for 2-propanol as compared to water. The increased contrast between the fluid and particles led to a lower power concentration threshold through greater acoustic force exerted on the particles, while the fluid-wall impedance mismatch led to less efficient coupling of energy from the wall into the liquid. Larger particles in the micrograph are agglomerations of particles. Although for aesthetic reasons, the tube is pictured horizontally, the tube was vertical for this experiment.

4.10-Multiple Transducers

The next set of experiments investigated the effect of driving pairs of transducers in several relative spatial and phase relationships. The motivation and results to the position and phase relationships for the investigation could be explained by the dipole and quadrupole modes diagrammed in Fig. 4-21a and 21b respectively. Figure 4-21a is the externally rigidly bound (1,1) Bessel mode; Figure 4-21b is the externally rigidly bound (2,1) Bessel mode. Vertical amplitude represented the displacement amplitude within the cavity demarcated by the circular external boundary. It can be observed that the opposite sides of the cavity would be

180 degrees out of phase in the dipole mode, and in-phase in the quadrupole mode, which occurred at a higher frequency than the coupled dipole resonance. These assertions are confirmed by the multiple transducer excitation experiments. As discussed in a previous chapter, the dipolar coupled mode is preferred for particle concentration, a point that is further confirmed by the results discussed above.

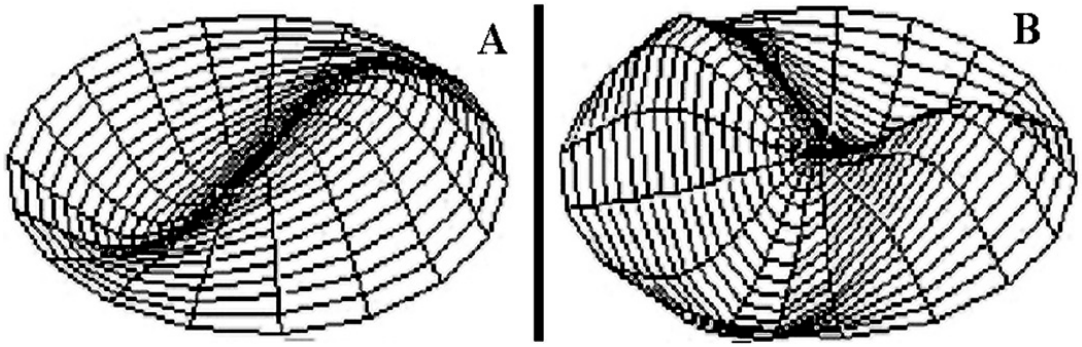

Figure 4-21. Diagram of (A) Dipole (B) Quadrupole vibrational modes.

A photograph of the apparatus used for the experiments is displayed in Fig. 4-22. Transducers on the same side and in-line with each other showed minimum power consumption when driven in phase with each other. When separately driven transducers are placed with their ends within 10mm of each other in-line, vortices are created in front of and between the transducers when the sum of the power input into each transducer exceeded

the threshold established with one transducer for the tube. When the distance between the transducers is greater than 10mm, vortices only appeared in front of each transducer. Vortices reproducibly appeared at the same points each time they are induced and reoccurred at approximately one-wavelength intervals along the axis. Neighboring vortices rotated counter to each other. Rayleigh streaming provides the most likely explanation for this behavior. No acoustic streaming of less than or greater than one wavelength scale is observed. When coaxial, collinear transducers are excited at 180 degrees out of phase, no particle concentration is observed between or in front of the transducers, but is present outside of this region.

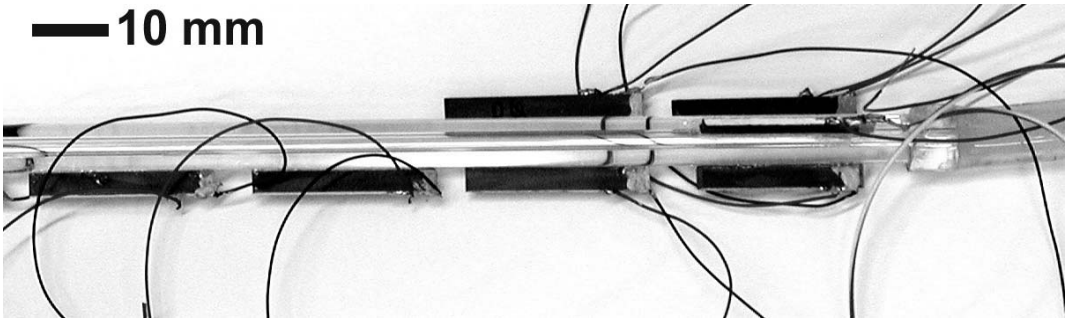

Figure 4-22. Photograph of thick quartz tube used for multiple transducer spatial and temporal relationship investigation.

Transducers on opposite sides, even when axially offset, yielded the greatest efficiency when driven 180 degrees out of phase with one another.

Again, the sum of input power to each transducer is required to be less than the vortex threshold for stable particle concentration to occur. When the transducers are at 90 degrees, driving the transducers at a phase relationship of other than 90 degrees relative phase causes destructive interference between the driven transducer signals and hence reduction in concentration quality. Driving at 90 degrees relative phase exhibited much weaker concentration than the coaxial, collinear or coaxial, opposing transducer arrangements.

For the spatial and phase relationship investigation above, the power input into the two transducers was identical. When one of the transducers is driven at a significantly greater power level, the same effects are visible, but power levels are not additive in the induction of vortices. Another assumption made in the above multiple transducer investigation described in the previous section was identical frequency for the driven transducers. When the transducers are driven at different frequencies, the power differences became most evident. The transducer with slightly higher power dominated the standing wave, and thus the quality of concentration. Additionally, a traveling wave is generated along the tube central axis that served to drive the particles along the axis of the tube. Very little sum and difference frequency generation is observed. Power consumption is equal to or greater

than the single driven transducer case for any of the multiple source trials. Concentration speed and quality improved only when the distantly separated transducers matched the local resonances of the tube and the phase relationships described above are obeyed.

4.11-Conclusion

Two microscopy methods were utilized to image the concentration pattern. Four types of tube, three sizes of particles, and two types of fluid were utilized in the process of the investigation.

The tube-cavity coupled dipole resonance of the tubes is shown to efficiently concentrate particles to the central axis of the tube. Additionally, it was demonstrated that the inner diameter of the tube was the dominant factor in determining the frequency of coupled dipole resonance. Perturbations to the exterior of the tube only appeared to affect axial standing waves. Coupling quality of the transducer to the tube is shown to be the primary factor in concentration speed and quality.

An investigation of the efficacy of multiple transducer excitation of the tube was performed. The results demonstrated a 180-degree phase difference between the opposite sides of the tube down the entire length of tube at concentration resonances, further supporting the hypothesis of dipole

dominance in generating concentration. Driving transducers down the length of the tube collinearly did not increase concentration quality, but did increase concentration speed. Driving multiple transducers generated greater power consumption. The primary benefit of collinear drive transducers is the avoidance of vortices or thermal convection at higher input powers. No limitation was observed to structural excitation distance with a single transducer. The vibration phase, when no axial standing wave is present, remained the same down the length of the tube.

It is shown both theoretically, in chapter 3, and experimentally, in the present chapter, that greater acoustic forces are exerted on the particles perpendicular to the face of the drive transducer along the phase symmetry line along the normal to the transducer face as compared to parallel to the transducer face. An investigation of limitations on excitation power demonstrated critical points beyond which vortex formation significantly disturbed the concentration pattern. Axial standing waves manifestation occurred at any power level capable of concentration, so long as the necessary power is reached for maintaining suspension. Powers at which thermal convection or cavitation occurred exceeded the power necessary to induce vortices in the fluid.

An investigation was performed into the experimental limitation on

particle size for concentration. Since the force on the particles is proportional to the cube of the product of the particle radius and the wavenumber, smaller particles would concentrate slower than larger particles at the same frequency. As expected, decreasing the chamber radius thereby increasing the resonant frequency, or increasing particle size consequently increased acoustic radiation pressure on the particles. .

Changing the suspending fluid from water to isopropanol, and thereby the acoustic contrast ratio 880% between the fluid and the particles caused an expected shift in resonant frequency while slightly lowering the necessary input power for particle concentration. The expected lowering of power consumption is less than expected based on the fluid-particle concentration ratio most likely due to the change in acoustic contrast between the fluid and the structure.

5-INHERENT LIMITATIONS

5.1-Introduction

The limitations of concentration by structural excitation inherent in the method arise predominately through: acoustic contrast ratio, higher power disruptive effects, cavity size/excitation frequency, thermal resonance perturbation, and particle resonance perturbation. The inherent limitations on the method are discussed in order of magnitude with contrast ratio having the greatest effect and particle resonance perturbation having the least. Methods for extending the usable range of the method will also be discussed.

5.2-Acoustic Contrast Ratio

The acoustic contrast ratio consists of four terms corresponding to the four acoustic forces on particles in the field; density contrast, compressibility contrast, viscosity contrast, and thermal conductivity contrast respectively. The first term is familiar from King; the compressibility term was put forth separately but equivalently by Yosioka and Kawasima, and Gorkov. Danilov[101,102] introduced the fluid viscosity compensation term, which was later modified by Doinikov to include force contribution of the viscosity contrast between the fluid and the particles. Doinikov[102-105] also introduced

the last term to account for thermal dissipative effects.

Doinikov obtained the full expressions for acoustic force by solving for the linear scattering coefficients for a particle of arbitrary radius, density, compressibility, thermal conductivity, and viscosity including both viscous and thermal dissipative mechanisms. Equations 5.1 through 5.6 describe the motion and thermodynamics of a viscous heat-conducting fluid. The variables are as follows: v, ρ, and p are the fluid velocity, density, and pressure respectively. Absolute temperature is expressed as T, s is the specific entropy, κ represents thermal conductivity of the fluid , δ_{ik} is the Krohnecker delta, η and ξ are shear and bulk viscosity of the fluid respectively. Summation of repeated indices is implied. The sound speed in the fluid is represented by c, C_p is the specific heat of the fluid at constant pressure, γ is the ratio of specific heats of the fluid, and α represented the coefficient of volumetric thermal expansion of the fluid.

$$\frac{\partial}{\partial t}(\rho v_i) = \frac{\partial}{\partial x_k}(\sigma_{ik} - \rho v_i v_k) \tag{5.1}$$

$$\frac{\partial \rho}{\partial t} + \frac{\partial}{\partial x_i}(\rho v_i) = 0 \tag{5.2}$$

$$\rho T\left(\frac{\partial s}{\partial t} + v_i \frac{\partial s}{\partial x_i}\right) = (\sigma_{ik} - \rho \delta_{ik}) \frac{\partial v_i}{\partial x_k} + \frac{\partial}{\partial x_i}\left(\kappa \frac{\partial T}{\partial x_i}\right) \tag{5.3}$$

$$\sigma_{ik} = -p\delta_{ik} + \eta\left(\frac{\partial v_i}{\partial x_k} + \frac{\partial v_k}{\partial x_i} - \frac{2}{3}\frac{\partial v_j}{\partial x_j}\delta_{ik}\right) + \xi \frac{\partial v_j}{\partial x_j}\delta_{ik} \tag{5.4}$$

$$d\rho = \left(\frac{\gamma}{c^2}\right) dp - \alpha \rho \, dT \tag{5.5}$$

$$ds = \left(\frac{C_p}{T}\right) dT - \left(\frac{\alpha}{\rho}\right) dp \tag{5.6}$$

The stress tensor for a perfect fluid can be expressed in terms of first order quantities. Solving for an imperfect fluid requires solution of the time-averaged equations of the fluid motion to accuracy in the second-order terms of the incident wave amplitude. Doinikov chose to approach the problem by first solving in the linear approximation and then, after averaging over time, determining the solutions in the second approximation. The velocity could be separated into the scalar(ψ) and vorticity(Ψ) velocity potentials of first order as

$$v^{(1)} = (\nabla \psi^{(1)} + \nabla \times \Psi^{(1)}) \tag{5.7}$$

The incident sound field is assumed to possess temporal variation of the form, $e^{i\omega t}$. If no vorticity is present in the incident field, then the general form of the first-order solution after linearizing can be expressed in terms of the scalar velocity potential and temperature as

$$\psi_I^{(1)} = e^{-i\varpi t} \sum_{n=0}^{\infty} A_n j_n \left(\frac{\omega}{c\sqrt{\beta_3}} r \right) P_n(\cos\theta) \tag{5.8}$$

$$T_I^{(1)} = \frac{i\beta_3(\beta_1 - \frac{\omega^2}{c^2\beta_3})}{\omega\alpha} \psi_I^{(1)} \tag{5.9}$$

$$\beta_1 = \frac{\gamma\omega^2\rho}{1 - i\omega\gamma(\xi + \frac{4\eta}{3})} \tag{5.10}$$

$$\beta_2 = \frac{i\omega\sqrt{\rho C_p}(\rho c^2\gamma + 1 - i\omega\gamma(\xi + \frac{4\eta}{3}) - \rho c^2)}{\sqrt{\kappa}\gamma(1 - i\omega\gamma(\xi + \frac{4\eta}{3}))} \tag{5.11}$$

$$\beta_3 = \frac{1 - i\omega\gamma(\xi + \frac{4\eta}{3})}{\rho c^2} \tag{.(5.12)}$$

Equations 5.8 through 5.12 describe the transmission of an acoustic wave through a viscous heat-conducting fluid when inclusions such as particles are absent, and thus describe the incident acoustic wave and

possess a subscript I. The function $P_n(\cos(\theta))$ is the associated Legendre polynomial. The equations also included a spherical Bessel function j_n.

The scattered wave is described as written in equations 5.13 through 5.18. The equations contain spherical Hankel functions of the first kind and a vortical component. The coefficients α_{1n}, α_{2n}, and α_{3n} are the dimensionless linear scattering coefficients, determined by the boundary conditions at the particle surface, and the conditions of continuity of velocity, stress, temperature, and heat flux. Although, some of the material properties such as viscosity, thermal conductivity and volumetric thermal expansion coefficient show a weak temperature dependence, they are assumed to be independent of temperature for small temperature variations.

$$\psi_S^{(1)} = \sum_{n=0}^{\infty} \frac{A_n\left(\alpha_{1n} h_n^{(1)}(k_3 r) + \alpha_{2n} h_n^{(1)}\left((1+i)\sqrt{k_2} r\right)\right) P_n(\cos\theta)}{e^{i\omega t}} \tag{5.13}$$

$$T_S^{(1)} = \sum_{n=0}^{\infty} \frac{i\beta_3 A_n\left((\beta_1 - k_3^2)\alpha_{1n} h_n^{(1)}(k_3 r) + (\beta_1 - 2ik_2)\alpha_{2n} h_n^{(1)}\left((1+i)\sqrt{k_2} r\right)\right) P_n(\cos\theta)}{\omega\alpha_0 e^{i\omega t}} \tag{5.14}$$

$$\Psi_S^{(1)} = \varepsilon \sum_{n=0}^{\infty} \frac{A_n \alpha_{3n} h_n^{(1)}\left((1+i)\sqrt{k_1} r\right) P_n(\cos\theta)}{e^{i\omega t}} \tag{5.15}$$

$$k_1 = \frac{w}{2\nu} \tag{5.16}$$

$$k_2 = \frac{w\rho C_p}{2\kappa} \tag{5.17}$$

$$k_3 = \frac{\omega}{c\sqrt{\beta_3}} \tag{5.18}$$

By time averaging equations 5.1 through 5.3, Doinikov obtained equations 5.19 through 5.21, which describe stationary temperature distribution and acoustic streaming.

$$\eta\Delta\left\langle v^{(2)}\right\rangle=\rho\left\langle v^{(1)}(\nabla\cdot v^{(1)})+(v^{(1)}\cdot\nabla)v^{(1)}\right\rangle-(\xi+\frac{\eta}{3})\nabla(\nabla\cdot\left\langle v^{(2)}\right\rangle-\nabla\left\langle p^{(2)}\right\rangle \tag{5.19}$$

$$\nabla\cdot\left\langle v^{(2)}\right\rangle=-\frac{1}{\rho}\nabla\cdot\left\langle p^{(1)}v^{(1)}\right\rangle \tag{5.20}$$

$$\kappa\Delta\left\langle T^{(2)}\right\rangle=\left\langle(\rho T^{(2)}+T\rho^{(1)})\frac{\partial s^{(1)}}{\partial t}\right\rangle+\rho T\left\langle v^{(1)}\cdot\nabla s^{(1)}\right\rangle$$

$$-(\xi+\frac{2\eta}{3})\times\left\langle(\nabla\cdot v^{(1)})^2\right\rangle-\frac{\eta}{2}\left\langle(\frac{\partial v_i^{(1)}}{\partial x_k}+\frac{\partial v_k^{(1)}}{\partial x_i})^2\right\rangle \tag{5.21}$$

The time-averaged velocity could be broken into fluid velocity in the absence of the particle and velocity of the acoustic streaming arising around the particle as written in Eq. 5.21. The fluid flow defined by the velocity in the absence of the particle, v_I gives rise to an analogue to Stokes' drag force arising from acoustic streaming. The scattered field can be written in terms of the scalar and vorticity velocity potentials of the acoustic streaming as

$$\left\langle v^{(2)}\right\rangle=\left\langle v_I^{(2)}\right\rangle+\left\langle v_S^{(2)}\right\rangle \tag{5.22}$$

$$\left\langle v_S^{(2)}\right\rangle=\nabla\Phi+\nabla\times\Psi \tag{5.23}$$

Axial symmetry of the problem dictated that the vorticity velocity potential of acoustic streaming must be of the form $\Psi=\mathbf{e}_\varepsilon f(r,\theta)$ and thus the divergence of Ψ equals zero. The expressions for Φ and Ψ are

$$\Delta\Phi = -\frac{1}{\rho_0}\nabla\cdot\left\langle \rho^{(1)} v^{(1)} \right\rangle_{IS+SS} \tag{5.24}$$

$$\Delta\Psi = -\frac{1}{\nu_0}\nabla\times\left\langle v^{(1)}(\nabla\cdot v^{(1)}) + (v^{(1)}\cdot\nabla)v^{(1)} \right\rangle_{IS+SS} \tag{5.25}$$

After solving for the velocity potentials, Doinikov obtained an expression for radiation force on a sphere in a fluid. The results are summarized in equations 5.26 through 5.29, where F is the total force, F_r is the radiation force on the particle, F_d is the drag force due to acoustically generated fluid flow in the absence of the particle, R_0 is the equilibrium particle radius, v_{lz} is the acoustically-driven fluid velocity in the absence of particles, η is the coefficient of shear viscosity of the liquid, and the subscripts f and p refer to the fluid and particle respectively.

$$F = F_r + F_d \tag{5.26}$$

$$F_r = \pi \frac{3}{2} \rho_f \sum_{n=0}^{\infty} \frac{n+1}{(2n+1)(2n+3)} \times \left(Z_n A_n A^*_{n+1} + Z^*_n A^*_n A_{n+1} \right) \tag{5.27}$$

$$F_d = 3\pi\eta_f R_0 \int \left\langle v^{(2)}_{Iz} \right\rangle \Big\|_{r=R_0} \sin\theta d\theta - 3\pi\rho_f \left| x_1 \right|^2 \tag{5.28}$$

$$\times \sum_{n=0}^{\infty} \frac{n+1}{(2n+1)(2n+3)} \times \mathrm{Re}\left\{ \frac{A_n A^*_{n+1}}{x_3^2} \left[x^*_1 \left| j'_n(x_1) \right|^2 + x_1 \left| j'_{n+1}(x_1) \right|^2 \right] \right\}$$

$$Z_n = \sum_{j=1}^{3} \left(F_n^{(0j)} \alpha^*_{jn+1} + F_n^{(j0)} \alpha_{jn} \sum_{k=1}^{3} F_n^{(jk)} \alpha_{jn} \alpha^*_{kn+1} \right) \tag{5.29}$$

The function Z_n is defined in Eq. 5.29. The exact expressions for F_n, expressed in equations 5.30 through 5.44, below, hold true for any values of x_1, x_2, or x_3.

$$F_n^{(01)} = \frac{1}{2}\left[X_n^{(11)}(x_1, x_1) + X_n^{(21)}(x_1, x_1) \right] \tag{5.30}$$

$$F_n^{(02)} = \frac{1}{2}\left[X_n^{(11)}(x_1, x_2) + X_n^{(21)}(x_1, x_2) \right] \tag{5.31}$$

$$F_n^{(03)} = \frac{1}{2}\left[Y_n^{(110)}(x_1) + Y_n^{(210)}(x_1) \right] \tag{5.32}$$

$$F_n^{(10)} = \frac{1}{2}\left[X_n^{(11)}(x_1, x_1) + X_n^{(12)}(x_1, x_1) \right] \tag{5.33}$$

$$F_n^{(11)} = X_n^{(11)}(x_1, x_1) \tag{5.34}$$

$$F_n^{(12)} = X_n^{(11)}(x_1, x_2) \tag{5.35}$$

$$F_n^{(13)} = \left[Y_n^{(110)}(x_1) \right]^* \tag{5.36}$$

$$F_n^{(20)} = \frac{1}{2}\left[X_n^{(11)}(x_2, x_1) + X_n^{(12)}(x_2, x_1) \right] \tag{5.37}$$

$$F_n^{(21)} = X_n^{(11)}(x_2, x_1) \tag{5.38}$$

$$F_n^{(22)} = X_n^{(11)}(x_2, x_2) \tag{5.39}$$

$$F_n^{(23)} = \left[Y_n^{(110)}(x_2) \right]^* \tag{5.40}$$

$$F_n^{(30)} = \frac{1}{2}\left[Y_n^{(101)}(x_1) + Y_n^{(201)}(x_1) \right] \tag{5.41}$$

$$F_n^{(31)} = Y_n^{(101)}(x_1) \tag{5.42}$$

$$F_n^{(32)} = \left[Y_n^{(101)}(x_2) \right]^* \tag{5.43}$$

$$\begin{aligned} F_n^{(33)} = {} & n(n+2)\{(n+1)x_3^2\left[H_{n\ n+1}^{(011)}(x_3, x_3) - H_{n\ n+1}^{(211)} \times (x_3, x_3) \right] \\ & + ix_3^2\left[H_{n+1\ n}^{(011)}(x_3, x_3) - H_{n+1\ n}^{(211)} \times (x_3, x_3) \right] \\ & + (n+1)\left[h_n^{(1)}(x_3)(h_n^{(1)\prime}(x_3))^* + ((h_{n+1}^{(1)}(x_3))^* h_{n+1}^{(1)\prime}(x_3) \right]\} \end{aligned} \tag{5.44}$$

The variables x_1, x_2, or x_3 are defined as

$$X_1 = \frac{\omega\sqrt{\rho_f p}}{\sqrt{\rho_f {c_f}^2 - \omega\gamma_p(\varepsilon_f + \frac{4}{3}\eta_f)}} \quad (5.45)$$

$$X_2 = \frac{(1+i)\sqrt{\eta_f \rho_f C}}{\sqrt{2\kappa_f c_f}} \quad (5.46)$$

$$X_3 = \frac{(1+i)\sqrt{\varpi}}{\sqrt{2\upsilon}} \quad (5.47)$$

where the identities of the other variables are, ω is angular frequency, ρ_f is fluid density, η_f refers to fluid shear viscosity, c_f is fluid sound speed, κ_f is thermal conductivity, C is isobaric specific heat, γ_f is the specific heat under constant pressure divided by the specific heat at a constant volume.

The functions X and Y are defined in terms of H functions in Cartesian coordinates as

$$
\begin{aligned}
X_n^{(kl)}(x,y) = {} & \frac{1}{2}(ny^{2*} - (n+2)x^2)\left[H_n^{(0kl)}{}_{n+1}(x,y) - H_n^{(2kl)}{}_{n+1} \times (x,y)\right] \\
& + ixy^*\left[H_{n+1\,n}^{(0kl)}(x,y) - H_{n+1\,n}^{(2kl)} \times (x,y)\right] \\
& + \frac{y^{2*} - x^2}{(k_3 R_0)^2}\left[ny^* H_n^{(1kl)}{}_n(x,y) - xy^* H_{n+1\,n}^{(0kl)} \times (x,y) + (n+2)xH_{n+1\,n+1}^{(1kl)}(x,y)\right] \\
& - \frac{xy^*}{(k_3 R_0)^2}\left[y^* h_n^{(k)}(x)(h_n^{(l)\prime}(y))^* + (xh_{n+1}^{(k)}(x) \times (h_{n+1}^{(l)\prime}(y))^*\right], \\
& k,l = 1,2.
\end{aligned} \tag{5.48}
$$

$$
\begin{aligned}
Y_n^{(jkl)}(x,y) = {} & \frac{n+2k}{2}\{\left[(n+1)x^{2*} - (n+2l)(k_3 R_0)^2\right]\left[H_{n+k\,n+l}^{(01j)}(k_3 R_0, x) - H_{n+k\,n+l}^{(21j)} \times (k_3 R_0, x)\right] \\
& + x^*(k_3 R_0)^2\left[H_{n+k\;\;n+k}^{(-11j)}(k_3 R_0, x) - H_{n+1\,n}^{(11j)} \times (k_3 R_0, x)\right] \\
& - \frac{x^{2*} k_3 R_0}{(k_3 R_0)^2}[H_{n+l\;\;n+l}^{(-11j)}(k_3 R_0, x) - H_{n+l\;n+l}^{(11j)}(k_3 R_0, x)] + 2x^* h_{n+l}^{(1)\prime}(k_3 R_0)(h_{n+l}^{(j)\prime}(x))^*\} \\
& + (n+2k)(-1)^l \times \{x^* k_3 R_0\left[H_{n+k\,n+l}^{(01j)}(k_3 R_0, x) - H_{n+k\,n+l}^{(21j)} \times (k_3 R_0, x)\right] \\
& + \frac{(n+1)x^{2*}}{(k_3 R_0)^2} h_{n+k}^{(1)}(k_3 R_0)(h_{n+k}^{(j)\prime}(x))^* \\
& + \frac{x^{2*}}{(k_3 R_0)^2}[(n+1)x^* H_{n+k\,n+k}^{(11j)} \times (k_3 R_0, x) - (n+2l)(k_3 R_0) H_{n+l\;n+l}^{(11j)}(k_3 R_0, x)]\}, \\
& j = 1,2, k,l = 0,1.
\end{aligned} \tag{5.49}
$$

$$
\begin{aligned}
& H_{mm}^{(jkl)}(x,y) = \int z^{-j} h_n^{(k)}(xz)[h_m^{(l)}(yz)]^* dz, \\
& j = -1,0,1,2, k,l = 1,2.
\end{aligned} \tag{5.50}
$$

Equation 5.50 defines the H function in terms of spherical Hankel functions. The function $h_m^{(k)}$ is the spherical Hankel function of the k-th kind and the prime denotes differentiation.

While the above equations are applicable to a spherical particle of arbitrary radius, density, compressibility, and thermal conductivity, it is instructive to calculate the linear scattering coefficients for the case of a compressible particle much smaller than a wavelength and much bigger than the viscous and thermal wavelengths in the fluid as a means of qualitatively estimating inherent limitations of the method. The resulting equation, derived by Barmatz and Collas[130], for a compressible spherical particle in a cylindrical standing wave is

$$F=-\nabla\left\{2\pi\varepsilon R^3\sum_{n=0}^{\infty}A_n\left\{-\frac{Z_0}{3}\alpha-\frac{Z_1\rho_f}{2}\left[\beta-\varsigma\right]^2\right\}e^{jn\theta}\right\}-\pi\varepsilon\left(\frac{\omega R_0}{c_f}\right)^3\frac{2\eta_f}{\omega R_0^2} \tag{5.51}$$

$$\alpha=J_n^2(k_{rf}r)\cos^2(k_{zf}z) \tag{5.52}$$

$$\beta=\left(\frac{k_r}{\sqrt{k_r^2+k_z^2}}J_{n+1}(k_{rf}r)+\frac{2n}{r\sqrt{k_r^2+k_z^2}}J_n(k_{rf}r)\right)\cos(k_{zf}z) \tag{5.53}$$

$$\varsigma=\frac{k_z}{\sqrt{k_r^2+k_z^2}}J_n(k_{rf}r)\sin(k_{zf}z) \tag{5.54}$$

$$Z_0=\frac{2}{9}\left(\frac{\omega R_0}{c_f}\right)^3\left(\frac{\rho_f c_f^2}{\rho_p c_p^2}-\frac{3}{2+\dfrac{\rho_f}{\rho_p}}-\frac{\sqrt{\dfrac{2\eta_f}{\rho_f\omega}}}{R_0}Z_v^*+\frac{\sqrt{\dfrac{2\kappa_f}{\rho_f C_f\omega}}}{R_0}Z_t\right) \tag{5.55}$$

$$Z_1=\frac{2}{9}\left(\frac{\omega R_0}{c_0}\right)^3\left(\frac{1-\dfrac{\rho_f}{\rho_p}}{2+\dfrac{\rho_f}{\rho_p}}+\frac{\sqrt{\dfrac{2\eta_f}{\rho_f\omega}}}{R_0}Z_v\right) \tag{5.56}$$

$$Z_v=3\left(\frac{1-\dfrac{\rho_f}{\rho_p}}{2+\dfrac{\rho_f}{\rho_p}}\right)^2\frac{(1+i)\left[1+\dfrac{\rho_f}{\rho_p}\sqrt{\dfrac{\eta_f\rho_p}{\eta_p\rho_f}}+\dfrac{2\rho_f}{R_0\rho_p}\sqrt{\dfrac{2\eta_p}{\rho_p\omega}}+2\left(\dfrac{\rho_f}{\rho_p}\sqrt{\dfrac{2\eta_p}{\rho_p\omega}}\right)^2\right]+\dfrac{2i\rho_f}{R_0\rho_p}\dfrac{\eta_f}{\eta_p}\sqrt{\dfrac{2\eta_f}{\rho_f\omega}}}{\left(1+\dfrac{\rho_f}{\rho_p}\sqrt{\dfrac{\eta_f\rho_p}{\eta_p\rho_f}}+\dfrac{\rho_f}{R_0\rho_p}\sqrt{\dfrac{2\eta_p}{\rho_p\omega}}\right)^2+\left(\dfrac{\rho_f}{\rho_p}\sqrt{\dfrac{2\eta_p}{\rho_p\omega}}\right)^2} \tag{5.57}$$

$$Z_t=\frac{3(1+i)\left((\gamma_f-1)\rho_p c_p^2-\dfrac{\alpha_f}{\alpha_p}(\gamma_p-1)\rho_f c_f^2\right)\left(\dfrac{\alpha_f}{\alpha_p}\dfrac{2\kappa_f}{\rho_p C_f\omega}-\dfrac{\kappa_f}{\kappa_p}\dfrac{2\kappa_p}{\rho_p C_p\omega}\right)}{2\rho_p c_p^2\dfrac{\alpha_f}{\alpha_p}\sqrt{\dfrac{2\kappa_f}{\rho_p C_f\omega}}\left(\sqrt{\dfrac{2\kappa_f}{\rho_f C_f\omega}}+\dfrac{\kappa_f}{\kappa_p}\sqrt{\dfrac{2\kappa_p}{\rho_p C_p\omega}}\right)} \tag{5.58}$$

where F_d is defined in Eq. 5.28, and , ω is angular frequency, η refers to shear viscosity, γ refers to the ratio of specific heats, c is sound speed, κ is thermal conductivity, C refers to heat capacity, α refers to coefficient of volumetric thermal expansion, k_r is radial wavenumber, k_z is axial wavenumber, R_0 is particle radius, and ε is energy density of the field in the fluid. The subscripts p and f refer to particle and fluid properties respectively. Viscous effects can be treated as a change in phase and amplitude relations between primary and scattered fields. The number of cross terms makes determination of contrast factor limitations unclear.

The algebraic separability of the planar standing wave system as compared to the inseparability of the cylindrical standing wave system simplifies the analysis of the contrast terms. Although the equations below described a sinusoidal planar standing wave, the same limitations on the contrast terms contained in square brackets remain true for cylindrical standing wave problems. The resulting simplification is

$$F = \pi\rho_f \varepsilon \sin\left(\frac{2\omega d}{c_f}\right)\left[\left(\frac{\omega R_0}{c_f}\right)^3 CF\right] - \pi\varepsilon\left(\frac{\omega R_0}{c_f}\right)^3 \frac{2\eta_f}{\omega R_0^2} \tag{5.59}$$

$$CF = \left(\frac{5\rho_p - 2\rho_f}{3(2\rho_p + \rho_f)} - \frac{c_f^2 \rho_f}{3c_p^2 \rho_p} + \mathrm{Re}(Z_v)\frac{\sqrt{\frac{2\eta_f}{\rho_f \omega}}}{R_0} - \mathrm{Re}(Z_t)\frac{\sqrt{\frac{2\kappa_f}{\rho_f C_f \omega}}}{R_0} \right) \tag{5.60}$$

The four terms in the contrast factor(CF) correspond to the four acoustic forces on particles in the field; density contrast, compressibility contrast, fluid viscosity, and thermal conductivity respectively. The viscous and thermal terms, Z_v and Z_t respectively are defined in equations 5.57 and 5.58.

It can be seen in Eq. 5.59 that the force exerted on the particles is proportional to the cube of the frequency divided by the wavenumber in the suspending fluid multiplied by a term proportional to particle volume. This explains the inability to tightly concentrate 3-micron particles at 417 kHz in thin quartz, but easily concentrate 2-micron particles at 840 kHz in borosilicate capillary tube.

It is instructive to compare the effect of particle material properties to establish applicability limits to this concentration method.

The relative magnitudes of the four acoustic forces are compared individually as the particle density, compressional sound speed, fluid viscosity, thermal conductivity, and heat capacity are varied. Figure 5-1 showed the magnitude of the first two terms in Eq. 5.60 as a function of particle density and compressibility for materials from cork through gold. The medium is assumed to be water. The upper left corner shows a blue region corresponding to particles with densities and compressibilities near that of water. The area above and to the left of the blue region corresponds to materials with negative acoustic contrast, while the area below and to the right of the blue region corresponded to positive acoustic contrast. Negative contrast translates to particles that would be driven pressure antinodes, as they are more compressible and/or less dense than the suspending fluid. Positive contrast translates to particles that would be driven to pressure nodes, as they are less compressible and/or more dense than the suspending fluid. The dark red region in the upper left corner is a gradient, but for ease of visibility of the larger plot, is clipped. The actual magnitudes in that region are approximately ten times larger at the farthest top left corner than the gray bar scale indicated, corresponding to cork. The region below and to the right of the blue region corresponded to plastics, glasses, and metals. Particle materials of industrial interest would be plastics and metals.

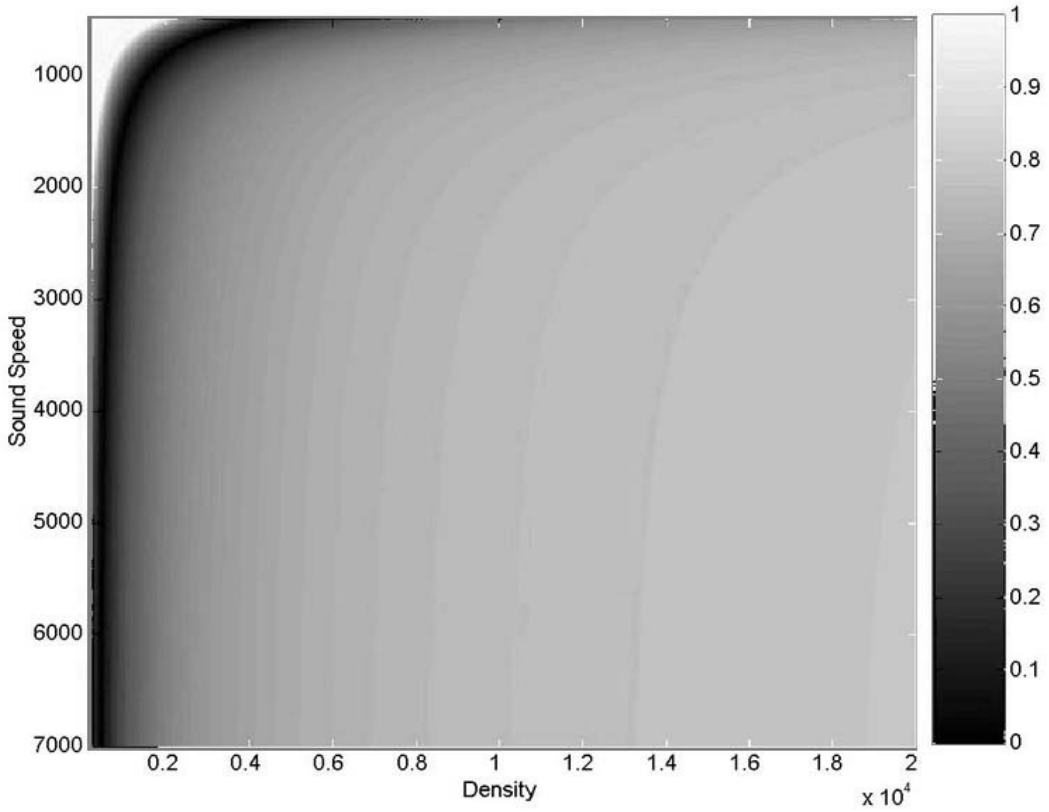

Figure 5-1. Calculations of acoustic contrast factor due to density and compressibility for large range of materials.

Table 5-1 summarizes the material properties of some common solids of industrial interest. The table is grouped into plastics, glasses, and metals separated by double line demarcations. The longitudinal and shear sound speeds are designated C_{long} and $C_{shear.}$. As expected, the acoustic contrast factor is greatest for metals, and least for plastics. The acoustic contrast factor only includes the density and compressibility, not frequency or particle

radius. As can be seen in the figure, the denser and less compressible particles are expected to experience greater acoustic force.

Material	ρ(kg/m^3)	C_{long}(m/s)	C_{shear}(m/s)	Acoustic Contrast Factor
LDPE	920	1950	540	0.0945
HDPE	960	2430	1117	0.1896
Styrene	1050	2400	1120	0.2276
PVC	1380	2380	1094	0.3401
Neoprene	1330	1550	713	0.1928
Polycarbonate	1200	2300	1100	0.276
Pyrex	2320	5640	3280	0.5574
Flint	3880	3980	2380	0.6501
Crown	2240	5100	2840	0.547
Aluminum	2700	6420	3040	0.5923
Copper	8930	5010	2325	0.7505
Gold	19700	3240	1200	0.7926
Lead	11400	1960	690	0.7535
Nickel	8900	6040	3000	0.7513
Silver	10400	3650	1610	0.7592
Steel	7900	5960	3220	0.7414
Titanium	4500	6070	3125	0.6789
Zinc	7100	4210	2440	0.7288

Table 5-1. Table of common material properties, and relative acoustic contrast factor values to water.

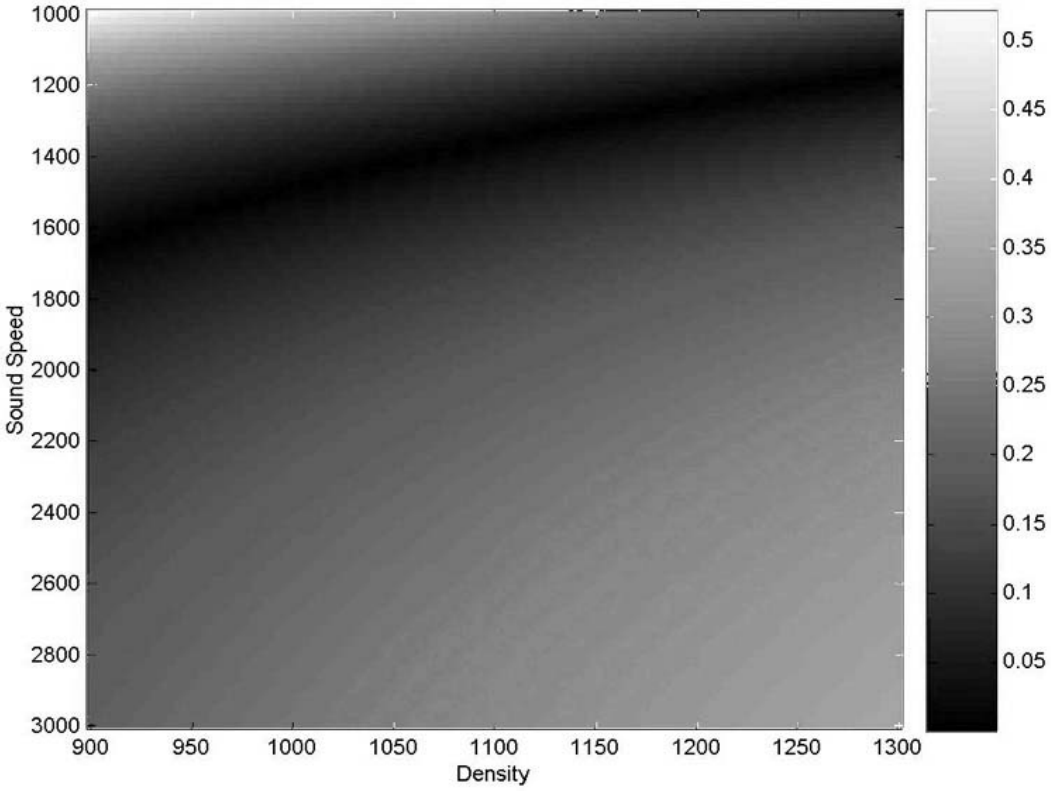

Figure 5-2. Calculations of acoustic contrast factor due to density and compressibility for plastic particles.

Figure 5-2 shows a magnified view of the region corresponding to plastics and glasses. Figure 5-3 displays the magnitudes of the viscous force term for a range of particle densities covering cork to common metals, against a range of fluid viscosities from just below water to pure glycerin. A table containing the viscosity of various liquids is presented in table 5-2. As can be seen in the graph, all of the values are positive, and would therefore only serve to push particles to the pressure nodes. As the viscosity

approaches that of glycerin the force due to fluid viscosity approaches the same order of magnitude as the density compressibility force terms. The viscous contribution to the acoustic force is proportional to the wavelength in the liquid and cross sectional area of the particles.

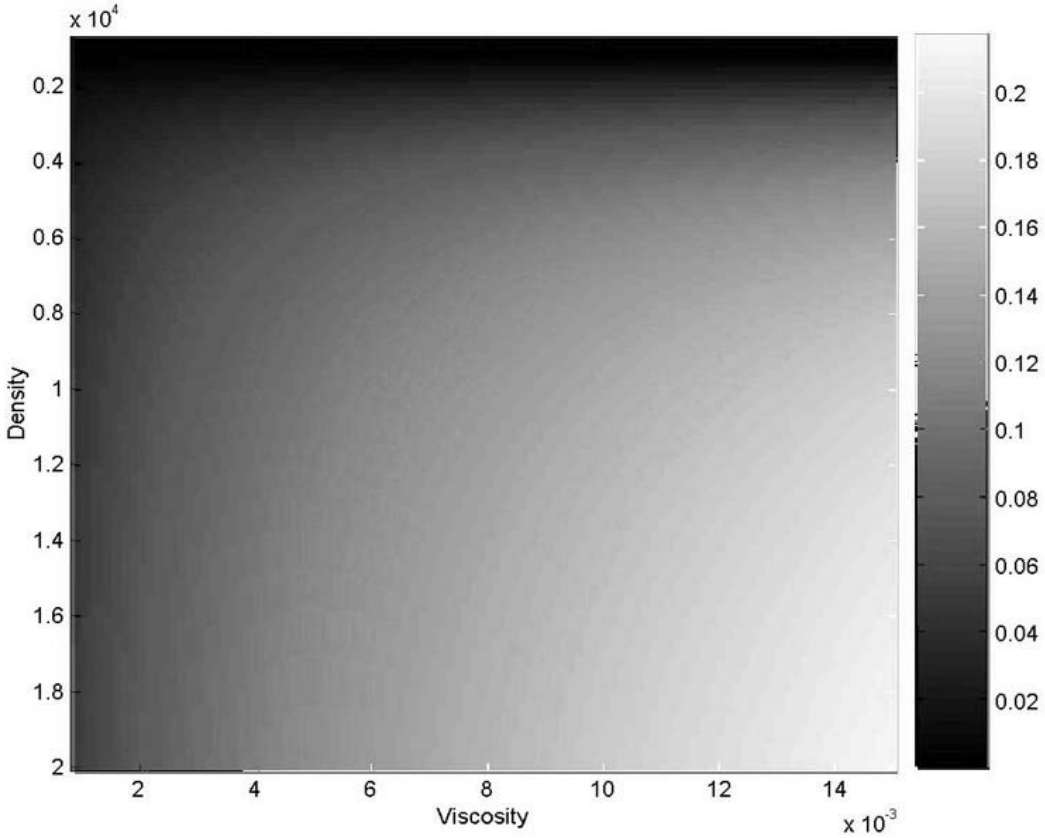

Figure 5-3. Calculations of acoustic contrast factor due to fluid viscosity for large range of materials.

Liquid	ρ(kg/m^3)	C_{fluid}(m/s)	η(Ns/m^2)	S.H.(J/kgK)	κ(W/mK)
Ethyl Ether	710	1010	2.30E-04	2290	0.14
Acetone	790	1170	3.00E-04	2150	0.17
Octane	700	1193	5.50E-04	2230	0.12
Methanol	790	1197	5.50E-04	2610	0.22
Water	1000	1487	1.00E-03	4182	0.59
Ethanol	810	1150	1.20E-03	2470	0.16
Glycerin	1260	1904	1.50E-02	2430	0.29
Olive Oil	900	1440	8.40E-02	2000	0.19

Table 5-2. Table of common fluid properties: density, sound speed, viscosity, specific heat, and thermal conductivity.

For ease of visualization within the range of particle materials such as plastic, or biological cells, Figure 5-4 presents the viscous force term magnitude over a smaller density range. A small region is visible at the top of Figure 5-4, which would seem to be indicative of a change of sign, but this is not the case. The viscous force term remains positive for all densities. Within the range of densities corresponding to plastics or biological cells, the viscosity contrast term does not exceed 0.007, or approximately one tenth of the density and compressibility terms.

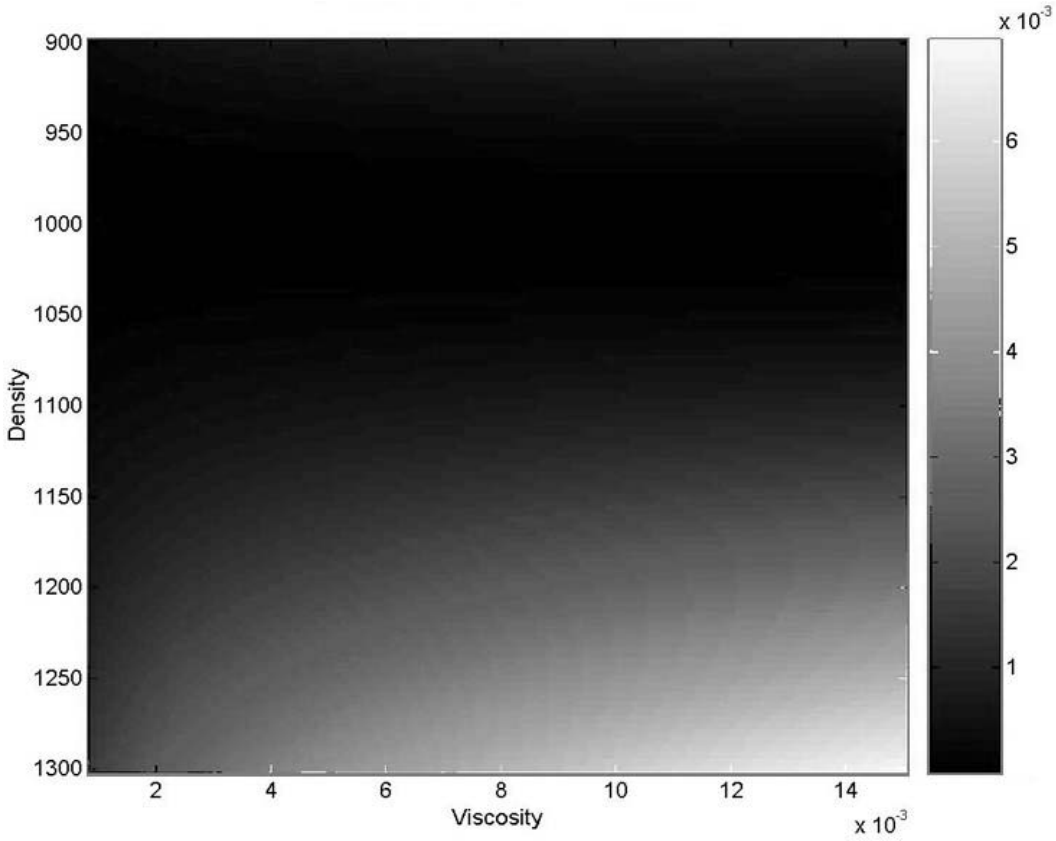

Figure 5-4. Calculations of acoustic contrast factor due to suspending fluid viscosity for plastic particles.

The last of the four terms in equation 5.60 is due to thermal conductivity contrast between the particles and liquid. Since the solvent of interest in this research is water, it is used for the following calculations. Figure 5-5 displays the thermal conductivity force magnitude as density and thermal conductivity are varied.

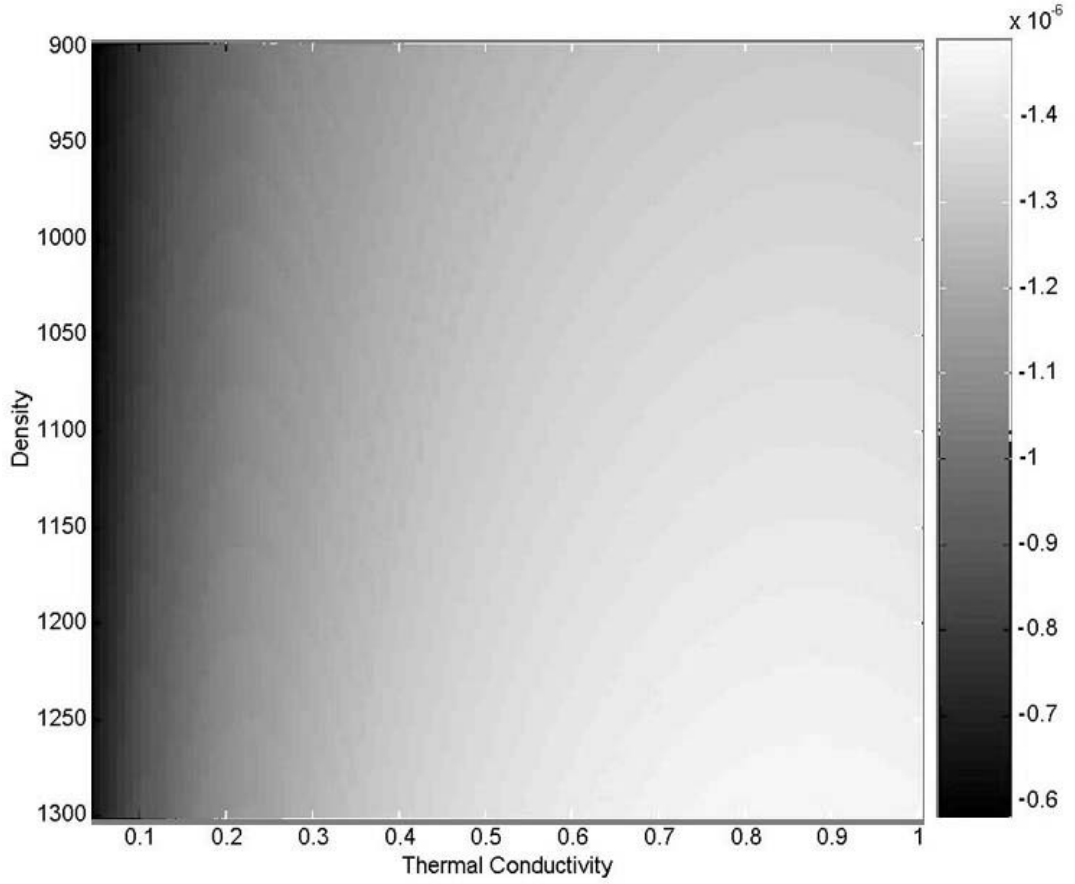

Figure 5-5. Calculations of acoustic contrast factor due to thermal conductivity for plastic particles in water while varying density relative to thermal conductivity.

On both plots, all magnitudes are listed as negative due to the action of the thermal conduction force terms in driving the particles towards the pressure antinodes. It should be noted that the magnitude of the thermal force is at least four orders of magnitude smaller than the density/compressibility term and at least 2 orders of magnitude smaller than

the viscosity force term even when calculated for higher specific heat and lower density particles or different fluids. The results displayed here are indicative of all other permutations investigated.

For further comparison of relative magnitudes of the four acoustic force terms, an array of fluid/particle material pairings are made. Particle/fluid material incompatibility is noted for blood cells in octane or acetone. The approximate values for blood cell properties are found from Apfel et al[11]. The results of the acoustic contrast calculations for each pairing are presented in tables 5-3, 5-4, and 5-5.

Liquid	Blood Cell	LDPE	HDPE	Aluminum	Nickel
Ethyl Ether	0.364	0.3467	3.86E-01	0.6376	0.7751
Octane	---------	0.325	3.74E-01	0.6391	0.7756
Acetone	---------	0.2797	3.33E-01	0.6177	0.7685
Methanol	0.2821	0.2749	3.30E-01	0.6175	0.7684
Water	0.0735	0.0945	1.90E-01	0.5673	0.7513
Ethanol	0.2821	0.2728	3.25E-01	0.6131	0.7669
Glycerin	-0.2992	-0.212	-2.96E-02	0.5061	0.7295
Olive Oil	0.1505	0.1628	2.45E-01	0.5902	0.7592

Table 5-3. Table of acoustic contrast factor values for common fluid-particle material pairings due to density and compressibility.

Liquid	Blood Cell	LDPE	HDPE	Aluminum	Nickel
Ethyl Ether	0.0022	0.001	1.30E-03	0.014	0.0292
Octane	---------	0.0017	2.30E-03	0.0222	0.0456
Acetone	---------	0.0004	6.00E-04	0.0134	0.0307
Methanol	0.0018	0.0005	9.00E-04	0.0181	0.0416
Water	0.0001	0.0002	0.00E+00	0.0152	0.0462
Ethanol	0.0022	0.0005	1.00E-03	0.0256	0.0602
Glycerin	0.0035	0.0107	7.90E-03	0.0317	0.1446
Olive Oil	0.0062	0.0001	1.10E-03	0.1723	0.4592

Table 5-4. Table of acoustic contrast factor values for common fluid-particle material pairings due to viscosity.

Liquid	Blood Cell	LDPE	HDPE	Aluminum	Nickel
Ethyl Ether	-2.194E-06	-2E-06	-1.88E-06	-1.7E-06	-2E-06
Octane	----------	-2E-06	-1.83E-06	-1.67E-06	-2E-06
Acetone	----------	-2E-06	-1.94E-06	-1.75E-06	-2E-06
Methanol	-2.234E-06	-2E-06	-1.83E-06	-1.63E-06	-2E-06
Water	-1.847E-06	-1E-06	-1.35E-06	-1.14E-06	-1E-06
Ethanol	-2.029E-06	-2E-06	-1.70E-06	-1.53E-06	-1E-06
Glycerin	-1.884E-06	-1E-06	-1.48E-06	-1.29E-06	-1E-06
Olive Oil	-2.311E-06	-2E-06	-1.93E-06	-1.73E-06	-2E-06

Table 5-5. Table of acoustic contrast factor values for common fluid-particle material pairings due to thermal conductivity.

As can be seen when comparing tables 5-3, 5-4, and 5-5, density and compressibility contrast provided the largest contribution to the acoustic force, but for cases of higher density contrast and/or greater fluid viscosity, viscous terms become comparable to the density and compressibility terms. It should also be noted that the density and compressibility contrast terms become negative for certain liquid/solid pairings. This indicates that in such material pairings, the particles would be driven to pressure antinodes, or if the fluid were mixed with a fluid of positive contrast, a point would exist where the particles would not experience any acoustic force due to density and compressibility. Acoustic forces arising from viscosity or thermal conductivity could still be exhibited in such a case. The force due to thermal conductivity is always negative and the force due to viscosity is always positive.

The emerging pattern indicates the possibility of a dimensionless number for the characterization of the system. While the four terms described above do provide dimensionless contrast factors, they did not adequately account for the effect of particle radius or excitation frequency. When the four terms are summed and multiplied by the ratio of particle radius to wavelength of sound, I obtain a dimensionless contrast factor that more adequately represents the system. Concentration is experimentally possible when the absolute value of the contrast factor exceeded 1.5E-6 for 1W power input. Example values for 3-micron particles/cells of the previous material pairings are summarized in Table 5-6.

Liquid	Blood Cell	LDPE	HDPE	Aluminum	Nickel
Ethyl Ether	5.731E-06	5E-06	5.98E-06	1.11E-05	1E-05
Octane	----------	4E-06	4.22E-06	8.54E-06	1E-05
Acetone	----------	3E-06	3.80E-06	7.98E-06	1E-05
Methanol	3.167E-06	3E-06	3.61E-06	7.96E-06	1E-05
Water	**5.17E-07**	**7E-07**	**1.33E-06**	4.67E-06	7E-06
Ethanol	3.463E-06	3E-06	3.87E-06	9.15E-06	1E-05
Glycerin	**-1.176E-06**	**-6E-07**	**9.90E-08**	3.06E-06	7E-06
Olive Oil	**1.427E-06**	1E-06	1.88E-06	1.3E-05	3E-05

Table 5-6. Table of acoustic contrast factor values for common fluid-particle material pairings at 417 kHz for 3-micron particles.

Values highlighted in bold fall below the threshold level and thus would not be expected to concentrate. Increasing the excitation frequency increases the contrast factor. Table 5-7 presents the contrast factor if the

frequency are doubled from 417 kHz to 834 kHz and consequently reducing the tube radius to maintain dipole character of the resonance. The necessity of maintaining a dipolar resonance is discussed in a previous chapter. Particles that would not concentrate at 417 kHz would concentrate at 834 kHz as evidenced in the comparison of tables 5-6 and 5-7.

Liquid	Blood Cell	LDPE	HDPE	Aluminum	Nickel
Ethyl Ether	2.267E-05	2E-05	2.38E-05	4.26E-05	6E-05
Octane	----------	1E-05	1.67E-05	3.23E-05	4E-05
Acetone	----------	1E-05	1.51E-05	3.07E-05	4E-05
Methanol	1.252E-05	1E-05	1.44E-05	3.03E-05	4E-05
Water	2.06E-06	3E-06	5.30E-06	1.79E-05	3E-05
Ethanol	1.366E-05	1E-05	1.54E-05	3.43E-05	5E-05
Glycerin	-4.82E-06	-3E-06	**1.30E-07**	1.12E-05	2E-05
Olive Oil	5.35E-06	5E-06	7.45E-06	4.18E-05	9E-05

Table 5-7. Table of acoustic contrast factor values for common fluid-particle material pairings at 834 kHz for 3-micron particles.

5.3-Disruptive Effects

The primary radial and secondary axial acoustic forces are functions of the acoustic energy density ε, a measure of the energy residing in the wave field. A common method of energy density estimation is equilibrating gravitational force with the primary acoustic force on particles whose properties are well known. A linear proportionality relationship can then be assumed for energy density to voltage. This method cannot be applied to resonant systems due to disturbance of the sound field. A slight change in

resonance hugely perturbs the energy density in the system. At resonance, the electrical impedance of the system reaches a local minimum while power and current reach a local maximum for constant input voltage. The unitless quality factor, Q is a common characterization method for oscillatory systems. [131] It is defined as the ratio of the product of energy density and angular frequency divided by the power input which can also be expressed in terms of an experimentally determined absorption coefficient α which also included the effective sound pressure and compressibility. The definition is[132]

$$Q = \frac{\varepsilon\omega}{P} = \frac{k}{2\alpha} \tag{5.61}$$

Resonators driven at frequencies with high values of Q require lower power input to generate a given energy density. Driving a cavity at lower "quality" resonances leads to inefficient concentration, inhomogeneous heating of the resonator, temperature gradients and consequent convective flow within the cavity. According to Shutilov[133] , the absorption coefficient for liquids in terms of the viscosity of the liquid μ is described by

$$\alpha = \frac{\omega^2}{2\rho c^3}(\mu' + \frac{4}{3}\mu) \tag{5.62}$$

Since the acoustic energy density is a measure of energy in the wave field, it can be expressed in terms of the time-averaged potential and kinetic energy densities, E_{pot} and E_{kin} respectively which are expressed in Eq. 5.26.

Consequently, the energy density can be rewritten as

$$E_{pot} = \frac{\beta_f}{2} < (p_0 \sin(kw)\sin(wt))^2 > \quad (5.63)$$

$$E_{kin} = \frac{\rho_f}{2} < (v_0^2 \cos(kw)\cos(wt))^2 > \quad (5.64)$$

$$\varepsilon = \frac{\beta_f p_0^2}{4} \quad (5.65)$$

Since the rate of particle movement to fixed nodal or anti-nodal positions within the fluid is directly proportional to the applied standing wave pressure amplitude, increasing sound pressure might be used as a method to accelerate the segregation process. However, increased sound pressure also increases the potential for acoustic cavitation and streaming, which interferes with efficient particle concentration in standing wave fields. The last term outside of the brackets in Eq. 5.59 arises from the solution of the time-averaged equations of second order. The additional force due to attenuation in the fluids or absorption in the particles induces acoustic streaming and consequently additional drag forces on the particles leading to increased scattered field amplitude. It induces stationary fluid flow in the absence of particles and is also known as acoustic streaming.

Acoustic streaming is defined as non-oscillatory steady fluid motion originating from spatial non-uniformity of the sound field or from energy

dissipation at the interfaces. There are four general classifications of streaming; Rayleigh, Schlichting[133], Eckart[134], also called “quartz wind”, and cavitation streaming. Rayleigh streaming results from vortex flow outside of the boundary layer on the order of a wavelength. Schlichting streaming is caused by vortex flow inside the boundary layer of the solid-liquid interface and is restricted to a region much less than a wavelength. Eckart streaming is due to attenuation of the sound field in the bulk fluid and thus extends over much larger than a wavelength. Cavitation streaming is caused by the pulsation of non-inertial bubble oscillation and is typically restricted to a region less than a wavelength.

The last term in Eq. 5.59 accounts for acoustic streaming. In the derivation of the equation, it is assumed that no thermal gradient is present. The following discussion will be restricted to Rayleigh, Schlichting, and Eckart streaming. Streaming can be further broken into streaming around particles and acoustically driven steady fluid motion in the absence of particles. Both types of streaming arise from the second order terms in the time-averaged equations of the fluid motion.

The total acoustic force on the particle is defined as the sum of the acoustic radiation pressure on particles and the drag force. In order for concentration to occur, the force on the particles must be greater than the

drag force from streaming. The inequality can be expressed as

$$\pi\rho_f \varepsilon \sin\left(\frac{2\omega d}{c_f}\right)\left[\left(\frac{\omega R_0}{c_f}\right)^3 CF\right] \geq \pi\varepsilon\left(\frac{\omega R_0}{c_f}\right)^3 \frac{2\eta_f}{\omega R_0^2} \tag{5.66}$$

If the common terms on each side of the inequality are cancelled and the remaining terms are rearranged, Eq. 5.66 could be rewritten as

$$\frac{CF}{2} \geq \frac{\eta_f}{\omega\rho_f R_0^2} \tag{5.67}$$

The resulting dimensionless inequality establishes the point at which streaming dominates. The other acoustic effect that disrupts efficient concentration is acoustic cavitation. Acoustic cavitation is the generation of bubbles or vapor cavities in fluids in response to an alternating pressure field. In a pure fluid with no nucleation sites under ideal unperturbed conditions, the cavitation threshold is equal to its tensile strength. The formation of cavitation bubbles occurs at nucleation sites. Unlike the other three types of acoustic streaming, the direction of cavitation jet streaming is stochastic. In a fluid with impurities, dissolved gases and nucleation sites, however, the cavitation threshold can be two to three orders of magnitude smaller[135]. The bubbles concentrate energy by transforming the low energy density in a sound field into a localized high energy density characteristic of the

surroundings and interior of a collapsing bubble. When the collapse of the bubbles is capable of producing high fluid velocities, shock waves, and/or jetting, the cavitation is deemed “inertial”. For inertial bubbles, it is not uncommon for the bubbles to double their size in a few acoustic cycles then rapidly collapse. For cavitation where the bubble size changes relatively little, the term “non-inertial” is applied. Typically inertial cavitation occurs at lower frequencies than non-inertial cavitation due to limited time for bubble growth at higher frequencies.

Gould et al. [136] investigated the effects of low levels of cavitation on the behavior of particles in a fluid. They compared water saturated with oxygen to degassed water. They found that the first sign of cavitation occurred at approximately eight times the pressure required to concentrate the particles with sustained concentration until sound pressures exceeded approximately twenty seven times the minimum concentration pressure. They also observed that bubbles smaller than the particle size are attracted to pressure antinodes, but once the bubbles grew larger than the particle size, they are attracted to pressure nodes. Due to transient noise produced during rapid collapse of bubbles in the standing wave field, measurement of noise could be used to qualitatively estimate cavitation within the cavity.

During the course of our experiments cavitation is only observed at

input power levels exceeding approximately 10 times the minimum energy required to concentrate and approximately 5 times the energy required to induce disruptive streaming. Hence, the useful power-input threshold preceded the cavitation threshold for our system.

5.4-Cavity Size/Excitation Frequency

As noted in section 5.2, the acoustic radiation pressure exerted on particles is proportional to the product of the wavenumber cubed and particle volume. Two methods could be used to compensate for smaller particles; increase in energy density, or increase in excitation frequency. Increase in energy density would be limited by the power limits discussed in the previous section. Since efficient particle concentration occurs at the tube-cavity coupled dipole resonance of the system, the resonance frequency would have to be shifted up as well. The inner cavity dimension of the tube would thus be reduced proportionally. In a previous chapter, the resonance frequency is increased from 417 kHz in soft glass to 841 kHz in glass capillary tube, allowing concentration of 1-micron polystyrene beads. Three limitations exist to the scalability. When the resonance of the transducers is tuned by halving the thickness, the acoustic force exerted by the piezoceramic drive transducer is reduced. Driving a thicker transducer at a

higher harmonic of the thickness resonance can compensate for such an effect. The second limitation of higher frequencies and corresponding smaller cavity dimension is due to the perturbative effect of large particles in a small cavity on the acoustic field. Further discussion of this effect will be presented in a later section. The third limitation arises from fluid attenuation of higher frequencies. Transmission loss due to attenuation in a fluid is represented in terms of an attenuation coefficient 'α' with the units of dB/m. There are two primary causes of attenuation, viscous friction, and ionic relaxation[137]

Attenuation due to viscous friction refers to the conversion of sound energy to heat due to transfer of energy to the internal vibrational modes of the fluid molecules. Viscous friction is the dominant mode of attenuation at frequencies above 1 MHz. The attenuation coefficient is strongly frequency dependent with attenuation increasing rapidly with frequency. An approximate expression for the attenuation coefficient (α_1) for water due to viscous friction only is given by:

$$\alpha_1 = (2.1\text{E-}10*(\text{T-}38)^2 + 1.3\text{E-}7)\text{f}^2 \qquad (5.68)$$

where T is the temperature (centigrade) and f is the frequency in kHz.

The presence of certain dissolved salts in water increase the attenuation coefficient further. Ionic relaxation refers to the dissassociation-

reassociation of ions in solution due to the pressure fluctuation in the sound wave. A similar empirical absorption coefficient that accounts for the cumulative ionic relaxation phenomena is given by:

$$\alpha_2 = \sum_{i=0}^{n} b_i f_i (1+(\frac{f_i}{f})^2)^{-1} \quad (5.69)$$

where n is the number of ion disassociation-reassociation reactions, f_i is an empirically derived temperature dependent constant for the i-th reaction, and bi is also an empirically derived constant for the i-th reaction. The total attenuation in a fluid can be expressed as

$$A = (\alpha_1 + \alpha_2)D \quad (5.70)$$

where D is the cavity diameter.

5.5-Thermal Perturbation

Another deleterious effect that could disrupt acoustic concentration is a change in resonance of the system during the concentration process. The resonance of the system can be shifted by several phenomena. The largest of these is a temperature change of the system. This induces changes in sound speed and density of the fluid, tube and piezo-ceramic transducer. The combined effects lead to a detuning of the system and consequently, higher power consumption to achieve concentration of the particles. The

largest thermal effect is due to the change in sound speed of the fluid.

The problem of sound speed variation of water as a function of temperature has been thoroughly investigated by a number of scientists. The best-known measurements are probably those by Greenspan and Tschiegg[138], Wilson[139, 140], Del Grosso and Mader[141], and Del Grosso[142,143]. Several empirical relations have been proposed for the functional dependence of sound speed on temperature. Del Grosso and Mader applied a fifth order polynomial fit to their data for pure water at atmospheric pressure and temperatures between 0^{o} C and 100^{o}C, which is converted to the 1990 International Temperature Scale by Bilaniuk and Wong[144]. Marczak[145], combined the experimental measurements of Del Grosso and Mader, Kroebel and Mahrt[146] and Fujii and Masui[147] and produced a fifth order polynomial based on the 1990 International Temperature Scale. Lubbers and Graaff produced a second order Eq. with a restricted temperature range of 10^{o}C to 40^{o}C for medical ultrasound applications, including tissue mimicking materials and test objects. Within the quoted temperature ranges they claim that the maximum error is approximately 0.18 ms^{-1} in comparison with experimental data or more detailed equations such as Bilaniuk and Wong. Their empirical formulae for sound speed are:

$$c = a_0 + a_1 T - a_2 T^2 + a_3 T^3 - a_4 T^4 + a_5 T^5 \quad (5.71)$$

Model:	a_0	a_1	a_2*10^{-2}	a_3*10^{-4}	a_4*10^{-6}	a_5*10^{-9}
Bilaniuk-Wong	1402.382	5.0383	5.8117	3.3463	1.4825	3.1658
Marczak	1402.385	5.0388	5.7991	3.2871	1.3988	2.7878
Lubbers-Graff	1405.03	4.624	3.83E-2	0	0	0

where the coefficients are given in the table shown above.

Belogol'skii et al. [149] made measurements of sound speed as a function of pressure and temperature combined with the Eq. of Bilaniuk and Wong at atmospheric pressure to develop an algorithm which took pressure into account. His equation is written in Eq. 5-72. It is valid for 0°C to 40°C and 0.1 MPa to 60 Mpa. The variables T and P are temperature in degrees Celsius and pressure in megaPascals respectively.

$$\begin{aligned} c(T,P) &= c(T,0) + M_1(P-0.101325) + M_2(P-0.101325)^2 + M_3(P-0.101325)^3 \\ c(T,0) &= a_{00} + a_{10}T + a_{20}T^2 + a_{30}T^3 + a_{40}T^4 + a_{50}T^5 \\ M_1 &= a_{01} + a_{11}T + a_{21}T^2 + a_{31}T^3 \\ M_2 &= a_{02} + a_{12}T + a_{22}T^2 + a_{32}T^3 \\ M_3 &= a_{03} + a_{13}T + a_{23}T^2 + a_{33}T^3 \end{aligned} \quad (5.72)$$

Coefficient	Numerical Value
a_{00}	1402.38744
a_{10}	5.03836171
a_{20}	-5.81172916E-2
a_{30}	3.34638117E-4
a_{40}	-1.48259672E-6
a_{50}	3.16585020E-9
a_{01}	1.49043589
a_{11}	1.077850609E-2
a_{21}	-2.232794656E-4
a_{31}	2.718246452E-6
a_{02}	4.31532833E-3
a_{12}	-2.938590293E-4
a_{22}	6.822485943E-6
a_{32}	-6.674551162E-8
a_{03}	-1.852993525E-5
a_{13}	1.481844713E-6
a_{23}	-3.940994021E-8
a_{33}	3.939902307E-10

The temperature change also induces dimensional changes of the tube and PZT transducer following the linear coefficients of expansion. The coefficients of expansion are approximately 8.5E-3 mm/K for soft glass, 3.0E-3 mm/ K for quartz glass, and 1.5E-3 mm/ K for PZT. The radial dimension of the inner cavity defined by the tube governs the dimension of the liquid column and thus the wavelength of coupled dipole resonance. For comparison, the combined effect of fluid and tube temperature variation, assuming thermal equilibration, would be 382 Hz/K for soft glass and –1064 Hz/K for quartz glass. If the fluid flow rate is fast enough to prevent any heat transfer to the fluid from the tube, then the frequency shift in soft glass is –

1136 Hz/K due exclusively to the change in inner tube diameter. The drive transducer resonant frequency shifts approximately 100 Hz/K due to change in thickness.

To establish the thermal limits on concentration, a series of experiments are performed at temperatures ranging from 10^{o}C to 46^{o}C. Two types of glass are used for the thermal measurements, thick quartz and soft glass. A picture of the apparatus including a copper temperature regulation coil and heat exchanger with fan is presented in Fig. 5-6.

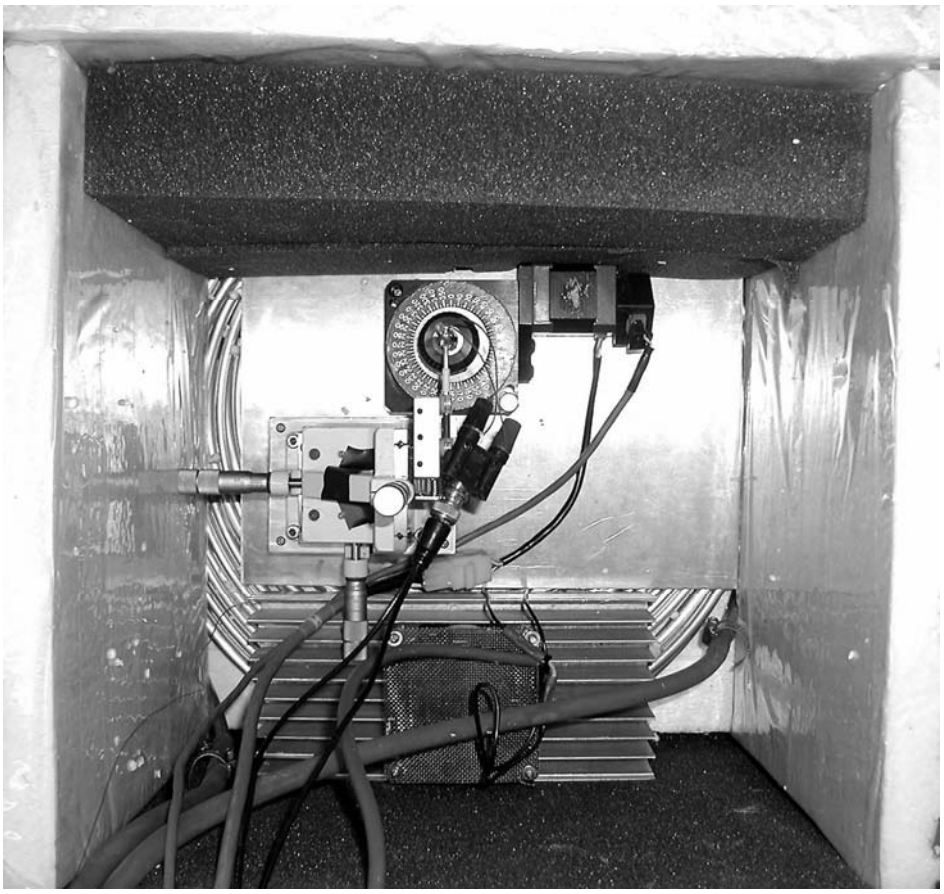

Figure 5-6. Picture of apparatus used for thermally controlled angular scan of tube. .

Angular measurements were performed at 5 angular degree increments at 2 thermal degree intervals. A section of soft glass was characterized from 10 to 45 degrees Celsius when empty and filled with water. Figure 5-7A displays the frequency spectrum as a function of temperature for the empty soft glass. The frequency spectrum as a function of temperature for the water-filled soft glass tube is shown in Fig. 5-7B.

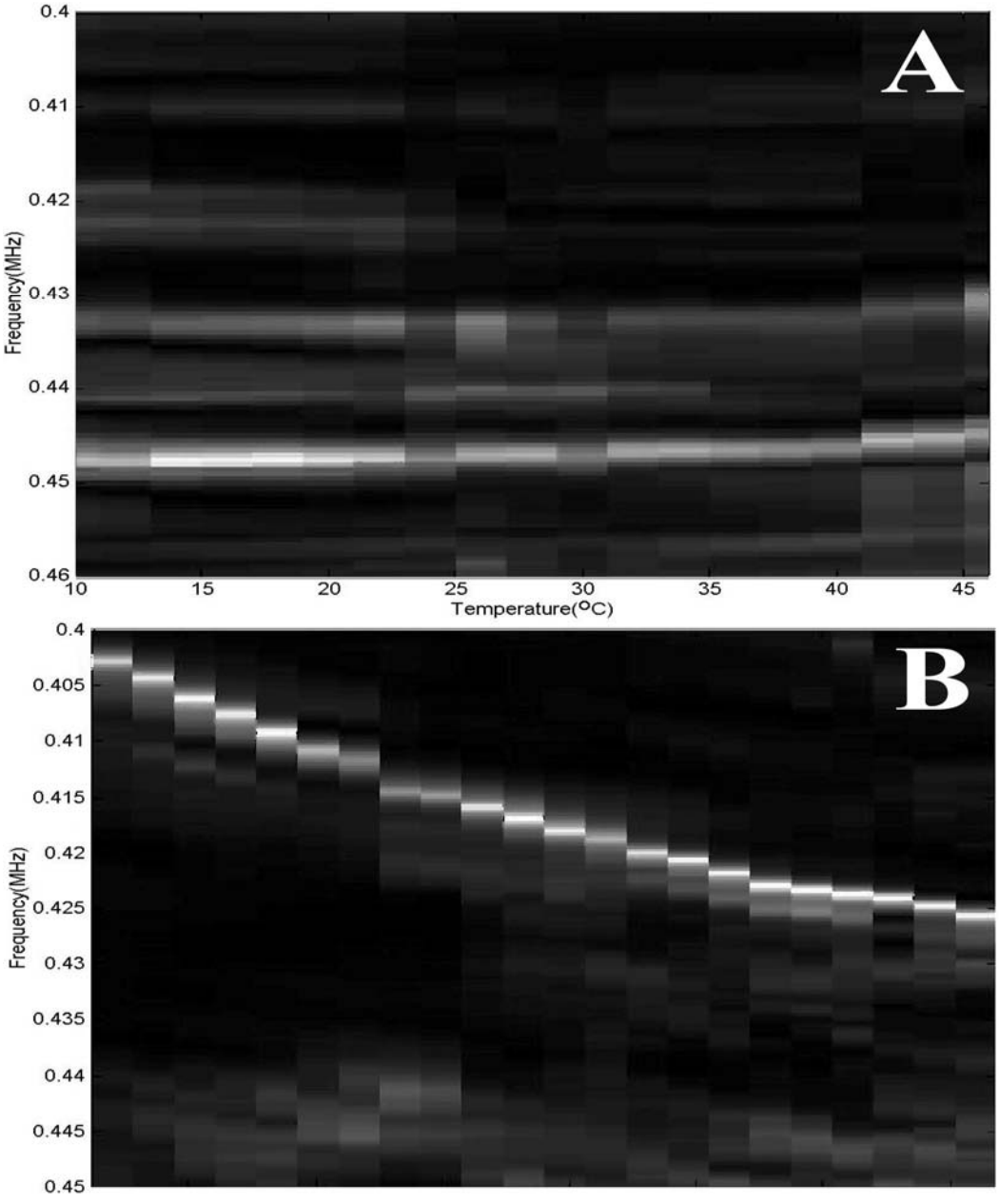

Figure 5-7. Data from thermal and angular scan of soft glass tube.(A)Empty (B)Water-filled

As can be seen when comparing Fig. 5-7A and 5-7B, the resonance shift due to the expansion of glass is approximately –5 kHz over the whole temperature range, while the shift when water is present in the cavity is approximately +25 kHz. A similar experiment was undertaken with thick quartz glass from –10 to 30 degrees Celsius. The result of the water-filled spectral measurement is presented in Fig. 5-7B.

The structure-cavity coupled dipolar resonance of thick quartz tube shifts by approximately 20 kHz over the whole temperature range. For both types of tube, the concentration capability of the claimed resonance at different temperatures was verified with 10-micron particles.

5.6-Particle Perturbation

Another mechanism for resonance frequency shift, although smaller than the thermal perturbation effect, is a change in sound speed caused by the process of concentration of particles in the fluid, leading to a periodic variation in the local index of refraction. Leung et al. [150]calculated the frequency shift for rigid spheres in a cavity. They found that the frequency shift for a rigid sphere displaced from the pressure antinode to the pressure node could be expressed as

$$\Delta\nu = \frac{-\nu_0 V_p}{4V_{cav}}(5\cos(2kx)+1) \tag{5.73}$$

where ν_0 is the resonance frequency in the absence of the spheres, V_p is the volume of the particle, and V_{cav} is the volume of the resonant cavity.

Kwiatkowski and Marston characterized and modeled this effect for the purpose of aqueous suspension characterization using a low intensity probe signal. For compressible spheres in an inviscid liquid, they applied the principle of adiabatic invariance to obtain the relationship

$$\Delta\nu = \frac{-\nu_0 V_p}{2V_{cav}}\left(\left(-\frac{\beta_p}{\beta_f} - \frac{5\rho_p - 2\rho_f}{2\rho_p + \rho_f}\right)\cos(2kx) + \frac{\beta_p}{\beta_f} - \frac{4\rho_f - \rho_p}{2\rho_p + \rho_f}\right) \tag{5.74}$$

for the frequency shift

For the case of 0.25% by volume 10-micron polystyrene beads in a 2mm inner diameter soft glass tube, the resonance shift using the above relations would be approximately 180Hz. Experimental measurements verified a frequency shift from unconcentrated to concentrated particles of 200 Hz. $^{+}/_{-}$ 50 Hz. The predicted shift for a change of pure deionized water to 0.25% by volume 10-micron polystyrene beads is a shift of –180 Hz since particles at the pressure node can be approximated as a delta function as they minimally interact with the standing wave so long as the particles are much smaller than a wavelength.

Merely tracking and maintaining the resonance of the system could

correct this up to the limit when kR_p, the resonance wavenumber times the particle radius approaches one. Also noted above is the particle size limitation of Brownian motion. Greater input power or lower temperatures are the most common methods of combating that limitation. The negative effects of resonance frequency change by either temperature perturbation or particle perturbation on concentration could be mitigated through time varying excitation frequency to maintain resonance. Phase lock loops, amplitude lock loops, impedance lock loops, or swept frequency excitation are all methods for achieving and maintaining resonance of the system and thereby assuring successful concentration.

5.7-Conclusion

Certain limitations exist to the concentration of particles by structural excitation. The limitations discussed are inherent in the method and arose predominately through five aspects: acoustic contrast ratio, higher power disruptive effects, cavity size/excitation frequency, thermal resonance perturbation, and particle resonance perturbation. Although the limitations are not completely avoidable, higher power, selection of geometry for higher coupled dipole resonance frequency, larger particles or larger agglomerations of particles, and resonance maintenance through feedback

loops can be used to extend the usable range of structural excitation for concentration.

The acoustic contrast ratio more specifically refers to four terms in the acoustic force equations. The terms are dependent on sound speed, density, viscosity, and thermal conductivity differences between the fluid and the particles.

In addition to the four contrast terms, there is also a cubic dependence of the acoustic force on frequency of resonance and particle size. Hence changing the cavity dimensions, and thereby the resonance frequency, or increasing the particle size also improved the concentration efficiency.

Due to the distributed nature of structural excitation, high power is not necessary for efficient particle concentration. If higher flow rates, or smaller particle increased the power requirements of the system, convective heating and acoustic streaming would provide limits on the maximum useful power input. Transducer heating of the tube could be reduced by either changing the drive transducer, or by utilizing efficient cooling on the excitation transducer. An expression was derived for the power limitation imposed by acoustic streaming.

Tracking and maintaining resonance of the system could mitigate the remaining two terms, corresponding to thermal perturbation of resonance or

particle perturbation of resonance. This could be used up to the limit when kR_p, the resonance wave number times the particle radius approaches one. Also noted in chapter 5, another remaining limitation on the minimum particle size by competition of acoustic concentration with Brownian motion. Greater input power or lower temperatures are the most common methods of combating that limitation.

The negative effects of resonance frequency change by either temperature perturbation or particle perturbation on concentration could be mitigated through variation of the excitation frequency to maintain resonance. Phase lock loops, amplitude lock loops, impedance lock loops, or swept frequency excitation are all methods for achieving and maintaining resonance of the system and thereby assuring successful concentration.

6-APPLICATION

6.1-Introduction

The objective of this project is to investigate the use of structural excitation as a potentially efficient concentration/fractionation method for particles in suspension. It is shown in previous chapters that structural excitation of a cylindrically symmetric cavity, such as a tube, allows non-invasive, fast, and low-power concentration of particles suspended in a fluid. Once this was demonstrated, the next logical step is a preliminary demonstration of acoustic concentration applicability to a problem of practical interest. Such an application is found in replacement of sheath flow in flow cytometry.

Flow cytometers have applications in many areas including medicine (HIV and cancer diagnosis), homeland defense (biological point detection, bio-surveillance, and forensic analysis) and general biomedical research (ligand-receptor studies, molecular assembly analysis, high throughput screening and genotyping). The many powerful applications have made flow cytometers a fixture in nearly every university, medical school, pharmaceutical company, and diagnostic lab. However, the size, expense and requirement for large amounts of consumables have limited their use to

formal laboratory settings. The elimination of sheath fluid would reduce power and consumable requirements, resulting in increased portability of the instrument. Our novel technique will allow a sheathless portable flow cytometer to achieve conventional particle analysis rates, while using a fraction of the power and consumables of a conventional flow cytometer. Importantly, it does not damage biological cells[117, 151,152].

6.2-Background

A conventional flow cytometer, such as that shown in Fig. 6-1, injects a sample stream into the center of a higher velocity laminar sheath flow. The resultant hydrodynamic force generates a narrowly focused sample stream. This focused sample stream is interrogated by focused laser beams with spot sizes ranging from 10μm to 100μm in diameter, within the very small interrogation volume formed by the intersection of the laser spot and the sample stream.[51] Scattered light, along with several wavelength bands of fluorescence, are collected using sensitive detectors such as photomultiplier tubes and avalanche photodiodes.

The light is scattered into different directions depending on the refractive index, size and shape of each particle. Light scattered in small angles of the laser beam indicates the particle size. Scattered light collected

in a cone in the orthogonal direction of the laser beam is called side scatter. It indicates size as well, but is influenced by surface and internal structures.

Depending on the staining mechanism, fluorescence signals indicate various states and functionality. Fluorescence analysis makes it possible to quantify fluorescence from single cells up to millions of cells after a single sample run. Signals are detected and displayed for cell distribution analysis. Statistical data such as mean fluorescent intensity when correlated to shifts in time or dependence on cell function has become a standard technique for this purpose.

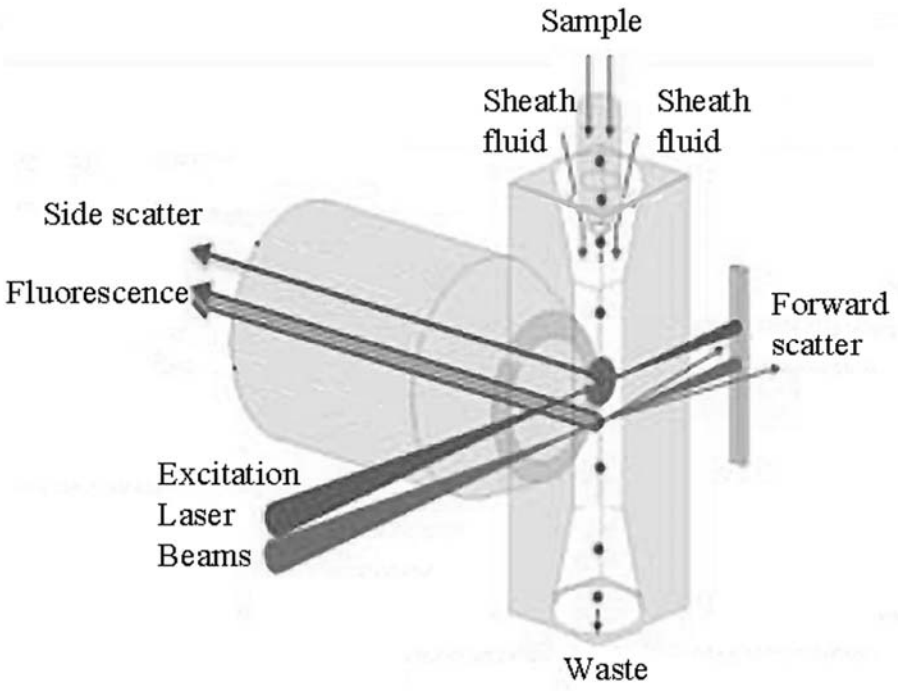

Figure 6-1: Schematic of a typical flow cytometer

With careful design, flow cytometers have achieved typical detection limits as low as 100 fluorescent molecules per cell at conventional analysis rates and single fluorophores with reduced analysis rates[153,154]. Submicron particles such as small bacteria or picoplancton are also well resolved. The high linear velocity and small interrogation volume result in transit times of a few μs, requiring flow cytometers to use high speed analog to digital converters (ADCs) to record the fluorescence and scatter signals. In contrast, microscopic analysis is based on a very limited number of cells seen on a

slide, typically less than 100. The visualization of submicron particles and structures in a microscope is also difficult.

Particle-by-particle analysis of a high velocity sample stream enables the multi-parameter observation of population distributions and provides continuous kinetic resolution at analysis rates of greater than 10000 per second [51,.] Cells and microspheres under analysis largely exclude free fluorophore from the interrogation volume. Therefore, background from unbound fluorescent probe is low, which allows sensitive measurement of particle-associated probes without separation steps [155]. Furthermore, the high analysis rates of flow cytometry make it suitable for high throughput sample analysis [156]. The flow velocity is in the range of meters per second, which results in a stable laminar flow condition and a high event rate of up to several thousand cell per second.

6.3-Value

The applications of such instruments are numerous as flow cytometry is a powerful biomedical assay technology used for many clinical purposes including HIV and cancer diagnosis as well as ongoing treatment decisions for these diseases. Additionally, flow cytometry is used in many areas of biochemistry such as ligand-receptor, cell cycle and molecular assembly

studies.

Clinical	Biochemical
CD4+ cell counting for AIDS assessment [157,158,159,160,161]	Single Nucleotide Polymorphism analysis [162,163,164,165,166,167]
Reticulocyte counting for anemia patients [168]	Cellular Apoptosis [169,170,171,172]
Differential leukocyte counting [173]	Kinetic analysis of cellular adhesion [174,175,176]
$CD34^+$ cell counting for transplantation [177,]	Multivalent receptor affinity studies [178,179,180]
Cancer diagnosis [181,182,183,184]	Molecular assembly analysis [155, 185]
Minimal Residual Disease analysis in Leukemia Treatment [186,187,188,189]	High-throughput screening of peptide-protein interactions [190,191]
Diagnosis of infectious diseases [192,]	Mechanistic study of DNA cleavage by endonucleases [193,194]
Cytokine expression analysis [181, 195,196,]	Evolution of single chain antibodies [155,197,198,199,200,201,202,203,]
Pathogenic bacteria detection[204,].	*E. Coli* protease optimization [205,]

Table 6-1. Abbreviated flow cytometry application list.

As can be seen in Table 6-1, flow cytometry is an integral technology in nearly every medical discipline including diverse biological assays in clinical settings. Perhaps the most important application of flow cytometry is

the accurate counting of CD4+ and CD8+ T-cells, which provides for AIDS progression assessment and assists treatment decisions. Similar approaches have been used to count other specific cell subsets as well as assist in the diagnosis of many forms of cancer and assessment treatment effectiveness. In addition to these applications flow cytometry is also gaining favor in the diagnosis of infectious diseases and as a tool to detect pathogenic bacteria. These applications are making it even more important to develop instrumentation that is portable for field use and inexpensive for use in third world settings.

The number of biochemical applications of flow cytometry rivals the number of clinical applications. Flow cytometry is particularly adept in the analysis of molecular assemblies and it has been extensively used in ligand-receptor studies, where it has unmatched sensitivity and throughput. It is also gaining favor in the analysis of enzymatic activities such as endonucleases and proteases. Flow cytometry in combination with yeast and bacterial cellular display has also become a powerful method to select for improved binding molecule by directed evolution. Furthermore, flow cytometry can analyze soluble micro sphere arrays containing up to 100 individual elements, which allows 100 reactions to be simultaneously analyzed within a single sample. This, along with new sample delivery technology, is making

flow cytometry a high throughput method to analyze many biochemical reactions.

6.4-Extinction Experiment

As a preliminary method of verifying optical detection of acoustic concentration, a laser extinction experiment was constructed. Figure 6-2 displays a diagram of the experimental apparatus.

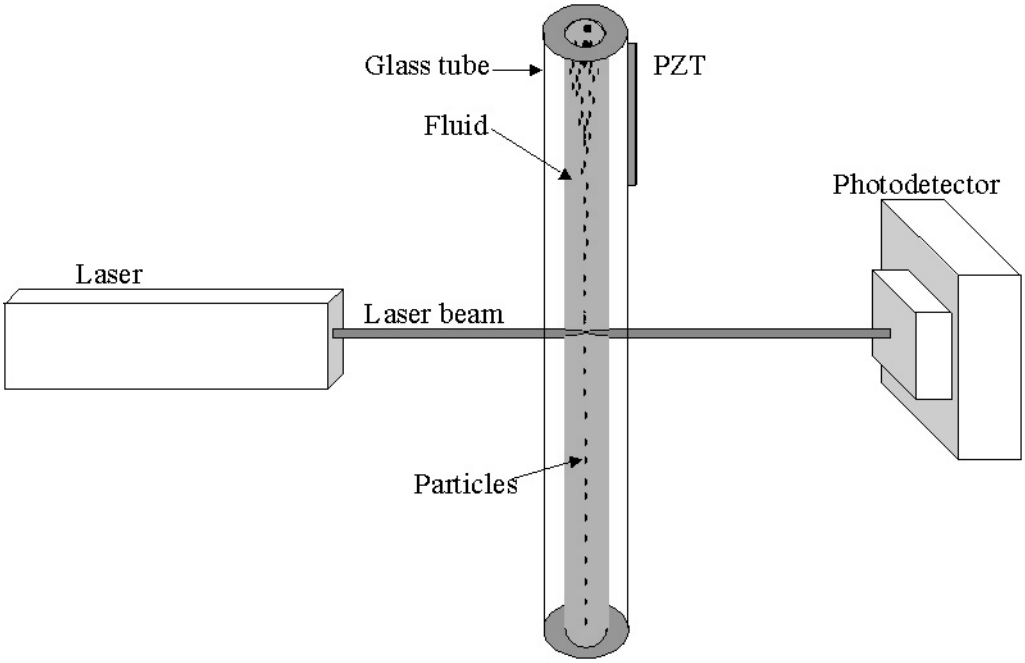

Figure 6-2: Schematic of extinction experimental apparatus.

A 4.5mW He-Ne laser with a 0.9mm beam diameter is used as a source; an amplified photo detector on the opposite side of the tube is connected to a digital oscilloscope for light extinction and scattering

measurements. Since the beam is collimated when exiting the laser and the tube acted as a lens to focus the light within the cavity with a net focal length of approximately 8mm, no lenses were used in the experiment. The detector is placed at 4mm from the tube such that the beam exiting the tube covered the majority of the detection area.

The tube was cleaned and polished to minimize surface scattering of the light. To eliminate the effect of ambient light, the light out of the laser was chopped at 100Hz locked to the detector. The detector amplification was set such that the voltage signal was 10.6Vpp when the tube was filled with distilled water, just below the maximum detector output voltage of 11Vpp. A 0.25% by volume concentration of 10-micron polystyrene beads was mixed and used for the experiment.

The optical beam focusing by the tube was calculated assuming an incident Gaussian beam profile with no wave-front curvature and a beam diameter of 0.9mm. Launching of optical guided modes in the cylindrical tube wall is assumed negligible. Experiments where a narrow wire is placed down the center of the cavity to block the direct path of light without contacting the internal tube surface yield no detectable level of light, supporting the guided wave negligibility assumption. Losses within the water and/or glass tube are compensated for by using transmission through the system in the absence of

particles as the incident intensity in the calculations. The standard ray matrices used were

$$\begin{pmatrix} 1 & 0 \\ \frac{n_2 - n_1}{n_2 R} & \frac{n_1}{n_2} \end{pmatrix} \text{ Curved Dielectric Interface Radius R} \tag{6.1}$$

$$\begin{pmatrix} 1 & d \\ 0 & 1 \end{pmatrix} \text{ Homogenous Medium Length d} \tag{6.2}$$

.

The matrices are multiplied from right to left by an initial condition vector consisting of y-position and y-slope at entry to the system of optical elements. The optical elements are chosen to be:

1) Curved interface of air to glass with radius of curvature -2mm.
2) Homogeneous glass for a distance of 1mm
3) Curved interface of glass to water with radius of curvature -1mm.
4) Homogeneous water for a distance of 2mm
5) Curved interface of air to glass with radius of curvature +1mm.
6) Homogeneous glass for a distance of 1mm
7) Curved interface of glass to water with radius of curvature +2mm.
8) Homogeneous air for a distance of 10mm

Calculations were made at evenly sampled 0.1mm intervals through

the optical system along the x-axis. A diagram of a cross-section of the tube with the laser beam focusing is shown in Fig. 6-3. Due to the focusing of the beam by the tube, the beam interrogated a fluid volume of approximately 1.12ml and had a beam diameter at the center of the cavity of 0.6mm.

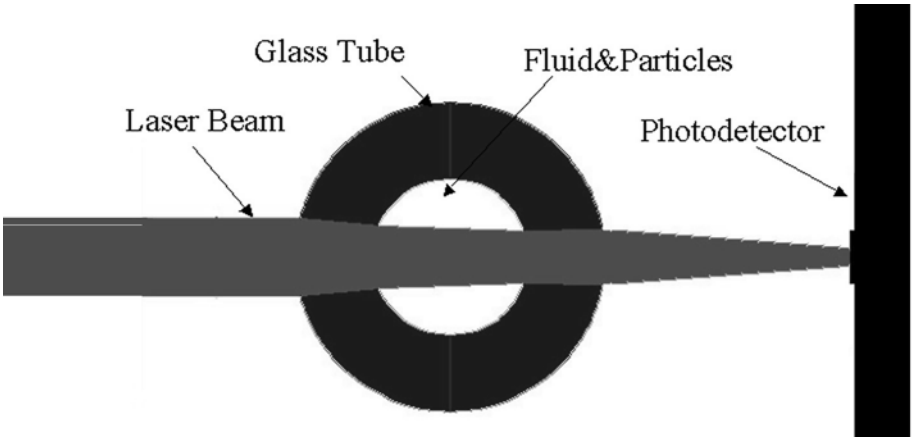

Figure 6-3: Cross-section of extinction experimental apparatus with approximate position of detector indicated.

The Beer-Lambert Law describes the proportionality between optical absorbance of a solution and concentration. It can be re-expressed to calculate number of particles in the interrogation volume from transmitted light measurements as

$$N=\ln\left(\frac{I_0}{I}\right)\frac{V}{\sigma d} \tag{6.3}$$

where N is the number of particles in the interrogation volume V, I_0 is the incident light intensity, I is the exit light intensity, d is the path length of

light, and σ is the absorption cross-section also called the extinction coefficient. For the purpose of these experiments, the extinction coefficient is determined using the first data point corresponding to the homogeneous particle distribution for each trial. The coefficients for the three trials are summarized in table 6-2.

Trial 1	9.59566E-07 cm^2/particle
Trial 2	9.58732E-07 cm^2/particle
Trial 3	9.56238E-07 cm^2/particle

Table 6-2. Calculated σ values for the three experiments.

As can be seen in Table 6-2, the sigma values are nearly equal for the three trials. The value of d is taken as the average path-length of the beam, approximately 1.84mm. The resulting values for N are normalized against the number of particles in the entire cavity, based on the initial 0.25% homogeneous distribution in the fluid, equating to approximately 4.55E6 particles/ml.

No flow is utilized, so particles are observed to eventually settle out of suspension. In the first trial the data, shown in Fig. 6-4, was taken every 30 seconds; subsequent experiments were taken at 10 second intervals. A 0.1W acoustic field was applied just after the time equal to zero point. Each of the trials shows approximately the same amount of time for concentration. The region to the right of the peak observed in each dataset corresponds to

settling of the particles out of solution and thus out of the interrogated beam. The settling of particles occurred as a column down the central axis of the tube.

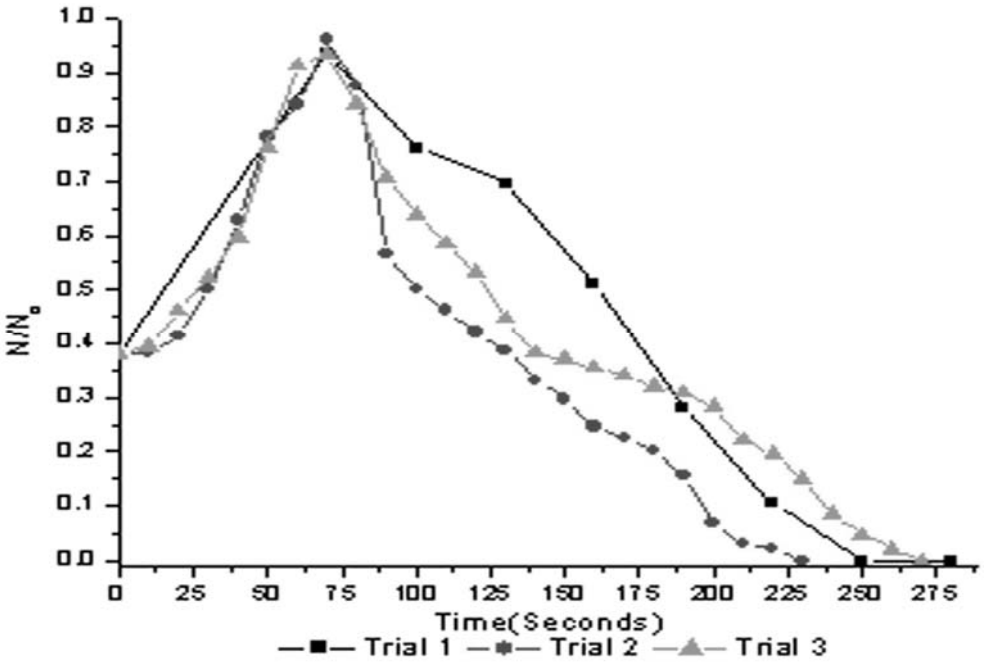

Figure 6-4: Data calculation of number of particles contained in the interrogated volume under acoustic excitation normalized against total number of particles in the whole cavity.

6.5-Acoustics in Flow Cytometry

After successful optical detection of acoustic concentration using the extinction apparatus described in the previous section, the next logical step is

validation of structural excitation as a method of acoustic focusing in a standard flow cytometry optics test bench.

Commercial flow cytometry sorters use orifice sizes ranging from 50 to 400 microns in diameter to accommodate analysis and sorting of particles of varying sizes. Using the rule of thumb that a channel must have a diameter 5x greater than the particle under analysis to prevent clogging from aggregates and because most particles of interest (microspheres, eukaryotic cells, and bacteria) will have less than 30 micron diameters, it will be possible to use nearly 150 micron channels (which will significantly limit clogging) to analyze samples at concentrations as high as 1×10^6 particles/ml. Furthermore, reducing particle size and channel diameter will allow analysis of samples with concentrations as high as 10^8 particles/ml.

Assuming a cylindrical volume element defined by the intersection of the 20 μm wide laser beam and a 150 μm diameter flow channel, the volume from which particles will be concentrated from is simply the height of the laser beam multiplied by the cross sectional area of the channel, or 62.8 nanoliters.

Using a low particle concentration of 5×10^3 /ml and given 100% concentration efficiency, on average 0.314 particles will be found in the cylindrical volume element and thus in the interrogation volume formed by

the focused stream and the laser beam. If 10 μm diameter particles were used, they would be spaced by about 60 microns on average along the centerline of the channel, which is sufficient separation to clearly distinguish optical pulses. If concentrations that generate 0.5 particles within the interrogation volume is considered set as the maximum limit before coincidence becomes an issue, then decreasing the channel size will allow for higher concentrations of particles to be analyzed without coincidence effects under slower flow conditions than used in conventional flow systems, which use hydrodynamic focusing from sheath flow.

The average flow velocity for the acoustics experiments was approximately 25 m m/sec. The particles migrated to the center of the chamber and formed a stream approximately 35μm wide in a 2mm diameter channel. Since the structural excited acoustic system investigated both focuses and concentrates particles, it is possible to analyze high numbers of particles at low linear velocities. For example, a volumetric sample delivery rate of 2.5 ml/minute through a 2 mm diameter channel provides a core velocity (2x average velocity) of 8 cm/s (3). This is much slower than a traditionally focused flow cytometer, giving a transit time of about 250 μs through a 20 μm interrogation volume but because of the concentration effect

of the acoustic method, given a concentration of 10^6 particles/ml flowing through a 2 mm channel this allows approximately 1300 particles per second to be analyzed. Importantly, even at this high analysis rate the transit time is 250 μs. This slow transit time (~20 to 100 times slower than conventional systems) allows high particle analysis rates using lower speed data acquisition systems that are less expensive, smaller and require less power. Furthermore, the extended transit times provides an opportunity to collect optical signals for longer times and thus allows high sensitivity measurements using lower power light sources, further lowering power requirements.

The sample was delivered into the cell with a precision syringe pump. It is very important that the particle stream be positioned as precisely as possible through the optical interrogation point (laser spot). Structural excitation of the tube is advantageous for two reasons. First, the extended source formed by the entire test flow structure as the source aperture translates into longer residence times of the particles within the acoustic positioning field. The longer residence time allows for the use of lower pressure levels to drive the acoustic focusing field. This alleviates the problem associated with cavitation in an ultrasonic field that would be responsible for damaging fragile biological particles (e.g. red blood cells or

leukocytes).

Second, by allowing the flow channel structure to serve as a three dimensional extended source with circular symmetry, the wave field creating the acoustic force potential within the flow chamber will have a predominantly radial dependence. In a wave field driven with a dipole type excitation constrained by circular symmetry, the particles are transported to the exact center of circular symmetry – the axis of the circular flow chamber. The high degree of radial symmetry equates into a precise position of the particle stream down the channel axis and results in a sample stream focused in two dimensions (parallel and perpendicular to the drive transducer face).

The structural acoustic concentrator was placed on a standard flow cytometry test bench. Measurements were made of 10-micron fluorescently tagged polystyrene spheres. A top-view diagram of the test apparatus is shown in Fig. 6-5. Since the laser beam diameter is approximately 1mm at the exit of the diode laser, a collimating lens system was used to reduce the beam waist to 200μm without introducing wave-front curvature. A syringe pump, not shown in the diagram, was used at 0.5ml/min and 2ml/min flow rates to flow particles through the tube at a calibrated volumetric rate. The fluorescence detector consisted of a photomultiplier tube (PMT) and collection optics. A small light was placed in-line with the PMT to assist in

assuring alignment between the laser, tube, and detector, measured with the alignment camera. Optical filters are used to select the fluorescence wavelengths and ignore the scattered light. The computer designated DAQ at the far right of diagram captured the signals.

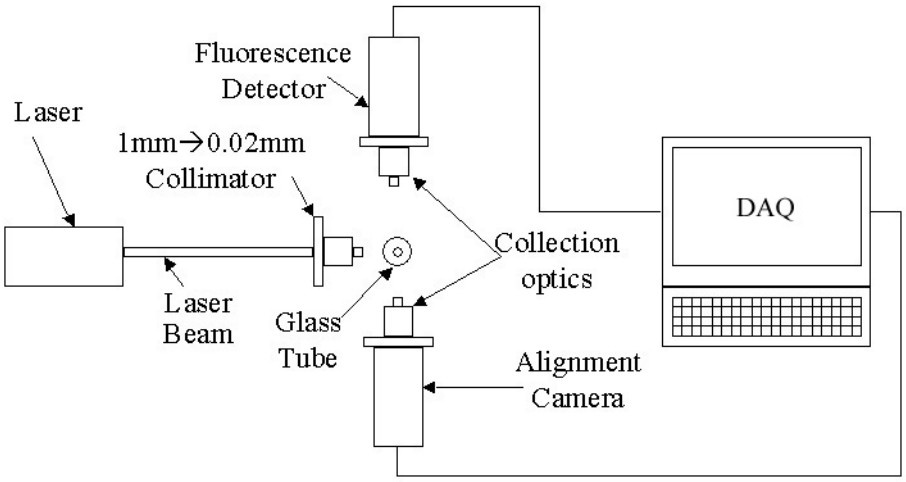

Figure 6-5. Diagram of test setup used in preliminary application in flow cytometry system.

A photograph of the apparatus is presented in Fig.6-6. The diode laser is visible on the far left, while the syringe pump is on the far right. The tube is centered in the image at the intersection of the laser, fluorescence detector and alignment camera (front-center). Figure 6-7 displays the intersection region in greater detail.

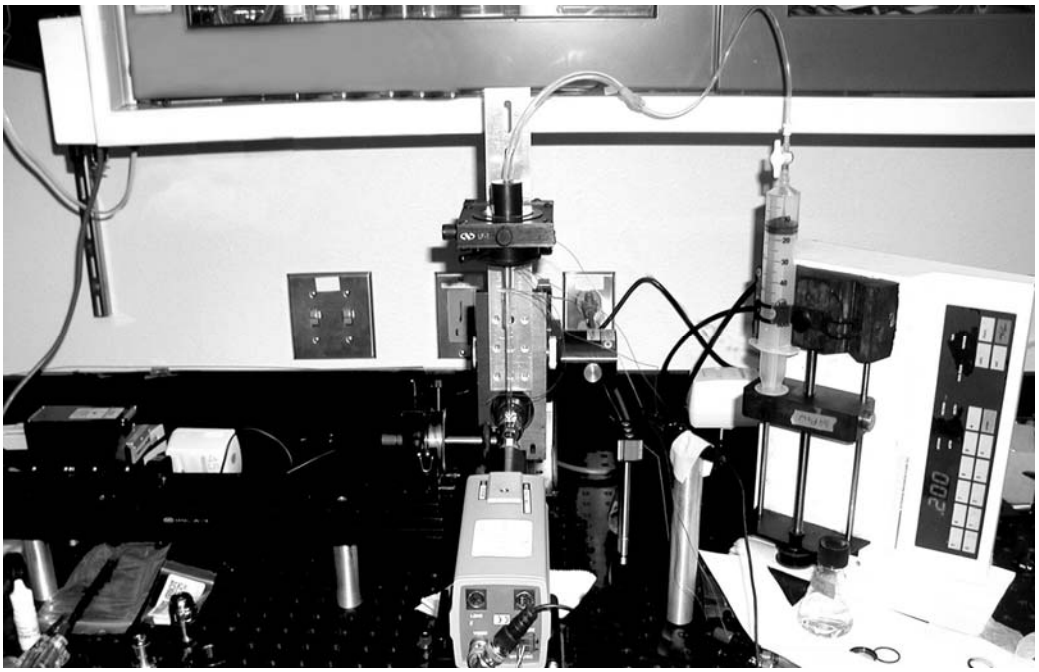

Figure 6-6. Picture of test setup used in preliminary application in flow cytometry system.

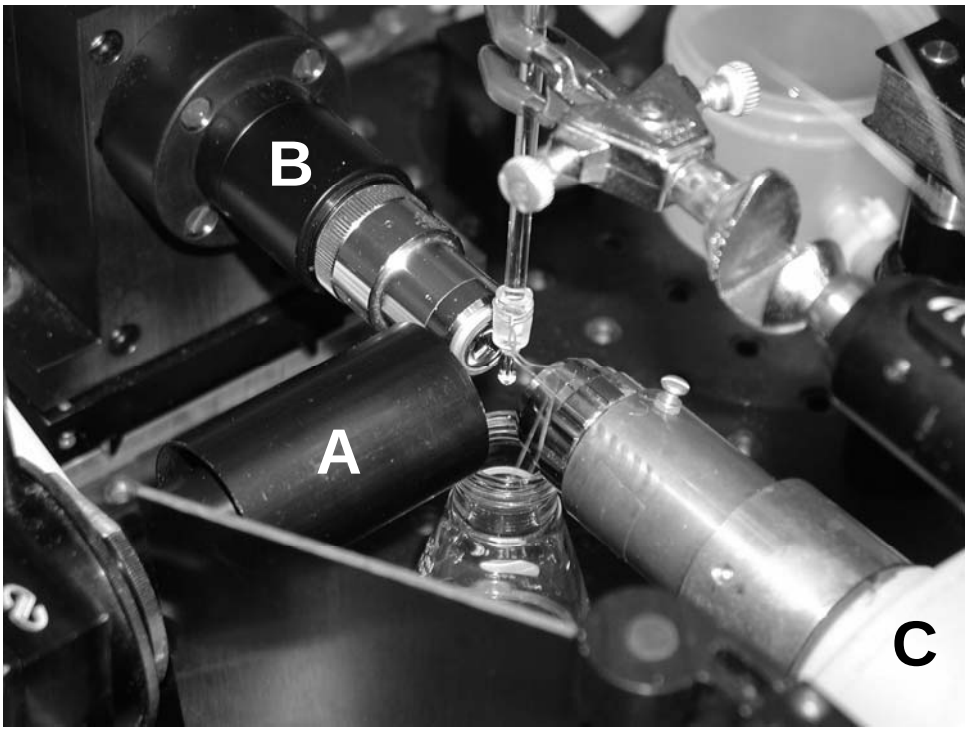

Figure 6-7. Close up of interrogation region used in preliminary test system. (A) Laser & Collimator (B) Fluorescence camera (C) Alignment camera

The tube entering from the bottom left is the laser collimation lens system. The fluorescence collection optics are at the top left; the alignment camera is at the bottom right. The soft glass tube, including the coupler and square cuvette is at the center of the region between the three lenses.

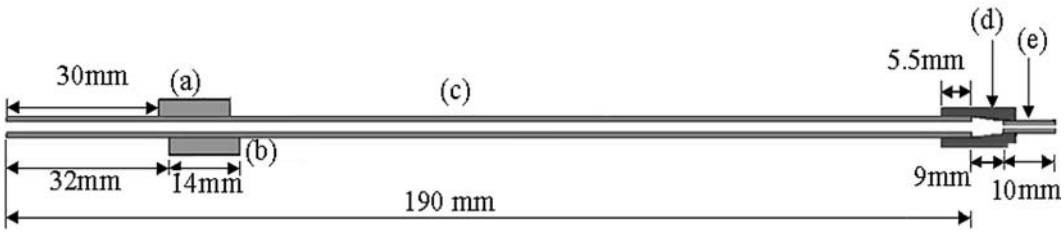

Figure 6-8. Diagram of tube setup used in preliminary application in flow cytometry system.

Certain parts of the setup are designated a-e Fig. 6-8. Elements (a) and (b) are the driven and tuning transducers respectively. They are both approximately 14mm long, 1.5mm wide and 3mm thick (vertical). The soft glass tube is designated (c). It is 190mm long with inner and outer diameters of 1.9mm and 3.92mm respectively. At the end of the tube, a conical transition and connector designated (d), are fashioned with a polystyrene tapered tube inside a $1/8^{th}$ inch inner diameter, $1/4^{th}$ inch outer diameter section of Tygon tube. Element (e) is 10mm long section of 2.2mm wide square flow cuvette. The walls are 1mm thick, yielding a 200μm cavity. The purpose of the square cuvette is the avoidance of cylindrical focusing of the interrogation laser beam by the soft glass tube.

The 10-micron fluorescent polystyrene particles are diluted to a concentration of 0.11% by volume using distilled water. The tubes are vortexed before each experiment to break agglomerations of particles. All

fluid and experimental apparatus are equilibrated at room temperature. Acoustic power levels are approximately 0.5W at 413.4 kHz. The shift of coupled dipole resonance frequency is probably due to the differences between the sound speeds in the fluid. Resonance is stable throughout the experiment. It is measured and maintained using a receive transducer opposite the drive transducer. Two pairs of data were captured at 0.5ml/min and 2ml/min with and without the acoustic concentrating field.

The results of the 0.5ml/min flow experiments are presented in Fig.6-9. The x-axis corresponds to fluorescence intensity bins. The y-axis corresponds to number of particles in each of the bins. If particles are evenly distributed throughout the cavity, they will intercept varying amounts of the excitation laser beam, and will therefore only have some of their fluorophores excited. The resulting fluorescence emission intensity from each particle is proportional to the number of excited fluorophores. The resulting data would be an even distribution of intensities in the bins. If, on the other hand, the particles are focused to the center of the cavity and intercept the beam completely, then all of the particles would experience equal intensity of the exciting laser, and a relatively narrow distribution of fluorescence intensity would be observed in the data.

As can be seen in Fig.6-9a, in the absence of an acoustic field, the

noise amplitude is relatively large, and there is no sharply defined peak. In the case when an acoustic field is applied, as Fig. 6-9b, there is a very sharply defined peak, with much smaller noise amplitude. The coefficient of variance of the peak is much smaller, as expected which indicates good concentration.

The next experiment was at 2ml/min flow rate. The results of those experiments are displayed in Fig.6-10. As before, Figure 6-10a shows the data without an acoustic field and Figure 6-10b shows the data with an acoustic field. The coefficient of variation(CV), defined as the standard deviation of the particle positions divided by the mean position, is much smaller when acoustic concentration is employed. The width of the peak is slightly wider than the 0.5ml/min experiment, which is expected due to smaller residence times of particles in the concentration field.

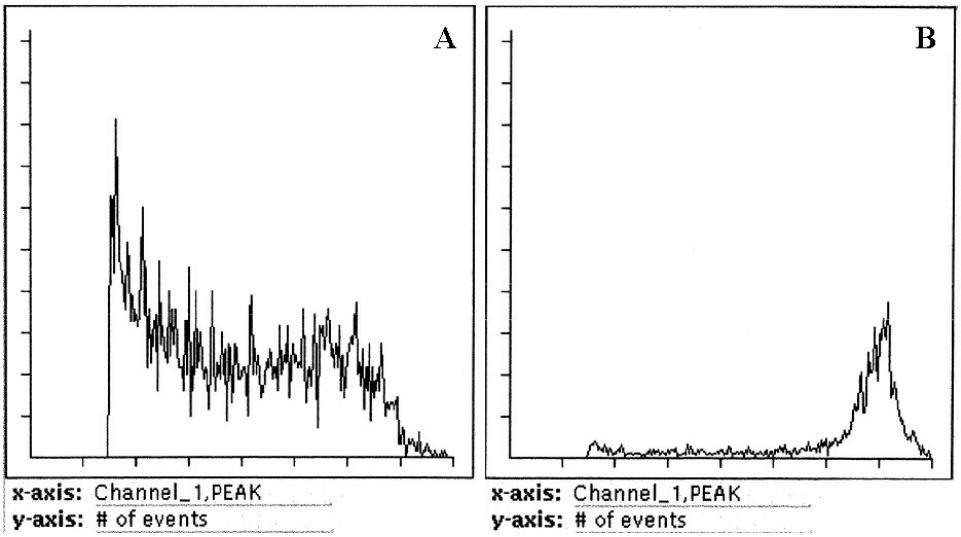

Figure 6-9. Results from 0.5ml/min flow experiments. (A) Without acoustic field (B) With acoustic field.

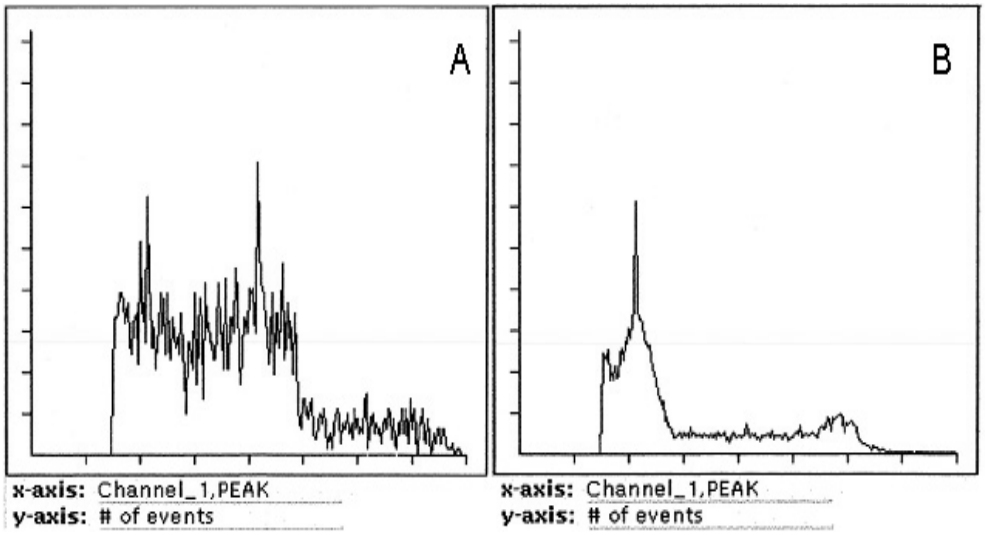

Figure 6-10. Results from 2ml/min flow experiments. (A) Without acoustic field (B) With acoustic field.

Video capture at the two flow rates yielded a particle stream width of 40μm to 60μm. The quality of the line could be improved in three ways: transducer/tubing coupling, higher power, or higher drive frequency. The transducer/tubing coupling could be improved with more careful alignment of the transducer, or, as in previous experiments, by flattening one side of the tube. The limitations on higher power and higher frequency are discussed in a previous chapter. It was observed in these experiments that higher power with faster flow rates required less power to disrupt the concentration process. If a vortex was generated, it passed through the tube much faster than in prior experiments and would thereby disrupt any concentration before

the vortex could dissipate. Due to the dependence asserted thus far on coupled fluid-structure dipole resonance for axial concentration, increasing the frequency would require tube inner diameter reduction. This solution offers several benefits. The flow rate is required to be high and/or the concentration of particles is required to be low to maintain the detection rates used by standard flow cytometers. Although a limitation of clogging or resonance perturbation of the cavity would restrict the smallest dimension of the cavity, the ideal would be nominally above that limit, as forces would be maximized at that point.

6.6-Technique Evaluation

Since the experiments are intended as a validation of possible applicability of acoustic concentration under standard flow cytometry conditions, only standard fluorescent 10-micron beads were measured. Hence, the experiment only served as a qualitative validation of applicability.

For quantitative evaluation of acoustic concentration as a replacement for sheath flow, the acoustic focusing flow cell would require evaluation both by video imaging of the flowing stream and by collecting fluorescence and scatter measurements of flow cytometry calibration and alignment microspheres. Alignment microspheres are extremely monodisperse in size

and fluorescence intensity and the variation of the fluorescence and scatter values will quantitatively characterize the fluidic stability of an optimally aligned system[204]. The CV of flow cytometry alignment microspheres flowing in the system serves as a metric of system stability [204].

The fluidic stability of the system could be evaluated by simply flowing fluorescent dye in the sample stream and measuring fluorescence intensity as a function of time and flow rates as well as observing microspheres in flow. Sample steam instability would be revealed as fluctuations in the fluorescence measurements and would result in decreased resolution of the alignment microspheres and thereby increased coefficient of variation. Sensitivity could be evaluated using flow cytometry calibration microspheres (84) and other microspheres with precisely determined low levels of surface attached fluorophores. Both of these approaches are common and accurate in reporting the measurement sensitivity and precision of flow cytometers.

The ability of the system to resolve free vs. bound probe molecules could be evaluated by placing fluorescein calibration microspheres in increasing concentrations of free fluorescein-dextran, which does not bind to the calibration microspheres. The ability of the of the flow cells to discriminate free vs. bound would then be quantified by their ability to resolve dimly labeled microspheres within a fluorescent background. This is

important as acoustic focusing is different than traditional methods and it must be ascertained if the acoustic focusing flow cell can maintain resolution of free vs. bound fluorophores. All evaluation parameters (stability, sensitivity, and free vs. bound) of the acoustic flow cell would then be compared to standard flow cytometry flow cells.

6.7-Conclusion

Once structural excitation is shown to be a potentially efficient concentration/fractionation method for particles in suspension, the next step was a preliminary demonstration of acoustic concentration applicability to the replacement of sheath flow in flow cytometry. The high analysis rates, lack of separation steps, and varied applications ranging from medicine to homeland defense has made flow cytometers a fixture in nearly every research and diagnostic lab. However, the size, expense and requirement for large amounts of consumables have limited flow cytometry to formal laboratory settings.

Acoustic concentration can allow a sheathless portable flow cytometer to achieve conventional particle analysis rates, maintain excellent optical and analytical properties and increase instrument portability, while using a fraction of the power and consumables of a conventional flow cytometer.

This will allow the construction of a truly portable flow cytometer. Such an instrument would make the full range of applications of flow cytometry available to all clinicians and researchers, which would have an enormous impact on the advancement of world health and research where it has critical applications in AIDS progression monitoring and cancer diagnosis.

Two experiments were performed to verify the feasibility of acoustic concentration. In the first experiment, optical extinction was measured to approximately determine the efficiency of particle movement to the central axis. These experiments showed nearly 100% concentration to within 300μm of the central axis. In the second validation experiment, the structural acoustic concentrator was placed on a standard flow cytometry test bench. Measurements were made of fluorescently tagged polystyrene spheres. The coefficient of variation was found to decrease significantly and reproducibly when a resonant acoustic field is applied to the system. While the concentrated particle stream had a spatial deviation of approximately +/- 15-microns, further system optimization has improved the stream to +/-5-micron deviation for 10-micron spheres and +/-1-micron deviation for 1-micron spheres under higher frequency excitation. The relatively tight focus of these particles demonstrates the potential utility of this method in eliminating sheath from a flow cytometer, thereby greatly reducing the consumables and

increasing the field portability of the system. Future research directions could include further quantification, which would be necessary to accurately evaluate stability and resolution of structural acoustic concentration against standard hydrodynamic focusing methods currently used in flow cytometers in the instrument engineering process.

7-CONCLUSION

The objective of this project was the investigation of structural excitation as a potentially efficient concentration/fractionation method for particles in suspension. The traditional methods of acoustic concentration utilize quarter wave matching layers, half-wavelength cavities and require careful alignment for an axially non-symmetric system. Using an inherently symmetric geometry for the system eliminates the need for careful alignment. Any small imperfections in the tube translate into small perturbations in the field, which are usually ameliorated by a small frequency change. Once the appropriate frequency is determined, the system never changes.

Traditionally, when opposing transducers are used in a cavity, the position of the transducer is used to adjust the resonance of the cavity. Over time, the transducers misalign from small jolts to the system. The far more intriguing possibility is in the excitation of the field. In all traditional acoustic separation and manipulation techniques, the acoustic field is only present directly in line with the exciting transducer. In flowing systems, the residence time of the particles in the acoustic field is limited by the physical size of the transducer. This limitation demands larger amounts of energy be pumped into the transducer to compensate for this short interaction time scale. This

large energy pumping into the flow volume leads to large temperature fluctuations, cavitation and convection. By exciting the entire tube structure, the active region is not limited by the size of the transducer, but rather by the size of the structure. The acoustic field is dispersed throughout this larger volume leading to significantly lower acoustic energy densities within the flow stream. Thus, temperature effects are not induced and residence times of the particle in the field are dramatically increased. It was demonstrated that structural excitation of a cylindrically symmetric cavity, such as a tube, allows non-invasive, fast, and low power concentration of particles suspended in a fluid. The following sections are split into summaries of the work described in the preceding chapters.

7.1-Concentration Experiments

The central focus of this research was the ability to concentrate particles in aqueous suspensions. The acoustic forces experienced by the particles consisted of primary and secondary components. An expression for acoustic forces on particles in the acoustically excited cavity, accounting for viscous and thermal dissipative mechanisms, was developed and applied predictively. Two microscopy methods were utilized to image the concentration pattern. Four types of tube, three sizes of particles, and two

types of fluid were utilized in the process of the investigation.

The coupled tube-cavity dipolar resonance is shown to efficiently concentrate particles to the central axis of the tube. Additionally, it was demonstrated that the inner diameter of the tube is the dominant factor in determining the frequency of coupled dipole resonance. Perturbations to the exterior of the tube only appeared to affect axial standing waves. Coupling of the transducer to the tube is shown to be the primary factor in determining concentration speed and quality.

An investigation of the efficacy of multiple transducer excitation of the tube was performed. Driving transducers attached serially along the length of the tube collinearly did not increase concentration quality, but did increase concentration speed. Excitation using multiple transducers required greater power consumption with the only observed benefit being the avoidance of vortices or thermal convection at higher input powers. The net effect was the reduction of power input into each transducer, thus further distributing the energy throughout the tube. No limitation is observed to structural excitation distance along the tube with a single transducer. The vibration phase and for the most part, amplitude, when no axial standing wave is present, remained the same down the length of the tube and supported the characterization of concentration resonances as dipolar.

It is shown both theoretically and experimentally that greater acoustic forces are exerted on the particles perpendicular to the face of the drive transducer along the phase symmetry line as compared to parallel to the transducer face. An investigation of limitations on excitation power demonstrated critical points beyond which vortex formation significantly disturbed the concentration pattern. Axial standing waves manifestation occurred at any power level capable of concentration, so long as the necessary power is reached for maintaining suspension. Powers at which thermal convection or cavitation occurred exceeded the power necessary to induce vortices in the fluid so vorticies are used as indicators of deleterious power levels.

7.2-Model of Structural Excitation

A general two-dimensional model for a line driven cylindrical tube was developed. The validity of the model was experimentally verified for several types of empty and fluid-filled glass tube. Dipole vibration of the exterior of the tube is predicted and experimentally verified as indicative of efficient coupling from the cylindrical structure into the fluid-filled cavity. Furthermore, the potential use of alternate tube materials was theoretically evaluated. It is argued that while all materials are capable of dipolar vibration, the greatest

coupling of energy into the cavity occurred with glass tube. Metals are predicted to be a poor choice to replace the glass tube used for these experiments. Predictions of asymmetry of acoustic forces within the cavity are also made based on the theoretical predictions. Generalization to the 3-dimensional case was possible, but was not performed in the interest of computational efficiency.

7.3-Limitations on Technique

Certain limitations exist to the concentration of particles by structural excitation. The limitations discussed are inherent in the method and arose predominately through five aspects: acoustic contrast ratio, higher power disruptive effects, cavity size/excitation frequency, thermal resonance perturbation, and particle resonance perturbation. Although the limitations are not completely avoidable, higher power, selection of geometry for higher coupled dipole resonance frequency; larger particles or larger agglomerations of particles, and resonance maintenance through feedback loops can be used to extend the usable range of structural excitation for concentration.

The acoustic contrast ratio more specifically refers to four terms in the acoustic force equations. The terms are dependent on sound speed, density,

viscosity, and thermal conductivity differences between the fluid and the particles. For polystyrene beads in water, the density and sound speed contrast terms are approximately four orders of magnitude greater than the viscosity term and approximately six orders of magnitude greater than the thermal conductivity contrast term.

An experiment was performed which changed the suspending fluid material and thereby the acoustic contrast ratio between the particles and the fluid causing an expected shift in resonant frequency while slightly lowering the necessary input power for particle concentration.

In addition to the four contrast terms, there is also a cubic dependence of the acoustic force on frequency of resonance and particle size. Hence changing the cavity dimensions, and thereby the resonance frequency, or increasing the particle size also improved the concentration efficiency.

An experimental investigation was performed into the experimental limitation on particle size for concentration. As expected, decreasing the chamber radius and thereby increasing the resonant frequency, or increasing particle size consequently increased acoustic radiation pressure on the particles. .

Due to the distributed nature of structural excitation high power is not necessary for efficient particle concentration. If higher flow rates, or smaller

particle increased the power requirements of the system, convective heating and acoustic streaming would provide limits on the maximum useful power input. Since acoustic attenuation of water is nearly the lowest of any fluid, thermal convection would arise predominately through transducer heating of the tube. This could be reduced by either changing the drive transducer to a higher impedance piezoceramic, or by utilizing efficient cooling on the excitation transducer. An expression was derived for the power limitation imposed by acoustic streaming.

The remaining two contrast terms, corresponding to thermal perturbation of resonance or particle perturbation of resonance could be mitigated by tracking and maintaining resonance of the system. This could be used as a compensatory technique up to the limit when kR_p, the resonance wavenumber times the particle radius approaches one. Also noted in chapter 5, another remaining limitation on the minimum particle size arises through the competition of acoustic concentration forces with Brownian motion. Greater input power or lower temperatures are the most common methods of combating that limitation. The negative effects of resonance frequency change by either temperature perturbation or particle perturbation on concentration could be mitigated through phase lock loops, amplitude lock loops, impedance lock loops, or time-dependent frequency excitation to

maintain resonance of the system and thereby assure successful concentration.

7.4-Flow Cytometry Application

Once structural excitation is shown to be a potentially efficient concentration/fractionation method for particles in suspension, the next step is a preliminary demonstration of acoustic concentration efficacy towards the intended application of sheath flow replacement in flow cytometry.

The high analysis rates, lack of sample/molecular tag separation steps, and varied applications ranging from medicine to homeland defense has made flow cytometers a fixture in nearly every research and diagnostic lab. However, the size, expense and requirement for large amounts of consumables have limited flow cytometry to formal laboratory settings.

Acoustic concentration can allow a sheathless portable flow cytometer to achieve conventional particle analysis rates, maintain excellent optical and analytical properties and increase instrument portability, while using a fraction of the power and consumables of a conventional flow cytometer. This will allow the construction of a truly portable flow cytometer, making the full range of applications of flow cytometry available to all clinicians and researchers, which would have an enormous impact on the advancement of

world health and research where it has critical applications in AIDS progression monitoring and cancer diagnosis.

Two experiments were performed to verify the feasibility of acoustic concentration. In the first experiment, optical extinction was measured to approximately determine the efficiency of particle movement to the central axis. All of the particles in the cavity were focused to within 300 μm of the center of the cavity. In the second validation experiment, the structural acoustic concentrator was placed on a standard flow cytometry test bench.

While the concentrated particle stream had a spatial deviation of approximately +/- 15-microns in initial experiments, further system optimization has improved the stream to +/-5-micron deviation for 10-micron spheres and +/-1-micron deviation for 1-micron spheres under higher frequency excitation. Future research directions could include further quantification, which would be necessary to accurately evaluate stability and resolution of structural acoustic concentration against standard hydrodynamic focusing methods currently used in flow cytometers in the instrument engineering process.

7.5-Future Directions

While the experiments thus far have been successful in proving the

efficacy of structural excitation as a method of acoustic concentration, several directions would benefit from further exploration beyond the scope of this research. These directions are not critical to the understanding of the physics behind the method, but whose clarity would allow for easier engineering of instruments based on the method. The questions can be separated into several categories based on the properties of the system: static, computational, and dynamic. While this list is not exhaustive in any sense, it does offer directions of particular interest to the author.

Within the remaining questions about static properties of the system, tube materials, coupling efficiency, and pertubative effects are of particular interest.

For the experiments, only variations in type of glass tube were investigated. Predictive calculations were performed using the global matrix method for resonance frequency and quality for several types of metal and plastic tube. Experimental verification of these predictions would be instructive for the optimization of the system. Furthermore, only PZT was used for these experiments, other piezoelectric, or magnetostrictive materials might work more efficiently. Again, this direction focuses on optimization of the system.

The transducer/tubing coupling was achieved using hand alignment

and cyanoacrylate glue. It is observed that assuring good contact is important not only for power consumption, but also for the preferential excitation of particular orthogonal modes of the tube. This direction is also primarily focused towards system optimization.

Although preliminary experiments involving acid, base, and polymer coating treatments of soft glass tube into the effects of internal surface treatment and coatings to the tube showed no substantial effects, greater depth of experimentation would be necessary if the application intended for the method required either surface functionalization, or passification, if only to verify no effect.

Another interesting direction of study into static aspects of the system is the geometry of the system. Experiments that investigated the effects of flattening one side of the tube or asymmetric tube showed resonance broadening, but no change was made to the inherent symmetry of the cavity. It would be interesting and instructional to determine the limits of geometric perturbation, or simply investigate the structural resonances of other geometries and the ability of those systems to manipulate particles.

Future computational directions of investigation can be described as generalization of the model to include effects such as fluid viscosity, fluid-solid interactions, or allow for geometrical variation. The model put forth in

this paper made several large assumptions. The first of these is assumption of perfectly cylindrical geometry with infinite bandwidth transducer. Modeling of the transducer material and the characteristic resonances of the excitation source would allow for mass loading and resonance peak width inclusion. No significant effects are observed by neglecting any asymmetry in the physical system, but the perturbations are relatively small, even for the thick quartz tube.

The fluid is assumed to be inviscid and only possessing radial interaction with the internal surface of the tube. Viscosity in this statement is referring to the self-interaction effects, while liquid-solid interactions include chemical, charge, and boundary layer interactions. Although these inclusions add complexity to the equation, they are necessary for a quantitative analysis of forces on the particles in the fluid.

In chapter 2, a model was developed to describe the system. Several calculations were done to predict particle trajectories. A quantitative comparison to predictions and a correlation of predicted and observed concentration speed would be extremely valuable in the system optimization process.

The final category of investigative interest is flow. Relatively low flow rates were used for all of the experiments described in previous chapters.

For the purposes of scaling, it would be important to find the nonlaminar flow limit at which acoustic concentration is no longer possible. Another instructive point for experimentation is the stability and concentration quality of stepping the fluid column radius down using a coupler to accelerate the flow rate and decrease radial distribution of the sample stream.

[1] A. Kundt, and O. Lehmann, “Ueber longitudinale Schwingungen und Klang-figuren in cylindrischen Flussigkeitssaulen”, *Annalen der Physik und Chemie (Poggendorff’s Annalen)*, **153**,1-11 (1874)

[2] K. Yasuda, S. S. Haupt, S Unemura, “Using acoustic radiation force as a concentration method for erythrocytes,” *J. Acoust. Soc. Am* **102**, 642-645 (1997)

[3] K. Yasuda, “Non-destructive, non-contact handling and concentration of μm-sized particles in liquid using superposition method of ultrasound,” in *Micro-Electro-Mechanical Systems (MEMS).* 2000, ASME International Mechanical Engineering Congress and Exposition, Nov. 2000, Orlando, 393-396, (2000)

[4] P. Vainshtein, M. Fichman, K. Shuster, C. Gutfinger, “The effect of centerline particle concentration in a wave tube,” *J. Fluid Mech.* **306**, 31-42 (1996)

[5] K. Yasuda, S. Unemura, K. Takeda, “Concentration and fractionation of small particles in liquid by ultrasound,” Jpn*. J. Appl. Phys. Pt 1 5B*. **34,** 2715-2720, (1995)

[6] A. Goldshtein, K. Shuster, P. Vainshtein, M. Fichman, C. Gutfinger, “Particle motion in resonance tubes,” *J. Fluid. Mech.* **360,** 1-20 (1998)

[7] T. L. Tolt, D. L. Feke, “Separation devices based on forced coincident response of fluid-filled pipes,” *J. Acoust. Soc. Am.* **91**, 3152-3156(1992)

[8] T. L. Tolt, D. L. Feke, “Separation of dispersed phases from liquids in acoustically driven chambers,” *Chem. Eng. Sci.* **48**, 527-540 (1993)

[9] S. Gupta, D. L. Feke, “Fractionation of mixed particulate solids according to compressibility using ultrasonic standing wave fields,” *Chem. Eng. Sci.*, **50**, 3275-3284 (1995)

[10] M. C. Bekker, J. P. Meyer, L. Pretorius, D. F. Van Der Merwe, “Separation

of solid-liquid suspensions with ultrasonic acoustic energy," *Wat. Res.* **31**, 2543-2549 (1997)

[11] G. Whitworth, M. A. Grundy, W. T. Coakley, "Transport and harvesting of suspended particles using modulated ultrasound," *Ultrasonics*, **29**, 439-444, (1991)

[12] G. Whitworth, W. T. Coakley, "Particle column formation in a stationary ultrasonic field," *J. Acoust. Soc. Am.* **91,** 79-85 (1992)

[13] C. M. Cousins, J. R. Melin, W. A. Venables, W. T. Coakley, "Investigation of enhancement of two processes, sedimentation and conjugation, when bacteria are concentrated in ultrasonic standing waves," *Bioseparation* **9**, 343-349 (2001)

[14] T. Masudo, T. Okada, "Particle Characterization and Separation by a Coupled Acoustic−Gravity Field", *Analytical Chemistry,* **73,** 3467-3471 (2001)

[15] R. K. Gould, W. T. Coakley, "The effects of acoustic forces on small particles in suspension", in *Proceedings of the 1973 Symposium on Finite Amplitude Wave Effects in Fluids*, edited by L. Bjorno, Pergamon, Guildford, 1974, 252-257

[16] H. M. Hertz, "Standing-wave acoustic trap for nonintrusive positioning of microparticles," *J. Appl. Phys*. **78,** 4845-4849 (1995)

[17] A. Haake, J. Dual, "Micro-manipulation of small particles by node position control of an ultrasonic standing wave," *Ultrasonics* **40**, 317-322 (2002)

[18] M. Takeuchi, K. Yamanouchi, "Ultrasonic micromanipulation of small particles in liquid," *Jpn. J. Appl. Phys Pt.1 5B.* **33,** 3045-3047(1994)

[19] Y. Yamakoshi, Y. Noguchi, "Micro particle trapping by opposite phases ultrasonic traveling waves," *Ultrasonics*, **36**, 873-878 (1998)

[20] W. T. Coakley, D. W. Bardsley, M. A. Grundy, F. Zamani, D. J. Clarke, “Cell manipulation in ultrasonic standing wave fields,” *J. Chem Tech. Biotechnol.* **44** 43-62, (1989)

[21] W. T. Coakley, G. Whitworth, M. A. Grundy, R. K. Gould, R Allman, “Ultrasonic manipulation of particles and cells,” *Bioseparation* **4**, 73-78 (1994)

[22] J. J. Hawkes, D. Barrow, W. T. Coakley, “Microparticle manipulation in millimetre scale ultrasonic standing wave chambers,” *Ultrasonics*, **36**, 925-931 (1998)

[23] W. T. Coakley, J. J. Hawkes, M. A. Sobanski, C. M. Cousins, J. Spengler, “Analytical scale ultrasonic standing wave manipulation of cells and microparticles,” *Ultrasonics*, **38**, 638-641 (2000)

[24] K. Higashitani, M. Fukushima, Y, Matsuno, “Migration of suspended particles in plane stationary ultrasonic field”, *Chem. Eng. Sci.* **36**, 1187-1192 (1981)

[25] M. Saito, K. Itagaki, K. Hayashi, K. Tsubata, “Composite materials with ultrasonically induced layer or lattice structure,” Jpn. J. Appl. Phys. Pt. 1 5B**38**, 3028-3031, (1999)

[26] S. Yamahira, S. Hatanaka, M. Kuwabara, S. Asai, “Orientation of fibers in liquid by ultrasonic standing waves,” Jpn. J. Appl. Phys. Pt. 1 5B**39**, 3683-3687(2000)

[27] Z. Mandralis, W. Bolek, W. Burger, E. Benes, D. L. Feke, “Enhanced synchronized ultrasonic and flow-field fractionation of suspensions,” Ultrasonics, **32(2)**, 113-121, (1994)

[28] Z. Mandralis, D. L. Feke, “Continuous suspension fractionation using acoustic and divided-flow fields,” Chem. Eng. Sci., **38(23)**, 3897-3905, (1993)

[29] T. L. Tolt, D. L. Feke, “Separation of dispersed phases from liquids in acoustically driven chambers,” Chem. Eng. Sci. **48**, 527-540(1993)

[30] S. N. Semyonov, K. I. Maslow, “Acoustic field-flow fractionation,” J. Chromatography, **446**, 151-156, (1988)

[31] W. T. Coakley, D. W. Bardsley, M. A. Grundy, F. Zamani, D. J. Clarke, “Cell manipulation in ultrasonic standing wave fields,” J. Chem Tech. Biotechnol. **44** 43-62, (1989)

[32] G. Whitworth, M. A. Grundy, W. T. Coakley, “Transport and harvesting of suspended particles using modulated ultrasound,” Ultrasonics, **29** 439-444, (1991)

[33] A. Haake, J. Dual, “Micro-manipulation of small particles by node position control of an ultrasonic standing wave,” Ultrasonics **40** 317-322(2002)

[34] Y. Yamakoshi, M. Koshiba, Y. Ozawa, N. Masuda, “Trapping of micrometer size bubbles by ultrasonic waves,” Jpn. J. Appl. Phys. Pt. 1 5B **40** 1526-1527 (2001)

[35] T. Kozuka, T. Tuziuti, H. Mitome, F. Arai, T. Fukuda, Three-dimensional acoustic micromanipulation for using four ultrasonic transducers, In *Proc. 2000 International Symposium on Micromechatronics and Human Science,* IEEE Institute of Electrical and Electronics Engineers, pp 201-206 (2000)

[36] H. M. Hertz, “Standing-wave acoustic trap for nonintrustive positioning of microparticles,” J. Appl. Phys. **78** 4845-4849(1995)

[37] M. Wiklund, S. Nilsson, H. M. Hertz, “Ultrasonic trapping in capillaries for trace-amount biomedical analysis,” J. Appl. Phys., **90(1)**, 421-426, (2001)

[38] M. Wiklund, P. Spegel, S. Nilsson, H. M. Hertz, “Ultrasonic trap-enhanced selectivity in capillary electrophoresis,” Ultrasonics, **41**, 329-333, (2003)

[39] M. Saito, Y. Imanishi, “Host-guest composites containing ultrasonically arranged particles,” J. Material Science **35**, 2373-2377(2000)

[40] M. Saito, K. Itagaki, K. Hayashi, K. Tsubata, “Composite materials with ultrasonically induced layer or lattice structure,” Jpn. J. Appl. Phys. Pt. 1 5B**38**, 3028-3031, (1999)

[41] M. Saito, T. Daian, K. Hayashi, S. Izumida, “Fabrication of a polkymer composite with periodic structure by the use of standing waves,” J. Appl. Phys. **83(7)**, 3490-3494, (1998)

[42] G. J. Sparey-Taylor, C. Lewis, E. Chapper, P. Schiller, P. Kern, D. A. Barrow, J. J Cefai, Automated ultrasonic particle processing microsystem, In *Smart Electronics and MEMS II*, Proceedings of SPIE, **4236**, 2001 SPIE, 107-114, (2001)

[43] E. Benes, M. Gröschl, H. Nowotny, F. Trampler, T. Keijzer, H. Böhm, S. Radel, L. Gherardini, J.J. Hawkes, R. König, C. Delouvroy, Ultrasonic separation of suspended particles. In *Proc. 2001 IEEE Ultrasonics Symposium*, IEEE Institute of Electrical and Electronic Engineers, Atlanta, pp. 649-659

[44] M. Hill, R. J. K. Wood, “Modelling in the design of a flow-through ultrasonic separator,” Ultrasonics, **38** 662-665(2000)

[45] M. Hill, N. R. Harris, R. J. Townsend, N. M. White, S. P. Beeby, “Microfabricated ultrasonic particle manipulator with frequency selectable nodal planes,” in *WCU 2003, Paris,* September, 7-10,2003 1647-1650

[46] H. Bohm, L. G. Briarty, K. C. Lowe, J. B. Power, E. Benes, M. R. Davey, “Quantification of a novel h-shaped ultrasonic resonator for separation of biomaterials under terrestrial gravity and microgravity conditions,” Biotechnology and Bioengineering, **82(1)**, 74-84, (2003)

[47] Y. D. Zhang, J. I. Budnick, W. A. Hines,”Three dimensional alignment of

magnetic particles," J. Appl. Phys, **81**,5647-5649(1997)

[48] N. R. Harris, M. Hill, S. Beeby, Y. Shen, N. M. White, J. J. Hawkes, W. T. Coakley, "A silicon microfluidic ultrasonic separator," Sensors and Actuators B, **95** 425-434 (2003)

[49] T. Kozuka, "Non-contact acoustic filtering of particles in a standing wave field," In *2002 International Symposium on Micromechatronics and Human Science*, Proceedings of IEEE, **0-7803-7611-0**, 2002 IEEE, 165-168, (2002)

[50] L. Gherardini, S. Radel, S. Sielemann, O. Doblhoff-Dier, M. Groschl, E. Benes, A. J. McLoughlin, "A study of the spatial organization of microbial cells in a gel matrix subjected to treatment with ultrasonic standing waves," Bioseparation,**10**,153-162(2002)

[51] H. M. Shapiro, *Practical Flow Cytometry*. Hoboken, NJ: John Wiley & Sons, Inc. (2003)

[52] J. W. S. Rayleigh*, The Theory of Sound*, MacMillan Press, London, (1896)

[53] M. L. Baron, H. H. Bleich," Free and forced vibrations of an infinitely long cylindrical shell in an infinite acoustic medium," J. Appl. Mech., **21(2)**, 167-177, (1954)

[54] M. L. Baron, H. H. Bleich," Tables for frequencies and modes of free vibration of infinitely long thin cylindrical shells," J. Appl. Mech., **21(2)**, 178-184, (1954)

[55] A. E. H. Love, A Treatise on the Mathematical Theory of Elasticity, Dover, New York, (1944)

[56] W. Flugge, *Statik und Dynaamik der Shalen*, Springer-Verlag, Berlin, (1934)

[57] V. Z. Vlasov, "General theory of shells and its application to engineering,"

Moscow-Leningrad, 1949, NASA Tech. Trans, **99**, 1964-1968, (1949)

[58] L. H. Donnell, “A discussion of thin shell theory,” Proc. Fifth Int. Congr. Appl. Mech., (1938)

[59] L. H. Donnell, “Stability of thin walled tubes under torsion,” NASA Tech. Rep. 479, (1933)

[60] J. L. Sanders, “An improved first approximation theory for thin shells,” NASA Tech. Rep. R24, (1959)

[61] A. W. Leissa, “Vibrations of shells,” NASA SP-288, Washington DC, 1973, Natl. Tech. Inf. Serv., U.S. Dept. of Commerce, Springfield, VA 22162, (1973)

[62] I. Mirsky, G. Hermann, “Axially symmetric motions of thick cylindrical shells, “J. Appl. Mech., **25(1)**, 97-103, (1958)

[63] I. Mirsky, G. Hermann, “Nonaxially symmetric motions of thick cylindrical shells,” J. Acoust. Soc. Am., **29**, 116-123, (1957)

[64] A. H. von Flotow, “Disturbance propagation in structural networks,” J. Sound Vib. **106(3)**, 433-450, (1986)

[65] G. V. Borgiotti, E. M. Rosen, “The state vector approach to the wave and power flow analysis of the force vibrations of a cylindrical shell part I: Infinite cylinders in vacuum,” J. Acoust Soc. Am. **91**, 911-925(1992)

[66] G. V. Borgiotti, E. M. Rosen, “The state vector approach to the wave and power flow analysis of the force vibrations of a cylindrical shell part II: Finite cylinders in vacuum,” J. Acoust. Soc. Am. **93**, 864-874(1993)

[67] E. A. Skelton, J. H. James, “Acoustics of an anisotropic layered cylinder,” J. Sound and Vibration, **161,251**-264(1993)

[68] B. K. Sinha, T. J. Plona, S. Kostek, S. K. Chang, “Axisymmetric wave

propagation in fluid-loaded cylindrical shells I: theory," J. Acoust. Soc. Am. 92, 1132-1143, (1992)

[69] T. J. Plona, B. K. Sinha, S. Kostek, S. K. Chang, "Axisymmetric wave propagation in fluid-loaded cylindrical shells II: theory versus experiment," J. Acoust. Soc. Am., 92, 1144-1155, (1992)

[70] D. P. Schmitt, "Dipole logging in cased boreholes," J. Acoust. Soc. Am., **93**, 640-657, (1993)

[71] J. S. Sastry, M. L. Munjal, "Response of a multi-layered infinite cylinder to a plane wave excitation by means of transfer matrices," J. Sound and Vibration, **201(1)**, 99-121, (1998)

[72] D. L. Folds, C. D. Loggins, "Transmission and reflection of ultrasonic waves in layered media," J. Acoust. Soc. Am. **62(5)**, 1102-1109, (1977)

[73] L. Wang, S. I. Rokhlin, "Stable reformulation of transfer matrix method for wave propagation in layered anisotropic media," Ultrasonics, **39**, 413-424, (2001)

[74] L. Knopoff, "A matrix method for elastic wave problems," Bull. Seism. Soc. Am. **54** 431-438, (1964)

[75] M. J. S. Lowe, "Matrix techniques for modeling ultrasonic waves in multilayered media," IEEE Trans. Ultrason. Ferroelec. Freq. Contr. UFFC-42 525-542, (1995)

[76] D. C. Ricks, H. Schmidt, "A numerically stable global matrix method for cylindrically layered shells excited by ring forces," *J. Acoust. Soc. Am.* **95**, 3339-3349 (1994)

[77] F. B. Jensen, W. A. Kuperman, M. B. Porter, H. Schmidt, *Computational Ocean Acoustics* (American Institute of Physics, Woodbury, NY, 1994)

[78] A. Akay, S. Sener, G. C. Gaunaurd, "Acoustic scattering from fluid-filled,

concentric, submerged, cylindrical, elastic shells," J. Acoust, Soc. Am., **94**, 3277-3294(1993)

[79] H. C. Strifors, G. C. Gaunaurd, "Differences in the acoustic echoes from submerged elastic shells containing different fluids," Ultrasonics, **30**, 107-112(1992)

[80] G. C. Gaunaurd, D. Brill, "Acoustic spectrogram and complex-frequency poles of a resonantly excited elastic tube," J> Acoust. Soc. Am. **75**, 1680-1693, (1984)

[81] G. C. Gaunaurd, M. F. Werby, "Resonance response of submerged acoustically excited thick and thin shells," J. Acoust. Soc. Am., **77**, 2081-2093, (1985)

[82] N. D. Veksler, "The analysis of peripheral waves in the problem of plane acoustic wave scattering by a circular cylindrical shell," Acustica, **69**, 63-72, (1989)

[83] G. C. Gaunaurd, M. F. Werby, "Acoustic resonance scattering by submerged elastic shells," ASME Appl. Mech. Rev. **43**, 171-207, (1990)

[84] A. Akay, "Scattering of sound from concentric cylindrical shells," J. Acoust. Soc. Am., **89**, 1572-1578, (1991)

[85] N. H. Sun, P. L. Marston, "Ray synthesis of leaky lamb wave contributions to backscattering from thick cylindrical shells," J. Acoust. Soc. Am. **91**, 1298-1402, (1992)

[86] F. Leon, F. Lecroq, D. Decultot, G. Maze,"Scattering of an obliquely incident acoustic wave by an infinite hollow cylindrical shell," J. Acoust. Soc. Am., **91**, 1388-1397(1991)

[87] N. D. Veksler, V. M. Korsunskii, S. A. Rybak, "Scattering of an obliquely incident plane wave by a circular cylindrical shell, " Sov. Phys. Acoust. **36**,

5-7, (1990)

[88] G. Cramer, "Intr. à l'analyse de lignes courbes algébriques." Geneva, 657-659, (1750).

[89] B.A. Auld, *Acoustic Fields and Waves in Solids Vol.1 & II*, Wiley-Interscience, New York, 1973,

[90] W. Konig, “Hydrodynamisch-akustische Untersuchungen: II. Uber die Krafte zwischen zwei Kugeln in einer schwingenden Flussigkeit und uber di Entstehung der Kundt’s schen Staubfiguren”, Ann. Phys. Chem., **42**, 549-563, (1891)

[91] V. F. K. Bjerknes, Die Kraftfelder: Vieweg und Sohn, Braunschweig, Germany 1909

[92] King, L. V., “On the acoustic radiation on spheres,” Proc. R. Soc. A.,**147**, 212-240, (1933)

[93] T.F.W. Embleton, “Radiation force acting on a sphere in a cylindrical sound field,” J. Acoust. Soc. Am., **28**, 155-155 (1956)

[94] T.F.W. Embleton, “The radiation force on a spherical obstacle in a cylindrical sound field“, Can. J. Phys.**34** no.3, .276-287,(1956)

[95] T.F.W. Embleton, “Mean force on a sphere in a spherical sound field .1. (theoretical)“, J. Acoust. Soc. Am. **26**, 40-45, (1954)

[96] K. Yosioka, Y. Kawasima, “Acoustic radiation pressure on a compressible sphere,” Acustica **5** 167-169(1955)

[97] L. P. Gor’Kov, “On the forces acting on a small particle in an acoustical field in an ideal fluid”, Sov. Phys.-Doklady, **6** 773-775, (1962)

[98] W. L. Nyborg, “Radiation pressure on a small rigid sphere”, J. Acoust. Soc. Am. **42**, 947-950, (1957)

[99] K. Higashitani, M. Fukushima, Y. Matsuno, “Migration of suspended particles in a plane stationary ultrasonic field”, Chemical Engineering Science*;* **36(12)**, 1877-1882, (1981)

[100] P. J. Westervelt, “The theory of steady forces caused by sound waves,” J. Acoust. Soc. Am., **23**, 312-315, (1951)

[101] S. D. Danilov, M. A. Mironov, “Radiation pressure force acting on a small particle in an ideal fluid,” Sov. Phys. Acoust., **30(4)**, 280-283, (1984)

[102] S. D. Danilov, M. A. Mironov “Mean force on a small sphere in a sound field in a viscous fluid” Journal of the Acoustical Society of America; **107(1)**,143-153, (2000)

[103] A. A. Doinikov, “Acoustic radiation pressure on a compressible sphere in a viscous fluid”, J. Fluid Mech., **267**, 1-21, (1994)

[104] A. A. Doinikov, “Theory of acoustic radiation pressure for actual fluids,” Phys. Rev. E, **54(6)**, 6297-6303, (1996)

[105] A. A. Doinikov, “Acoustic radiation force on a spherical particle in a viscous heat-conducting fluid I-general formula,” J. Acoust. Soc. Am., **101(2)**, 713-721, (1997)

[106] A. A. Doinikov, “Acoustic radiation force on a spherical particle in a viscous heat-conducting fluid II-force on a rigid sphere,” J. Acoust. Soc. Am., **101(2)**, 722-730, (1997)

[107] A. A. Doinikov, “Acoustic radiation force on a spherical particle in a viscous heat-conducting fluid III-force on a liquid drop,” J. Acoust. Soc. Am., **101(2)**, 731-740, (1997)

[108] TM. Barmatz, P. Collas, “Acoustic radiation potential on a sphere in plane, cylindrical, and spherical standing wave fields,” J. Acoust. Soc. Am, **77(3)**, 928-945, (1985) T

[109] F. Hager, E. Benes, A summary of all forces acting on spherical particles in a sound field, at *Ultrasonics International,* **91**, 283-286, (1991)

[110] T. Gaida, O. Doblhoff-Dier, K. Stutzenberger, H. Katinger, W Burger, M. Groschl, B. Handl, E. Benes, "Selective retention of viable cells in ultrasonic resonance field devices," Biotechnol. Prog. **12**, 73-76 (1996)

[111] O. Doblhoff-Dier, T Gaida, H. Katinger, W. Burger, M. Groschl, E. Benes, "A novel ultrasonic resonance field device for the retention of animal cells," Biotechnol. Prog. **10**, 428-432(1994)

[112] G. Whitworth, "Flow generated around particle clusters in a rotating ultrasonic waveguide," J. Acoust. Soc. Am. **104**, 1284-1288,(1998)

[113] G. Whitworth, W. Nyborg, "A rotating ultrasonic waveguide for studying acoustic radiation forces on particles," J. Acoust. Soc. Am., **90**,2091-2096, (1991)

[114] R. K. Gould, W. T. Coakley, "The effects of acoustic forces on small particles in suspension", in *Proceedings of the 1973 Symposium on Finite Amplitude Wave Effects in Fluids*, edited by L. Bjorno, Pergamon, Guildford, 1974, 252-257

[115] M. Hilpert, C. T. Miller, "Experimental investigation on the resonance of a liquid column in a capillary tube," J. Coll. And Inter. Sci., **219**, 62-68(1999)

[116] T.F.W. Embleton, "Mutual interaction between 2 spheres in a plane sound field", J. Acoust. Soc. Am., **34**, 1714-1718, (1962)

[117] M. A. H. Weiser, "Interparticle forces on red cells in a standing wave field," Akustica, **56**, 114-119, (1984)

[118] L. A. Crum, "Bjerknes forces on bubbles in a stationary sound field," J. Acoust. Soc. Am., **57**, 1363-1371, (1975)

[119] A. Doinikov, "Effects of the second harmonic on the secondary bjerknes

force", Phys. Rev. E., **59,** 3016-3021 (1999)

[120] A. Doinikov, "Acoustic radiation interparticle forces in a compressible fluid," *J. Fluid Mech.*, **444**, 1-21(2001)

[121] X. Zheng, R. E. Apfel, "Acoustic interaction forces between two fluid spheres in an acoustic field," J. Acoust. Soc. Am., **97(4)** 2218-2226, (1995)

[122] T. Hasegawa, Y. Watanabe, "Acoustic radiation pressure on an absorbing sphere," J. Acoust. Soc. Am. **63(6)**, 1733-1737,(1978)

[123] J. Awatani, "Study on acoustic radiation pressure(IV Memoirs Of The Institute Of Scientific And Industrial Research; **12**, 95-102, (1955)

[124] J. Awatani, "Studies on acoustic radiation pressure, I, J. Acoust. Soc. Am., **27(2)**, 278-281, (1955)

[125] J. Wu, G. Du, "Acoustic radiation force on a small compressible sphere", J. Acoust. Soc. Am. **87**,997-1003(1989)

[126] S. M. Woodside, B. D. Bowen, J. M. Piret, "Measurement of ultrasonic forces for particle-liquid separations," AIChE Journal, **43(7),** 1727-1736, (1997)

[127] S. M. Woodside, J. M. Piret, M. Groschl, E. Benes, B. D. Bowen, "Acoustic force distribution in resonators for ultrasonic particle separation", AIChE Journal, **44(9)**, 1976-1983, (1998)

[128] G. Haar, S. J. Wyard, "Blood cell banding in ultrasonic standing wave fields: a physical analysis," Ultasound Med. Biol., **4**, 111-124, (1978)

[129] C. S. Kwiatkowski, P. L. Marston, "Resonator frequency shift due to ultrasonically induced microparticle migration in an aqueous suspension: observations and model for the maximum frequency shift," J. Acoust. Soc. Am. **103**, 3290-3300(1998)

[130] M. Barmatz, P. Collas, “Acoustic radiation potential on a sphere in plane, cylindrical, and spherical standing wave fields,” J. Acoust. Soc. Am, **77(3)**, 928-945, (1985)

[131] M. A. H. Weiser, R.E. Apfel, “Extension of acoustic levitation to include the study of micron-size particles in a more compressible host liquid,” J. Acoust. Soc. Am. **71** 1261(1982)

[132] Thomas, Dominic, Watson, Q-SORTING AND MIS RESEARCH: A PRIMER Communications of the AIS v8 n1 2002

[133] V. A. Shutilov, Fundamental physics of ultrasound, Gordon and Breach Science Publ., New York, 1988

[134] H. Schlicting, *Boundary Layer Theory* McGraw-Hill, New York (1955)

[135] N. Riley, “Acoustic Streaming”, Theoret. Comput. Fluid Dynamics, **10**, 349-356, (1998)

[136] R. K. Gould, W. T. Coakley, M. A. Grundy, “Upper sound pressure limits on particle concentration in fields of ultrasonic standing-wave at megahertz frequencies,” Ultrasonics, **34(4)**, 239-243, (1991)

[137] J. D. Pohlhammer and W. D. O’Brien, Jr. “The Relationship Between Ultrasonic Attenuation and Speed in Tissues and Constituents: Water, Collagen, Protein and Fat” *Medical Physics of CT and Ultrasound: Tissue Imaging and Characterization*, eds. G.D. Fullerton and J. A. Zagzebski, 409-435, Med. Phy. Mon. **6**, AIP, NY (1980)

[138] M. Greenspan, C. E. Tschiegg, “Speed of sound in water by a direct method,” J. Res. NBS Report No. 2795, **59**, 249(1957)

[139] W. D. Wilson, “Speed of sound in distilled water as a function of temperature and pressure,” J. Acoust. Soc. Am., **31**, 1067-1071, (1959)

[140] W. D. Wilson, “equation for the speed of sound in sea water,” J. Acoust.

Soc. Am., **52**, 1357-1361, (1960)

[141] V. A. Del Grosso, C. W. Mader, “Speed of sound in pure water,” J. Acoust. Soc. Am. **56**, 1442-1446, (1972)

[142] V. A. Del Grosso, “New equation for the speed of sound in natural waters,” J. Acoust. Soc. Am., **56**, 1084-1088, (1974)

[143] V. A. Del Grosso, “New equation for the speed of sound in natural waters,” J. Acoust. Soc. Am., **56**, 1084-1088, (1974)

[144] N. Bilaniuk, G. S. K. Wong, “Speed of sound in pure water as a function of temperature,“*J. Acoust. Soc.Am.*, **93(3)**, 1609-1612, (1993)

[145] W. Marczak, “Water as a standard in the measurements of speed of sound in liquids,” J. Acoust. Soc. Am.,**102(5)**, 2776-2779, (1997)

[146] W. Kroebel and K. H. Mahrt, “Recent results of absolute sound velocity measurements in pure water and sea water at atmospheric pressure,” Acoustica, **35**, 154-164, (1976)

[147] K. Fujii, R. Masui, “Accurate measurements of the sound velocity in pure water by combining a coherent phase-detection techniqud and a variable path-length interferometer,” J. Acoust. Soc. Am., **93**, 276-282(1993)

[148] J. Lubbers, R. Graff, “A simple and accurate formula for the sound velocity in water,” Ultrasound Med. Biol. **24(7)**, 1065-1068, (1998)

[149] J V. A. Belogol’skii, S.S. Sekoyan, L. M. Samorukova, S. R. Stefanov, V. I. Levtsov, “Pressure dependence of the sound velocity in distilled water,” Measurement Techniques, **42(4)**, 406-413

[150] E. Leung, C. P. Lee, N. Jacobi, T. G. Wang, “Resonance frequency shift of an acoustic chamber containing a rigid sphere,” J. Acoust. Soc. Am., **72(2)**, 615-620, (1982)

[151] M. Saito, N. Kitamura, M. Terauchi, “Ultrasonic manipulation of locomotive microorganisms and evaluation of their activity”. *J. Appl. Phys.* **92**: 7581-7586 (2002)

[152] K. Yasuda, S. Haupt, S. Umemura, “Using acoustic radiation force as a concentration method for erythrocytes” *J. Acoust. Soc. Am.* **102**: 642-645, (1997)

[153] E. Chase, RA. Hoffman, “Resolution of dimly fluorescent particles: A practical measure of fluorescence sensitivity”. *Cytometry* **33**: 267-279, (1998)

[154] P. Goodwin, W. Ambrose, R. Keller, “Single-molecule detection in liquids by laser-induced fluorescence”. *Accounts Of Chemical Research* **29**: 607-613, (1996**)**

[155] R. Murphy. Ligand, Binding, Endocytosis and Processing. In *Flow Cytometry and Sorting*, ed. MR Melamed, Lindmo, T., Mendelsohn, M.L., pp. 355-366. New York, NY: Wiley-Liss, Inc. (1990)

[156] L. Sklar, B. Edwards, S. Graves, J. Nolan, E. Prossnitz, “Flow cytometric analysis of ligand-receptor interactions and molecular assemblies”. *Annual Review Of Biophysics And Biomolecular Structure,* **31**: 97-119, (2002)

[157] R. Hoffman, V. Maino, D. Recktenwald, H. Webster, “BD biosciences contributions in CD4 counting and immune status for HIV/AIDS”, *Cytometry* **15,** 129-132, (2002)

[158] I. Jani, G. Janossy, D. Brown, F. Mandy, “Multiplexed immunoassays by flow cytometry for diagnosis and surveillance of infectious diseases in resource-poor settings”, *Lancet Infectious Diseases* **2**, 243-250, (2002)

[159] G. Janossy, I. Jani, M. Kahan, D. Barnett, F. Mandy, H. Shapiro, “Precise CD4 T-cell counting using red diode laser excitation: For richer, for poorer”, *Cytometry* **15**: 78-85, (2002)

[160] F. Mandy, M. Bergeron, G. Houle, J. Bradley, J. Fahey, “Impact of the international program for Quality Assessment and Standardization for Immunological Measures Relevant to HIV/AIDS: QASI” *Cytometry* **15**: 111-116, (2002)

[161] F. Mandy, J. Nicholson, B. Autran, G. Janossy, “T-cell subset counting and the fight against AIDS: Reflections over a 20-year struggle”, *Cytometry* **15,** 39-45, (2002)

[162] H. Cai, P. White, D. Torney, A. Deshpande, Z. Wang, B. Marrone, J. Nolan, “Flow cytometry-based minisequencing: A new platform for high-throughput single-nucleotide polymorphism scoring”, *Genomics* **66**: 135-143, (2000)

[163] J. Chen, M. Iannone, M. Li, J. Taylor, P. Rivers, A. Nelsen, K. Slentz-Kesler, A. Roses, M. Weiner, “A microsphere-based assay for multiplexed single nucleotide polymorphism analysis using single base chain extension”, *Genome Research* **10**, 549-557, (2000)

[164] L. Green, H. Cai, D. Torney, D. Wood, F. Uribe-Romeo, L. Kaderali, J. Nolan, P. White, High-throughput SNP scoring with GAMMArrays: Genomic analysis using multiplexed microsphere arrays. *Proceedings Of The Society Of Photo Optical Instrumentation Engineers* **3**, 308-315, (2002)

[165] M. Iannone, J. Taylor, J. Chen, M. Li, P. Rivers, K. Slentz-Kesler, M. Weiner, “Multiplexed single nucleotide polymorphism genotyping by oligonucleotide ligation and flow cytometry”, *Cytometry* **39**: 131-140, (2000)

[166] K. Kellar, M. Iannone, “Multiplexed microsphere-based flow cytometric assays”, *Experimental Hematology* **30**: 1227-1237, (2002)

[167] J. Taylor, D. Briley, Q. Nguyen, K. Long, M. Iannone, M. Li, F. Ye, A. Afshari, E. Lai, M. Wagner, J. Chen, M. Weiner, “Flow cytometric platform

for high-throughput single nucleotide polymorphism analysis", *Biotechniques* **30**: 661, (2001)

[168] C. Brugnara, "Use of reticulocyte cellular indices in the diagnosis and treatment of hematological disorders", *International Journal Of Clinical & Laboratory Research* **28**, 1-11, (1998)

[169] Z. Darzynkiewicz, E. Bedner, P. Smolewski, "Flow cytometry in analysis of cell cycle and apoptosis", *Seminars In Hematology* **38**: 179-193, (2001)

[170] M. Ormerod, "The study of apoptotic cells by flow cytometry", *Leukemia* **12,** 1013-1025, (1998)

[171] R. Sgonc, J. Gruber, "Apoptosis detection: An overview", *Experimental Gerontology* **33**: 525-533, (1998)

[172] I. Vermes, C. Haanen, C. Reutelingsperger, "Flow cytometry of apoptotic cell death", *Journal Of Immunological Methods* **21,** 1-2, (2000)

[173] A. Chigaev, A. Blenc, J. Braaten, N. Kumaraswamy, C. Kepley, R. Andrews, J. Oliver, B. Edwards, E. Prossnitz, R. Larson, L. Sklar. "Real time analysis of the affinity regulation of alpha(4)-integrin - The physiologically activated receptor is intermediate in affinity between resting and Mn2+ or antibody activation", *Journal Of Biological Chemistry* **28**: 48670-48678, (2001)

[174] Chigaev, G. Zwartz, S. Graves, D. Dwyer, H. Tsuji, T. Foutz, B. Edwards, E. Prossnitz, R. Larson, L. Sklar, "Alpha 4beta 1-integrin affinity changes govern cell adhesion", *J Biol Chem* **278**: 38174 – 38182, (2003)

[175] L. Sklar, B. Edwards, S. Graves, J. Nolan, E. Prossnitz. "Flow cytometric analysis of ligand-receptor interactions and molecular assemblies", *Annual Review Of Biophysics And Biomolecular Structure,* **31**: 97-119, (2002)

[176] T. Holyoake, F. Nicolini, C. Eaves. "Functional differences between

transplantable human hematopoietic stem cells from fetal liver, cord blood, and adult marrow", *Experimental Hematology,* **27**: 1418-1427, (1999)

[177] X. Song, J. Nolan, B. Swanson, "Optical biosensor based on fluorescence resonance energy transfer: Ultrasensitive and specific detection of protein toxins", *Journal Of The American Chemical Society,* **11**: 11514-11515, (1998)

[178] X. Song, J. Nolan, B. Swanson, "Optical signal transduction triggered by protein-ligand binding: Detection of toxins using multivalent binding", *Journal Of The American Chemical Society,* **20**: 4873-4874, (1998)

[179] X. Song, J. Shi, J. Nolan, B. Swanson, "Detection of multivalent interactions through two-tiered energy transfer", *Analytical Biochemistry,* **291**: 133-141, (2001)

[180] J. Bienvenu, G. Monneret, N. Fabien, J. Revillard, "The clinical usefulness of the measurement of cytokines", *Clinical Chemistry And Laboratory Medicine,* **38**, 267-285, (2000)

[181] F. Giner, A. Orfao, "Applicability of flow cytometry in the diagnosis and follow-up of acute leukemias", *Medicina Clinica,* **30**, 423-436, (2002)

[182] K. Han, A. Pantuck, A. Belldegrun, J. Rao, "Tumor markers for the early detection of bladder cancer", *Frontiers In Bioscience,* **7**, E19-E26, (2002)

[183] R. Rampaul, A. Miremadi, S. Pinder, A. Lee, I. Ellis, "Pathological validation and significance of micrometastasis in sentinel nodes in primary breast cancer", *Breast Cancer Research,* **3**, 113-116, (2001)

[184] J. Nolan, F. Mandy, "Suspension array technology: New tools for gene and protein analysis", *Cellular And Molecular Biology,* **47**, 1241-1256, (2001)

[185] D. Campana, E. Coustan-Smith, "Detection of minimal residual disease in

acute leukemia by flow cytometry", *Cytometry*, **15**, 139-152, (1999)

[186] F. Giner, A. Orfao, "Applicability of flow cytometry in the diagnosis and follow-up of acute leukemias", *Medicina Clinica,* **30,** 423-436, (2002)

A. Orfao, G. Schmitz, B. Brando, A. Ruiz-Arguelles, G. Basso, R. Braylan, G. Rothe, F. Lacombe, F. Lanza, S. Papa, P. Lucio, J. San Miguel, "Clinically useful information provided by the flow cytometric immunophenotyping of hematological malignancies: Current status and future directions", *Clinical Chemistry,* **45**, 1708-1717, (1999)

[188] B. Pui, D. Campana. "New definition of remission in childhood acute lymphoblastic leukemia", *Leukemia,* **14**, 783-785, (2000)

[189] M. Iannone, T. Consler, K. Pearce, J. Gray, "Molecular interactions of nuclear receptors by flow cytometry", *Cytometry,* **11**, 36-37, (2002)

[190] M. Iannone, T. Consler, K. Pearce, J. Stimmel, D. Parks, J. Gray, "Multiplexed molecular interactions of nuclear receptors using fluorescent microspheres", *Cytometry,* **44**, 326-337, (2001)

[191] G. Janossy, I. Jani, M. Kahan, D. Barnett, F.Mandy, H. Shapiro, "Precise CD4 T-cell counting using red diode laser excitation: For richer, for poorer.", *Cytometry,* **15**, 78-85, (2002)

[192] J. Nolan, B. Shen, M. Park, L. Sklar, "Kinetic analysis of human flap endonuclease-1 by flow cytometry", *Biochemistry,* **10**, 11668-11676, (1996)

[193] Shen, J. Nolan, L. Sklar, M. Park, "Essential amino acids for substrate binding and catalysis of human flap endonuclease 1", *Journal Of Biological Chemistry,* **19**, 9173-9176, (1996)

[194] P. Pala, T. Hussell, P. Openshaw, "Flow cytometric measurement of intracellular cytokines", *Journal Of Immunological Methods,* **21**, 1-2, (2000)

[195] P. Daugherty, G. Chen, B. Iverson, G. Georgiou, “Quantitative analysis of the effect of the mutation frequency on the affinity maturation of single chain Fv antibodies”, *Proceedings Of The National Academy Of Sciences Of The United States Of America,* **29**, 2029-2034, (2000)

[196] P. Daugherty, G. Chen, M. Olsen, B. Iverson, G. Georgiou, “Antibody affinity maturation using bacterial surface display”, *Protein Engineering,* **11**, 825-832, (1998)

[197] P. Daugherty, M. Olsen, B. Iverson, G. Georgiou, “Development of an optimized expression system for the screening of antibody libraries displayed on the Escherichia coli surface”, *Protein Engineering,* **12**, 613-621, (1999)

[198] M. Feldhaus, R. Siegel, L. Opresko, J. Coleman, J. Feldhaus, Y. Yeung, J. Cochran, P. Heinzelman, D. Colby, J. Swers, C. Graff, H. Wiley, K. Wittrup, “Flow-cytometric isolation of human antibodies from a nonimmune Saccharomyces cerevisiae surface display library”, *Nature Biotechnology,* **21**, 163-170, (2003)

[199] Orr, L. Carr, K. Wittrup, E. Roy, D. Kranz, “Rapid method for measuring ScFv thermal stability by yeast surface display”, *Biotechnology Progress,* **19**, 631-638, (2003)

[200] T, Van den Beucken, H. Pieters, M. Steukers, M. Van der Vaart, R. Ladner, H. Hoogenboom, S. Hufton, “Affinity maturation of Fab antibody fragments by fluorescent-activated cell sorting of yeast-displayed libraries”, *Febs Letters,* **10**, 2-3, (2003)

[201] J. VanAntwerp, K. Wittrup, “Fine affinity discrimination by yeast surface display and flow cytometry”, *Biotechnology Progress,* **16**, 31-37, (2000)

[202] Ivnitski, I. Abdel-Hamid, P. Atanasov, E. Wilkins, “Biosensors for detection of pathogenic bacteria”, *Biosensors & Bioelectronics,* **14**, 599-624, (1999)

[203] M. Olsen, D. Stephens, D. Griffiths, P. Daugherty, G. Georgiou, B. Iverson,. “Function-based isolation of novel enzymes from a large library”, *Nature Biotechnology,* **18**, 1071-1074, (2000)

[204] S. Graves, J. Nolan, J. Jett, J. Martin, L. Sklar, “Nozzle design parameters and their effects on rapid sample delivery in flow cytometry”, *Cytometry,* **47**, 127-137, (2002)

[205] A. Schwartz, E. Fernandez-Repollet, “Quantitative flow cytometry”, *Clinics In Laboratory Medicine,* **21**, 743, (2001)


Los Alamos
NATIONAL LABORATORY
EST.1943